Leibniz-Institut
für Festkörper- und
Werkstoffforschung
Dresden

Annual Report 2018

Publisher:
Leibniz Institute for Solid State and Materials Research Dresden

Executive Board:	Prof. Dr. Bernd Büchner, Scientific Director
	Dr. Doreen Kirmse, Administrative Director
Address:	Helmholtzstraße 20
	D-01069 Dresden
Phone:	+49 (0) 351 4659 0
Fax:	+49 (0) 351 4659 540
Internet:	www.ifw-dresden.de
e-mail:	info@ifw-dresden.de

Leibniz-Institut
für Festkörper- und
Werkstoffforschung
Dresden

Annual Report 2018

Contents

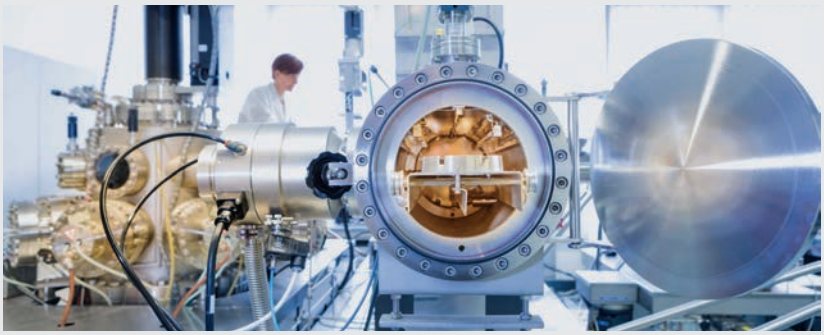

Review of 2018

2018 was a year in which we have achieved a lot: trying to set the course for the future development of IFW. The most prominent decision in this respect was made by the panel of international referees within the Germany's Excellence Strategy, a program designed to strengthen top-level research at universities in Germany. The Technical University of Dresden could place six full proposals preselected in the first stage of the highly competitive procedure. The IFW participated in three of them to different degrees. It was a great success that among these three proposal the one with the broadest IFW involvement has been approved, namely the Center of Excellence – Complexity and Topology in Quantum Matter at TU Dresden and University of Würzburg – in short ct.qmat. The IFW will be part of this unique research platform for comprehensive studies of the fundamental physics of topological quantum materials and their vast application potential. This achievement can be seen as a confirmation of the leading position of the IFW's research on quantum and functional materials. It also presents an ideal context in which the IFW can continue to strengthen its strategic position in the scientific landscape both locally and internationally.

Another forward-looking decision was to start the preparations for a new building and for strategic enlargement of IFW. The need for more laboratories comes from the strong involvement of IFW in the ct.qmat cluster. Additionally the new building shall provide space for the realization of an enhanced technology transfer including flexible application labs for quantum and nanomaterials, endowed professorships and a business incubator center to foster spin-offs in IFW research fields. In 2018 we discussed these plans in detail both internally as well as with the Scientific Advisory Board and the Board of Trustees. We are very happy to get strong support in this matter from both Boards, the ministry and the municipal administration.

The prerequisite for the realization of our ambiguous plans is a strongly positive vote of the evaluation panel in 2021, not only for the strategic plans but also for the research output of previous years. We are optimistic that we can achieve top marks for

Strained Nanoarchitectures Lab,
Photo: Jürgen Lösel

our scientific work and will make every effort. Our research program with the three pillars of Quantum Materials, Functional materials and Nanoscale Materials provides a proven framework for that. It is well focused on the investigation of yet unexplored properties of novel materials with the aim to establish new functionalities and applications. At the same time it is flexible enough to include new developments and upcoming topics.

A good measure for the competitiveness of IFW is the success of third party funding proposals, especially by the German Research Foundation (DFG). In this respect the IFW was very successful in 2018. A big success was the approval of the second funding period for the Collaborative Research Centre "Correlated Magnetism: From Frustration to Topology" (SFB 1143) at the TU Dresden. The IFW is strongly involved in this Collaborative Research Centre. In the new funding period, from 2019 to 2022, the SFB will consist of 19 subprojects four of them based at IFW. In 2018, the IFW continues the strong engagement in DFG Priority Programs. The IFW coordinates two DFG Priority Programs, one on high temperature superconductivity in Iron pnictides (SPP 1458) and one on caloric effects in ferroic materials (SPP 1599). In further five priority programs we participate with several projects, among them the newly formed SPP on skyrmions.

In 2018, Dr. Aliaksei Charnukha has been awarded a prestigious German national Emmy Noether Starting Grant funded by the DFG for a period of five years to establish an independent Junior Research Group in the field of correlated-electron systems at IFW. The new group investigates ordering and emergent phenomena as well as dynamic electronic properties of quantum materials by means of novel terahertz near-field microscopy and spectroscopy at cryogenic temperatures.

Another field of competition and source of funding is the Leibniz Association. In February 2018, Dr. Michael Melzer launched the first Leibniz Junior Research Group on compliant magnetic sensors for e-skins, soft robots and healthcare. It will be co-funded by the Leibniz Association for 5 years. Also in 2018 two IFW proposal

Lecture for Junior Doctors held by Prof. Jens Freudenberger and Dr. Andy Thomas, Photo: Hans-Günther Lindenkreuz

Branchentreff at IFW – meeting place for students with industry, Photo: Crispin-Iven Mokry

Honorary Colloquium for Prof. Jörg Fink on the occasion of his 80th birthday, Photo: Hans-Günther Lindenkreuz

in the Leibniz competition have been approved: We get funding for a second Leibniz Junior Research Group on correlated materials from first principles which will start in 2019 and for the appointment of a female professor on the vacant directors position.

In 2018 we launched the joint Ukrainian-German Project UKRATOP funded by the Federal Ministry of Education and Research for four years. The scientific goal of the project with the title "Topological order of electrons in solids: New materials, Phenomena & application Concepts" is to design new high-quality materials with exceptional surface and edge conditions resulting from their topological nature. After the first recruiting workshop in Kiev in May 2018 eight young scientists and students started their work at IFW in October 2018. In December we organized the International UKRATOP Workshop "Topological Phenomena in Quantum Materials" at IFW.

Another important project funded by the Federal Ministry of Education and Research over the next three years is the network Q.Link.X for tap-proof communication. The IFW is among the 24 partners that have joined their forces in the Q.Link.X network to explore the key technology of quantum repeaters. The IFW project is concerned with semiconductor quantum dots that can emit entangled pairs of photons and thus become ideal information carriers for long-range quantum communication.

All these projects – and those financed by the European Commission – have been acquired in a highly competitive mode. The success in these procedures is far more than a financial asset, but proves the quality and competitiveness of IFW in its core fields.

Three appointment procedures kept us busy in 2018. Despite significant efforts to accelerate the recruitment of a new director of the IFW Institute for Complex Materials this position is still vacant. We hope that our success in the Leibniz Program for Women Professors will give new impetus to the joint procedure with TU Dresden and

Prof. Oliver G. Schmidt recieves the Leibniz Price of the German Research Foundation 2018, Photo: David Ausserhofer

Laser Lab, Photo: Jürgen Lösel

Laureate Colloquium at IFW on the occasion of the Leibniz Prize 2018 awarded to Prof. Oliver G. Schmidt, Photo: Hans-Günther Lindenkreuz



lead not only to a successful appointment in 2019 but also to more female leadership in science. The second appointment procedure was that for a temporary Joint Junior Professorship with TU Dresden. In a very quick and cooperative procedure Prof. Dr. Anna Isaeva has been appointed. The third appointment procedure has been launched for a research group leader at IFW combined with a temporary professorship for materials functionalization at the TU Bergakademie Freiberg. The announcement has been published by the end of 2018. We are now looking forward to a successful recruitment.

Looking back to 2018, some highlights of the Institute's life will certainly be remembered. The most prominent one was the Leibniz Prize award ceremony on March 19 in Berlin. Prof. Dr. Oliver G. Schmidt received the Leibniz Prize in recognition of his outstanding work in the investigation, manufacturing and innovative application of functional nanostructures. On this occasion we organized a colloquium at IFW where the Saxon State Minister for Higher Education, Research and the Arts, Dr. Eva-Maria Stange, and the President of Leibniz Association, Prof. Dr. Matthias Kleiner, appreciated the work of Oliver Schmidt in their speeches. Afterwards the prize winner held an impressive talk on his research that gave a taste of future projects for which he would use the prize money.

Another highlight in 2018 was the "International Workshop on Electron and photon spectroscopies of quantum materials" in the end of January, combined with the honorary colloquium on the occasion of the 80th birthday of Prof. Dr. Jörg Fink. Fifteen years after retirement, the former director of the IFW Institute for Solid State Research still comes to work almost every day, contributing to the scientific output of the institute in a very productive manner. His reputation in the scientific community became visible in the broad and prominent participation in the workshop.

The IFW was also very active in organizing workshops and symposia outside the institute and in the framework of conferences, for example the session "Geometry and Topology-Controlled Nanoarchitectures" and two further symposia during the Joint

Long Night of Sciences 2018 at IFW Dresden,
Photos: IFW Dresden

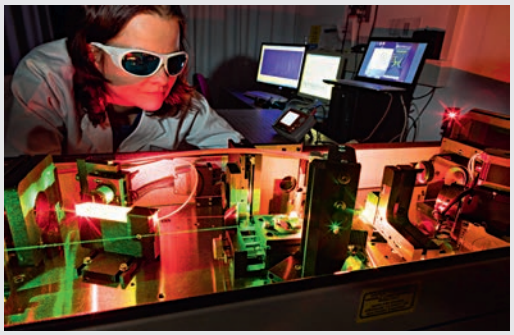

Conference of the Condensed Matter Divisions of the DPG and EPS, in March in Berlin. Other examples are the Heraeus-Seminar on thermoelectrics in Bad Honnef, the workshop on spin, waves & interactions in Greifswald and the bilateral workshop at SPINTEC in Grenoble. In October 2018 the International Surface Acoustic Wave Sensor & Actuator Symposium 2018 took place in Dresden. It was the second time jointly organized by IFW Dresden, SAW Components Dresden GmbH and Silicon Saxony e. V. Last but not least there have been some internal events that brought together IFW members in a more social context, like the IFW summer day, the IFW health day and the Christmas celebration.

Essentially publicly funded, we are obliged to make our research results public. In 2018, IFW scientists have published about 420 articles in scientific journals and conference proceedings. 171 invited talks were presented by IFW scientists at conferences, workshops, seminars and other occasions around the world. In 2018, we were granted 12 patents, and applications for 4 more patents have been made. Apart from these scientific communications the IFW continued its large efforts to make scientific work accessible for the general public and to inspire young people to study science or engineering. In total, we published 17 press releases. A particularly large media attention was reached on a press release concerning a new broadband optical antenna for highly efficient extraction of entangled photons. With a yield of 37% per pulse, it is the brightest source of entangled photons reported so far. An article in nature electronics on improved thermoelectric devices also received much attention in the media.

The IFW has been engaged in joint events of the Dresden network of universities and research institutions. The most prominent event in this respect is the Dresden Long Night of Sciences which takes place once a year before the summer vacancies. In 2018, again, the IFW offered an ample program which attracted about 3500 visitors. Another activity of the network is the event “Junior Doctor”. The IFW contributed not only with an experimental lecture for about 80 kids on low temperature physics in January but also with a special science show in the graduation ceremony which

Laboratories at IFW Dresden,
Photos: Jürgen Lösel



took place in September. Besides these big events we organized almost weekly lab-tours for various visitor groups, from school classes through official representatives to guests from foreign organization.

So we are looking back to a successful year 2018 in the Institute's development. We are quite aware that this is due to the sustainable network of colleagues and partners in universities, research institutes and industry, both, on the regional and the international scale. We thank all of them for their constructive cooperation and are looking forward to taking up future challenges together. Special tribute is paid to the members of the Scientific Advisory Board and of the Board of Trustees as well as the funding organizations that continuously support and foster the positive development of the IFW.

Prof. Dr. Bernd Büchner
Scientific Director

Dr. Doreen Kirmse
Administrative Director

Dr. Oleg Janson, head of the new Leibniz Junior Research Group on correlated materials from first principles, Photo: private

Dr. Michael Melzer, head of the new Leibniz Junior Research Group on magnetic sensors, Photo: private

Dr. Aliaksei Charnukha, head of the new Emmy Noether Research Group at IFW, Photo: IFW Dresden



Facts & Figures

Organization

The Leibniz Institute for Solid State and Material Research Dresden (IFW) is one of currently 95 institutes of the Leibniz Association in Germany. It is a legally independent association, headed by the Scientific Director, Prof. Dr. Bernd Büchner, and the Administrative Director, Dr. Doreen Kirmse.

The scientific body of the IFW Dresden is structured into five institutes, the directors of which are simultaneously full professors at Dresden, respectively Chemnitz Universities of Technology:

- IFW Institute for Solid State Research, Prof. Dr. Bernd Büchner
- IFW Institute for Metallic Materials, Prof. Dr. Kornelius Nielsch
- IFW Institute for Complex Materials, Dr. Thomas Gemming (temporary)
- IFW Institute for Integrative Nanosciences, Prof. Dr. Oliver G. Schmidt
- IFW Institute for Theoretical Solid State Physics, Prof. Dr. Jeroen van den Brink

Further divisions are the Research Technology Division and the Administrative Division.

Financing

The institutional funding of IFW is supplied by the Federal government and by the German states (Länder). In 2018, this funding was EUR 32,862,000 in total.
In addition, the IFW receives project funding from external sources of about 8.2 million Euro. Thereof, about 4.2 million Euro came from German Research Foundation (DFG), 1.6 million Euro from European Union programs, 1.1 million Euro from Federal Government projects, 0.3 million Euro from industry and 1.0 million Euro from other donors including the Free State of Saxony.

Photos: Jürgen Lösel

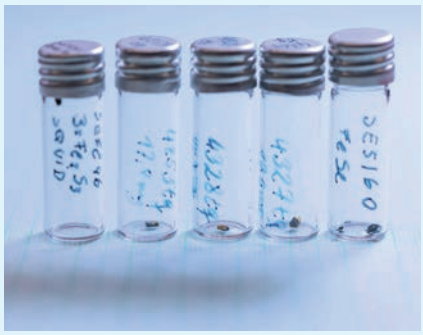

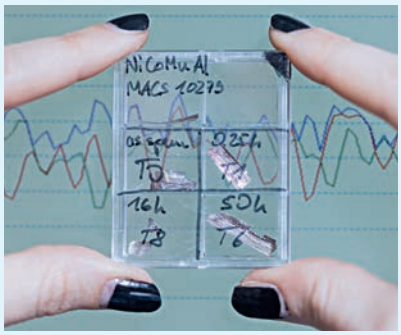

Personnel

On 31 December 2018, 481 staff members were employed at the IFW, including 93 doctorate students as well as 18 apprentices in six different vocational trainings and two business students of a vocational academy. Additionally 48 fellowship holders worked at IFW, among them 19 doctorate students.

Gender equality, as well as work life balance, are defined goals of the IFW Dresden. In 2018, the percentage of women in scientific positions was 24 % and the percentage of women in scientific leading positions was 27 %. The IFW is regularly audited for the certificate “audit berufundfamilie” – a strategic management tool for a better compatibility of family and career.

Number of publications and patents

In terms of publications, the qualitative and quantitative level remains high at the IFW. In 2018, IFW scientists have published 420 refereed journal articles, a considerable number of them in high impact journals. Furthermore, IFW members held 171 invited talks at conferences and colloquia.

By 31 December 2018, the IFW holds 87 patents in Germany and 105 international patents.

Photos: Jürgen Lösel

Research Area 1: Functional Quantum Materials

Pressure-induced dimerization and valence bond crystal formation in the Kitaev-Heisenberg magnet α-$RuCl_3$

G. Bastien, R. Yadav, R. Beltrán Rodríguez, R. Ray, L. Hozoi, A. U. B. Wolter, B. Büchner and J. van den Brink

Abstract

The magnetic properties of α-$RuCl_3$ are described by an anisotropic model of magnetic interactions between the Ru ions, whereby such interactions depend on the direction of the Ru-Ru bonds (Kitaev interactions) on top of isotropic Heisenberg interactions. A remarkable feature of such combined isotropic and anisotropic interactions is the occurrence of a quantum spin liquid state under in an applied magnetic field. We investigated the effect of hydrostatic pressure on the magnetic properties of α-$RuCl_3$ by performing magnetization measurements, X-ray diffraction and *ab-initio* electronic structure calculations. We discovered a pressure-induced magneto-structural transition marked by a shortening of one-third of the Ru-Ru bonds and a simultaneous formation of non-magnetic dimers along such bonds. As a result, with increasing pressure, the magnetization collapses and a non-magnetic valence bond crystal is realized. Overall, our study reveals the competition between the Kitaev magnetic interactions and the formation of metal-metal bonds in α-$RuCl_3$ [1].

Introduction to the Kitaev-Heisenberg magnet α-$RuCl_3$

Ruthenium- and iridium-based materials are known to crystallize in different geometries and, due to strong spin-orbit coupling, exhibit a rich physical phenomena. Of particular interest is the layered honeycomb magnet α-$RuCl_3$, where the Ru^{3+} ions within a layer span a regular hexagonal network (honeycomb lattice). Each Ru^{3+} ion is surrounded by 6 Cl^- ions forming an octahedra and two nearest-neighbor (NN) ions share an edge of this octahedra. A large spin-orbit coupling of the 4*d* Ru ions in such an edge-shared hexagonal network leads to a new type of anisotropic magnetic interactions: the Kitaev interaction [2, 3], implying that the dominant spin component involved in the interaction between two NN magnetic Ru^{3+} ions depends on the direction between the magnetic ions. Due to large inter-layer separation in this van-der-Waals layered compound, the low-energy physics of α-$RuCl_3$ is described by Kitaev interactions between the Ru^{3+} ions with pseudospin-1/2 on the two-dimensional honeycomb lattice in addition to the more isotropic Heisenberg interactions [4]. The spin-1/2 Kitaev model of a two-dimensional honeycomb lattice is an exactly solvable model which supports a quantum spin liquid (QSL) state [3]. QSLs are novel states of matter characterized by the absence of long-range magnetic order down to lowest temperatures together with a high entanglement of spins, and their magnetic excitations cannot be understood within the framework of "conventional" magnets. Therefore, a physical realization of such a state/model is of immense interest theoretically as well as experimentally.

While the presence of small but finite Heisenberg couplings in α-$RuCl_3$ results in an antiferromagnetic long-range order at $T_N \sim 7$ K, a magnetic field of the order of 7–8 T applied in the honeycomb plane can suppress this magnetic order toward the Kitaev-QSL state [5, 6, 7]. However, the role of other tuning parameters in inducing the QSL state and realizing novel ground states stills needs to be elucidated further. In this study, we, therefore, investigated the magnetic properties of α-$RuCl_3$ when subjected to hydrostatic pressure.

Magnetization measurements under pressure

Magnetization measurements under hydrostatic pressure were carried out using a high resolution pressure cell developed at the IFW Dresden for a high accuracy magnetization measurement under hydrostatic pressure up to 6 GPa. Single crystals of α-$RuCl_3$ obtained via a collaboration with the Oak Ridge National Laboratory, USA were measured with this pressure cell.

The magnetic susceptibility χ of α-$RuCl_3$ in the *ab* plane (honeycomb plane) is presented in Figure 1 (a) as a function of temperature and for different pressures. At ambient pressure a phase transition into an antiferromagnetic state was clearly observed at $T_N \approx 7$ K. Under a small hydrostatic pressure of 0.24 GPa, another transition occurs at a much higher temperature $T_{S2} = 140$ K marked by a reduction of the magnetic susceptibility. This transition occurred at different temperatures when the sample was warmed and cooled. At 0.6 GPa and higher pressures this transition is shifted to higher temperatures, followed by a strong suppression of the magnetic susceptibility below T_{S2}, indicating the onset of a non-magnetic ground state of α-$RuCl_3$ under applied pressure. This suppression of the magnetization under pressure is a rather unusual feature and reveals a new characteristic of the Kitaev-Heisenberg magnet α-$RuCl_3$.

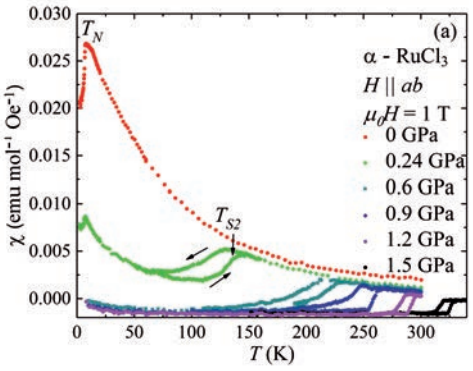

Figure 1. (a) Magnetic susceptibility χ of α-$RuCl_3$ as a function of temperature for different pressures. A magnetic field of 1 T was applied in the honeycomb plane ab. The cooling and warming curves are indicated by black arrows around the 0.24 GPa curve.

The magnetization at 2 K as a function of the magnetic field applied in the basal plane is represented in Figure 1 (b). At ambient pressure, the magnetization starts from zero and slowly increases with the strength of the applied magnetic field, as expected for an antiferromagnet until a critical value of $\mu_0 H_c = 7$–8 T, where the antiferromagnetic long-range order is suppressed and a QSL state is realized [6]. At higher pressure $p = 0.24$ GPa, the magnetization already shows such an upward step at $\mu_0 H_c = 4.3$ T. Since the temperature scan at 5 T, shown in the inset of Figure 1 (b), confirms the absence of an antiferromagnetic transition above 4.3 T, this jump corresponds to the suppression of the antiferromagnetic order by an external magnetic field, similar to the situation at ambient pressure [6]. Thus, the critical field necessary to induce the QSL state is strongly reduced from the corresponding ambient pressure value for $p = 0.24$ GPa. This suggests competition between the QSL phase of α-$RuCl_3$ and a non-magnetic state with increasing pressure. At even higher pressures of 0.6 GPa and 1.8 GPa, the non-magnetic state wins over as seen by the clear collapse of the magnetic response up to 5 T.

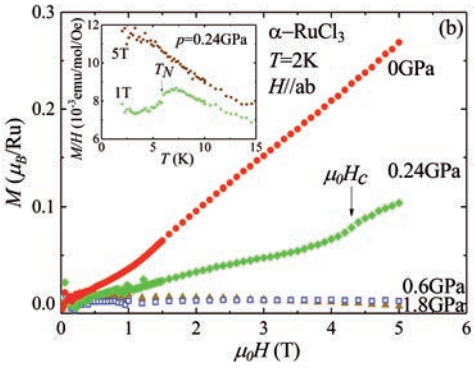

Figure 1. (b) Magnetization of α-$RuCl_3$ at 2 K as a function of magnetic field applied in the *ab* plane for different pressures. H_c indicates the phase transition from the antiferromagnetic order toward the field-induced quantum spin liquid. The inset shows the renormalized magnetization M/H at $p = 0.24$ GPa as a function of temperature for magnetic fields of $\mu_0 H = 1$ T and $\mu_0 H = 5$ T. T_N indicates the magnetic phase transition from the antiferromagnetic order to the paramagnetic state.

These results are summarized in the temperature-pressure phase diagram of α-$RuCl_3$ given in Figure 2. α-$RuCl_3$ undergoes a pressure-induced phase transition at a rather low pressure of 0.2 GPa from an antiferromagnetic into a non-magnetic state. The transition temperature T_{S2} increases rapidly with pressure and reaches room temperature around $p = 1.3$ GPa.

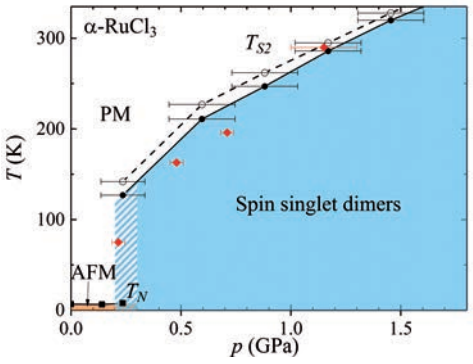

Figure 2. Temperature-pressure phase diagram of α-$RuCl_3$. The filled and open black circles represent the transition temperature T_{S2} at which the magnetization collapses, obtained, by cooling and by warming the sample, respectively. The red squares represent the transition temperature T_{S2} from x-ray diffraction. The striped area represents the region where phase separation occurs.

X-ray diffraction under hydrostatic pressure and quantum chemistry calculations

In order to elucidate the microscopic origin of the pressure-induced transition at T_{S2} toward a non-magnetic ground state and the nature of this state, high-resolution x-ray diffraction under hydrostatic pressure was carried out by collaborators from the Technische Universität Dresden, Germany and ESRF Grenoble, France. It was found that T_{S2} also corresponds to a structural transition from a monoclinic into a triclinic phase, where one third of the Ru-Ru links become shorter, as schematically shown in Figure 3, i.e. a dimerization including all Ru ions takes place. The magnitude of this change of the structure is remarkable: the corresponding Ru-Ru distance reduces from 3.5 to 2.9 Å.

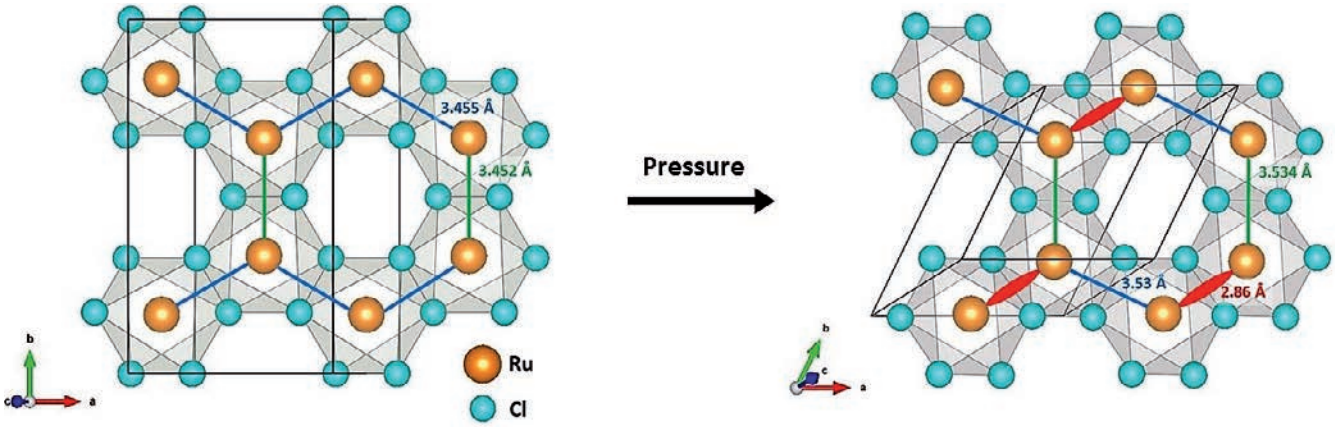

Figure 3. Honeycomb layer of the α-$RuCl_3$ structure at 300 K in the monoclinic phase at ambient pressure (left) and in the triclinic phase at 2.08 GPa (right). The red ellipses represent the pressure-induced Ru-Ru dimers.

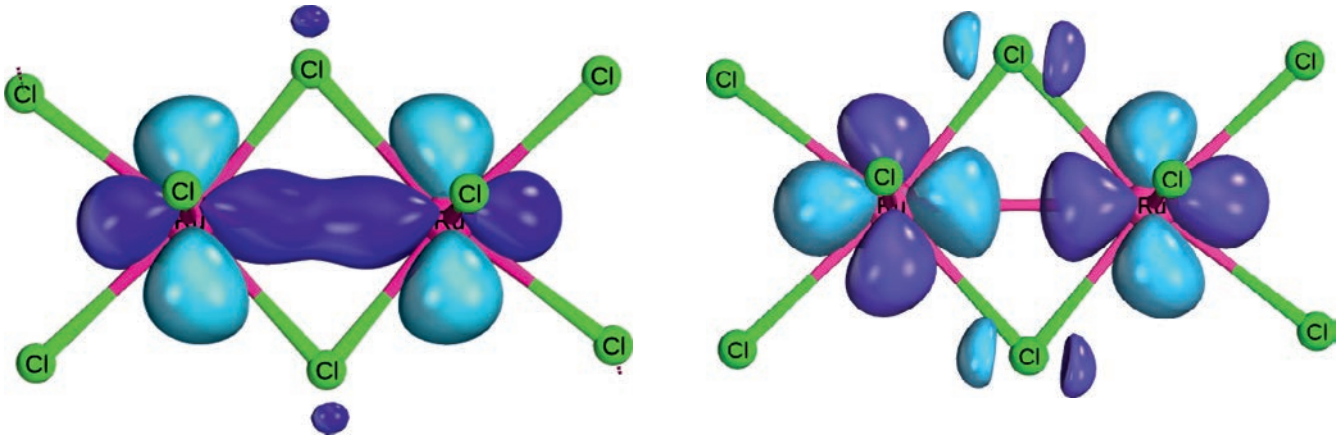

Figure 4. Bonding (left) and antibonding (right) combinations of the relevant Ru orbitals on the shorter Ru-Ru bonds of the crystal structure in the dimer state as obtained by *ab-initio* electronic structure calculations, clearly showing an enhanced overlap in the bonding combination (left panel).

To clarify the implications of this structural transition and its relation to the magnetic interactions, we further performed *ab-initio* electronic structure calculations at the IFW Dresden based on the refined crystal structures at different pressures as determined by x-ray diffraction. These calculations revealed an enhanced overlap of the higher energy occupied orbitals of the Ru^{3+} ions (see Figure 4) which favors an opposite alignment of spin moments at the Ru sites participating in the shorter bonds. This antiferromagnetic interaction between such neighboring Ru ions implies the formation of non-magnetic dimers forming a valence bond crystal and explains the collapse of the magnetization under hydrostatic pressure.

In summary, the combination of magnetization measurements, x-ray diffraction and electronic structure calculations enabled us to determine the nature of the pressure-induced phase transition in α-$RuCl_3$. Our study shows that in α-$RuCl_3$, under pressure, Kitaev physics is in competition with the formation of spin singlet valence bonds: indeed, α-$RuCl_3$ shows the occurrence of both a quantum spin-liquid state under magnetic field, which is relevant for its topological properties, and a spin solid under hydrostatic pressure, the spin singlet valence bond crystal.

[1] G. Bastien et al., Phys. Rev. B 97 (2018) 241108(R).
[2] A. Banerjee et al., Nat. Mater. 15 (2016) 733.
[3] A. Kitaev, Ann. Phys. 321 (2006) 2.
[4] R. Yadav et al., Sci. Rep. 6 (2016) 37925.
[5] S.-H. Baek et al., Phys. Rev. Lett. 119, (2017) 037201.
[6] A. U. B. Wolter et al., Phys. Rev. B 96, (2017) 041405(R).
[7] R. Hentrich et al., Phys. Rev. Lett. 120 (2018) 117204.

Funding

DFG Collaborative Research Center SFB 1143
DFG Research Grant WO 1532/3-2
European Union's Horizon 2020 research and innovation program under the Marie Skłodowska-Curie Grant Agreement No 796048

Cooperation

Oak Ridge National Laboratory, USA
Technische Universität Dresden, Germany
ESRF Grenoble, France

Engineering Kitaev exchange in stacked iridate layers: impact of inter-layer species on in-plane magnetism

R. Yadav, M. S. Eldeeb, R. Ray, S. Aswartham, M. I. Sturza, S. Nishimoto, J. van den Brink and L. Hozoi

Abstract

Novel functionalities may be achieved in oxide electronics by appropriate stacking of planar oxide layers of different metallic species, MOp and M'Oq. The simplest mechanism allowing to tailor the electronic states in such stacked architectures is of electrostatic nature: M–M' charge imbalance. To clarify the effect of interlayer electrostatics on Kitaev magnetic interactions, we focused on the iridate $H_3LiIr_2O_6$, a recently proposed realization of the Kitaev spin liquid. By quantum chemical calculations, we show that the precise position of H^+ cations between magnetically active $[LiIr2O_6]^{3-}$ honeycomb layers has a strong impact on Kitaev couplings. In particular, stacking with straight interlayer O-H-O links is detrimental to in-plane Kitaev exchange since coordination by a single H-ion of the O ligand implies an axial Coulomb potential and unfavorable polarization of the O 2p orbitals mediating Ir-Ir interactions. Our results therefore provide valuable guidelines for the rational design of Kitaev quantum magnets, indicating unprecedented Kitaev couplings of ≈ 40 meV if linear interlayer linkage is removed.

Kitaev exchange and spin-liquid ground states in honeycomb iridates

The prospect of realizing spin-liquid (SL) ground states in layered honeycomb materials with strong spin-orbit interactions has triggered intense research activity in relation to these lattice systems. Quantum SLs are of particular interest in connection with properties such as protection of quantum information and the emergence of Majorana fermions. On a honeycomb lattice (Figure 1), the essential ingredient for the formation of a quantum SL state is the so-called Kitaev coupling (*K*) between nearest-neighbor (NN) magnetic sites, a bond-dependent Ising-like exchange that must be large enough as compared to the more conventional NN Heisenberg *J*. It reaches quite robust values for d^5 electron configurations in iridium honeycomb oxides such as Na_2IrO_3 [1] but also in the ruthenium halide $RuCl_3$ [2]. In the latter, a SL phase is realized by applying an external magnetic field [3].

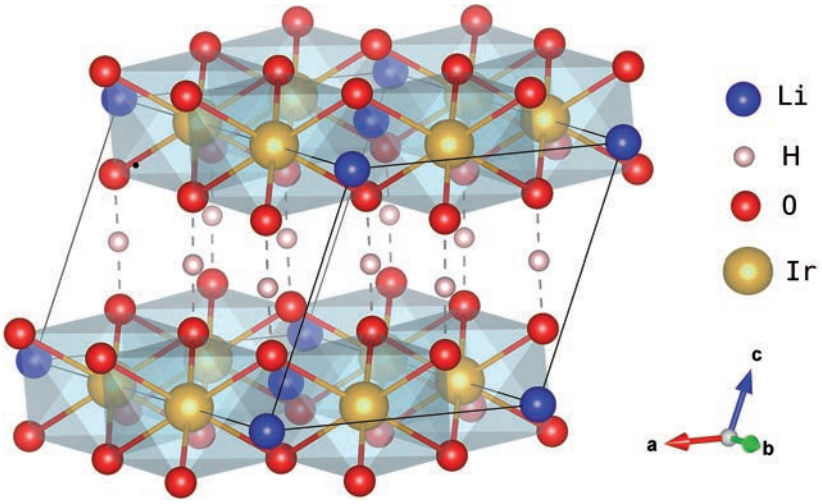

Figure 1: Layered honeycomb network of IrO_6 octahedra in $H_3LiIr_2O_6$. For the the most idealized stacking pattern, interlayer connectivity is realized through linear O-H-O links.

One peculiar prediction on the quantum chemical computational side is an enhancement of the Kitaev coupling K at large Ir-O-Ir bond angles [4]. The Ir-O-Ir bond angles are 90° for cubic edge-sharing octahedra, but in most honeycomb compounds they reach larger values due to trigonal compression of the oxygen cages. The largest Ir-O-Ir bond angles so far have been reported for $H_3LiIr_2O_6$, nearly 100°. Interestingly, a SL ground state was recently inferred for this material [5]. We examined in this context the Kitaev interactions of $H_3LiIr_2O_6$ by quantum chemical computational methods [6, 7] but for ideal stacking of the honeycomb layers found rather modest K values as compared to, *e.g.*, Na_2IrO_3 [1] and earlier predictions for 100° Ir-O-Ir angles [4]. In particular, on both types of Ir-Ir links the Kitaev K is ferromagnetic, with $K \approx -10$ meV [6, 7]. The bond 'asymmetry' is only 5 % and residual Heisenberg interactions are weak; the ratio $|K/J|$ is $|K/J| \approx 6$, which puts the system relatively close to the 'pure' Kitaev limit. The additional exchange anisotropies Γ can even exceed J in magnitude but being frustrating they do not act towards long-range magnetic order.

From the values and bond asymmetry of the NN magnetic interactions, $H_3LiIr_2O_6$ appears to be indeed closer to the Kitaev model than any other A_2IrO_3 iridate (A = Li, Na) considered so far. It is known, however, that in the A_2IrO_3 systems it is not the residual NN couplings that cause, at low temperatures, the experimentally observed zigzag ordered state, but the longer-range magnetic interactions that are present as well, even if the latter can be weak and of the order of a few meV. To test the situation for $H_3LiIr_2O_6$, we computed a generic phase diagram by using the NN quantum chemistry coupling parameters plus farther-neighbor isotropic Heisenberg J's, second-neighbor (J_2) and third-neighbor (J_3). These calculations [6] were performed as exact diagonalizations for 24-site clusters with periodic boundary conditions, in analogy to earlier IFW studies [1, 2, 4]. We found that the quantum SL phase is quickly destabilized by farther-neighbor interactions of Heisenberg type (see Figure 2). If in $H_3LiIr_2O_6$ the values for J_2, J_3 are similar to the ones in the A_2IrO_3

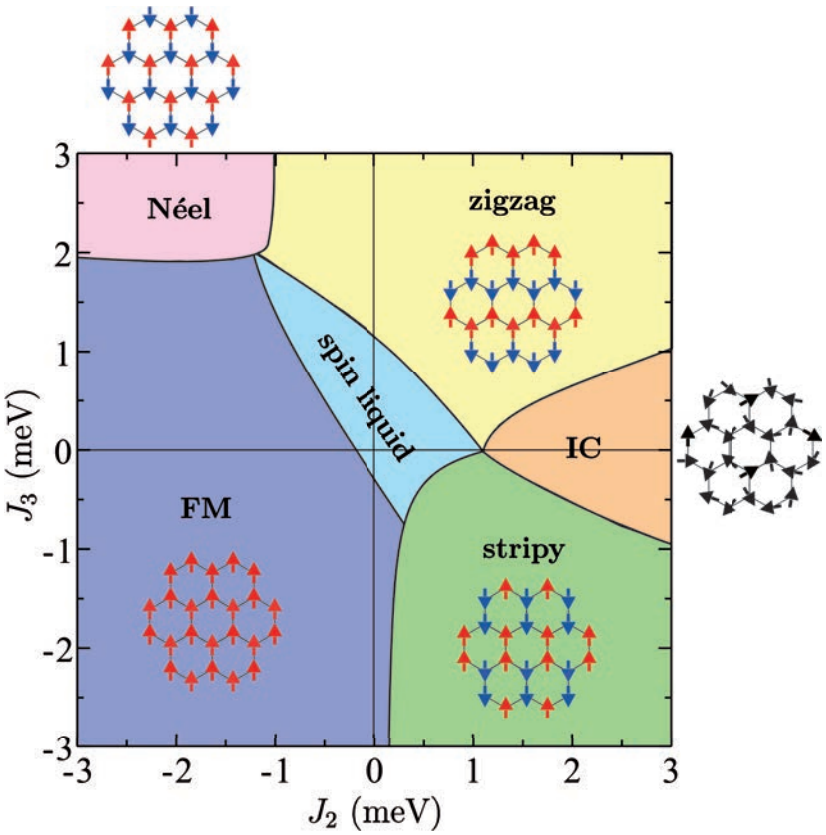

Figure 2: Phase diagram obtained by exact-diagonalization calculations using *ab initio* NN interactions and variable second- and third-neighbor isotropic couplings J_2 and J_3. Schematic spin configurations are also shown.

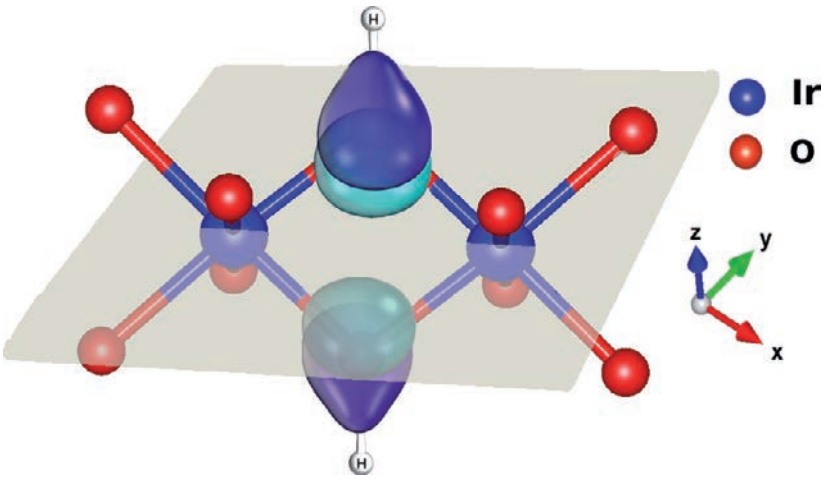

Figure 3: Ir_2O_2 plaquette and the O 2p orbitals mediating superexchange on that plaquette. There are two 5d t_{2g} components per Ir site (not shown) having direct, π-type overlap with the O 2p orbitals depicted in the figure. Adjacent H's strongly affect the d–p overlap matrix elements, through unfavorable polarization of the bridging-ligand 2p functions

family, long-range magnetic order of zigzag type is expected for the NN effective couplings computed on the basis of the crystal structure derived from x-ray diffraction data [5]. A possibility for a quantum SL ground state remains only when $J_2 + J_3 \lesssim 1.2$ meV. If such is indeed realized in $H_3LiIr_2O_6$, the question arises why the farther-neighbor magnetic interactions in this material are so much smaller than estimates made for the A_2IrO_3 systems.

Interlayer electrostatics, impact on Kitaev couplings

From a structural point of view, two groups of compounds can be identified within the family of $5d^5$ honeycomb iridates: Na_2IrO_3 and α-Li_2IrO_3, where each cation in-between the honeycomb-like sheets has six adjacent oxygen sites, and Cu_2IrO_3 plus $H_3LiIr_2O_6$ displaying O-M′-O contacts with just two oxygen NNs for each inter-layer cation M′, if stacking faults are absent. For the latter type of interlayer connectivity, coordination by a single M′ cation of each O ligand implies an out-of-plane field and polarization of the O 2p valence electronic cloud along the O-M′-O axis. We quantified the effect of such anisotropic out-of-plane fields in additional calculations where the two hydrogen ions next to the two O sites shared by Ir NNs were simply taken away. We found that removal of two H's next to the bridging ligands results in a nearly four-fold increase of the Kitaev exchange between in-plane NN pseudospin-1/2 sites: from ≈ –10 meV to –40 meV by spin-orbit configuration-interaction calculations.

A large amount of stacking faults was evidenced in $H_3LiIr_2O_6$, most probably related to the rare situation in which H is bridging two adjacent O sheets. Having the hydroxyl bond in mind, it has been pointed out that an alternative way of writing the chemical formula of this compound is $LiIr_2O_3(OH)_3$. An idealized picture arising from this formula is then that of alternating $[LiIr_2O6]^{3-}$ and $[LiIr_2(OH)_6]^{3+}$ honeycomb-like layers (or slabs), the latter with all bridging O's replaced by hydroxyl groups, as in the related material $Li_2Pt(OH)_6$. The weak bonding between layers and the inherent stacking disorder is even better highlighted in such a representation, the frail hydrogen bonds O-H-O being more apparent. In this context, our results strongly suggest the existence of both 'ideally stacked' (*i.e.*, weak, ≈ –10 meV) and 'fault-present' (*i.e.*, strong, ≈ –40 meV) Kitaev exchange couplings in $H_3LiIr_2O_6$, which then makes the modelling of the extended magnetic lattice more complicated.

In sum, linear interlayer linkage with oxygen and inter-layer cation sites aligned in three-center O-M′-O bonds reduces orbital overlap along Ir-O-Ir paths within the honeycomb-like $LiIr_2O_6$ sheets and the Kitaev couplings, through polarization and bending towards the vertical O-M′-O axis of the Kitaev-active O 2p orbital. We demonstrated this for stacked $[LiIr_2O_6]^{3-}$ honeycomb sheets with O-H-O linear linkage but similar effects should govern the magnetism of related compounds such as Cu_2IrO_3. For the latter, the interlayer O-Cu-O linear contacts are also referred to as dumbbell bonds. Interestingly, for the lighter inter-layer cation, a large amount of stacking faults has been experimentally determined [5]. Our computational findings indicate that randomness in stacking of the honeycomb layers and H-ion vacancies would remove the axial cationic potential at least for part of the O ligands, which yields an unparalleled Kitaev interaction strength of –40 meV for Ir-O-Ir angles of ≈ 100°, larger by factors of 2–3 as compared to the honeycomb Kitaev-Heisenberg material Na_2IrO_3 [1] and 6 in comparison to RuCl3 [2]. Our results therefore provide valuable insights into the magnetism of the SL candidate $H_3LiIr_2O_6$ and additionally simple rules for achieving the Kitaev SL ground state in other honeycomb iridates: large Ir-O-Ir bond angles in the region of 98°, since $J \rightarrow 0$ in that range [4, 7, 8], and coordination of the honeycomb-plane ligands by more than one inter-layer cation. Both features, the nature and the position of ionic species next to the honeycomb sheets and the size of the Ir-O-Ir bond angles, can be in principle more effectively tailored in films and stacked heterostructures.

[1] V. M. Katukuri et al., New J. Phys. 16 (2014) 013056.
[2] R. Yadav et al., Sci. Rep. 6 (2016) 37925.
[3] S.-H. Baek et al., Phys. Rev. Lett. 119 (2017) 037201.
[4] S. Nishimoto et al., Nat. Commun. 7 (2016) 10273.
[5] K. Kitagawa et al., Nature 554 (2017) 341.
[6] R. Yadav et al., Phys. Rev. Lett. 121 (2018) 197203.
[7] R. Yadav et al., Chem. Sci. , DOI: 10.1039/c8sc03018a.
[8] R. Yadav et al., Phys. Rev. B 98 (2018) 121107.

Funding

This work was partially supported by the DFG (SFB-1143 and STU 695/1-1), the Free State of Saxony via the ESF project 100231947 (Young Investigators Group “Computer Simulations for Materials Design” – CoSiMa) and the European Union (ERDF).

Unraveling the Nature of Magnetism of the 5d^4 Double Perovskite Ba_2YIrO_6

S. Fuchs, T. Dey, G. Aslan-Cansever, A. Maljuk, S. Wurmehl, B. Büchner, V. Kataev

Abstract

Predictions of exotic quantum states in complex iridium oxides have yielded a strong interest to their magnetic properties. We report an electron spin resonance (ESR) study of a peculiar member of this family, the double perovskite Ba_2YIrO_6 [1]. On general grounds, it is expected to be nonmagnetic due to the strong coupling of the spin and orbital momenta of Ir^{5+} ($5d^4$) ions. However, controversial reports on either strong antiferromagnetism with static order at low temperatures or just a weak paramagnetism have triggered a discussion on the breakdown of the conventional scenario of the strongly spin-orbit coupled ground states in the $5d^4$ iridates and the emergence of a novel exotic magnetic state. We show that the magnetism of Ba_2YIrO_6 is solely due to a few percent of Ir^{4+} and Ir^{6+} magnetic defects while the regular Ir^{5+} sites remain nonmagnetic. Remarkably, ESR data evidence spin-spin correlations between these sites, suggesting a long-range character of superexchange in the double perovskites.

Introduction

Complex transition metal (TM) oxides feature an intimate interplay of spin, orbital and lattice degrees of freedom as well as strong electronic correlations which give rise to such fascinating phenomena as high temperature superconductivity (HTS), colossal magnetoresistance, multiferroicity and many other intriguing effects. The carrier of spin S and orbital L magnetic moments in these compounds are TM ions with the incompletely filled d-electronic shell. The superexchange interactions between magnetic ions provided by chemical bonds yield complex quantum spin networks of different topology which often exhibit unconventional magnetic behavior.

In many of the prominent members of the TM oxides family such as the celebrated HTS cuprates the orbital momentum of Cu^{2+} ($3d^9$, $S = 1/2$) is quenched and the magnetic moment is of the almost pure spin origin rendering these compounds Heisenberg-like isotropic magnets. Importantly, for about 10 years, another subclass of TM oxides – complex iridium oxides – have attracted an unceasingly large amount of interest in the condensed matter community worldwide due to predictions of exotic ground states in these materials, such as a spin-orbit assisted Mott insulating state, quantum spin liquid phases, Weyl semimetallic behavior, and HTS (see, e.g., [2, 3]). In contrast to the cuprates, the Ir ion in oxides possesses an orbital momentum $L = 1$ and the strong spin-orbit coupling (SOC) characteristic of the heavy 5d TM ions couples S and L to the total angular momentum J. As a result, in its typical oxidation state Ir^{4+}, the Ir ion ($5d^5$, $S = 1/2$, $L = 1$) is characterized by the magnetic Kramers doublet $j_{\text{eff}} = 1/2$ which complex structure is in the core of theoretical models predicting exotic magnetic behavior of iridates [4]. In contrast, in the case of Ir^{5+} ($5d^4$), SOC should yield a singlet ground state with the total angular momentum $J = 0$, making Ir^{5+}-based iridates nonmagnetic.

In this respect, Ir^{5+} double-perovskite iridates Sr_2YIrO_6, Ba_2YIrO_6, and their solid solutions have received recently a great deal of interest due to controversial reports on the observation of either strongly antiferromagnetic behavior with static magnetic order at a low temperature [5, 6] or only a weak paramagnetism [7–9]. This has triggered in turn a substantial number of theoretical works developing various scenarios of the breakdown of the S-L coupling in $4d^4$ and $5d^4$ Mott insulators and its possible relevance to the Ir^{5+} double-perovskite iridates [10–15]. Considering the controversy

of experimental results and theoretical predictions, it was of paramount importance to identify the exact origin of magnetic behavior of these compounds and to consolidate experimental findings with existing theories.

ESR spectroscopic identification of magnetic species

In the challenging task of identifying the origin of unexpected magnetism of the title compound we have employed multifrequency electron spin resonance (ESR) spectroscopy which enables to separate different contributions to the total static magnetization, to study the dynamics and correlations of different spin species, to determine their spin multiplicity, and to measure their intrinsic spin susceptibility. Indeed, Ba_2YIrO_6 shows a rich ESR spectrum comprising several lines (Figure 1). At the smallest excitation frequency ν = 9.56 GHz one observes two low-field peaks characterized with the spectroscopic g-factors g_{left} = 2.00 and g_{mid} = 1.9 and the triplet set of lines at the high-field side with g_{right} = 1.49 (Figure1a). Here, $g = h\nu/(\mu_B H_{res})$ and h, μ_B, and H_{res} are Planck constant, Bohr magneton and resonance field, respectively. The single lines g_{left} and g_{mid} can be straightforwardly assigned to magnetic species carrying the spin S = 1/2. With increasing ν the g_{left} and g_{mid} lines as well as the central line of the g_{right} triplet are getting progressively more separated from each other (Figure 1b) as is expected for ESR signals from the spin species with different g-factors. Remarkably, this is not the case for the satellites of the g_{right} peak. Being resolved at ~10 GHz, at higher frequencies they remain hidden under the broadened main peak, suggesting that this group of lines is characterized by the same g -factor g_{right} = 1.49. Such a triplet structure typically arises from magnetic species carrying spin S = 3/2 which 4-fold degeneracy of the spin levels is partially lifted by the crystal field.

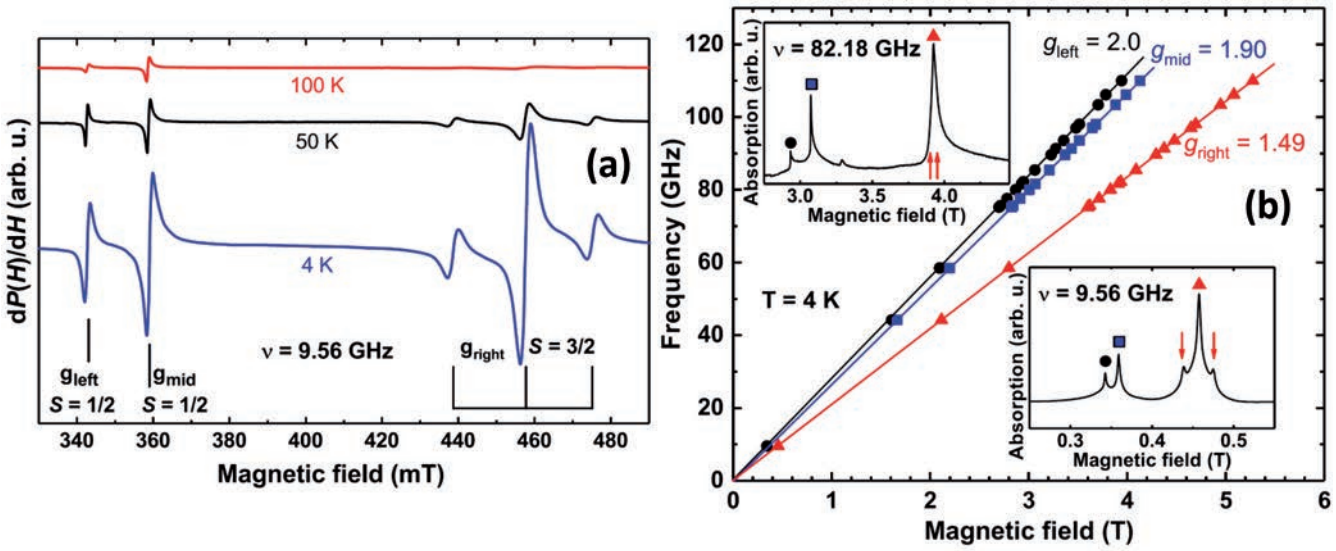

Figure 1: (a) ESR spectra (field derivatives of absorption) at ν = 9.56 GHz at three selected temperatures. The lines at ~340 and ~360 mT and a triplet structure centered around ~460 mT are labeled as g_{left}, g_{mid}, and g_{right}, respectively, with the spin values assigned to each line; **(b)** Frequency ν vs resonance field H_{res} dependence of the peaks in the ESR spectrum (data points). Solid lines are fits to the relation $h\nu = g\mu_B H_{res}$ yielding the g-factor values as indicated in the plot. The insets show spectra at two selected frequencies. Arrows in the upper inset indicate the expected positions of the satellites of the g_{right} peak in the spectrum at 82.18 GHz which are resolved at 9.5 GHz (lower inset).

Since the integrated intensity of an ESR signal I^{ESR} is proportional to the static susceptibility χ of the resonating spins [16], it is possible to evaluate individual contributions of the magnetic centers in Ba_2YIrO_6 to the total static magnetic response and to analyse them in terms of the Curie-Weiss law $I_i^{ESR} \sim \chi = C/(T - \theta)$. Here $C \sim g^2 S(S + 1)n_i$ is the Curie constant, n_i is the spin concentration, and θ is the Curie-Weiss temperature being a measure of the magnetic interaction strength. The results of such an analysis are summarized in Table 1. The total concentration of spins contributing to the ESR spectrum Σn_i is about 4 % per unit cell, in agreement with the static magnetic data [7]. The S = 3/2 centers have the largest $\theta \sim$ -10 K and, thus, are "more correlated" than other spin species contributing to the signals g_{left} and g_{mid}. In the ESR response these magnetic correlations manifest in the broadening of the signals below $T \sim$ 20 K (Figure 2).

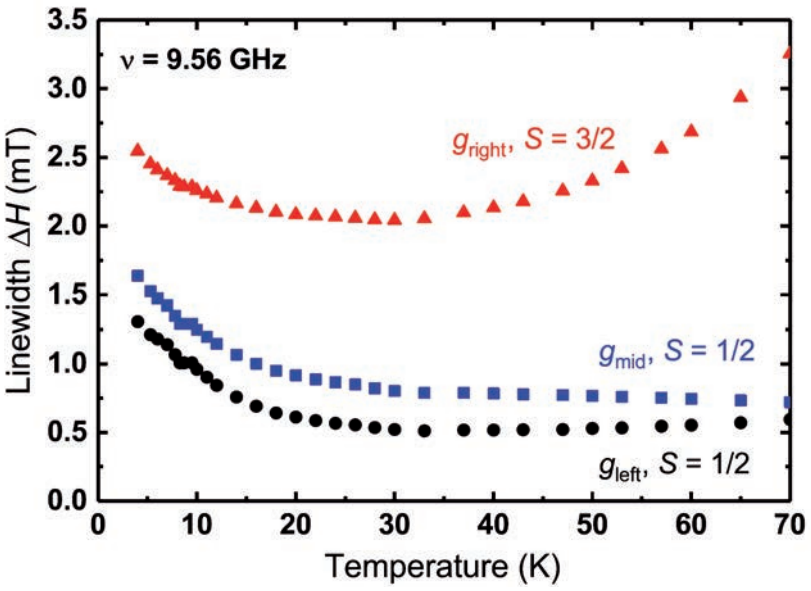

Figure 2: Temperature dependence of the width ΔH of the ESR signals g_{left}, g_{mid}, and g_{right} (main peak) at ν = 9.56 GHz. The growth of $\Delta H(T)$ below ~ 20 K indicates the onset of the critical regime characterized by the slowing down of the timescale of spin-spin correlations and a growth of their spatial extension. An increase of the width of the g_{right} line associated with S = 3/2 species above ~ 35 K is characteristic for S = 3/2 systems where the phonon modulation of the crystal field potential gives rise to a T-dependent spin-lattice relaxation at elevated temperatures.

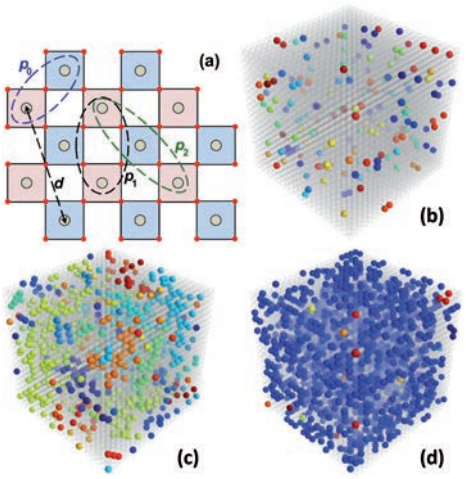

Figure 3: Statistical analysis of the distribution of magnetic centers on the double perovskite (DP) lattice $A_2BB'O_6$. If Ir^{4+} (S = 1/2) and Ir^{6+} (S = 3/2) centers can reside on both B and B′ sites the problem reduces to that on the simple perovskite (SP) lattice ABO_3. **(a)** Definition of exchange path units in the DP lattice: between nearest corner shared octahedral $B'O_6$ and BO_6 – p_0; via two oxygen bridges B′-O-O-B′ – p_1; via the bridge B′-O-B-O-B′ – p_2; d is the geometrical distance between two selected sites; **(b) – (d)** Examples of the clustering of defects (colored spheres) on an SP lattice with the edge length of N = 21 sites with increasing their concentration n. The defects are connected in a cluster by the maximum exchange path length of $2p_0$. Defects belonging to the same cluster have the same color. (a) n = 2 %, practically all defects are independent; (b) n = 4 %, defects are coupled in mid-size clusters; (c) n = 10 %, practically all defects belong to the same cluster.

Origin of magnetism of Ba_2YIrO_6

The small number of magnetic centers in the studied samples of Ba_2YIrO_6 enable a conclusion that the majority of Ir^{5+} ($5d^4$) ions in this compound is in the expected nonmagnetic J = 0 state. Thus, the observed magnetic response can be due to the defect Ir sites in the structure which are likely to occur in a real material. In this respect, particular striking are the S = 3/2 centers. Only Ir^{6+} ($5d^3$) ions have such a spin value and can exhibit such a triplet ESR structure. A strong negative shift of the g-factor g_{right} = 1.49 from the spin-only value of g_s = 2 can be naturally explained by a combined influence of the second order SOC effect and the counteracting effect of the strongly covalent character of Ir–O bonds of the highly oxidized Ir^{6+} [17]. The S = 1/2 ESR line g_{mid} is characterized by a smaller negative shift of the g-factor from g_s = 2. It can be assigned to Ir^{4+} ($5d^5$) centers with the effective spin j_{eff} = 1/2 covalently bonded with the ligands in agreement with ESR observations of Ir^{4+} centers in other hosts with nearly cubic local symmetry [18,19]. Finally, the ESR signal g_{left} = g_s = 2 presumably arises from some S = 1/2 defect centers without sizable covalency effects, presumably from stable radical centers localized at structural imperfections often found in oxide materials (see, e.g., [20]).

The fact that, despite a relatively small concentration of Ir-related defects, they exhibit spin correlated behavior at low temperatures implies the significance of long superexchange paths involving several oxygen bridges. This supports theoretical scenarios of the long-range character of magnetic interactions in the 5d double perovskites [21,22]. In this situation, as our numerical simulations show (Figure 3), magnetic defects may form extended correlated clusters even in a moderate concentration of ≤ 10 %.

Conclusion

Our multifrequency ESR experiments on the pentavalent iridium double perovskite Ba_2YIrO_6 reveal different paramagnetic centers with the total concentration of ~4 % and completely explain the overall static magnetic response. The major contribution can be unambiguously assigned to the defect Ir^{5+} S = 3/2 sites which show clear signatures of magnetic interaction at low temperatures. These experimental results give evidence that the regular Ir^{5+} ($5d^4$) ions remain in the nonmagnetic J = 0 state which rules out the scenario of the breakdown of the spin-orbit coupled j_{eff} states in the $5d^4$ double perovskite iridates and the occurrence of a weak magnetic moment on every Ir^{5+} ($5d^4$) site.

[1] S. Fuchs et al., Phys. Rev. Lett. 120, 237204 (2018)
[2] S. M. Winter et al., J. Phys. Condens. Matter Phys, 7, 195 (2016).
[3] G. Cao and P. Schlottmann, Rep. Prog. Phys. 81, 042502 (2018).
[4] G. Jackeli and G. Khaliullin, Phys. Rev. Lett. 102, 017205(2009), ibid. 105, 027204 (2010).
[5] G. Cao et al., Phys. Rev. Lett. 112, 056402 (2014).
[6] J. Terzic et al., Phys. Rev. B 96, 064436 (2017)
[7] T. Dey et al., Phys. Rev. B 93, 014434 (2016).
[8] L. T. Corredor et al., Phys. Rev. B 95, 064418 (2017).
[9] F. Hammerath et al., Phys. Rev. B 96, 165108 (2017).
[10] S. Bhowal et al., Phys. Rev. B 92, 121113 (2015).
[11] O. N. Meetei et al., Phys. Rev. B 91, 054412 (2015).
[12] K. Pajskr et al., Phys. Rev. B 93, 035129 (2016).
[13] A. Nag et al., Phys. Rev. Lett. 116, 097205 (2016).
[14] A. J. Kim et al., Phys. Rev. Lett. 118, 086401 (2017).
[15] C. Svoboda et al., Phys. Rev. B 95, 014409 (2017).
[16] A. Abragam and B. Bleaney, Electron Paramagnetic Resonance of Transition Ions, International Series of Monographs on Physics (Oxford University, New York, 2012).
[17] J.-H- Choi et al., J. Am. Chem. Soc. 117, 8557 (1995).
[18] J. H. E. Griffiths and J. Owen, Proc. R. Soc. A 226, 96 (1954).
[19] O. F. Schirmer et al., J. Phys. C 17, 1321 (1984).
[20] M. V. Ganduglia-Pirovano et al., Surf. Sci. Rep. 62, 219 (2007).
[21] X. Ou et al., Sci. Rep. 4, 7542 (2014).
[22] S. Kanungo et al., Phys. Rev. B 93, 161116 (2016).

Funding

Deutsche Forschungsgemeinschaft, Grant No. KA 1694/8-1, SFB 1143 (Project B01), and Emmy Noether Grant No. WU 595/3-3.

Table

Signal	g-factor	Spin	θ (K)	I_i^{ESR}/I_{tot}^{ESR} (%)	n_i (%)
g_{left}	2.00	1/2	~ -2	~ 7	~ 0.6
g_{mid}	1.99	1/2	~ -2	~ 20	~ 1.7
g_{right}	1.49	3/2	~ -10	~ 73	~ 1.9

Table 1: Parameters of the lines in the ESR spectrum of Ba_2YIrO_6: g-factor, spin value S, Curie-Weiss temperature θ obtained from the T-dependence of ESR intensities of individual lines $I_i^{ESR} \sim \chi = C/(T - \theta)$, relative spectral weights of the signals I_i^{ESR}, and absolute concentration of spins per unit cell n_i.

Multiplet of Skyrmion States on a Curvilinear Defect: Reconfigurable Skyrmion Lattices

V. Kravchuk, D. D. Sheka[1], A. Kákay[2], O. M. Volkov[2], U. K. Rößler, J. van den Brink, D. Makarov[2], Y. Gaididei[3]

Abstract

Geometrical curvature of magnetic film modifies properties of topological magnetic solitons: domain walls, vortices, skyrmions. Here we focus on new properties of chiral magnetic skyrmions arising due to the curvature. We show that a skyrmion can be effectively pinned on a localized curvilinear defect. The pinning can significantly lower the skyrmion energy. Thus, a skyrmion induced deformation of an elastic magnetic film is predicted. Periodically arranged curvilinear defects can result in a skyrmion lattice as the ground state. A skyrmion pinned on a curvilinear defect demonstrates a multiplet of equilibrium states forming a ladder of energy levels. A switching between these states can be controlled by the pulse of magnetic field.

Topology meets curvature in magnetism

Micromagnetism is an area of solid state physics where topological solitons (TS) are usual objects of study. A domain wall is the simplest example of a one-dimensional TS. Two-dimensional TS are divided into two groups: the meron-like and skyrmion-like solitons, which have half-integer and integer topological charge (defined by the "wrapping number" as degree of mapping from the physical two-dimensional space to the Bloch sphere encoding the orientation of the magnetization vector), respectively. Vortices in easy-plane magnets and chiral skyrmions in noncentrosymmetric magnets are typical examples of merons and skyrmions, respectively. Existence of 1D and 2D TS is reliably confirmed experimentally. This is in contrast to Hopfions – the 3D TS, which were predicted four decades ago but they still require an experimental evidence. All these objects are solitons because of spatially localized energy density and they are topological because there is no continuous and local deformation of the magnetization, which may unwind them, i.e. transforms them to the uniformly magnetized state.

Besides the topological charge, most TSs are characterized by chirality – the binary quantity, which is associated with clockwise (CW) or counter-clockwise (CCW) rotation. For example, chirality determines CW or CCW rotation of magnetization in a Bloch domain wall when moving from one domain to another, it determines CW or CCW magnetization circulation around the core of the magnetic vortex. In planar films and rectilinear wires the TSs are doubly degenerate with respect to the chirality. However, curvature of the magnet can lead to strong effects of the chirality symmetry breaking. For example, a domain wall on a Möbius stripe exhibits a coupling between geometrical chirality of the stripe and chirality of the domain wall magnetic structure, which selects a preferred chirality [1]. Velocity of the vortex domain wall on a tube is chirality dependent [2]. A magnetic vortex on a spherical shell experiences a chirality-dependent deformation [3] and demonstrates the chirality symmetry breaking in the process of the vortex polarity switching [4]. Many effects of the chirality symmetry breaking can be explained by emergence of the curvature induced exchange driven Dzyaloshinskii-Moriya interaction (DMI) [5]. A prominent example of this effect is stabilization of a magnetic skyrmion on a ferromagnetic spherical shell free of intrinsic chiral interactions [6], see Figure 1. Thus, chirality is the point where topology meets curvature.

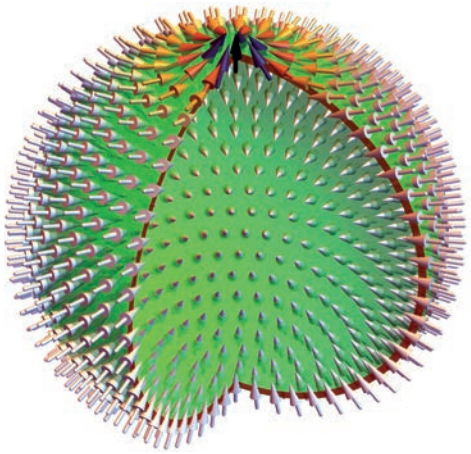

Figure 1: DMI-free magnetic skyrmion stabilized on the Co spherical shell with radius 17 nm and easy-normal anisotropy.

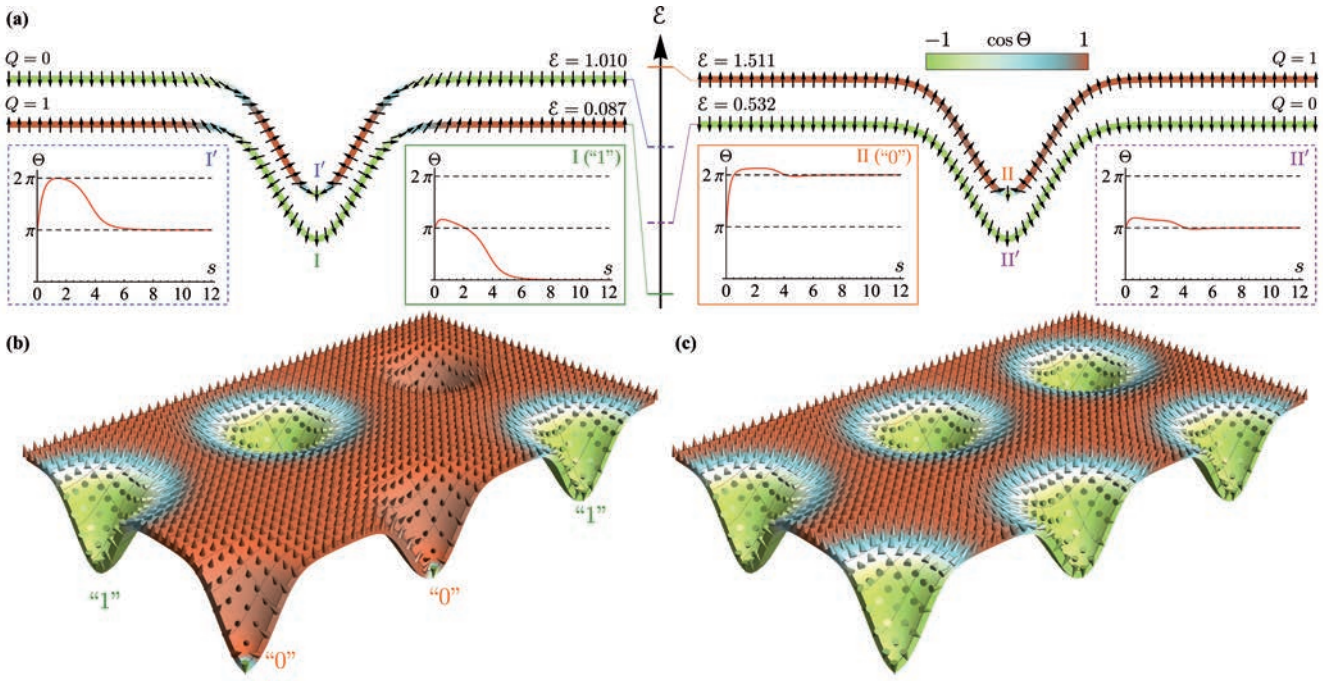

Figure 2: Individual skyrmion profiles and skyrmion lattices. **(a):** Equilibrium magnetization states of a single Gaußian-shaped concave bump are shown in a vertical cross-section view. Arrows indicate the magnetization distribution with the normal component coded by the color. The insets I, II, I′ and II′ show the magnetization profiles in terms of $\Theta(s)$ – the angle between magnetization and normal to the surface as a function of the distance along the surface. Vertical shows distribution of the corresponding energy levels in units of energy of the Belavin-Polyakov soliton. The Gaußian bumps have amplitude $A = 3l_m$ and radius $r_0 = l_m$. **(b):** Two skyrmion states with big (I) and small (II) radii are shown on the same bumps arranged in a square lattice. These skyrmion solutions can be considered as logical states "1" and "0" of an information bit. **(c):** Skyrmion lattice as a ground state.

Curvilinear defects enrich physics of magnetic skyrmions

A chiral skyrmion is a localized particle-like TS, which is stabilized in films of non-centrosymmetric magnets due to the presence of chiral interactions [7, 8]. Nontrivial topology of skyrmions and efficient coupling with spin currents are promising concepts for a number of spintronic applications, e.g. all current controlled computer memory and logic elements, relying on the topological Hall effect [9]. In order to use skyrmions in devices, their condensation into periodic lattices in the presence of magnetic field has been deemed an important effect necessary to employ their impact on electronic transport [8]. Our theoretical studies now demonstrate that an array of curvilinear defects periodically arranged on the magnetic film can induce a field free skyrmion lattice [10], see Figure 2(c). In this case, symmetry of the skyrmion lattice can be arbitrarily controlled.

In order to study the curvature effects on skyrmion properties we consider a simple model, which includes curvature and allows the skyrmion stabilization. Namely, we studied a thin curvilinear ferromagnetic film which has the following magnetic interactions: the isotropic exchange of the strength A, easy-normal uniaxial anisotropy of the strength K, and the interfacial DMI of the strength D. This system has a length scale $l_m = (A/K)^{1/2}$ and in statics it is completely controlled by a single dimensionless parameter $d = D\,(AK)^{-1/2}$. The physical meaning of length l_m is understood to fix a typical domain wall width, and for common magnetic materials one can estimate $l_m \approx 5$nm. Parameter d is the DMI strength measured in units of the domain wall energy density. For planar films, stable skyrmions exist under the condition $IdI<4/\pi$ and have the following features: (i) for a given value of d the skyrmion solution is unique; (ii) the skyrmion energy is always higher than the energy of the uniform perpendicular state, i.e. the planar skyrmion is an excitation of the ground state. The curvature changes both of these well known features.

For a curvilinear magnetic film in form of an arbitrary surface of rotation we derived a general equation, which describes all possible equilibrium magnetization states of the film [10]. Generally, this equation has topological as well as non-topological solutions. An example for a certain case of a curvilinear defect in form of Gaußian bump is shown in Figure 2. There is a number of principal differences as compared

to the planar case: (i) Topologically non-trivial ($Q = 1$) as well as trivial ($Q = 0$) solutions are generally not unique: for given values of geometrical and material parameters a set of equilibrium magnetization states can appear with a ladder of energy levels. This makes the curvilinear defect conceptually similar to a quantum well with a finite number of discrete energy levels. However, in contrast to the quantum systems only transitions between levels with the same Q are allowed. Such transitions are expected to be accompanied by emission or absorption of magnons. (ii) The lowest energy level can be a topological non-trivial ($Q = 1$) skyrmion state. Therefore, curvilinear defects arranged in a periodical lattice generate a zero-field skyrmion lattice as a ground state of the system, see Figure 2(c).

Let us consider skyrmions of small and big radii, which are shown in the Figure 2 (a,b) as states I ("1") and II ("0"), respectively. Their radii are close to extrema points of the Gaußian curvature. The radius of skyrmion II is one order of magnitude smaller than the radius of the skyrmion stabilized by the intrinsic DMI in a planar film for the same value of d. Thus, the small radius skyrmion is stabilized mostly by the curvature induced DMI [6], while the big radius skyrmion is a result of the cooperative action of the intrinsic DMI and curvature. Note also that the big and small skyrimons have opposite chiralities. This is a result of direct competition of the intrinsic and curvature induced DMIs. The topologically trivial state I′ can be treated as a joint state of small and big radii skyrmions, which compensate topological charges of each other. And the state II′ is an intermediate one between uniform $\boldsymbol{m} = \boldsymbol{e}_z$ and normal $\boldsymbol{m} = \boldsymbol{n}$ states, what reflects the competition between exchange and anisotropy interactions. The structures of the states I and I′ as well as states II and II′ are very close but differ in the presence or absence of the small-radius skyrmion at the bump center. In Figure 2(a) we show only stable solutions with the total change of magnetization tilt angle not larger than π. Solutions with the larger variation of the tilt angle, so called skyrmioniums are in principle also possible.

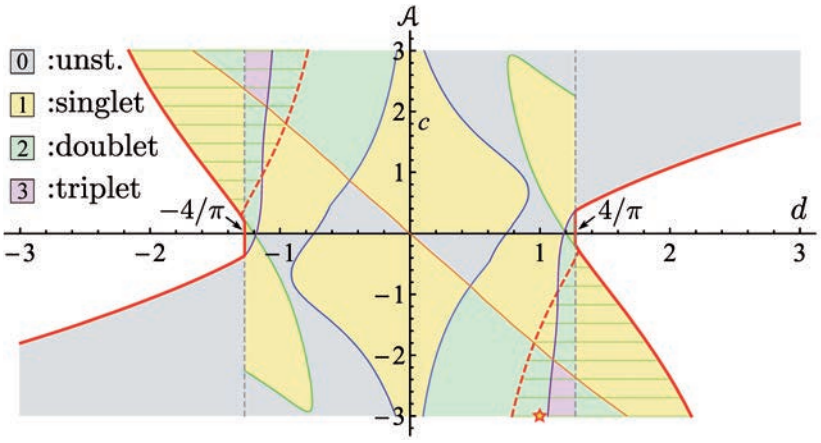

Figure 3. Diagram of skyrmion states for Gaußian bump with radius $r_0 = l_m$. In the white area the skyrmion solutions does not exist. Number of any other area (see legend) coincides with the number of stable skyrmion solutions. At least one skyrmion solution exists within the gray area '0', however the bump center is a position of unstable equilibrium for it. Within the other areas the corresponding number of skyrmions are pinned at the bump center. The horizontal dashing shows areas where one of the multiplet skyrmion states is the ground state of the system. Star marker shows parameters of Figure 2.

In order to systematize possible skyrmion solutions that can appear on Gaußian bumps, we build a diagram of skyrmion states, see Figure 3. For the given bump amplitude and value of the DMI constant all equilibrium radially symmetrical solutions (topological as well as non-topological) of the Landau-Lifshitz equation have been numerically constructed. Then a linear stability analysis was applied for each of the solutions. The results are presented in form of the diagram, Figure 3. The following general features can be established: (i) The range of skyrmions existence widens with increasing bump amplitude. (ii) For a wide range of parameters (gray area '0') the skyrmion centered on the bump experiences a displacement instability because the bump center is a position of unstable equilibrium. (iii) In the vicinity of the critical value $IdI = 4/\pi$ there is a wide area of parameters (the dashed area), where the skyrmion state has the lowest energy in the class of radially symmetrical solutions.

Our systematic theoretical study establishes bumpy or otherwise curvilinearly distorted ferromagnetic films as promising arena for the stabilization and control topological solitons. In particular, switching between different pinned skyrmion states may endow such films with novel functionalities for spintronic applications.

[1] O.V. Pylypovskyi, et al., Phys. Rev. Lett, 114, 197204 (2015).
[2] M. Yan, et al., Appl. Phys. Lett. 100, 252401 (2012).
[3] V. Kravchuk et al., Phys. Rev. B 85, 144433 (2012).
[4] M. Sloika et al., Appl. Phys. Lett., 104, 252403 (2014).
[5] Yu. Gaididei et al., Phys. Rev. Lett. 112, 257203 (2014).
[6] V. Kravchuk et al., Phys. Rev. B 94, 144402 (2016).
[7] R. Wiesendanger et al., Nature Rev. Mater 1 16044 (2016).
[8] N. Nagaosa et al., Nature Nanotech. 8, 899 (2013).
[9] A. Fert et al., Nature Rev. Mater. 2 17031 (2017).
[10] V. Kravchuk, et al., Phys. Rev. Lett. 120, 067201 (2018).

Funding

This work has been supported by the Ukrainian-German Excellence Center (UKRATOP), DFG via SFB 1143 and by ERC within the EU 7th Framework Programme (ERC Grant No. 306277) and the EU FET Programme (FET-Open Grant No. 618083).

Cooperation

[1] Taras Shevchenko National University of Kyiv, Kyiv, Ukraine;
[2] Helmholtz-Zentrum Dresden-Rossendorf e.V., Institute of Ion Beam Physics and Materials Research, Dresden, Germany;
[3] Bogolyubov Institute for Theoretical Physics of National Academy of Sciences of Ukraine, Kyiv, Ukraine;

Mapping Chiral 3D Magnetic Textures at the Nanoscale

D. Wolf, S. Schneider, D. Pohl, F. Harder, J. Krehl, B. Rellinghaus, K. Nielsch, B. Büchner, A. Lubk

Abstract

Novel synthesis methods and the discovery of complex magnetic textures at the nanoscale triggered an expansion of nanomagnetism into three dimensions (3D) exploring unconventional magnetic configurations [1] such as skyrmions with corresponding applications in field sensing [2], magnetic memory [3], and spintronics [4, 5]. Further advances in nanomagnetism including skyrmionics particularly depend upon the ability to build a fundamental understanding of the full 3D spin texture including its coupling to surfaces and interfaces as present in devices. Here we report on the development of high-resolution 3D magnetic field mapping techniques and application to chiral magnetic textures (including skyrmions), addressing several technological and conceptual challenges.

Introduction

Advances in nanomagnetism depend upon the ability to build a fundamental understanding of materials in which complex 3D magnetic textures can be generated, stored and manipulated. A prominent example is the large class of chiral textures, such as magnetic vortices and skyrmions, which occur by balancing multiple magnetic interactions, with the symmetry of the latter playing a crucial role. In particular, magnetic skyrmions are stable and highly mobile textures with a topologically non-trivial non-coplanar spin structure. The existence of skyrmions has been theoretically predicted with crucial contributions from scientists of the IFW Dresden [6–8] before their direct observation in bulk and thin film chiral magnets [9, 10]. The concept has transformed our approach to spintronics because it provides an example of how nanometre scale magnetic inhomogeneities may address fundamental challenges of high data rate, low energy electronics for information technologies. Indeed, in the wake of this discovery, a whole zoo of non-trivial textures [e.g. 11–13] including different types of skyrmions, magnetic bobbers, or merons have been theoretically predicted and eventually found in different material classes and geometries – with the goal to exploit these nanosized solitons as information bits in data storage and to perform logical operations by moving them in magnetic nanostructures [14, 15]. Studying 3D magnetic configurations at the nanoscale requires new techniques for high resolution imaging of spin textures.

Several Transmission Electron Microscopy (TEM) techniques such as in-line electron holography [5] or off-axis electron holography [16] have been heavily used for studying magnetic configurations in nanoscale geometries as they facilitate the quantitative measurement of the projection of in-plane (i.e. perpendicular to the beam) components of the magnetic induction (B-field) [21, 22]. In the double aberration-corrected FEI Titan3 80–300 microscope of the IFW, recently equipped with an electrostatic biprism for off-axis holography, magnetic structures, down to several nanometers depending on the thickness and magnetization of the sample of interest, can be resolved. A higher “magnetic” resolution in the magnetization component parallel to the electron beam and thus perpendicular to the sample surface may be achieved by means of a measurement of the electron-energy-loss magnetic chiral dichroism (EMCD) [18]. As with the X-ray counterpart of this approach (X-ray magnetic circular dichroism, XMCD), this method allows for the element-specific measurement of the asymmetry in projected density of states of the majority and minority out-of-plane spin and orbital angular momentum states of 3d transition metals [19].

To employ the technique for the investigation of nanomagnetic textures, we recently revisited the theory of EMCD in order to identify diffraction conditions, in particular the sample thickness and the crystal orientation, which maximize the typically small EMCD signal (e.g., in helimagnets) [20]. If additional symmetries or other boundary conditions are present it is occasionally possible to derive the 3D magnetic configuration from one projection only. However, the reconstruction of arbitrary fields (most notably chiral ones) calls for an extension of the conventional 2D mapping on which we elaborate in the following.

Tomographic Electron Holography

Indeed, combining off-axis electron-holographic magnetic field mapping and tomography (part of which developed in the IFW) allows for quantitatively reconstructing spin textures in 3D [21, 22]. In order to reconstruct the 3D distribution of the vector field $\boldsymbol{B}$, a tilt series of holograms (projections) has to be recorded and fed to tomographic reconstruction algorithms. By tilting about a particular axis, we obtain a complete set of projections of the Cartesian component parallel to that tilt axis, which suffices to reconstruct that component tomographically in 3D (see Figure 1). This approach has been previously used by us to study, e.g., magnetic nanowires [20, 21]. To reconstruct the full vector field $\boldsymbol{B}$ three tilt series around perpendicular axis are necessary. Commercially available TEM specimen holders, however, allow tilting only about two independent axes. Therefore, we have to use the solenoidal character of the $\boldsymbol{B}$-field, i.e. div $\boldsymbol{B}$ = 0, to obtain one unknown component. The whole acquisition and reconstruction process is elaborate involving various alignment, registration and reconstruction steps (see [21, 22] for details of these crucial steps). In the result section the first example of a full EHT reconstruction of magnetic states in a stacked Cu-Co nanowire is shown. Note that in addition to the previously mentioned limitations imposed by the tilt geometry of the specimen holder a number of other technological challenges currently prevent the application of the technique to a wider range of problems notably including magnetic textures under cryogenic conditions as well as magnetic textures stabilized by external magnetic fields such as skyrmions. Recently we undertook the first step to overcome these and result of a first EH tilt series on spin textures in isotropic helimagnets, namely $Fe_{0.95}Co_{0.05}Ge$, are shown below [23].

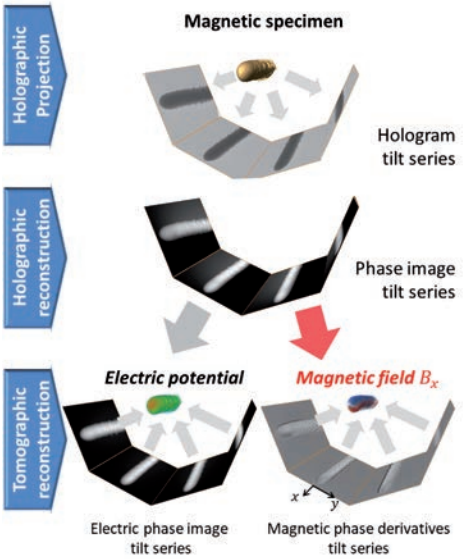

Figure 1: Principle of EHT for the 3D reconstruction of intrinsic electro-magnetic fields. A tilt series of holograms covering a tilt range of 360° is recorded, and reconstructed holographically. The resulting phase image tilt series is separated in its electric/magnetic part by calculating half of the sum/difference between opposite (180° mutually tilted) projections. To obtain the 3D electric potential the tilt series of electric phase image is tomographically reconstructed. To obtain the 3D magnetic field, i.e. one component in direction of the tilt axis, the magnetic phase images need to be differentiated in direction perpendicular to the tilt axis prior the reconstruction.

Results

Employing dual-tilt-axis EHT we reconstruct the remnant magnetic configuration of an electro-deposited Co/Cu multilayered nanowire (NW) (Figure 2). The 3D structural and chemical distribution was obtained simultaneously from the mean inner potential tomogram (Figure 1c) reconstructed from the electric phase shift of the NW. The 3D magnetic induction distribution has a spatial resolution of approximately 10 nm and reveals the presence of vortex states and homogeneously polarized states in the individual Co disks. Moreover the vortex states are individually canted with respect to the NW axis. A deeper analysis involving micromagnetic considerations reveals that the presence of different magnetic states as well as the canting can be traced back to the shape of the individual Co disks as well as local anisotropy variations.

To extend the tomographic investigation to skyrmion textures, notably those in B20 helimagnets ($Fe_{0.95}Co_{0.05}Ge$ in our case), the holographic tilt series has to be recorded under cryogenic conditions and applied external field rotating with the sample. While we currently work on a magnetic field holder, liquid nitrogen cooling can be facilitated by using a dedicated cooling holder. Pertaining technical limitations of these holders restrict the tilt angle to ±30° in this case preventing a full tomographic reconstruction.

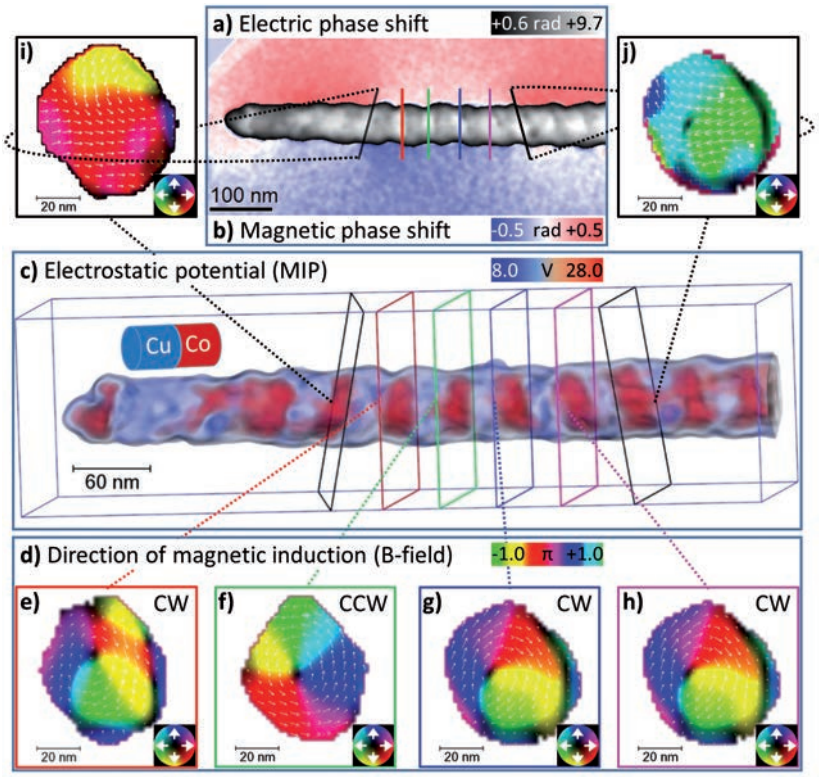

Figure 2: 3D reconstruction of a Co/Cu multilayered nanowire (NW) by EHT. (**a**) The electric phase shift (grey scale) is proportional to the projected potential of the NW. (**b**) The magnetic phase shift (red-white-blue) is proportional to the magnetic flux illustrating the stray field of the NW. (**c**) The electrostatic potential displays the 3D morphology of the Cu (blue) and Co (red) segments. (**d**) Direction of the 3D magnetic induction representing the magnetic configuration within the Co cylinders, i.e., (counter-)clockwise ([C]CW) vortex states (**e–h**). The outer Co segments (**i,j**) are magnetized almost homogeneously in mutually opposite direction. This explains why a magnetic stray field leaks out of the NW at these positions as observed in the magnetic phase shift (**b**).

We therefore compared the information obtained from a cryogenic external-field-free tilt-angle-limited tilt series of the helical phase and quantitative reconstructions of projected in-plane magnetic fields in the skyrmion lattice from off-axis holography with different surface modulations of the skyrmion texture, e.g., the chiral surface twist (Figure 3). The results suggest that none of the previously proposed 3D spin texture modulations for skyrmions can explain the observed effects of overall damping of the projected fields and their modulation under rotation, and more comprehensive tomographic studies are require to explore this surface modulation [23].

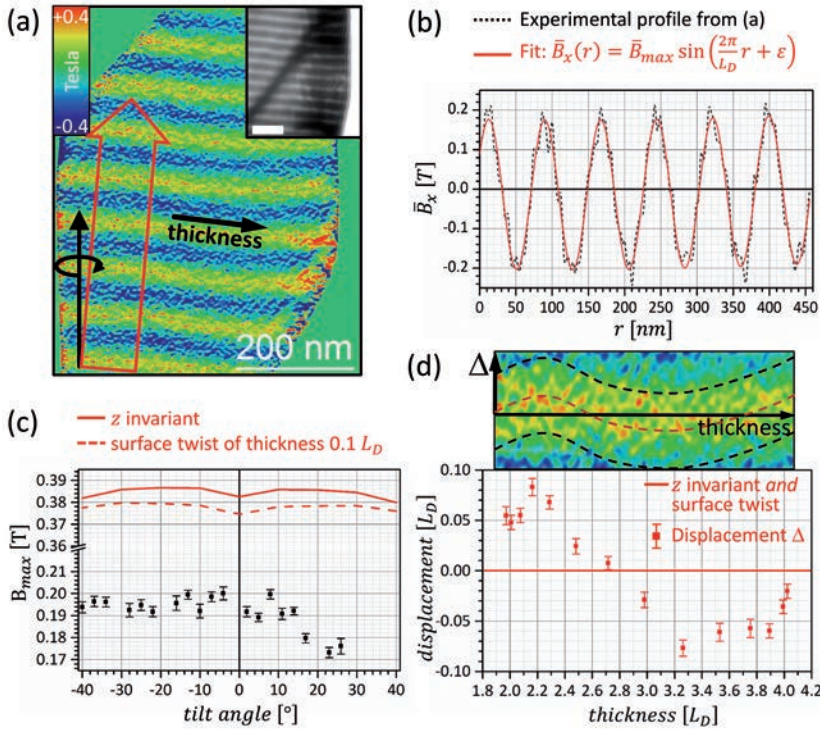

Figure 3: Dependence of the in-plane magnetic induction on the specimen tilt around the propagation axis of the helical phase in a $Fe_{0.95}Co_{0.05}Ge$ nanoplatelet. (**a**) In-plane component B_x normalized to the specimen thickness. The tomographic tilt axis and the direction of the thickness gradient are indicated by black arrows. The inset shows the corresponding L-TEM image. (**b**) Line profile of the projected in-plane magnetic induction Bx along the red arrow in (**a**) and sinusoidal fit using the function denoted above. (**c**) ***B***-field amplitudes B_{max} obtained from likewise determined fits to the induction maps as function of the tilt angle. Simulations for (z-invariant), pure helical spirals (solid line) and with chiral surface twist (dashed line) are included for comparison. (**d**) Amplitude Δ of the undulation of the magnetic stripe contrast (perpendicular to the helical axis) around its mean value as a function of the thickness in units of the modulation length L_D.

To sum up, our results facilitate the generation of a complex picture of the magnetization behaviour in various nanomagnetic configurations, which allows to set up a micromagnetic model including exchange, demagnetizing field, and crystalline anisotropy, within the exact geometry of the nanomagnet. We anticipate further improvements by including additional tilt series (e.g., employing improved 3-tilt axis tomography holders), improved vector field reconstruction schemes and adapted micromagnetic modeling of the magnetostatic potential, explicitly exploiting the a priori knowledge of the ***B***-field. The technique holds large potential for revealing complex 3D nanomagnetization patterns, e.g., in chiral magnets, nanomagnets (e.g, nanowires) and frustrated magnets, currently not possible with other methods at the considered spatial resolution regime.

[1] A. Fernandez-Pacheco, et al., Nat Commun 8 (2017) 15756.
[2] D. Karnaushenko, et al. Advanced Materials 27 (2015) 6582.
[3] S.S. Parkin, et al., Science 320 (2008) 190.
[4] A. Hoffmann, and S.D. Bader, Physical Review Applied 4 (2015) 047001.
[5] O. Fruchart, et al., arXiv: 1806.10918 [cond-mat] (2018).
[6] A.N. Bogdanov and D.A. Yablonsky, Zh. Eksp. Teor. Fiz. 95 (1989) 178.
[7] A.N. Bogdanov and U.K. Rößler, Phys. Rev. Lett. 87 (2001) 037203.
[8] U.K. Rößler, A.N. Bogdanov, and C. Pfleiderer, Nature 442 (2006) 797.
[9] S. Mühlbauer, et al., Science 323 (2009) 915.
[10] X.Z. Yu, at al., Nature 465 (2010) 901.
[11] F.N. Rybakov, et al., New Journal of Physics 18 (2016) 045002.
[12] F. Zheng, et al., Nat Nanotechnol 13 (2018) 451.
[13] X.Z. Yu, et al., Nature 564 (2018) 95.
[14] N.S. Kiselev, et al., J. Phys. D: Applied Physics 44 (2011) 392001.
[15] A. Fert, V. Cros, and J. Sampaio, Nat Nanotechnol 8 (2013) 152.
[16] C. Jin, et al., Nat Commun 8 (2017) 15569.
[17] The Aharonov-Bohm phase shift reconstructed holographically may be resolved with an accuracy in the range of 1 % measured in magnetic flux quanta.
[18] P. Schattschneider, et al., Nature 441 (2006) 486.
[19] P. Schattschneider, et al., Phys. Rev. B 78 (2008) 104413.
[20] S. Schneider, et al., Physical Review Materials 2 (2018) 113801.
[21] D. Wolf, et al., Chem Mater 27 (2015) 6771.
[22] P. Simon, et al., Nano Lett 16 (2016) 114.
[23] S. Schneider, et al., Phys Rev Lett, 2018, 120.

Funding

This work is partially supported by the DFG (project no. LU2261/2-1) and the European Research Council (ERC) under the Horizon 2020 research and innovation programme of the European Union (grant agreement No 715620).

Cooperation

CEMES-CNRS 29, rue Jeanne Marvig, B.P. 94347 F-31055, Toulouse Cedex, France
University of Wisconsin-Madison, Madison, WI, USA
Uppsala University, Uppsala, Sweden
Max Planck Institute for Chemical Physics of Solids, Dresden, Germany

Research Area 2: Function through size

Selective laser melting and recent trends in processing of Cu-based shape-memory alloys

T. Gustmann, P. Gargarella[1], U. Kühn and S. Pauly

Abstract

A Cu-based shape-memory alloy with the nominal composition (wt%) 81.95Cu-11.85 Al-3.2Ni-3Mn was additively manufactured via selective laser melting. Bulk as well as complex designed samples with a high relative density of up to 99 % could be fabricated in order to analyze the interrelations between the processing, microstructure and, for instance, the transformation behaviour. The transformation temperatures were studied by means of calorimetry and compared with those of other rapidly cooled specimens, viz. spray-formed material. The processing has a strong impact on the resulting grain size as well as the thermal history and, therefore, on the shape-memory properties.

The findings in our work imply that selective laser melting is a promising manufacturing technique for Cu-based shape-memory alloys in the near future. It allows an adjustment of the transformation temperatures already during manufacturing without the need of a subsequent heat treatment as usually required for conventional manufactured counterparts.

Cu-based shape-memory alloys

Often called “smart materials”, shape-memory alloys (SMAs) are able to recover a shape change caused by plastic deformation on heating. This reversible shape recovery is known as shape-memory effect (SME) [1–3]. It is related to the transformation of a low-temperature phase (martensite) to a high-temperature phase (austenite) and vice versa, which can be stress-induced or temperature-induced [1].

The probably most widely-used shape-memory alloy, near equiatomic NiTi, is only operational up to temperatures of about 353 K [1–2]. Hence, extensive research has been conducted in order to increase the transformation temperature (e.g. austenite-start: A_s) by developing new alloy compositions, that can be applied at temperatures above 373 K, the so-called high-temperature shape-memory alloys (HTSMAs) [3]. The HTSMAs based on NiTi like TiNiPt or NiTiHf are relatively expensive and difficult to manufacture [1]. Therefore, another group of materials derived from Cu-based alloys has attracted attention, mainly due to their relatively low manufacturing costs and promising shape-memory properties [4–7].

Especially Cu-Al-Ni-Mn alloys (e.g. 81.95Cu-11.85Al-3.2Ni-3Mn [5]) are interesting in terms of applications because of their improved thermodynamic stability and due to transformation temperatures that can be adjusted in a broad regime [1, 7]. This provides important advantages in the field of actuation and sensing, where SMAs can be used e.g. as springs, wires or strips [2]. Yet, these alloys are inherently brittle in the polycrystalline state due to intergranular cracking, which is mainly caused by a high elastic anisotropy [1]. This anisotropy is more pronounced in coarse-grained alloys, which are generally produced under relatively low cooling rates [1, 7]. It has been shown that the poor workability of coarse-grained Cu-Al-Ni-based alloys can be partially overcome by refining the microstructure through the addition of grain refiners such as Zr [5], Ti [7] or Mn [8]. An alternative route for grain refinement in Cu-based shape-memory alloys constitutes in rapid solidification like spray forming [9] or additive manufacturing, viz. selective laser melting [4–6].

With its high intrinsic cooling rates, selective laser melting (SLM) creates a bulk part layer by layer through melting of specific, predefined small volumes of a powder bed. The processing of a thin powder layer, typically below 100 µm, on massive substrate plates in combination with small laser spot diameters results in a fast removal of the heat comparable to quenching [10]. These unique processing conditions have a strong impact on the microstructure (e.g. grain size) and, in turn, also on the martensitic transformation. Especially the transformation temperatures of Cu-based shape-memory alloys are known to strongly depend on the grain size next to factors like chemical composition and the phases present [1, 5]. It is known that for Cu-based shape-memory alloys the transformation temperatures decrease with decreasing grain size [6, 9]. This makes SLM a very attractive method to process, because the resulting microstructure consists of relatively small grains. First of all, the material becomes more ductile [5]. On the other hand, the microstructure and the transformation temperatures can be tailored to some extent due to the possibility to control the energy dissipated into the powder layer (powder layer thickness z = constant) [13]:

$$E = P/v \cdot h \cdot z \qquad (1)$$

by adjusting the laser power (P), the scanning speed (v) and the spacing between two neighbouring tracks (h), the so-called hatching distance [4–6, 11]. This unique tool does not exist for conventional manufacturing techniques such as casting.

Selective laser melting of 81.95Cu-11.85Al-3.2Ni-3Mn

A key aspect of samples prepared by SLM is the resulting porosity, which can be relatively high compared to conventionally processed material (e.g. as-forged) and which is usually detrimental for the mechanical properties [12]. Therefore, the process parameters had to be optimized first for processing of the shape-memory alloy (wt%) 81.95Cu-11.85Al-3.2Ni-3Mn in order to obtain almost defect-free samples during SLM (see Figure 1a).

In order to determine a suitable process window for SLM fabrication, selected parameter combinations from single-track experiments (see [4]) were transferred to the manufacturing of bulk samples with 8 x 8 x 8 mm³ (z = 0.09 mm). The highest relative density was achieved for a range of energy inputs from 30 to 40 J/mm³ by using a high laser power of 330 W, which improves melting, scanning speeds from 700 to 1200 mm/s and hatching distances from 0.12 to 0.16 mm (cf. Tab. 1). A computer tomography image of a one-way shape-memory effect demonstrator (tension spring, see Figure 1b) shows the size and distribution of residual pores (see Figure 1c). The formation of pores during SLM, even if optimized parameters are used, strongly depends on the processing conditions such as the powder material, sample geometry or part orientation [12]. However, it could be observed that the process parameters developed for bulk parts were also suitable for the fabrication of lattice structures and more or less complex demonstrators with relative low porosity (tension spring: mean equivalent pore diameter - d_{90} = 0.085 mm; d_{min} = 0.03 mm; d_{max} = 0.138 mm).

Microstructure and transformation behaviour

A SLM sample with high relative density was used to study the phase formation by means of X-ray diffraction and compared to spray-formed material (see [9]). The chemical composition was found to be similar for both specimens and did show only slight deviations from the nominal composition (e.g. SLM in wt%: 82.05Cu-11.84Al-3.21Ni-2.9Mn). For both materials, only β'_1-martensite was found and the formation of oxides could be avoided due to the low amount of oxygen (< 200 ppm) in the samples.

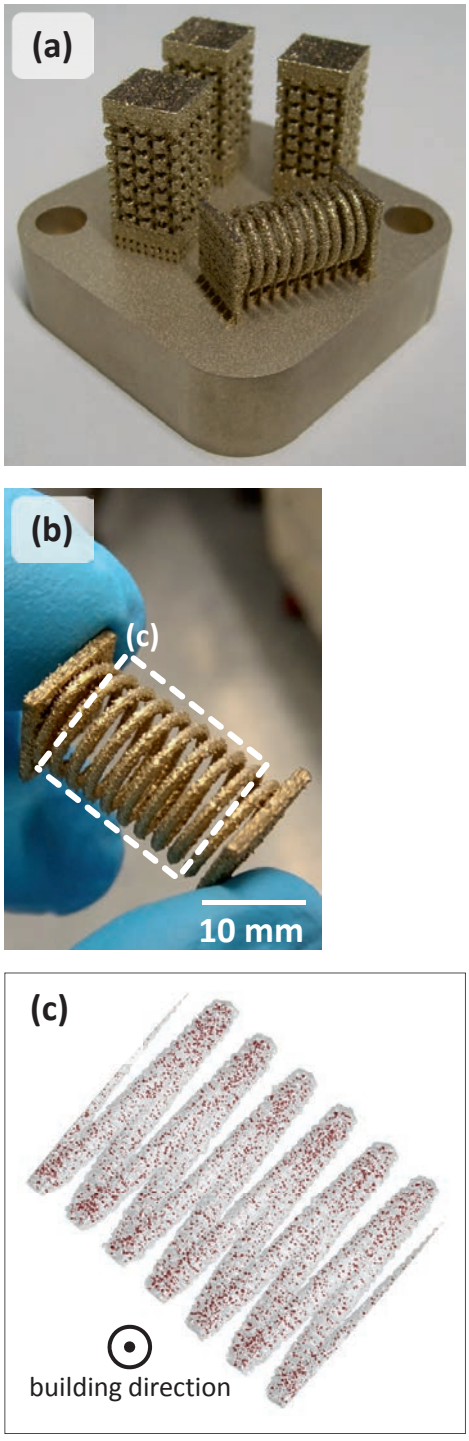

Figure 1: Substrate plate (50 x 50 x 15 mm³) with a set of scaffolds and a tension spring produced by SLM (**a**). The tension spring in the initial state (**b**) is used as a demonstrator to illustrate the one-way shape-memory effect. The depicted area was investigated by X-ray computer tomography (CT, top view illustration) before testing (**c**). It should be noted that all pores (red, volume fraction = 0.5 %) detected in the indicated sample volume by CT are projected onto the cross section.

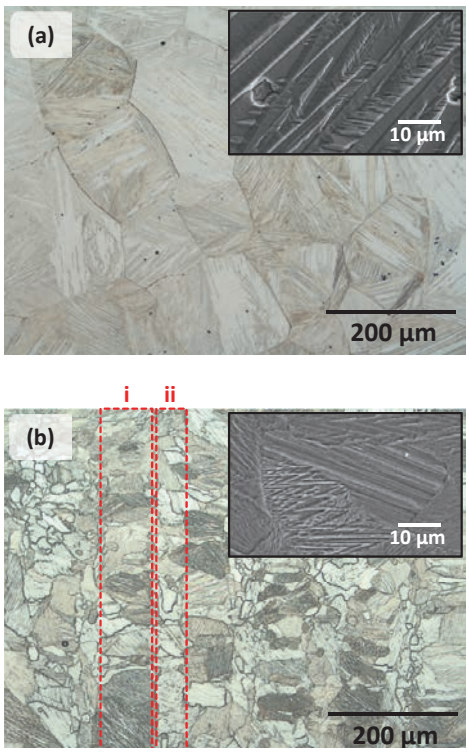

Figure 2: Optical micrograph from the centre of a spray-formed (**a**) and SLM sample perpendicular to the building direction (**b**). The insets show SEM images of the martensitic microstructure. Martensite laths are visible and can vary in size and arrangement.

In addition, the grain sizes were determined for the spray-formed and SLM material as shown in Figure 2 and Tab. 1. The insets of Figures 2a and 2b show the typical martensitic microstructure. The determination of the grain size is slightly aggravated because both processing techniques either lead to a more or less pronounced gradient microstructure (spray forming: see [4]) or elongated grains (SLM, see Figure 2b). The relatively large scattering of grain sizes in the SLM part is characteristic for this manufacturing process and also occurs for other alloys [11]. Smaller grains preferentially form at the overlap of melt track margins (region ii, see Figure 2b). Here, refined grains with typical sizes of about 15 µm can be found. In contrast, large grains (region i, around 65 µm), elongated in the direction of the heat flow, can be found in the center of each melt track. The grains in the spray-formed material are substantially bigger (138 ± 28 µm), owing to the large dimensions of the billet and thus the resulting lower cooling rate [9]. In the SLM samples, the grains exhibit only diameters around 45 ± 33 µm (SLM: high energy input, cf. Tab. 1). Thus, the SLM technique is an efficient method to produce refined microstructures of 81.95Cu-11.85Al-3.2Ni-3Mn.

Tab. 1 also lists the transformation temperatures of the spray-formed and SLM specimens. The transformation temperatures are in the range as referred in [9, 14]. A minimum of two samples each (two cycles) were measured by means of differential scanning calorimetry (DSC) and in Figure 3, the curves of the reverse (martensite-to-austenite: heating) and forward (austenite-to-martensite: cooling) transformation are plotted for both processing techniques. There is a reversible change from monoclinic β'_1 to a cubic β_1-phase. A relative small thermal hysteresis (A_f-M_s, cf. Figure 3) of around 15 K was found, what is consistent with literature [1, 7, 9]. While the hysteresis of SLM samples shows only slight deviations between the first (14 K) and the second cycle (13 K), the difference for spray-formed samples was more pronounced (13 K and 9 K, respectively). In other words, it can be seen that the transformation temperature differences between the first and second cycle are only negligible in contrast to the spray-formed material.

The transformation temperatures of Cu-based shape-memory alloys have been reported to depend on the grain size [7] and to obey a Hall-Petch relation [14]. The present results imply a similar behaviour as it can be seen by the shift of about 50 K of the curves towards higher temperatures if the grain size is increased (cf. Tab. 1). Furthermore, the DSC results reveal that the transformation temperatures of 81.95Cu-11.85Al-3.2Ni-3Mn can be controlled during selective laser melting by modifying the energy input [6]. This illustrates the high potential of SLM not only for processing this material with a refined microstructure but also to directly adjust its transformation temperatures.

Conclusions

The shape-memory alloy 81.95Cu-11.85Al-3.2Ni-3Mn was successfully processed by selective laser melting. The alloy solidifies into β'_1-martensite with a refined microstructure due to the high cooling rates during processing. Using an energy input between 30–40 J/mm^3, bulk specimens as well as more complex designed samples can be fabricated with high relative density.

The transformation temperatures in the present alloy are very sensitive to the grain size/cooling rate. With increasing grain size they tend to shift towards higher values. Nonetheless, the variation of the transformation temperatures in contrast to the deviation in the grain size is significantly small. As a reason, further microstructural investigations were conducted to fully clarify the correlation between the processing technique, the transformation behaviour and the mechanical properties (e.g. deform-

ability, shape recovery) [6, 15]. The present work shows that selective laser melting can be used to produce parts of a Cu-based shape-memory alloy whereby the transformation temperatures can be tailored in situ. In contrast to conventional manufacturing techniques, additional post-processing steps are not needed.

[1] K. Otsuka, C. M. Wayman: Shape Memory Materials, Cambridge University Press, 1998
[2] J. Mohd Jani et al., Mater. Des. 56 (2014) 1078–1113
[3] J. Ma et al., Inter. Mater. Rev. 55 (2010) 257–315
[4] T. Gustmann et al., Addit. Manuf. 11 (2016) 23–31
[5] T. Gustmann et al., SM Superelas. 3 (2017) 24–36
[6] T. Gustmann et al., Mater. Des. 153 (2018) 129–138
[7] T. W. Duerig, K. N. Melton, D. Stöckel, C. M. Wayman: Engineering Aspects of Shape Memory Alloys, London: Butterworth-Heinemann Ltd, 1990
[8] U. Sari, Int. J. Miner Metall. Mater. 17 (2010), 192–198
[9] R. D. Cava et al., J. Alloys Compd. 615 (2014) 602–606
[10] S. Pauly et al., Mater. Today 16 (2013) 37-41
[11] T. Bormann et al., J. Mater. Eng. Perform. 21 (2012) 2519–2524
[12] I. Yadroitsev et al., Physics Procedia 5 (2010) 551-560
[13] J.-P. Kruth et al., J. Mater. Process. Technol. 149 (2004) 616–622
[14] J. Dutkiewicz et al., J. Mater. Sci. Eng. A273 (1999) 703–707
[15] T. Gustmann, Doctoral thesis: Technische Universität Dresden (2018)

Funding

Deutsche Forschungsgemeinschaft e.V., Project/Grant: PA 2275/4-1

Cooperation

[1] Departamento de Engenharia de Materiais, Universidade Federal de São Carlos (UFSCar) – SP, Brasil

Tables

Tab. 1: Relative densities, grain sizes and the transformation temperatures of selected 81.95Cu-11.85Al-3.2Ni-3Mn samples prepared by spray forming and SLM (low energy input: E = 30.9 J/mm³, high energy input: E = 38.1 J/mm³). The characteristic temperatures are defined as in Figure 3 and represent the values from the second cycle.

Sample	Relative density	Grain size	A_{peak}	M_{peak}
	(%)	*(µm)*	*(°C)*	
Spray-formed	99.0 ± 0.5	138 ± 28	152 ± 1	140 ± 1
SLM (low energy input)	98.8 ± 0.1	44 ± 30	102 ± 1	89 ± 1
SLM (high energy input)	98.9 ± 0.1	45 ± 33	106 ± 1	90 ± 1

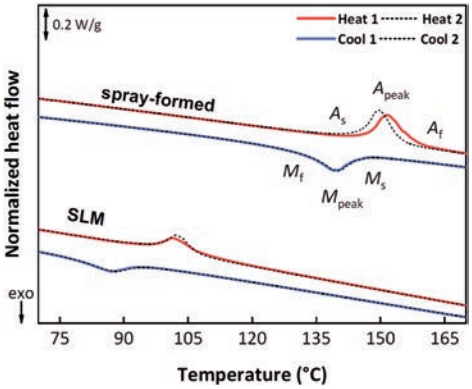

Figure 3: DSC-curves of a spray-formed and SLM sample (energy input: E = 33 J/mm³). The shift in the transformation temperatures to higher values in case of the spray-formed material is attributed to the lower cooling rate during processing or rather the larger grain sizes (cf. Figures 2a and 2b, see Tab. 1). Beside the peak values, the four characteristic temperatures of the diffusionless phase transformation are A_s, A_f, M_s and M_f which means austenite-start, austenite-finish, martensite-start and martensite-finish, respectively.

Integrated micro-thermoelectric coolers with rapid response time and high device reliability

G. Schierning, G. Li, J. Garcia Ferndandez*, N. Perez, D. Alberto Lara Ramos, V. Barati, I. Soldatov, H. Reith, and K. Nielsch
*) now with University of Oviedo, Spain

Abstract

The precise temperature control of optoelectronic devices is detrimental for their operation. Thermoelectric coolers produce chilliness when an electric current is applied, and could therefore be important elements of a local thermal management for such devices. But so far, miniaturized thermoelectric coolers have not yet been implemented for this purpose since a fabrication technology of micro-thermoelectric coolers (μ-TECs) that is compatible with semiconductor technology needed to be implemented and the performance of such devices demonstrated. Here we show that μ-TECs fabricated by a combination of lithographic structuring and electrochemical deposition techniques feature high reliability and fast response times. These devices survived more than 10 million duty cycles and one month of steady-state operation without degradation at cooling response times of one millisecond. To achieve these mile stones, fabrication technology as well as device design and device characterization were developed and optimized. By directly coating the deposits of the thermoelectric material after the electrochemical deposition, the electrical contact resistances between thermoelectric material and metal electrode could be drastically decreased. By using finite element analysis we further optimized the device geometry, especially the thicknesses of the electrical top and bottom contacts.

Local cooling by μ-TECs

Next generation electronic devices require intelligent thermal management strategies in order to remove high density heat fluxes from the active electronic parts. The thermal challenge grows with advancing levels of integration. Jointing more and more functionality into ever-decreasing space increases the thermal budget, i.e. the heat flux densities. Especially optoelectronic devices demand a very precise thermal stabilization in order to produce a precisely defined wavelength. Hence, hardware solutions for a smart and efficient thermal management are sought for. μ-TECs utilizing the Peltier effect could locally cool electronics, provide an active temperature control and mitigate hot spots. To make this vision reality, the fabrication technology needs to be developed, the μ-TEC device geometry with all its components optimized, as well as the performance of the μ-TECs characterized [1, 2].

Amongst the variety of thermoelectric materials and processing technologies, we realized the μ-TECs by the electrochemical deposition of tellurium-based thermoelectric thick films combined with micro-structuring by lithography. Such a technology is, in principle, compatible with semiconductor fabrication technology in the complementary metal-oxide-semiconductor (CMOS) back-end fabrication line. The deposition of the functional films is done at room temperature and the approach is scalable.

Specific features of the µ-TECs design and device integration

An as-prepared array of μ-TECs is shown in the scanning electron microscopy (SEM) image of Figure1 (left). A color-coding is added to parts of the SEM image to identify the components of the μ-TECs. The size of the active thermoelectric material (green and red) is approximately 30 µm x 40 µm x10 µm – the optimal geometry of the n-type and p-type material may vary as a consequence of different intrinsic material's

properties, Seebeck coefficient, electrical conductivity and thermal conductivity, of the two semiconductors. The metal top contact is free-standing. Usually, thermoelectric devices do not have a free-standing top contact but a second substrate with the top contacts, so that both substrates sandwich the active thermoelectric material. This creates a situation in which differences in the thermal expansion coefficients of the different materials (n-type, p-type semiconductor, metal) produce thermomechanical stress during operation because the constrained geometry does not allow for the expansion. But due to the free-standing design of the μ-TECs, thermal expansion during operation does not create a critical failure mechanism, as will be seen later.

The integration of the μ-TECs is envisioned in a way as shown in Figure 1 (right). The active laser component will be enclosed by the μ-TEC so that it is covered by the metal bridge. This still results in a situation in which the total device can expand to the top upon cycling and transfers the cooling to the component below the metal bridge.

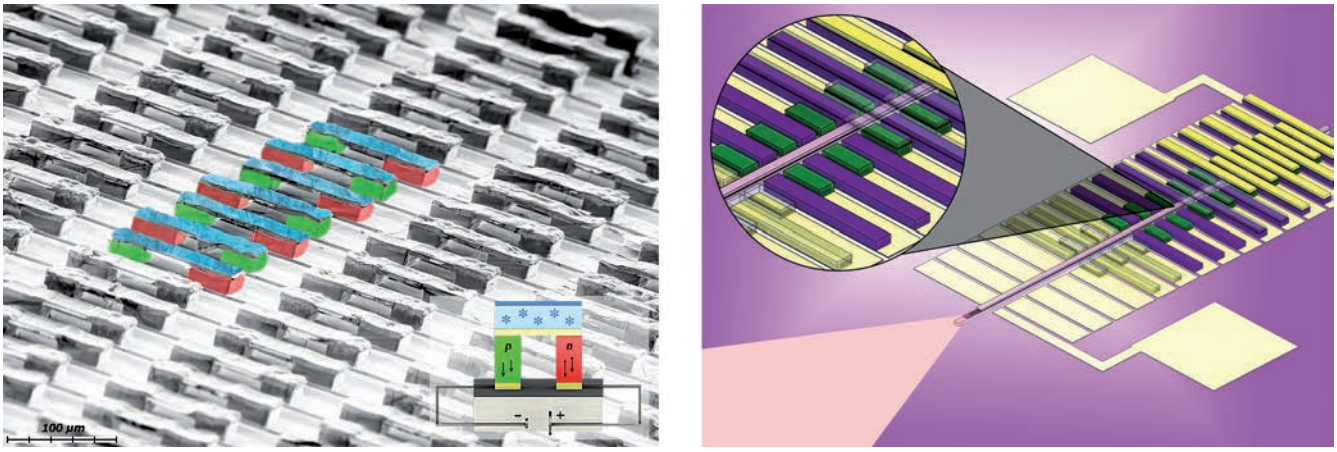

Figure 1) μ-TECs and concept of device integration. Left: Scanning electron microscopy view of μ-TECs characterized by their free-standing metal bridge, in part color-coded to visualize n-type and p-type (green and red) thermoelectric material, as well as free-standing metal-bridge (blue). Right: Concept of device integration, in an optimized design that refers to our thermoelectric n-type and p-type materials with different intrinsic materials properties, hence also different geometry of both legs. The schematics visualize the step-by-step fabrication technology, starting with bottom contacts, deposition of the thermoelectric legs of both types and deposition of the metal bridges. The µ-TECs encloses a laser and supports the control of the temperature stability.

Extremely high cycling reliability and stability of the µ-TECs

The cooling of the μ-TECs is characterized by a thermal imaging technique. Hereby, the temperature induced changes in the reflectivity of the top surface of the devices are measured while electrical current is applied. Given a calibration, the temperature difference between the device in its on- and off-state can be deduced. Further, the device's response during the full duty cycles is accessible, as well as the average response of several devices connected in series. An averaging over several duty cycles reduces the signal-to-noise ration. A false-colored thermal image of two μ-TECs in a series-connection during duty is shown in Figure 2 (a). Using this thermal imaging technique, it is demonstrated that the μ-TECs show an optimum cooling at an applied current of approximately 80 mA, see Figure 2 (b), well in accordance with a finite element (FE) simulation. The maximum cooling is reached within a time faster than 1 ms (not shown here) which represents a very fast response time of the device.

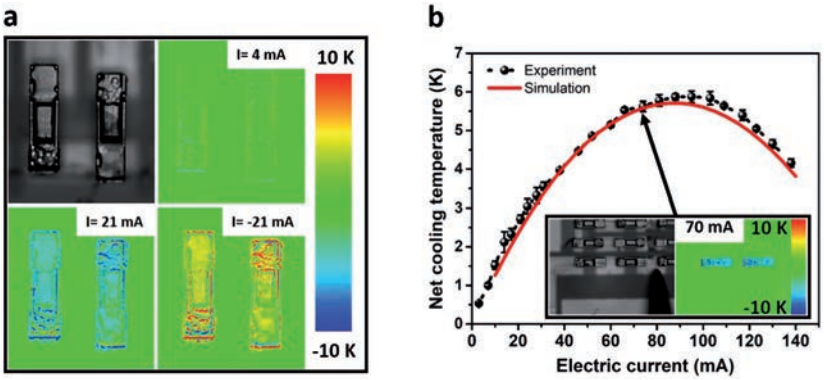

Figure 2: Cooling performance of μ-TECs. (a) Optical microscopy image of an integrated µ-TEC device and thermoreflectance images with applied electric current of 4 mA, 21 mA and -21 mA. (b) Net cooling temperature of two leg pairs in an electric current range from 5mA to 140mA at room temperature (~20 °C) and ambient environment. The inset shows the optical and thermoreflectance images with applied electric current of 70 mA. *Figure and figure caption reproduced with permission from Ref. [1], G. Li et al, Nature electronics 1 555-561 (2018), copyright Nature publishing group 2018.*

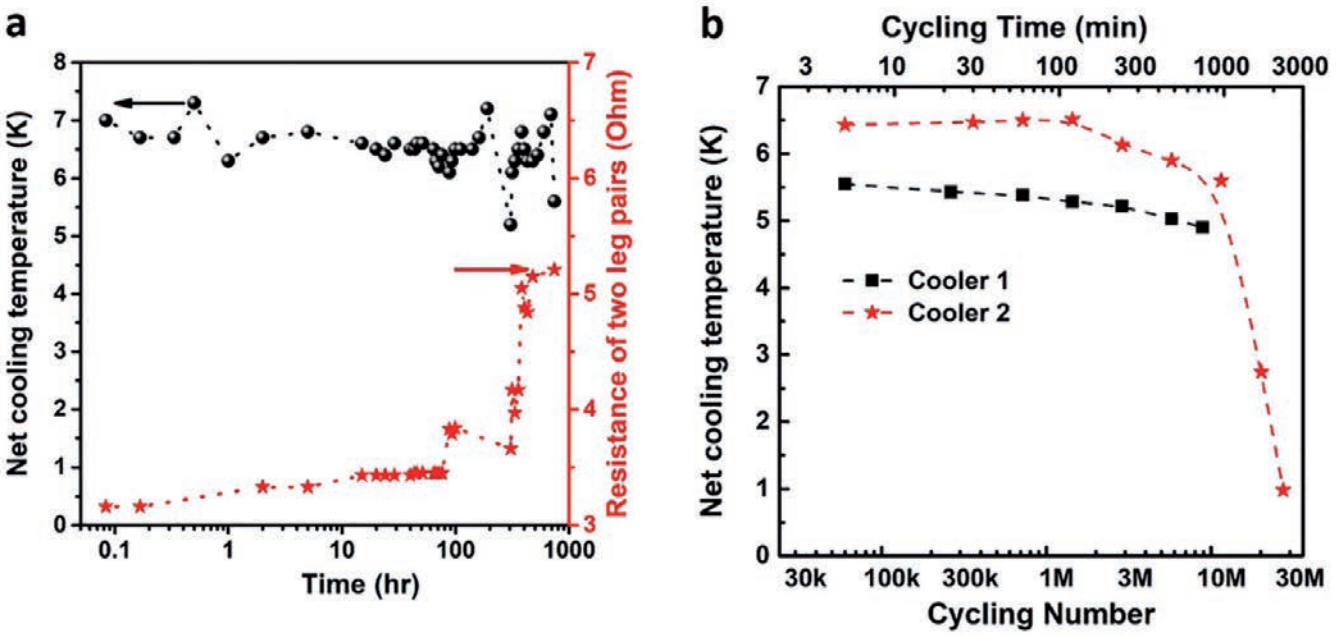

Figure 3: Device durability of μ-TEC devices. (a) Long-term cooling stability test of two-series connected μ-TECs with constant applied current of 70mA. The black dots represent the net cooling temperature and the red stars represent total resistance of these two µ-TECs. (b) Cycling reliability of μ-TECs with cooling pulses (1ms on and 4 ms off), represented as the cooling temperature as a function of cycling number and cycling time for two spate experiments: cooler 1 for the first experiment (black squares) and cooler 2 for the second experiment (red star). *Figure and figure caption reproduced with permission from Ref. [1], G. Li et al, Nature electronics 1 555-561 (2018), copyright Nature publishing group 2018.*

The most remarkable feature of the μ-TECs is their extremely high reliability. For approximately 1000 h of constant duty, there was almost no decrease in the measured temperature difference, ΔT, observed, characterized using two in-series connected μ-TECs, see Figure 3 (a). A slight increase in the internal resistance of those μ-TECs was seen in the first 100 h of the experiment, and a steeper increase after 100 h. In another experiment, fast electric current pulses were applied to μ-TECs, and their response characterized. Hereby, the electric current was applied for 1 ms, the off-time was 4 ms. It was shown for two different μ-TECs that more than 10 million cycles could be applied without degradation. This extremely high cycling reliability is a specific feature of the here prepared μ-TECs and has not been demonstrated in literature before. The reason is found in the fabrication technology (i) and in the device design (ii): (i) We implemented a processing in which the active thermoelectric material is instantly metallized after deposition. By this, we reduced the electrical contact resistances compared to state-of-the-art devices, and improved the adhesion between thermoelectric material and metallization. The interface between thermoelectric material and metallization is often the source of device failure or degradation, and consequently the improvements of the interface quality are reflected by a high device reliability and stability. (ii) We used a μ-TECs design that features a free-standing metal bridge. This allows for a thermal expansion with only a minimal thermomechanical stress within the devices. Therefore, this μ-TECs design supports a high device reliability and stability, too.

Design guidelines for µ-TECs by finite element analysis

The μ-TECs design and further performance optimization of the μ-TECs requires an analysis of the thermal and electrical fluxes within the devices. Therefore, the impact on the performance from the geometry of all components, i.e. thermoelectric material, bottom contact, top contact, as well as the arrangement of the μ-TECs on the substrate was analyzed by finite element simulation using realistic material's properties defined by our technology, as well as the geometrical constrains of the intended application. Especially the optimal thickness of the top and bottom contacts were in the focus. Other than in macroscopic thermoelectric devices, the distribution of the electrical current lines as well as the heat spreading ability of the contacts needs to be considered, resulting in specific design guide lines for micro-devices. By using finite element simulation, we obtained the current and temperature distributions of the μ-TECs under realistic materials' properties assumptions.

We showed that an increased thickness of the metallic contacts enables an overall reduction of the internal resistance of the device by minimizing Joule heating losses, being this a counterintuitive mechanism. Additionally the metallic contacts improve the heat spreading ability which results in an increase of performance of the μ-TECs.

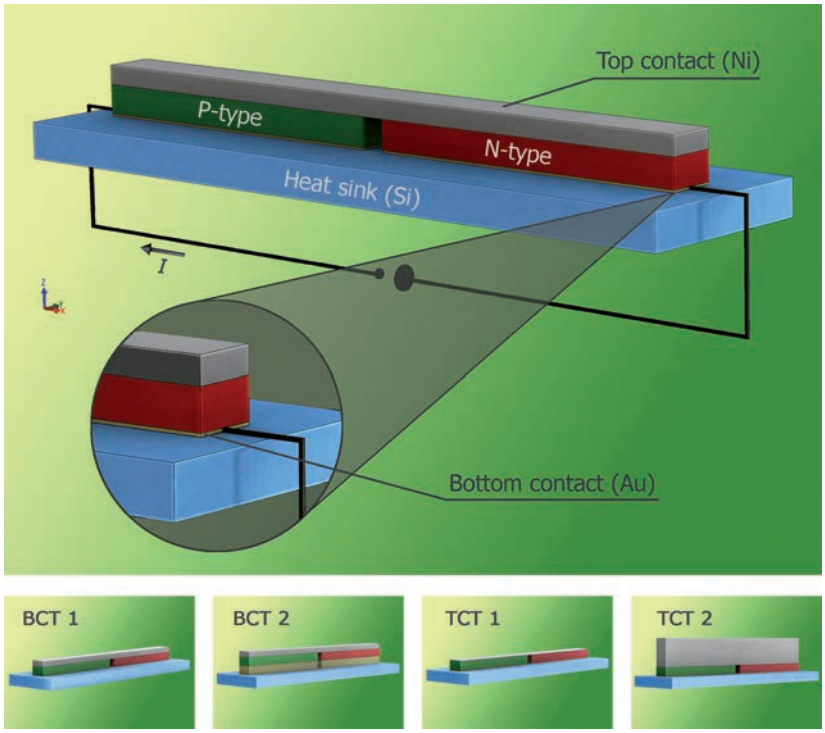

Figure 4: Upper part: Schematics of a two leg µTEC with the initial geometry before optimization. The following elements are comprised: Silicon substrate (blue), bottom gold contact (yellow), p-type semiconductor (green), n-type semiconductor (red) and top nickel contact (grey). Lower part: Schematics of the studied device for a thin bottom contact (BCT 1), thick bottom contact (BCT 2), thin top contact (TCT 1) and thick top contact (TCT 2). *This is a figure compilation from Ref. [2], the accepted version of the following article: D. A. Lara Ramos, V. Barati, J. Garcia, H. Reith, G. Li, N. Pérez, G. Schierning, K. Nielsch, Design guidelines for micro thermoelectric devices by finite element analysis, Adv. Sust. Syst., in print (2019). Reuse under the terms and conditions of the Wiley-VHS copyright agreement.*

Acknowledgements

The authors thank T. Sieger, H. Stein, C. Kupka and R. Uhlemann in IFW Dresden for helpful technical support and R. Uhlemann for support in the design of the graphics. Funding is gratefully acknowledged from the European Union (EU) and the Free State of Saxony through the European Regional Development Fund (ERDF) (SAB GroTEGx, grant no. 100245375), from the EU's Horizon 2020 research and innovation program (H2020 RIA Tips, grant no. 644453), and from the Mexican National Council for Science and Technology (grant no. CVU611106).

Collaboration

Tyndall National Institute (TNI, Ireland), Centre National de la Recherche Scientifique (CNRS, France) with Lyon Institute of Nanotechnology (INL-CNRS, France), Institute of Light and Matter (ILM-CNRS, France), Materials Institute Jean Rouxel (IMN-CNRS, France), Communicraft (Ireland), Alcatel-Lucent Bell Labs (Ireland), Alcatel-Lucent Bell Labs (France), Alcatel Thales III-V Lab (France), LioniX BV (Netherlands), Stokes Laboratories (Ireland), University of Hamburg

This highlight uses results from the following references:

[1] G. Li et al., Nat. electr. 1 (2018) 555.

[2] D. A. Lara Ramos et al., Adv. Sust. Syst. (2019) in print.

Rolled-up microcoils for ESR and NMR

D. Karnaushenko, D. Karnaushenko, H.-J. Grafe, V. Kataev, B. Büchner and O. G. Schmidt

Abstract

We report the realization of miniaturized electromagnetic resonators, inductive and mutually coupled coils, by rolling up ultrathin films into cylindrically shaped devices, and proof their functionality by electron spin resonance (ESR) and nuclear magnetic resonance (NMR) measurements, where such coils are used for excitation and detection of electronic and nuclear spins, respectively [1]. Further development of these coils have the potential for applications in electronic devices as well as in strongly downscaled, compact ESR and NMR spectrometer. The success of this work is based on the concentrated joint efforts of two institutes of the IFW and their specific expertise. On the one hand the unparalleled knowledge on rolled-up nanotechnology developed at the IIN, and on the other hand the profound expertise on NMR and ESR spectroscopy at the IFF.

Introduction

The key challenge of modern large scale ESR and NMR devices is the resolution and sensitivity which strongly depend on the filling factor of the resonator volume and on the strength and homogeneity of the applied static magnetic field. The latter factors require application of helium cooled superconducting magnets increasing the overall system cost and the size. The size of the system relates to the volume of the analyzed material, which should be kept as high as possible to approach a unity filling factor of the resonator. The resonator of an NMR system is a coreless magnetic solenoid that transfers energy in the form of radio frequency (1 MHz – 1 GHz) resonantly to the nuclei of a material. More complex geometric structures are required for ESR resonators due to much higher frequencies (5 GHz – 1 THz) to transfer energy to electrons. The combination of complimentary NMR and ESR techniques in portable devices will be a breakthrough in comprehensive materials analysis. Miniaturization of resonators is the crucial step towards the overall down-scaling of resonance based systems, their cost efficiency and a broad spreading via portable rapid analytical systems. Furthermore, soft-matter research and rapid testing of biological moieties often demand small analytical systems due to limited sample quantities of e.g. thin membranes, porous media, cells and low concentration biological solutions. Therefore, small volume detectors, sampling systems and miniature-integrated electronics are essential.

Small-scale NMR of sample volumes down to 5 nL was first demonstrated using a standard resonator copper coil, which was wrapped around a capillary [2]. Later, planar coils on a chip have been realized for both NMR [3, 4] and ESR [5–8]. This allowed high-throughput analysis by insertion of multiple probes into a single magnet [9] involving even a microfluidic system design [10] to sample probes. However, planar NMR coils on a chip suffer from low sensitivity and a construction-related inhomogeneous distribution of oscillating and static magnetic fields. For ESR, the main issue is the magnetic coupling efficiency of the oscillating magnetic field and the sample [6]. Moreover, special shim coils are usually applied for high resolution chemical NMR, and gradient coils are used for magnetic resonance imaging (MRI). On a micro scale, implementation of all the elements is, however, a challenging task.

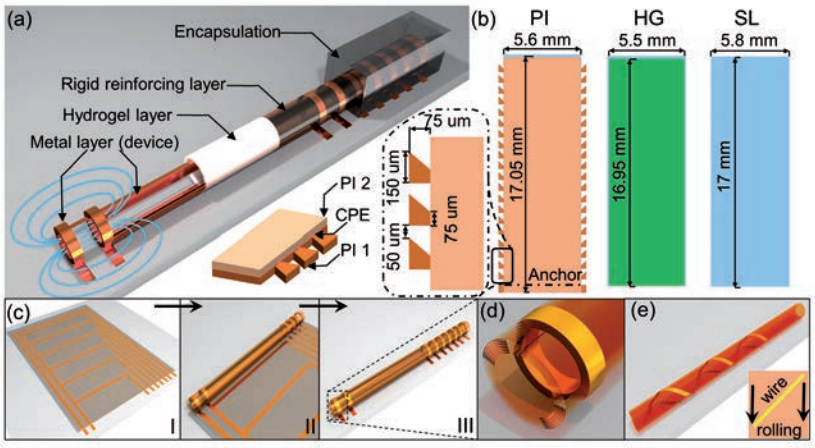

Figure 1: Illustration of the self-assembly of functional 3D magnetic components using shapeable ultrathin films. **a)** Self-assembled and encapsulated 3D device revealing coils and their mutually coupled configurations. **b)** Shapeable layer stack consisting of three distinct polymeric structures, namely, the sacrificial layer (SL), the hydrogel (HG) layer, and the reinforcing polyimide (PI) layer. **c)** The latter possesses a two-layer structure where the first layer (PI 1) is equipped with fixators and the second (PI 2) layer develops crack propagation edges (CPEs), which helps to release the brackets during the rolling process and guide the overall self-assembly process. **d)** Rolling of a straight wire leads to a Swiss roll coil, **e)** while rolling of the tilted wire forms a helix geometry.

Here, we report the fabrication of cylindrical micro coils (Figure 1a), and demonstrate their functionality by NMR and ESR experiments [1]. It is especially important to achieve an ideal cylindrical shape [11] of the resonators, shimming and gradient coils, and to integrate them within a single device on a chip to realize a high degree of magnetic field control at the micro scale. The small-scale cylindrically shaped devices are either created in a sequential one-by-one fabrication routine [12] or processed in parallel by planar microfabrication techniques requiring numerous preparation steps and large occupied areas on the microelectronic chip surface. The NMR and ESR experiments prove the unique features of these highly sensitive micro coil electromagnetic resonators, and their high quality factor.

Rolling up microcoils and their fabrication

Fabrication of microscale solenoid coils is a demanding task for conventional microfabrication technologies. Fortunately, the rolled-up technology is well suited for this task clearly demonstrating the potential for realization of various configurations of coils revealing inductors and transformers (Figure 1). Integrated with capacitors in a single fabrication process these devices could reveal extremely sharp resonances required for electronic and spectroscopic applications. The fabrication of the coils and whole resonators is accomplished on a planar surface applying conventional clean room based microfabrication processes and novel shapeable polymeric materials which were developed at the IFW [13, 14]. The fabrication begins with pretreatment of the wafer surface that imply cleaning and functionalization with self-assembled molecular layers that improve adhesion of the polymeric layers. Then the three layers of polymers, namely the sacrificial layer, the hydrogel layer and the reinforcing layer (Figure 1b) are directly lithographically patterned on these wafers. Once the polymers are ready, a layer of a conducting material (Cu) is structured on the surface of the reinforcing layer resulting in "Π" shaped conductors. The layers were self-assembled into tubular "Swiss-roll" architectures upon etching off the sacrificial layer and swelling of the hydrogel layer resulting in an enhancement of the inductance and reduction of the footprint area to almost 50 time its initial value (Figures 1c, d). A simple structuring of the planar conductor allow a fine tuning of the final 3D coils revealing zero pitch flat cable coils or helixes (Figure 1e).

Proof-of-principle ESR and NMR experiments using microcoils

We have applied the microscale self-assembled coil as an NMR transducer to probe nuclear spin states in a small volume of a model material. The self-assembled microcoil was introduced in a commercial NMR probe forming an LC resonator (Figures 2a, b). In this configuration, the microcoil is able to transfer energy into the material subsystem and receive the response signal. We used glycerin in the inner

opening of the rolled-up structure for the test measurement. Glycerin shows two hydrogen (^{1}H) peaks at about 3 and 4.5 ppm, which are revealed by a standard solenoid copper coil possessing a diameter of d = 0.6 mm and a length of l = 2 mm (Figure 2c). In the same figure, we demonstrate the first successful NMR measurements performed with the self-assembled microcoil. The signal shows a clear signature of ^{1}H in glycerin at the correct resonance frequency. The broader line width for the signal of the rolled-up microcoil compared to the standard solenoid copper coil is expected for small scale coils [2] and just confirms the functionality of the transducer.

Furthermore, we demonstrate the feasibility to realize high-quality LC resonators without using external capacitors just relying on an alternative planar layout of the conductor to form a parallel plate capacitor and the coil in a single-batch self-assembly process (Figure 2d). The resonator, in its 3D shape, was fabricated in the same process as the microcoils with the only difference in the planar layout of the conductor. The most prominent design (Figures 2e, f) achieved a quality factor > 40.000 (Figure 2g). In this design, the coil stripe (Figure 2e right) is shifted away from the capacitor stripe (Figure 2e left) in order to ensure spatial separation of electric and magnetic fields in the assembled state. The self-assembled structure contains a cylindrical parallel plate capacitor (Figure 2e) and the multi-winding inductor, resulting in a high quality factor resonator tank. For testing, a simple ESR setup was built integrating the microcoil ESR resonator (Figure 2f). The setup was equipped with a strong biasing electromagnet, a shimming couple of coils, and small field scanning coils supporting a very precise settling of the magnetic field between the pole shoes (± 2.5 µT). We used 2,2-diphenyl-1-picrylhydrazyl (DPPH) as the model material, which is an important functional agent in chemistry for ESR monitoring of the anti-oxidation activity of biologically relevant substances [14]. The material was loaded into the resonator and characterized with an applied magnetic field, which was swept around 196 mT. The central field of 196 mT corresponds to the ESR resonance of DPPH free radicals at about 5.5 GHz which is close to the resonance peak of the chosen resonator (Figure 2h). We had to choose the field and an appropriate frequency range between 5.48 and 5.53 GHz measuring the return loss (S11) to find resonance characteristics of the micro resonators (Figure 2g). The variation in characteristics of the resonators accounts for a slight sensitivity of the high-Q device to a deviation of geometric parameters of the rolled-up structure. A subtle variation in the diameter or the winding misalignment can be dramatic for the device performance affecting the capacitance or the inductance [15]. The resonator design is sufficiently tolerant toward this issue (Figure 1a) purely relying on the planar conductor design among other less stable structures (Figures 2i, j).

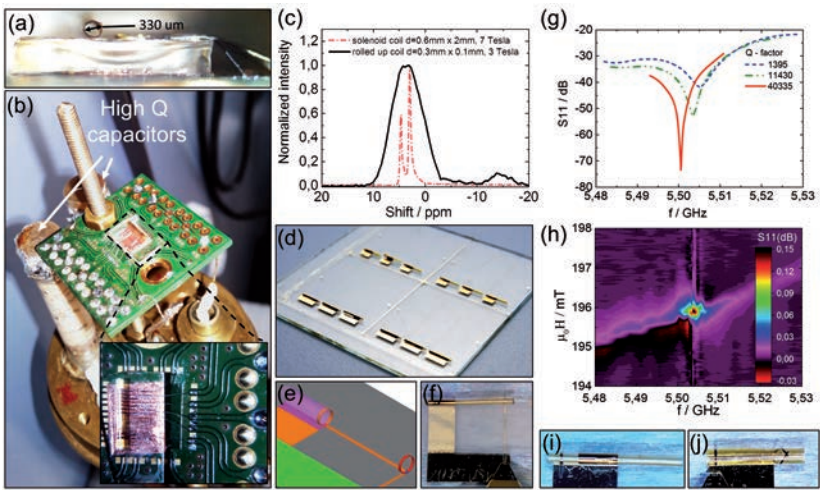

Figure 2: Self-assembled high-quality microcoils and microresonators applied for NMR and ESR characterization. **a)** Microtubular self-assembled architecture possessing an opening of 330 µm suitable for insertion of a small amount of an NMR sample. **b)** Rolled-up self-assembled devices integrated into a commercial NMR probe. Inset: Magnified view of the device. **c)** NMR response of glycerol shows characteristic peaks at the correct positions, which is compared to a regular Cu wire solenoid. **d)** Self-assembled high-quality microresonators that were fabricated in a batch wafer-scale process. **e, f)** Optimal design of the 3D resonator was simulated and fabricated using shapeable ultrathin films. **g)** The high-Q resonator demonstrates variation in the resonance frequency and the quality factor among three devices fabricated in a single run. **h)** Measured response peak of the DPPH radicals in a magnetic field of around 196 mT and f ≈ 5.5 GHz. **i,j)** Several versions of rolled up structures revealing various geometries of conductors.

Conclusion

We have designed, fabricated and tested rolled-up cylindrical micro coils, transformers and resonators relying on shapeable polymeric ultrathin films. We could demonstrate a fully parallel wafer scale process. The overall process allows omitting a number of intermediate steps, which are otherwise required in conventional 2D processing schemes. We showed for the first time that shaping of the initially planar structure like a conductor can lead to >50 times more compact 3D inductive coils with enhanced inductance. Sensitive micro coil electromagnetic resonators were realized, and their application for micro scale NMR and ESR spectroscopies was demonstrated. Application of NMR inert materials and other measures to create a homogeneous magnetic surrounding of the micro coil will substantially increase the resolution of the rolled-up NMR micro coils. Shimming and gradient coils can be accommodated within the same geometry to define the magnetic field profile of the resonators. We envision applications of these magnetic self-assembled devices in microelectronics, radio frequency, communication devices and power converters.

[1] Karnaushenko, D. D. et al. Adv. Electron. Mater. 4, 1800298 (2018)
[2] Olson, D. L. et al. Science 270, 1967 (1995).
[3] Trumbull, J. D. et al. IEEE Trans. Biomed. Eng. 47, 3 (2000).
[4] Wensink, H. et al. Lab Chip 5, 280 (2005).
[5] Boero, G. et al. Rev. Sci. Instrum. 74, 4794 (2003).
[6] Narkowicz, R. et al. Rev. Sci. Instrum. 79, (2008).
[7] Bienfait, A. et al. Nat. Nanotechnol. 11, 253 (2015).
[8] Kiss, S. Z. et al. J. Magn. Reson. 270, 169 (2016).
[9] Ryan, H. et al. Anal. Chem. 84, 3696 (2012).
[10] Kiss, S. Z. et al. J. Magn. Reson. 270, 169 (2016).
[11] Mansfield, P., and Chapman, B. J. Phys. E. 19, 540 (1986).
[12] Moazenzadeh, A. et al., J. Micromech. Microeng. 23, 114020 (2013).
[13] Karnaushenko, D. et al., Adv. Mater. 27, 6582 (2015).
[14] Karnaushenko, D. et al., Adv. Mater. 27, 6797 (2015).
[15] Baca-Solis, E., and Alamo, M. F., J. Anal. Bioanal. Tech. 7, 1 (2016).
[16] arnaushenko, D. D. et al., NPG Asia Mater. 7, 188 (2015).

Funding

This work was supported by the German Research Foundation DFG
(Grant No. FOR 1713, SCHM 1298/22-1, and grant MA 5144/2-1).

Cooperation

Electronics Laboratory, ETH Zürich, Gloriastraße 35, 8092 Zürich, Switzerland
Sensor Technology Research Center, University of Sussex, Falmer, Brighton, BN1 9QT, United Kingdom
Division of Neurodegenerative Diseases, Department of Neurology,
Technische Universität Dresden, D-01307 Dresden, Germany
Intelligente Werkstoffe und Funktionselemente,
Helmholtz-Zentrum Dresden-Rossendorf, Bautzner Landstraße 400, 01328 Dresden.

Coupling phenomena in microtube optical cavities

J. Wang, Y. Yin, Q. Hao, Y.-D. Yang, S. Valligatla, Y. Zhang,
E. Saei Ghareh Naz, Y. Li, C. N. Saggau, L. Ma, and O. G. Schmidt

Abstract

Nanomembranes have been explored as a fascinating platform for confining and guiding lightwaves. The investigation of optical confinement and energy transfer in nanomembrane-based photonic molecules potentially provides new insights into the manipulation of mode coupling for fundamental research and practical applications. Recently we proposed and experimentally demonstrated coupling phenomena in novel types of photonic molecules which are formed by trapping a microsphere into microtube cavity, and particularly concentric microtube ring cavities. These experimental demonstrations enable the formation of hybridized supermodes in nanomembrane-based photonic molecules and allow for flexible tuning between weak and strong coupling regime in an on-chip integrated form.

Split resonant modes in nanomembrane-based photonic molecules

Photonic molecules formed by coupling microcavities, especially those featuring whispering gallery mode (WGM) resonances, have been demonstrated as a powerful platform for studying strong interaction of two or more eigenstates and unfolding rich physical phenomena [1]. The conventional strategy requires precision manipulation of microcavities into close proximity so that evanescent field-assisted coupling occurs at the outer tangent site of neighboring cavities with the same shape [1, 2]. However, such a scheme might be prone to external disturbance. Recently, we have explored novel strategies of optical coupling in a system made of a microsphere trapped in a microtube [3], and in a concentric dielectric ring structure which enables efficient light interaction along the whole concentric resonant orbit [4], as shown in Figure 1.

Figure 1(a) schematically shows a photonic molecule consisting of a microtube formed by rolling up SiO_x/SiO_2 bilayer nanomembranes and a trapped microsphere. Resonant WGMs supported by the microsphere and microtube get coupled with each

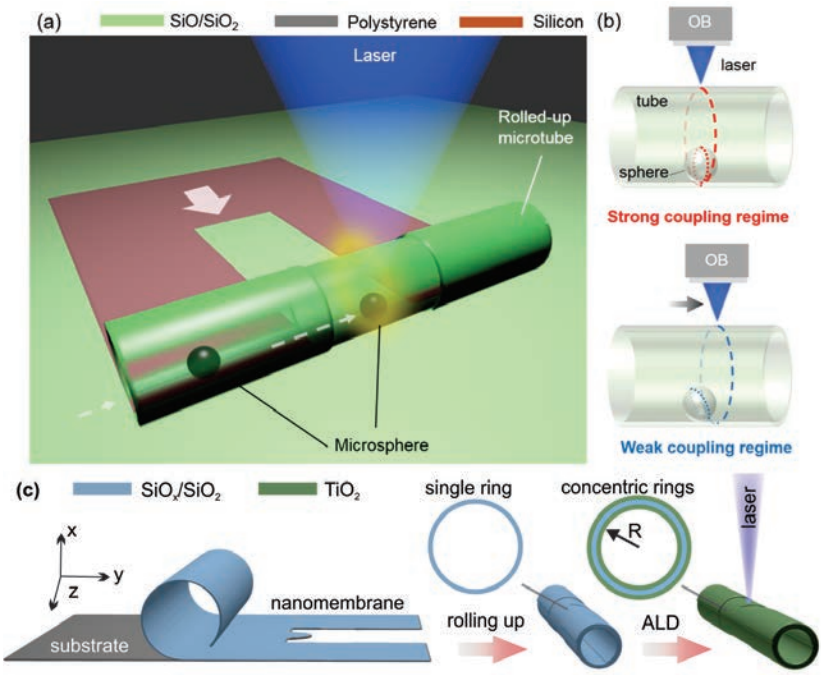

Figure 1: Schematics showing two types of photonic molecules formed by nanomembrane-based tubular cavities. (a) Tube-sphere system. (b) Schematic showing the varying excitation position and corresponding coupling regimes. (c) Process flow showing the formation of concentric microtube ring cavities.

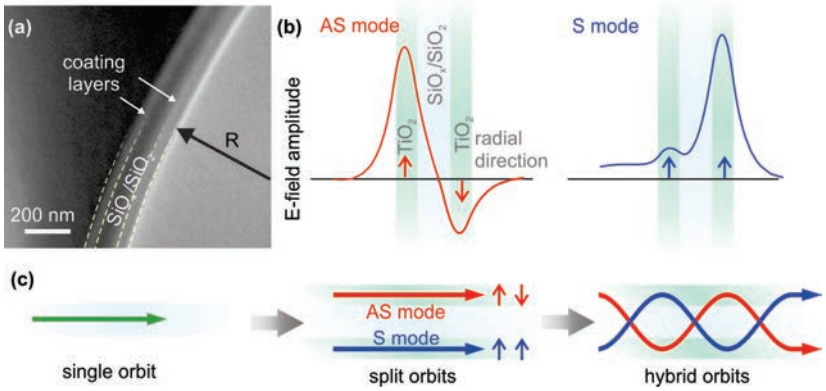

Figure 2: Scanning electron microscopy (SEM) image and schematic showing the concentric ring system and the supermodes. (a) SEM image showing the cross-sectional view of fabricated concentric rings after cutting by focused ion beam. (b) Calculated electric field amplitude of S and AS modes. (c) Schematic showing the evolution of the resonant orbit in a single ring and concentric rings

other, leading to the occurrence of hybrid modes. As illustrated in Figure 1(b), a resonant orbit overlapping with the tangent point of the sphere-tube system leads to maximized optical interactions in the strong coupling regime, while a shifted excitation leads to an enlarged coupling gap and suppressed coupling strength.

In an alternative strategy, coating of high-index TiO_2 layers on both inner and outer surface by atomic layer deposition (ALD) results in a concentric tubular structure (see Figure 1(c)). As such, the thin nanomembrane layer (down to ~100 nm) serves as a low-index spacing layer with rigid mechanical stability. The rolled-up nanomembrane thickness determines the inter-cavity coupling strength.

In the following, we focus on the concentric microtube ring cavities to illustrate the optical coupling phenomena in nanomembrane-based photonic molecules. As shown in Figure 2, a pair of split supermodes are revealed by numerical calculations, namely symmetric (S) and anti-symmetric (AS) modes (see Figure 2(b)). The S mode suggests parallel electric field vectors distributed in the inner and outer high-index layers while the AS mode comprises antiparallel vectors along the resonant orbits. Through spectral detuning of the two modes, strong coupling between two modes potentially leads to a hybridized resonant orbit, as shown in Figure 2(c). The mode intensity maximum oscillates across the concentric rings along the full orbit.

Figure 3(a) shows the evolution of resonant modes in TM (transverse-magnetic, electric fields parallel to the tube axis) mode upon a gradually increased coating thickness. The original high order axial modes are highly suppressed because of the degraded optical confinement along the axial direction. Meanwhile, the original fundamental mode splits into S and AS modes with decreased Q factors. Two-dimensional numerical simulations based on the finite-element method was carried out to visualize the split S and AS modes in the cross-sectional view. Figure 3(b) and (c) shows the simulated mode field intensity distributions of S and AS modes, respectively. The S mode suggests a strong overlap with the outer cavity and also a significant portion in the middle low-index spacing layer, while the AS mode reveals a strong mode localization in the inner cavity and a much weaker field in the spacing layer.

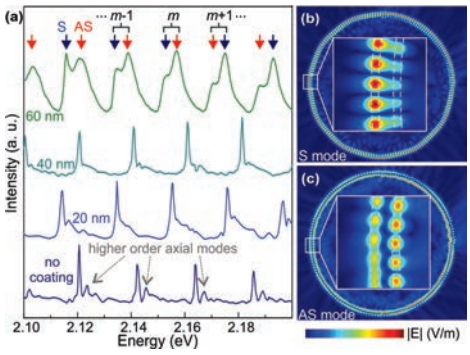

Figure 3: Measurement and simulation results of split modes in concentric rings upon TM polarization. (a) Evolution of resonant modes upon coating thickness of 0, 20, 40 and 60 nm. (b)-(c) Simulated electric field intensity distribution in a cross-sectional view for (b) S mode, (c) AS mode. Insets: zoom-in view.

Mode detuning by a varying nanomembrane winding.

The coupling strength between S and AS modes can be characterized by spectral detuning of one mode. The common scheme with localized thermal tuning could be technically difficult in a concentric ring system. Here the variation of winding number W along the axial direction effectively changes the average thickness of the middle spacing layer. As shown in Figure 4(a)–(b), a patterned nanomembrane with

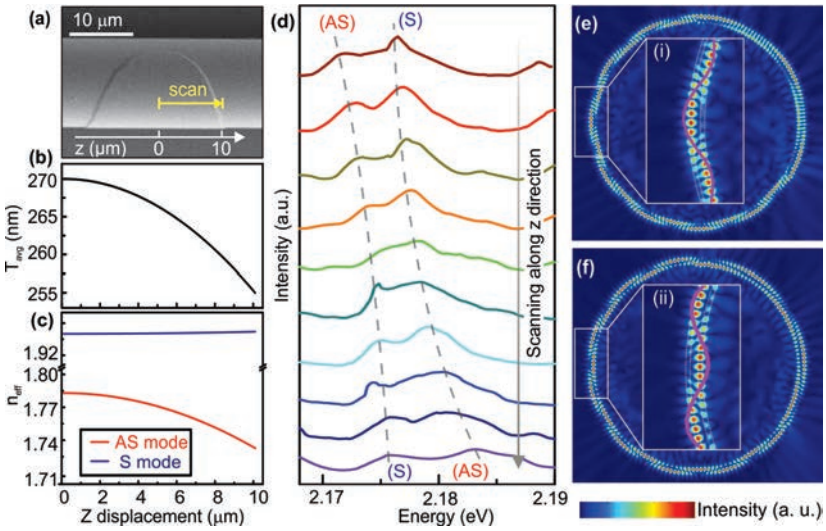

Figure 4: Spectral detuning of supermodes by spatially resolved measurement along the tube axis. (a) SEM image of the concentric cavity with a parabolic-shaped lobe design and the varying W from ~2.5 to ~2.25. (b) Calculated averaged thickness Tavg as a function of Z offset. (c) Calculated effective refractive index neff as a function of Z offset for AS and S modes. (d) Measured resonant spectra upon varying Z offset. (e)–(f) Simulated mode field intensity distribution of the two hybridized supermodes upon strong coupling. The insets show the oscillating behavior between concentric layers with opposite phase.

an additional parabolic-shaped segment (also termed as "lobe") leads to a varying W upon a tiny axial offset, which serves as a new degree of freedom to investigate the resonant coupling between S and AS modes.

Numerical calculation results reveal that a stronger perturbation to the AS mode occurs upon a varying W, while the effect on the S mode is much less prominent (see Figure 4(c)). Figure 4(d) summarizes the measured spectra upon spatial mapping along the tube axis around the lobe region. The AS mode is spectrally detuned across the S mode, which agrees with the trend shown in the calculation results. The mode spacing first decreases from 8.0 to 3.1 meV, and then increases to 4.8 meV upon a total offset of ~10 μm, which indicates the anti-crossing characteristic of the eigenenergies in the strong coupling regime [1, 4].

We further investigated the mode field profile under strong coupling by numerical simulation. Figure 4(e)–(f) shows the mode field distributions of the two hybridized supermodes. Instead of a dominant distribution in the outer (inner) ring for the S (AS) mode, a hopping-like mode profile between the outer and inner ring with opposite phase is formed. Such an oscillating hopping wave suggests new insights into the WGM resonances with potentially novel applications. For example, the hybridized supermodes reveal distinctive mode profiles at specific outer ring edge due to the mode orthogonality, which facilitates angle/position-resolved selective outcoupling in such a compact photonic molecule system.

Moreover, a convenient and highly flexible scheme for tailoring the coupling strength in such a concentric ring system is demonstrated by changing the winding number of the nanomembrane (i.e., effectively the thickness of the spacing layer). Simulation results for a winding number of ~4 suggest that the split modes cannot be described by S and AS modes. We term them as inner (IN) or exterior (EX) mode due to the localized distribution in either the inner or outer layer. Spatial mapping results reveal a spectral detuning of EX mode across the IN mode. Notably, the mode anticrossing cannot be observed due to the strongly suppressed coupling strength and the tuning from strong to weak coupling regime.

In summary, we have proposed and demonstrated two schemes for strong mode interaction using rolled-up nanomembrane based photonic molecules. Spectral anticrossing was observed as evidence of strong coupling. We envision such nanomembrane-based photonic molecule systems will be of significant research interest for fundamental studies such as non-Hermitian physics and exceptional points and practical applications such as self-referenced sensors and single-mode lasers.

[1] H. Cao et al., Rev. Mod. Phys. 87 (2015), 61
[2] T. Siegle et al. Light Sci. App. 6 (2017), e16224
[3] J. Wang et al., Adv. Opt. Mater. 1 (2018), 1700842
[4] J. Wang et al., Nano Lett. 11 (2018), 7261

Funding

This work is partially supported by the German Research Foundation DFG (Grant FOR 1713, SCHM 1298/22-1 and Leibniz program).

Cooperation

*State Key Laboratory of Integrated Optoelectronics, Institute of Semiconductors, Chinese Academy of Sciences, Beijing, 100083, China

Brightest source of entangled photons

Y. Chen, M. Zopf, R. Keil, F. Ding, O. G. Schmidt

Abstract

Many quantum photonic technologies require the efficient generation of entangled pairs of photons, but to date there have been few ways to produce them reliably. Sources based on parametric down conversion operate at very low efficiency per pulse due to the probabilistic generation process. Semiconductor quantum dots can emit single pairs of entangled photons deterministically but they fall short due to the extremely low-extraction efficiency. Strategies for extracting single photons from quantum dots, such as embedding them in narrowband optical cavities, are difficult to translate to entangled photons. Here, we build a broadband optical antenna with an extraction efficiency of 65 % ± 4 % and demonstrate a highly-efficient entangled-photon source by collecting strongly entangled photons (fidelity of 90 %) at a pair efficiency of 0.372 ± 0.002 per pulse. The high brightness achieved by our source represents a step forward in the development of optical quantum technologies.

Highly-efficient extraction of entangled photons from quantum dots using a broadband optical antenna

Sources of entangled photons lie at the heart of photonic quantum information processing [1]. They are most commonly based on spontaneous parametric down conversion (SPDC) of laser photons in nonlinear optical crystals [2]. The brightest SPDC-based sources have catalyzed recent breakthroughs such as ten-photon entanglement or satellite-based entanglement distribution. However, the major bottleneck is the intrinsically limited source efficiency: To avoid too much noise, photon pairs can only be produced at a low rate (p), typically $p < 0.1$ per excitation pulse [3].

Semiconductor quantum dots (QDs) are a promising alternative, as polarization-entangled photon pairs can be produced with almost 100 % probability [4]. The radiative cascade decay from the biexciton (XX) state to the ground state via intermediate exciton states (X) results in the two-photon state $|\phi\rangle = |H_X H_{XX}\rangle + |V_X V_{XX}\rangle$, with H (V) denoting horizontal (vertical) polarization. However, QD anisotropies give rise to a fine structure splitting (FSS) between the exciton states, weakening the entanglement. GaAs/AlGaAs QDs fabricated by nanohole etching and infilling exhibit vanishingly small FSS. They are reproducible to make and can emit highly indistinguishable and strongly entangled photons [5, 6].

Yet, the faintness of QD sources remains a major hurdle. Less than 1 % of photons escape the high refractive index semiconductor material due to total internal reflection. This limitation can be overcome by integrating QDs into microcavities or broadband dielectric nano-antennas. This approach resulted in entangled pair emission probabilities per pulse p of 0.12 and moderate entanglement fidelities F of 67 % [7]. However, so far the employed structures are technologically complex and challenging to improve, limiting wider application.

In this work, we design and fabricate a QD-based entangled photon source of high brightness, using a broadband dielectric photonic antenna. Under resonant pumping, highly-entangled photons are emitted with unprecedented photon pair efficiency p of 0.372 ± 0.002.

Optical antenna design and characterization

The GaAs QDs are fabricated by solid-source molecular beam epitaxy. *In-situ* Al droplet etching creates symmetric nano-holes on an AlGaAs surface that are then filled with GaAs and capped with AlGaAs. These QDs feature an average FSS of only (4.8 ± 2.4 µeV) and narrow wavelength distributions. Due to the high refractive index of AlGaAs (n_1 = 3.5), virtually no light is coupled into free space (n_2) beyond the critical angle of total internal reflection α_{c12} = arcsin (n_2/n_1). Instead, an exponentially decaying evanescent wave is formed at the semiconductor/air interface. We propose that, by bringing a high refractive index material (medium n_3 = 3.4) close to the interface in a well-adjusted distance, photons can be funneled efficiently into medium n_3 as the evanescent wave transforms into a propagating wave (Figure 1a).

The fabrication flow of the sample is shown in Figures 1e–f. We employ a commercially available Gallium Phosphide (GaP) semi-spherical lens, with a diameter of 2 mm and a refractive index n_3 very close to n_1. An anti-reflection layer of alumina is deposited on top using atomic layer deposition. We choose Polymethyl methacrylate (PMMA) with n_2 = 1.6 as the intermediate layer and its thickness can be well controlled by the spin coating speed. A single QD membrane, prepared via wet chemical etching, with a reflecting silver layer is glued to the center of the PMMA covered GaP lens. The QD layer is precisely positioned at the anti-node of the thin membrane cavity.

We theoretically investigate the photon extraction efficiency for different PMMA gap sizes, as shown in Figure. 1c. Without a gap, high extraction efficiencies can only be obtained by using objectives with high NA. Using 100 nm PMMA, a convergent emission in a NA = 0.42 objective can be achieved with an efficiency of 70 %. We avoid the commonly occurring air gaps between the uneven SIL surface and the substrate by using a thin/flexible QD- containing membrane which adapts to the SIL. Our design offers broadband operation (see Figure 1e), i.e. the energetically different X and XX photons are efficiently extracted simultaneously.

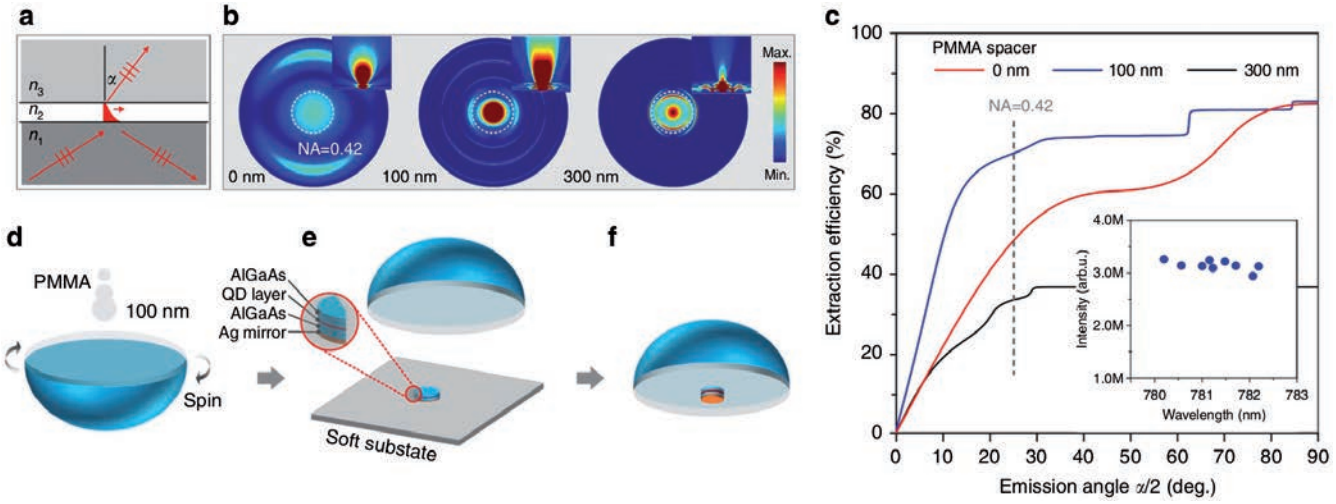

Figure 1: Dielectric antenna design and numerical results. **(a)** Sketch of light propagating at the media interfaces as in our design ($n_1 \geq n_3 > n_2$). The evanescent wave at the interface couples to the propagating wave when the intermediate gap decreases. **(b)** Far field view and cross section (inset) of dielectric antennas' emission for different PMMA spacer thicknesses, showing the best results for 100 nm. **(c)** Numerical results for the dielectric antenna as a function of emission angle α. Inset shows the broadband operation of the dielectric antenna. All QDs randomly chosen across the membrane are bright. **(d–f)** Fabrication flow of the device, which consists of a QD containing AlGaAs membrane (n_1), a low refractive index PMMA spacer (n_2) and the GaP solid immersion lens (SIL, n_3). A bottom silver mirror is used to reflect downward-emitted photons.

The QD photoluminescence (PL) is then measured in a helium flow cryostat. The QDs are excited above-band by a pulsed laser at a 76 MHz repetition rate. We measure a single-photon flux of over 3 MHz per second on the CCD for most of the randomly selected QDs. Power-dependent PL intensity of a QD in the antenna is recorded by an avalanche photodiode (APD) and shown in Figure 2a. An enhancement of a factor >100 in comparison with a bare QD substrate is observed, resulting in count rates of 3.3 MHz at saturation. At the first collection lens, the single-photon extraction efficiency η is calculated to be 65 % ± 4 %, for both X and XX photons.

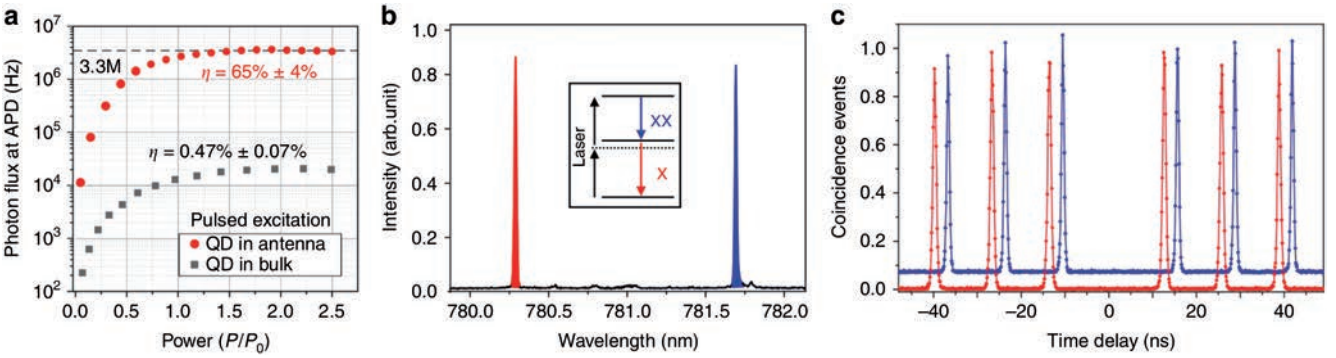

Figure 2: Characterization of the broadband dielectric antenna and pulsed resonant excitation of XX state. **(a)** Single photon flux measured on APD, plotted as a function of laser excitation power (in saturation units), for a QD in the dielectric antenna (red) and in the unprocessed substrate (gray). At saturation, 3.3 million single photons per second are detected. **(b)** QD emission spectrum under resonant excitation of the XX state using a two-photon pump scheme. **(c)** Intensity autocorrelation under resonant excitation, showing nearly ideal single-photon emissions for both X and XX photons ($g^{(2)}(0) \cong 0.002$).

Evaluating the degree of entanglement

We apply a two-photon pumping scheme in order to deterministically generate polarization entangled photons from single QDs (inset of Figure 2b). Residual laser background, spectrally in between the X and XX photons, is minimized by performing the experiment in a fiber-based closed-cycle cryostat with a confocal setup and notch filters inserted in the beam.

At π-pulse excitation, we obtain very pure emission and equal intensities for X and XX photons (Figure 2b). The XX population fidelity is estimated to be 88 %. Auto-correlation measurements (see Figure 2c) prove ultra-high purity of single photon emission of over 99.8 %. In combination with the determined extraction efficiency at the first collection lens of 65 % ± 4 %, we determine the entangled photon pair efficiency per excitation pulse to be p~0.372 (0.002). For optical fiber-based applications, a further optimization of the current design may be required, as it does not have a perfect Gaussian distribution.

Due to its large size, our dielectric antenna is insensitive to the lateral distribution of QDs, in contrast to photonic nanostructures requiring precise emitter displacement. Among many available QDs, one with a FSS of s = 1.5 ± 0.4 μeV is chosen. Figure 3a shows six polarization-dependent cross-correlation measurements on the XX and X photons, in the rectilinear (HV), diagonal (DA) and circular (RL) polarization basis. Strong bunching in VV, DD, RL together with strong anti-bunching in VH, DA, RR show that the XX and X photons are entangled. The fidelity to the maximally entangled state is obtained to be F = 90 ± 3 %. The exact two-photon quantum state is determined by performing quantum-state tomography based on 16 different cross-correlation measurements. The resulting two-photon density matrix (Figures 3b & c) exhibits a similar fidelity of F = 89 %.

Figure 3: Entanglement fidelity of a quantum dot with finite FSS. **(a)** XX-X cross-correlation measurements under resonant two-photon excitation for co- and cross-polarized photons in the rectilinear (HV), diagonal (DA) and circular (RL) polarization bases. The graphs for co-polarized (red) and cross-polarized (black) photons are shifted by 3 ns for clarity. A fidelity F = 90% is extracted. **(b)**, **(c)** Real (b) and imaginary (c) parts of the two-photon density matrix as reconstructed from 16 correlation measurements of the same QD by employing the maximum likelihood technique. The fidelity extracted from this matrix is F = 89 %.

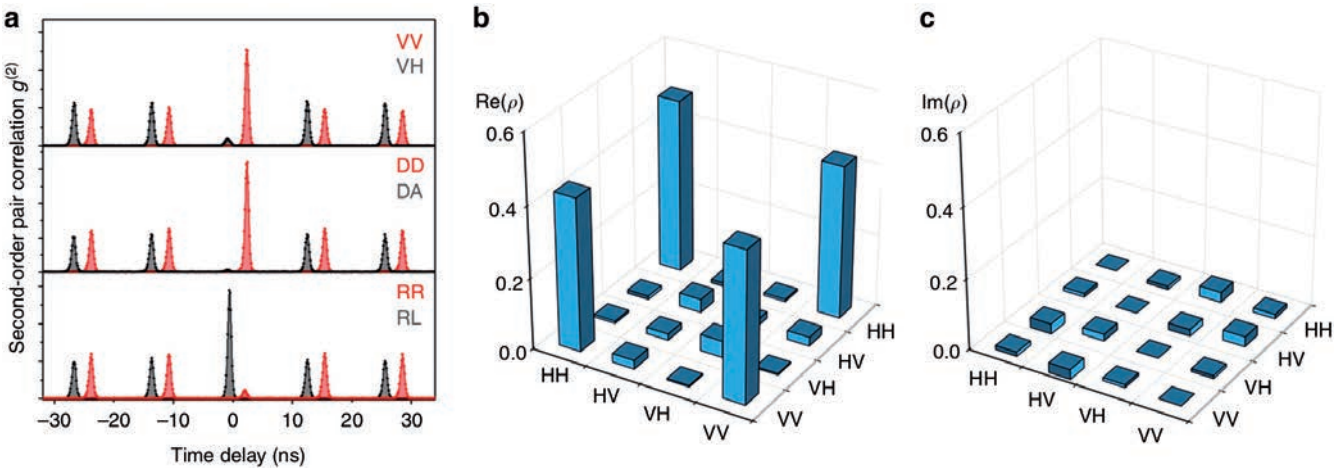

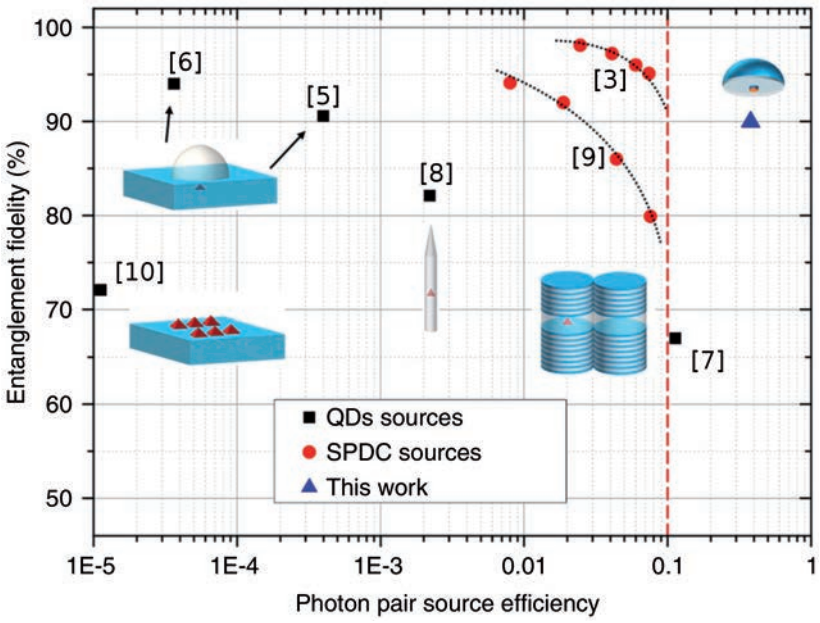

Figure 4: Comparison with other QD and SPDC entangled photon sources. Entanglement fidelity over source efficiency is shown for several different types of QD sources as black symbols. High quality SPDC entangled photon sources are shown as red symbols, see also [8]. Red dashed line indicates the efficiency limit of SPDC sources. The performance of the current device is shown as a blue triangle in the upper right corner, marking the highest combination of source brightness and entanglement fidelity.

Discussion and comparison with state-of-the-art

A comparison with other QDs and SPDC sources is shown in Figure 4. We plot the entanglement fidelity to a maximally entangled state over the photon-pair source efficiency p in the first collection optics. An ideal source would sit in the upper right corner of the diagram. While the SPCD source (red circles) efficiency must be kept below 0.1 to maintain an acceptable entanglement fidelity, QDs (dark squares) can reach near-unity efficiency and strong entanglement simultaneously. However, most QD based entangled photon sources to date are extremely inefficient ($p \sim 10^{-5}$ to 10^{-4}). Our experiment (blue triangle in Figure 4) demonstrates a simple and robust optical antenna with an unprecedented entangled photon pair efficiency p of 0.372 ± 0.002, with high single-photon purity (99.8 %) and entanglement fidelity (90 %). Therefore, we have shown that QDs have the potential to overcome the main deficiency of SPDC sources. Our device design is readily applicable to various optical-active materials. Because of its brightness, it is of particular interest for quantum communication protocols (using e.g. telecom QDs), quantum metrology or quantum imaging.

[1] H. J. Kimble, Nature 453, 1023–1030 (2008).
[2] P. G. Kwiat et al., Phys. Rev. Lett. 75, 4337–4341 (1995).
[3] X.-L. Wang et al., Phys. Rev. Lett. 117, 210502 (2016).
[4] O. Benson et al., Phys. Rev. Lett. 84, 2513–2516 (2000).
[5] R. Keil and M. Zopf et al., Nat. Commun. 8, 15501 (2017).
[6] D. Huber et al., Nat. Commun. 8, 15506 (2017).
[7] A. Dousse et al., Nature 466, 217–220 (2010).
[8] K. D. Jöns et al., Sci. Rep. 7, 1700 (2017).
[9] V. Scarani et al., Eur. Phys. J. D. 32, 129–138 (2005).
[10] G. Juska et al., Nat. Photon. 7, 527–531 (2013).

Funding

ERC Starting Grant No. 715770 (QD-NOMS), BMBF Q.Com-H (16KIS0106), European Union Seventh Framework Programme 209 (FP7/2007–2013) under Grant Agreement No. 601126 210 (HANAS).

Research Area 3: Quantum Effects at the Nanoscale

Delamination and intercalation of α-$RuCl_3$

M. Grönke, P. Schmidt[1], M. Valldor, S. Oswald, D. Wolf, A. Lubk, B. Büchner, C. Habenicht, E. Müller, M. Knupfer, S. Kretschmer, M. Richter, J. van den Brink, F. Börrnert, D. Nowak[2], A. Isaeva[2], Th. Doert[2], S. Hampel, A. Koitzsch

Abstract

α-$RuCl_3$ is a promising candidate for the realization of a quantum spin liquid ground state related to the Kitaev model and as such received broad attention recently. From a structural point of view it is a layered material with in-plane honeycomb lattice and weak interlayer forces. This implies the possibility to manipulate its properties by well known methods for typical 2D materials: exfoliation and intercalation. Here we synthesized thin α-$RuCl_3$ nanosheets with heights ≤ 30 nm via chemical vapor transport and thoroughly characterized the crystals properties before successfully delaminating it down to the monolayer limit. We also succeeded in intercalating α-$RuCl_3$ by potassium which effectively electron dopes the material and causes a peculiar charge- and spin disproportionation. These results demonstrate ways to modify and control material properties of α-$RuCl_3$.

Vapor growth of α-$RuCl_3$ nanosheets and delamination down to monolayer

Transition metal trihalides are of current interest due to their honeycomb structure of weakly coupled adjacent layers with strong bond anisotropy. Thus frustration could stabilize new patterns of cooperative magnetic interactions. [1–5] A promising candidate to realize a Kitaev Heisenberg (KH) model is the 2D layered honeycomb magnet α-ruthenium(III) chloride (α-$RuCl_3$). One branch of current research focuses on topological influences on the magnetic properties of ultrathin α-$RuCl_3$ nanosheets as compared to their bulk phase.[6] Here we present, to our knowledge, the first approach to synthesize phase pure α-$RuCl_3$ crystals on the nanoscale via short-term chemical vapor transport (CVT). Furthermore individualization and isolation of the as-grown nanocrystals was achieved by different delamination techniques (see Figure 1).

We investigated the vapor growth of α-$RuCl_3$ to achieve as-grown, high crystalline, isolated nanosheets on YSZ (yttria stabilized zirconia, ZrO_2:Y) substrates (see Figure 2a). In order to comprehend the occurring vapor phase mechanisms completely, we started to simulate the vapor transport process with the free available software TRAGMIN (see Figure 2b). According to applied transport temperatures (973 K to 773 K) we could evaluate the gas phase composition and confirm low transport rates (0,5 mg/h), essential for the deposition of thin sheets on suitable substrates

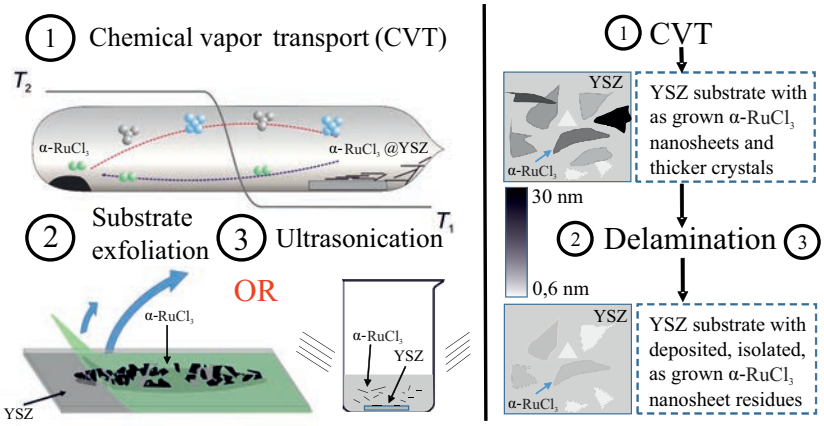

Figure 1: Concept of experimental approach for the synthesis of α-$RuCl_3$ nanosheets; firstly as-grown α-$RuCl_3$ nanosheets and thicker crystals are deposited on YSZ substrates by chemical vapor transport (CVT) following the delamination of thicker structures by two different approaches (substrate exfoliation or ultrasonication) resulting in isolated, as-grown α-$RuCl_3$ nanosheets and thin residues from thicker structures.

by means of CVT. Thereby vapor transport is mainly ensured by sublimation and self-transport of introduced $RuCl_3$ powder. According to pure short-time CVT it is possible to deposit thin sheets of α-$RuCl_3$ down to thicknesses of 18 nm (see Figure 2c) directly on substrates. Herein the key points are short timescales combined with a lower defect emergence (stacking faults). Furthermore we could visualize atomic planes of nanosheets by means of high resolution transmission electron microscopy (HR-TEM) and selected area electron diffraction (SAED) proving α-$RuCl_3$ with trigonal space group $P3_112$ (see Figure 2a). Despite the fact that nanomaterials tend to oxidize more than their bulk counterpart, we could show that α-$RuCl_3$ nanosheets are not oxidized and detected oxygen is only surficial adsorbed at the surface of nanosheets by means of X-ray photoelectron spectroscopy (XPS).

Since vapor transport techniques encounter limits regarding the minimum thickness of deposited structures, we applied several delamination techniques to exhaust the two dimensional structure of α-$RuCl_3$. By means of ultrasonication and NMP (N-methyl-2-pyrrolidone) as dispersing agent it was possible to generate isolated monolayers (see Figure 2e,f and AFM picture in 2a). Besides delamination, the majority (> 85 %) of thicker structures (> 200 nm) could be removed from the substrate surface using NMP at very short sonication times of only thirty seconds (see Figure 2d). By extending the sonication time up to three minutes, almost every thicker structure is eliminated and the number of thin sheets is enlarged greatly due to sonication effects. This combined approach (CVT & delamination) could be applied to other two dimensional systems for efficient synthesis of monolayer structures on substrates.

Our approach in general represents a potential anchor point for the synthesis of many other two dimensional materials with the need to produce thin sheets on top of substrates for the study of interesting physical phenomena. It includes low timescales, is easy to handle and very reproducible. Next to that, the combined approach (CVT and delamination) has an enormous potential for a broad range of two dimensional materials, not only transition metal trihalides.

Figure 2: Structural characterization of as-grown α-$RuCl_3$ nanosheets on YSZ substrates: **(a)** optical microscopy, HRTEM image of an α-$RuCl_3$ nanosheet taken along the [001] zone axis, investigated α-$RuCl_3$ monolayer by means of AFM, SAED measurement: electron diffraction pattern of an α-$RuCl_3$ nanosheet, **(b)** Thermodynamic simulation of chemical vapor transport with the program package TRAGMIN: transport efficiencies with transport agent Cl_2 (negative slope) and transport efficient gas species (positive slope) dominated by the sublimation of $RuCl_3$ and small amounts of $RuCl_4$ and Cl, **(c)** AFM-measurement of α-$RuCl_3$ nanosheets after pure chemical vapor transport (inset: images of investigated nanosheets), **(d)** size distribution of α-$RuCl_3$ structures after pure chemical vapor transport (orange), after 30 seconds of delamination (ultrasonication) with N-methyl-2-pyrrolidone (green) and after 3 minutes of delamination (ultrasonication) with N-methyl-2-pyrrolidone (purple), **(e)** investigated α-$RuCl_3$ nanocrystal by means of AFM (the red area indicates the AFM measurement of f) and (f) AFM measurement (inset: crystal structure of α-$RuCl_3$, the red dashed line indicating the theoretical layer thickness of a monolayer).

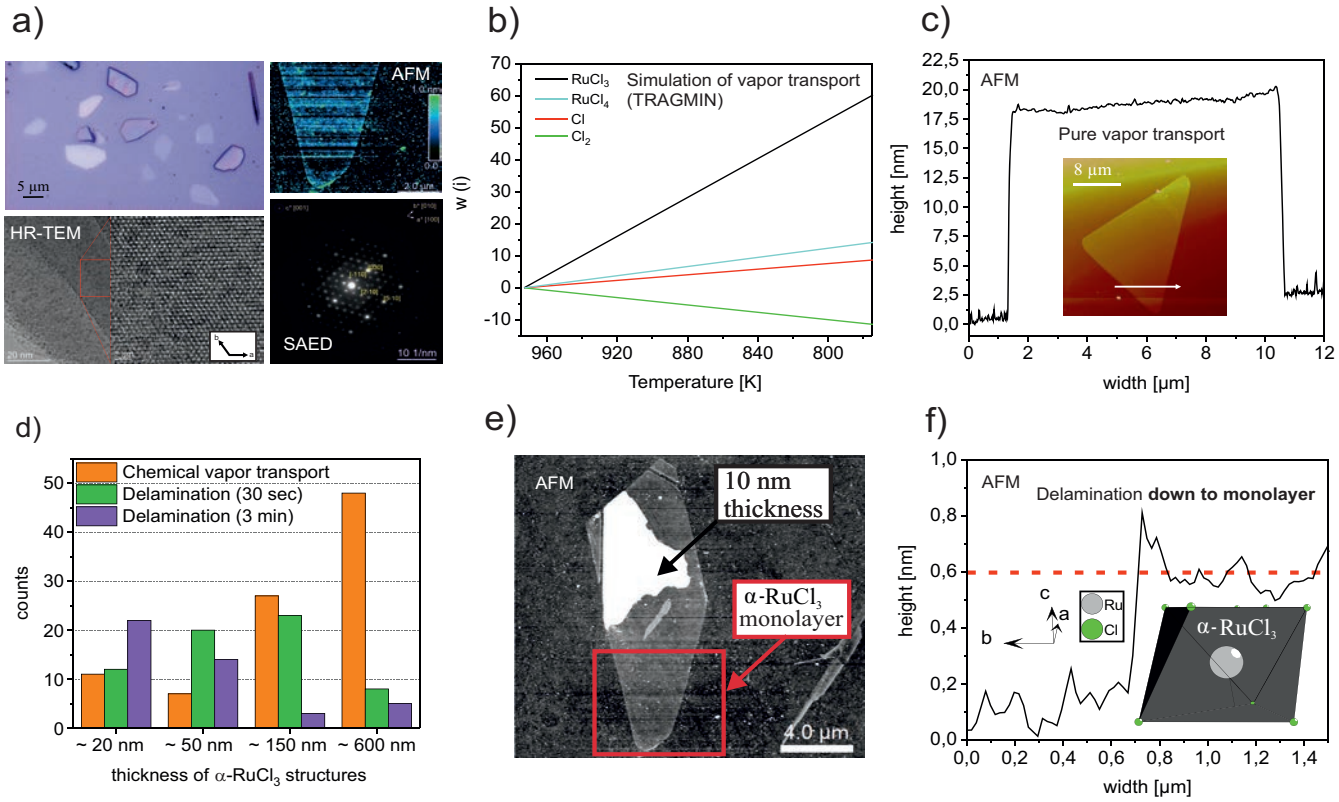

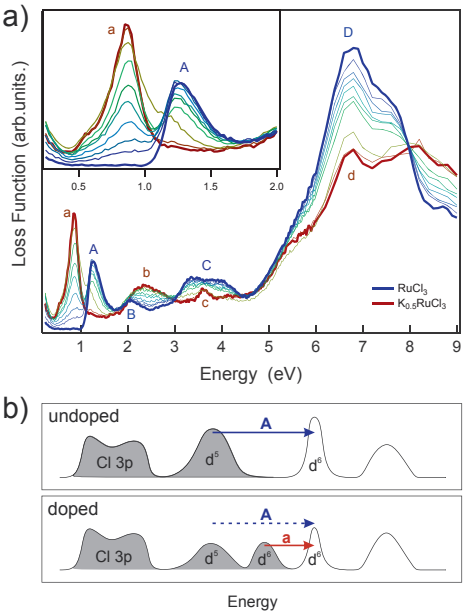

Figure 3: (a) Loss function measured by electron energy loss spectroscopy for different degrees of potassium intercalation. Capital letters mark peaks in the spectrum of the undoped material, while small letters mark peaks in the spectrum of the doped material. Inset: magnification of the gap region. (b) Schematic representation of the one-particle low-energy electronic structure of undoped and doped α-$RuCl_3$.

Potassium intercalation of α-$RuCl_3$

α-$RuCl_3$ is also a Mott insulator, which implies the possibility that novel exotic phases occur upon doping. Electron doping is achieved here by *in situ* potassium intercalation. An apparent and attractive goal of such an approach is to reach a metallic phase, where the underlying magnetic interactions may influence e.g. transport properties. However, a metallic state has not been created. Instead, we show by a combination of electron energy loss spectroscopy (EELS), photoemission spectroscopy (PES), and density functional theory (DFT) that electron doping alters the ground state of α-$RuCl_3$ in another peculiar fashion: a stable stoichiometry at $K_{0.5}RuCl_3$ is obtained. This gives rise to a charge disproportionation into formally Ru^{2+} ($4d^6$) and Ru^{3+} ($4d^5$). Every Ru $4d^5$ site with one hole in the t_{2g} shell is surrounded by nearest neighbors of $4d^6$ character, where the t_{2g} level is full and magnetically inert. Thus, each type of Ru site forms a triangular lattice, and nearest-neighbor interactions of the original honeycomb are blocked, an arrangement that may serve as a platform to study the interplay of nearest-neighbor and next-nearest-neighbor Kitaev exchange.[7]

Figure 3(a) shows the effect of successive K intercalation on the low-energy loss function measured by EELS in transmission, a bulk sensitive probe. The pristine spectrum shows a peak at E = 1.2 eV (labeled **A**), which corresponds to optical gap excitations. The peaks at higher energies **(B–D)** are due to crystal field and charge-transfer excitations.[5] K intercalation causes drastic changes to the electronic structure, in particular to the character of the gap. The inset of Figure 3(a) expands the low-energy region. We observe that with increasing K content, the spectral weight of the original **A** peak decreases and a new peak at lower energies appears (labeled **a**). Finally, at saturation, **A** completely vanishes. To find a rationale of these observations,

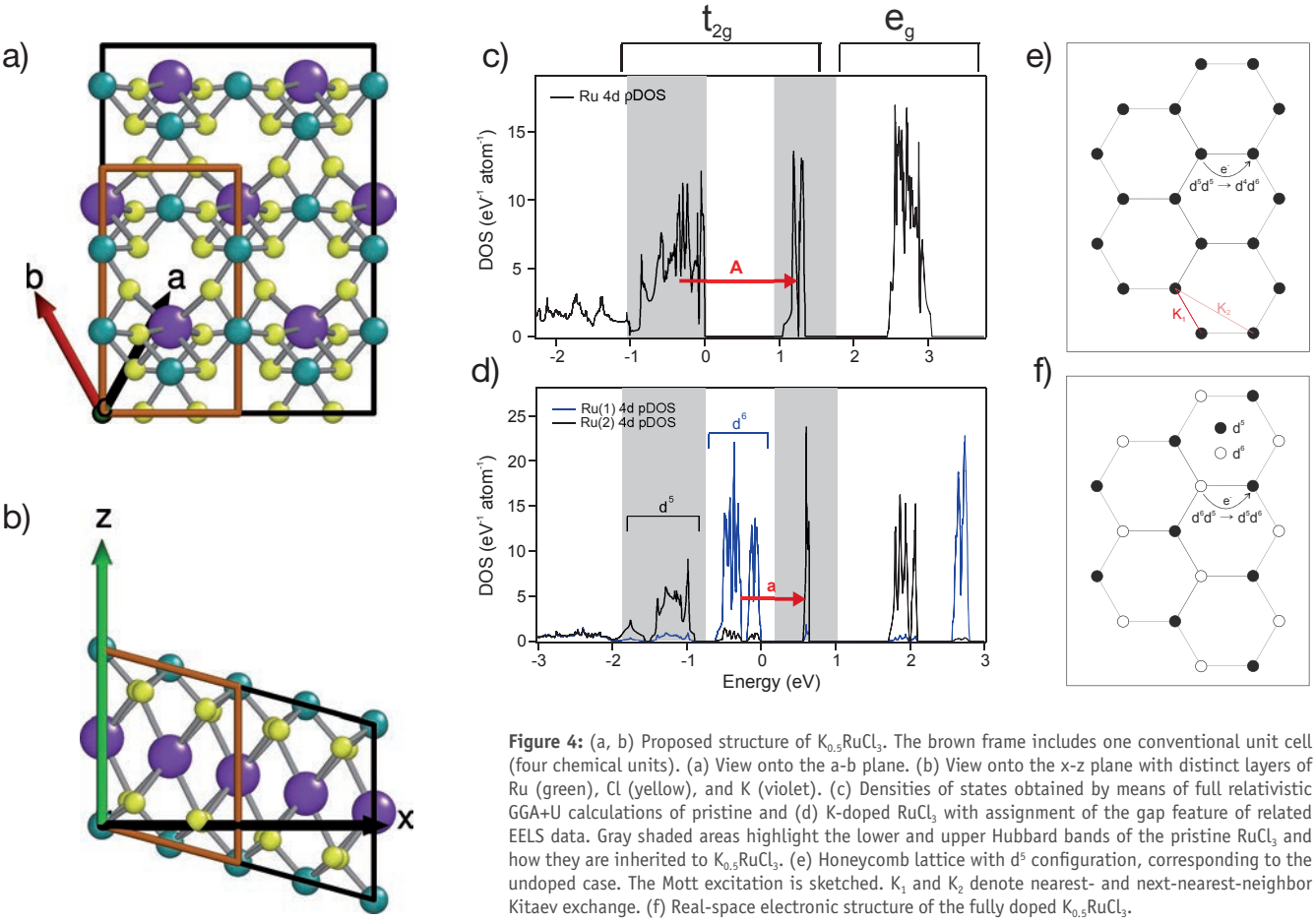

Figure 4: (a, b) Proposed structure of $K_{0.5}RuCl_3$. The brown frame includes one conventional unit cell (four chemical units). (a) View onto the a-b plane. (b) View onto the x-z plane with distinct layers of Ru (green), Cl (yellow), and K (violet). (c) Densities of states obtained by means of full relativistic GGA+U calculations of pristine and (d) K-doped $RuCl_3$ with assignment of the gap feature of related EELS data. Gray shaded areas highlight the lower and upper Hubbard bands of the pristine $RuCl_3$ and how they are inherited to $K_{0.5}RuCl_3$. (e) Honeycomb lattice with d^5 configuration, corresponding to the undoped case. The Mott excitation is sketched. K_1 and K_2 denote nearest- and next-nearest-neighbor Kitaev exchange. (f) Real-space electronic structure of the fully doped $K_{0.5}RuCl_3$.

we show a schematic picture of the low-energy electronic structure in Figure 3(b). Near the Fermi energy, the electronic states are dominated by Ru 4d character. In the undoped case, **A** corresponds to excitations across the Mott gap ($d^5d^5 \rightarrow d^4d^6$). With doping, new d^6 states are created inside the gap. The fact that **A** completely vanishes in the experiment could be naturally explained by full electron doping, that is, every Ru^{3+} ($4d^5$) ion is reduced to Ru^{2+} ($4d^6$) by the formation of $KRuCl_3$. Then, the d^5 states would disappear. However, this stoichiometry is not realized: quantitative x-ray photoemission spectroscopy (XPS), core-level EELS, and DFT consistently hint at a saturated stoichiometry $K_{0.5}RuCl_3$. This information allows us to construct a structural model in which the K intercalation takes place between two adjacent Cl layers and occupies interstitial sites (see Figure 4). Most intriguingly, within our DF calculations a ground state with charge order among the two Ru sites, denoted Ru(1) and Ru(2), is found. Further calculations show that this charge order is not driven by structural symmetry breaking due to the K intercalation.

The described situation is summarized in Figures 4(e) and 4(f) and explains the complete suppression of A upon half-doping. In the undoped case, the gap is defined by the Mott excitation $d^5d^5 \rightarrow d^4d^6$. In the doped case, this transition is blocked, as all d^5 sites are surrounded by d^6 sites. The gap excitation a is now associated with the charge fluctuation $d^6d^5 \rightarrow d^5d^6$.

Alkali metal intercalation offers a possibility to manipulate the charge and spin pattern of the honeycomb lattice in a controlled fashion. This is especially relevant because these patterns appear independently of the potassium lattice. The effect could be useful to study fundamental properties and to create qualitatively new magnetic ground states.

[1] Hentrich, R. et al. Unusual Phonon Heat Transport in α-$RuCl_3$: Strong Spin-Phonon Scattering and Field-Induced Spin Gap. Phys. Rev. Lett. 120, (2018).
[2] Grönke, M. et al. Chemical vapor growth and delamination of α-$RuCl_3$ nanosheets down to the monolayer limit. Nanoscale (2018).
[3] Wellm, C. et al. Signatures of low-energy fractionalized excitations in α-$RuCl_3$ from field-dependent microwave absorption. Phys. Rev. B 98, 184408 (2018).
[4] Koitzsch, A. et al. Low temperature enhancement of ferromagnetic Kitaev correlations in α-$RuCl_3$. arXiv 1709.02712 (2017).
[5] Koitzsch, A. et al. J_{eff} Description of the Honeycomb Mott Insulator α-$RuCl_3$. Phys. Rev. Lett. 117, 126403 (2016).
[6] Weber, D. et al. Magnetic Properties of Restacked 2D Spin 1/2 honeycomb $RuCl_3$ Nanosheets. Nano Lett. 16, 3578–3584 (2016).
[7] Koitzsch, A. et al., Nearest-neighbor Kitaev exchange blocked by charge order in electron-doped α-$RuCl_3$. Phys. Rev. Materials 1, 052001(R) (2017).

Funding

A. L. and D. W. acknowledge funding from the European Research Council via the ERC-2016-STG starting grant ATOM. This research has been supported by the DFG via SFB 1143.

Cooperation

[1] Institute of Applied Chemistry, Brandenburg University of Technology, Cottbus-Senftenberg, Universitätsplatz 1, 01968 Senftenberg, Germany
[2] Technische Universität Dresden, Department of Chemistry and Food Chemistry, D-01062 Dresden, Germany

Localization counteracts decoherence in noisy Floquet topological chains

M.-T. Rieder [1], L. M. Sieberer [2, 3, 4], M. H. Fischer [5] and I. C. Fulga

Abstract

The topological phases of periodically-driven, or Floquet systems, rely on a perfectly periodic modulation of system parameters in time. Even the smallest deviation from periodicity leads to decoherence, causing the boundary states to leak into the system's bulk. We show that in one dimension this decay of topologically protected end states depends fundamentally on the nature of the bulk states: a dispersive bulk leads to an exponential decay, while a localized bulk slows the decay down to a diffusive process. The localization can be due to disorder, which remarkably counteracts decoherence even when it breaks the symmetry responsible for the topological protection. We derive this result analytically, using a novel formalism which can be applied to any Floquet system, and confirm our findings with the help of numerical simulations. Our results are particularly relevant for experiments, where disorder can be tailored to protect Floquet topological phases from decoherence.

Topology and the conservation of energy

Topological insulators have a gapped bulk, but host protected gapless boundary states, which are responsible for robust, quantized observables. The most well-known example of a topological insulator is the quantum Hall effect [1], a two-dimensional system in which electrons propagate only along the edge, and only in one direction. Beyond the quantum Hall effect, there exists a very diverse zoo of theoretically proposed and experimentally demonstrated topological phases [2]. They can occur in one-, two-, and three-dimensional systems, and their boundary states often require one or more symmetries in order to remain protected. The quantum spin-Hall effect, for instance, relies on the conservation of time-reversal symmetry. Similarly, topological superconductors can only exist as long as particle-hole symmetry is intact, whereas the boundary states of so called "topological crystalline insulators" require crystal symmetries, such as reflection or rotation.

All of the above mentioned topological insulators are phases of matter occurring in time-independent systems. As such, all of them share the same, very basic requirement: the conservation of energy. The latter is often taken for granted in many areas of physics, and therefore often overlooked when discussing topology. However, it is an integral part of the definition of a topological insulator, since the distinction between a "gapped bulk" and a "gapless boundary" refers precisely to the fact that bulk and boundary states are separated in energy. Without energy conservation, the edge modes would leak into the bulk and the topological features of, say, the quantum Hall effect would be destroyed.

Periodically-driven systems: topology and noise

Is it then at all possible for topological insulators to exist if energy is not conserved? It turns out that the answer is yes, and one class of systems demonstrating this are periodically-driven, or Floquet topological phases [3]. The system Hamiltonian now changes as a function of time in a periodic fashion, often due to an externally applied driving field. Floquet systems can be engineered, for instance, by driving an alternating current with a fixed frequency through a sample. Alternatively, one can think of shining monochromatic laser light on a crystal, which means subjecting the surface to a periodically varying electromagnetic field.

Since the Hamiltonian changes all the time, its eigenvalues, the energies, are not conserved and cannot be used to make a distinction between gapped and gapless states. Instead of this, Floquet topology is diagnosed with the help of the time-evolution operator over one driving period. The latter is also known as the Floquet operator, and describes those states which return to their original forms after every period of the time evolution, as does the Hamiltonian. To each Floquet eigenstate corresponds an eigenphase of the Floquet operator, which is called a "quasi-energy", and plays an analogous role to the energy of time-independent systems. This allows for a direct translation between the topology characterizing static and driven systems. In particular, Floquet topological insulators are defined as having a bulk quasi-energy gap, and hosting robust boundary states which are gapless, again in a quasi-energy sense.

In spite of its apparent simplicity, the direct translation between energy and quasi-energy comes with an important caveat. Whereas the conservation of energy is a fundamental law of nature, quasi-energy conservation is not so easily achieved. Instead, the latter requires a perfectly periodic modulation of system parameters in time, which is impossible in any realistic laboratory conditions. Thinking again to the examples above, it is easy to imagine how the frequency of the AC current driving the system is not infinitely sharp, or how the intensity of the monochromatic laser light is not precisely constant. The result is then, invariably, noise-induced decoherence: in any realistic Floquet topological insulator, the boundary states will leak into the system's bulk, ultimately leading to a featureless steady state devoid of any topological properties.

Localization versus decoherence

In two recent works [4, 5], we decided to take a closer look at decoherence in Floquet systems, a problem which had not been thoroughly examined, despite its apparently grave implications for the existence of realistic, periodically-driven topological insulators. We focused on one of the simplest examples of Floquet topology, a one-dimensional chain hosting Floquet boundary states at both of its ends. The latter are separated in quasi-energy from bulk states, such that they are topologically protected. As discussed before, it is clear that if the Hamiltonian is not perfectly periodic in time then all topological features will be washed away in the infinite time limit. Is it however possible to (at least partially) mitigate the negative effects of decoherence, enabling the topological end state to be more easily observable in the lab?

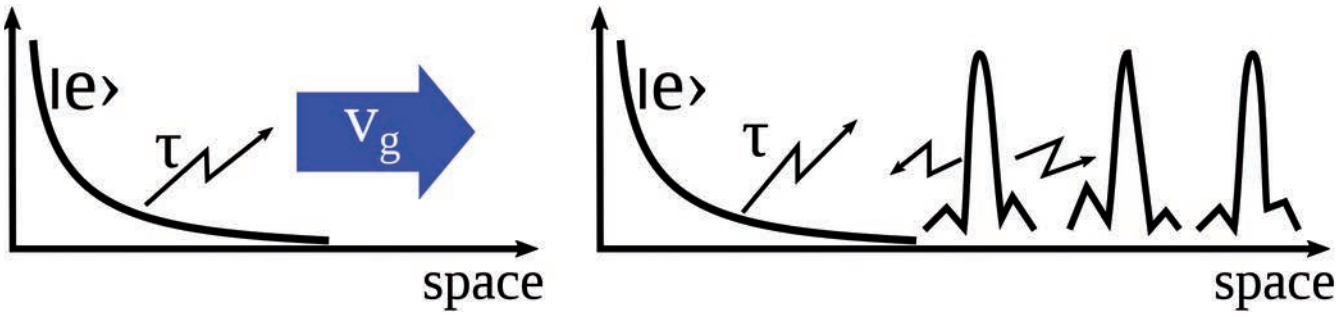

Figure 1: Due to mistakes in the periodic driving, a particle initialized in the topological end mode, $|e\rangle$, leaks into the bulk with a rate τ. If the bulk is dispersive (left panel), the wavefunction gets carried away with a group velocity v_g and never returns to the edge. However, if the bulk is localized (right panel), the wavefunction performs a random walk between localized bulk modes, and has a non-zero probability of returning to the edge.

To gain intuition about this problem, it is useful to first examine the limit of infinitesimally weak noise. We imagined that for many driving cycles, the Hamiltonian does change periodically in time, but that occasionally there is a "mistake" in the driving, a rare event at which the quasi-energies get mixed. As such, a particle initialized in the topological end state of the chain would remain in that end state until a mistake is encountered. At that point in time, part of it would leak into nearby bulk states. Afterwards, time evolution would continue with the periodic Hamiltonian until the next mistake is encountered, and so on.

Much to our surprise, the rate at which the end state decoheres depended fundamentally on the nature of bulk states (Figure 1). If the bulk is dispersive, then after every error of the driving protocol, the newly populated bulk states will freely move away from the boundary and that part of the wavefunction will never return to the edge. This results in a decay of the end state amplitude which is exponentially fast. However, a completely different picture emerges if the bulk is localized. In that case, every driving mistake causes part of the end state to enter a localized bulk mode positioned somewhere near the boundary. That newly populated state cannot move, and effectively remains "stuck" next to the edge until the next driving error is encountered. With every defect in the periodic driving, parts of the wavefunction have the chance to jump back and forth along the chain, such that the noisy time-evolution takes the form of a one-dimensional random walk between localized states. Crucially, this means there is a non-zero probability for the end state to get repopulated, which increases its average survival probability. This increase turns out to be by many orders of magnitude at long times (Figure 2), since the decay rate changes from an exponential to a diffusive one ($\sim 1/\sqrt{t}$, where t is time).

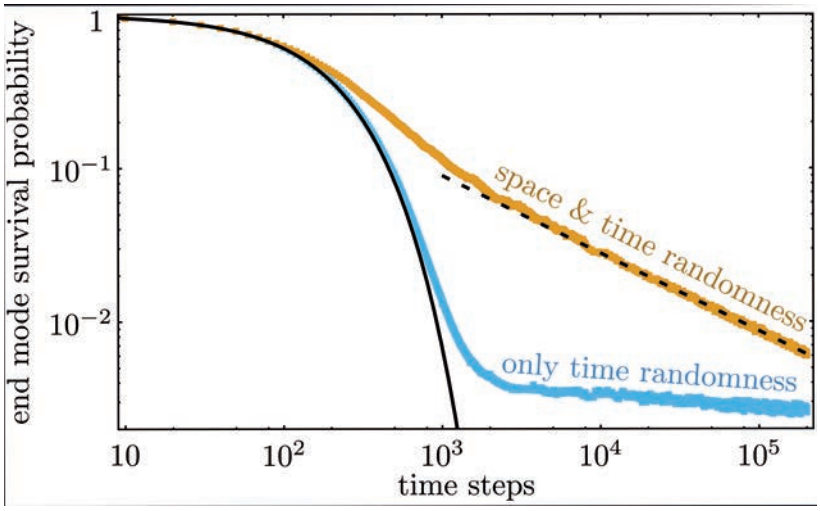

Figure 2: The survival probability of the topological end mode (vertical axis) is computed as the overlap between the initial and the time-evolved end mode wavefunction and is plotted as a function of time (horizontal axis). With only time randomness (blue), the bulk is dispersive and the end mode decays exponentially fast (solid line). The system quickly goes to a featureless state in which the end mode is spread out over the entire system length (flat region). With both disorder and time randomness (orange), the bulk is localized, so the decay of the end mode is algebraic in time t ($\sim 1/\sqrt{t}$, dashed line), showing an enhanced survival probability. For large systems and at long times, this enhancement can be by many orders of magnitude.

Remarkably, our result only relies on the fact that bulk states are localized, and not on any specific details of the topological phase or the way in which the system is driven. This means that it is universal – it will apply to any Floquet topological system in one dimension. Further, the localization of bulk states will occur naturally if the system is disordered. This suggests that experiments on Floquet systems can actively mitigate the negative effects of decoherence by purposely making their samples "dirty", a counter-intuitive result. Finally, we have shown analytically that the increased end mode robustness remains valid also away from the weak noise limit [5], and in doing so have developed a general framework which can tackle decoherence in any Floquet system. In the future, we hope to use this novel approach to study the robustness of periodically-driven systems also in higher dimensions.

[1] K. v. Klitzing, et al., Phys. Rev. Lett. 45, 494 (1980).
[2] M. Z. Hasan and C. L. Kane, Rev. Mod. Phys. 82, 3045 (2010).
[3] J. Cayssol, et al., Phys. Status Solidi RRL 7, 101 (2013).
[4] M.-T. Rieder et al., Phys. Rev. Lett. 120, 216801 (2018).
[5] L. M. Sieberer et al., Phys. Rev. B 98, 214301 (2018).

Funding

This work is partially supported by the ERC through the synergy grant UQUAM, and by the excellence program initiative of the IFW Dresden.

Cooperation

[1] Department of Condensed Matter Physics, Weizmann Institute of Science, Rehovot, Israel
[2] Department of Physics, University of California, Berkeley, USA
[3] Institute for Theoretical Physics, University of Innsbruck, Austria
[4] Institute for Quantum Optics and Quantum Information of the Austrian Academy of Sciences, Innsbruck, Austria
[5] Institute for Theoretical Physics, ETH Zurich, Switzerland

Strongly enhanced photoluminescence of monolayer MoS_2 on plasmonic nanodimer arrays

Q. Hao, J. Pang, Y. Zhang, J. Wang, L. Ma and O. G. Schmidt

Abstract

Monolayer molybdenum disulphide (MoS_2) is a two-dimensional (2D) semiconductor material with intriguing electric features and peculiar optical characteristics. The unique characteristics of MoS_2 atomic layers show great promise in photonic and optoelectronic applications. However, monolayer MoS_2 exhibits poor light absorption and emission which pose significant challenges for integrating MoS_2 into optoelectronic devices. The plasmonic materials can control light within nanoscale regions and provide strongly confined electromagnetic (EM) fields in their vicinity to promote the PL emission of MoS_2. We proposed a facile approach to fabricate centimeter-scale highly uniform dimer arrays utilizing porous anodic aluminium oxide (AAO) membrane as a nanomask. The fabricated plasmonic dimer arrays exhibit consistent sub-10 nm gaps and a high particle density up to 1.0 x 10^{10} cm^{-2} over a centimeter-scale area. The ultra-small dimer gaps provide strongly localized EM fields, which significantly enhance the PL emission by up to a factor of ~160. This strategy paves a way towards implementing the hybrid MoS_2/plasmonic dimer configuration in fabricating large-area, cost-efficient and high-performance optoelectronic devices.

Fabrication of plasmonic dimers

Plasmonic dimers consisting of pairs of coupled metallic nanoparticles have received increasing interest due to the ability to confine electromagnetic fields in their gaps. Implementation of dimers in practice requires repeatable, fast, and cost-efficient fabrication processes and the ability to efficiently optimize the dimer structure to cater to specific requirements. Among the current techniques to fabricate plasmonic dimers, top-down methods such as electron beam lithography (EBL) and focused ion beam (FIB) milling are time-consuming and costly especially for large area fabrication. With regard to bottom-up method, dimers fabricated by wet-chemical methods tend to have irregular orientations and are prone to aggregation which can dramatically alter the plasmonic response. We proposed and demonstrated the use of the versatile anodic aluminum oxide (AAO) nanotemplate in the preparation of patterned dimer arrays with a tunable dimer size and controllable dimer gap down to the sub-10 nm scale to boost the photoluminescence of MoS_2 [1].

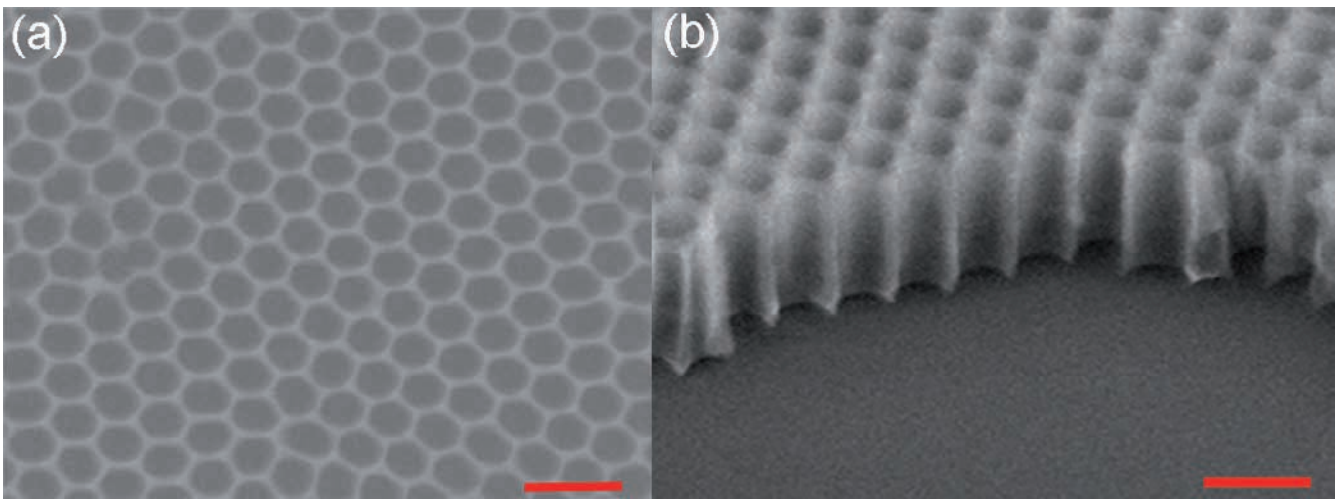

Figure 1: (a, b) Top view and side view scanning electron microscope (SEM) images of the prepared AAO nanomask on silicon wafer. The scale bars are 200 nm.

We fabricated ultra-thin AAO nanotemplates with a film thickness of ~200 nm by a three-step etching method [2]. The process begins with a typical anodization method in which AAO was produced on top of an aluminum foil. The initial film thickness of the AAO is determined by the anodization time. The AAO nanotemplate is composed of a close packed array of hexagonal cells, each containing six protuberances at the vertex of the hexagonal cell and a cylindrical central pore which extends down to the bottom (Figure 1). After anodization, top etching was conducted by immersing the AAO in a phosphoric acid solution to adjust the pore diameter. Afterwards, the AAO surface was spin-coated with a Polymethyl methacrylate (PMMA) protective layer on top of the AAO pores. The PMMA layer was melted into the AAO nanopores at 250 °C for 2 h. The melt PMMA layer provides complete coverage of the surface of the AAO pores and protects the membrane enabling continuous tuning of film thickness during the following etching procedures. Afterwards, the remaining aluminum foil was removed in a $CuCl_2$ solution. After the aluminum was removed, the PMMA/AAO membrane was automatically outstretched on water by surface tension. This membrane was then transferred to a phosphoric acid solution to further adjust the film thickness. After etching, the PMMA layer was dissolved in acetone.

The prepared AAO membranes were rinsed with distilled water and transferred to the target substrate as a nanomask to fabricate dimer arrays by angle-resolved shadow deposition (Figure 2) [3]. The dimer array exhibits defined dimer orientations and closely packed arrangements with a dimer density of up to 1.0 x 10^{10} cm^{-2} and gap distance of about 10 nm over a centimeter-sized area, thus providing an excellent platform for plasmon enhanced photoluminescence.

Plasmon enhanced photoluminescence of MoS_2

MoS_2 monolayer flakes grown by chemical vapor deposition were transferred onto the nanodimer array, as illustrated in Figure 3a. Figure 3b displays a SEM image a triangular monolayer MoS_2 flake suspended over the nanodimers, indicating the monolayer MoS_2 remains intact during the transfer.

The MoS_2 were excited by a 458 nm laser and a remarkable PL enhancement from the hybrid MoS_2/dimers system was observed. The 2D PL map from MoS_2/dimers and bare MoS_2 are displayed in Figure 4a, where considerable PL enhancement up to 160 times is observed from the MoS_2/dimers compared to the emission from MoS_2 on sapphire.

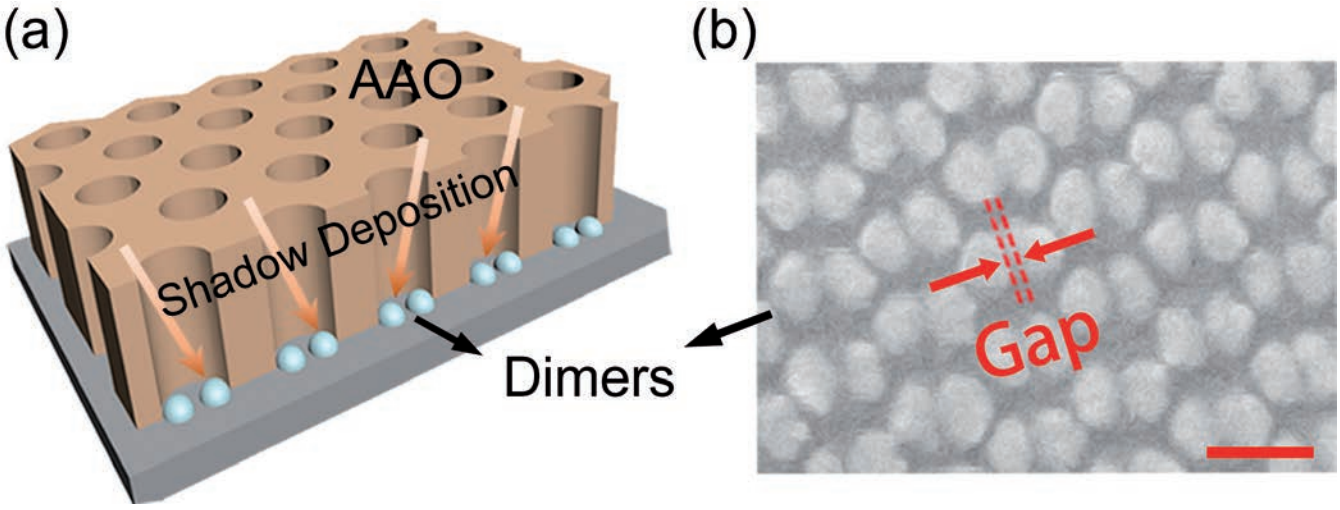

Figure 2: (a) Schematic of the fabrication of plasmonic dimers by using AAO nanotemplate in shadow deposition. (b) SEM image of the fabricated dimer arrays. The scale bar is 100 nm.

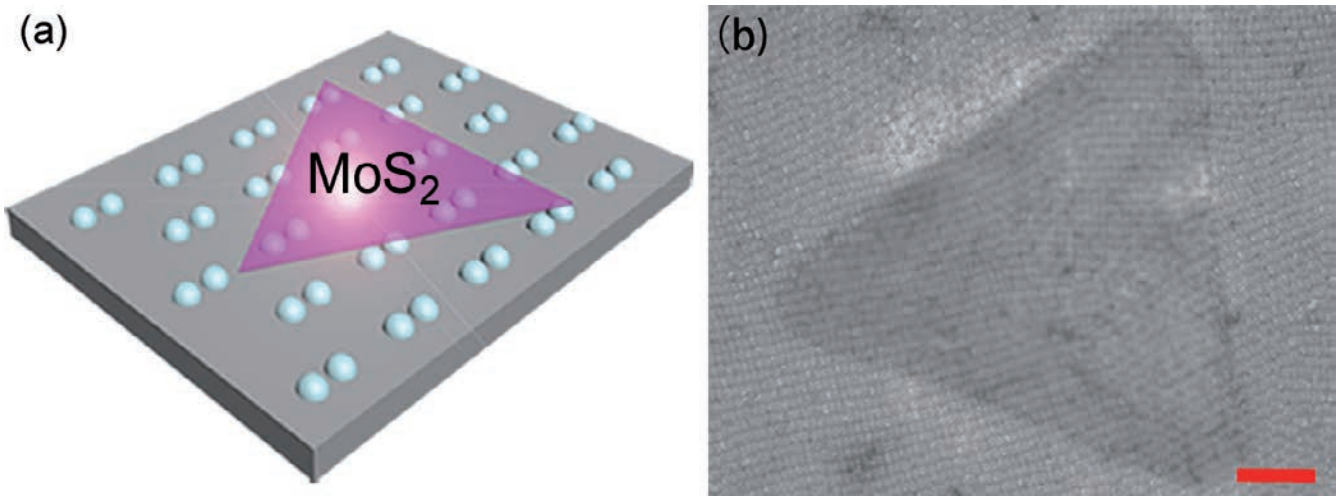

Figure 3: (a) Schematic figure and (b) SEM image of a triangular monolayer MoS_2 flake transferred onto the fabricated plasmonic dimer array.

Figure 4b shows the polarization-dependent PL mapping from the MoS_2/dimers. The maximum PL emission is observed when light polarization is parallel to the dimer axis, confirming the strongest enhanced emission in the vicinity of the dimer gaps. For plasmon enhanced photoluminescence, the excitation rate of MoS_2 is enhanced when there is a spectral overlap between the incident light and the plasmon resonance profile of the plasmonic structures. Figure 4c shows the extinction spectrum of the nanodimer array and it is clear that the PL excitation wavelength (473 nm) falls into the plasmon resonance range. On the other hand, plasmon resonances at the emission wavelength can accelerate the radiative decay rate and improve the quantum efficiency via the Purcell effect. The overall PL enhancement is determined by the product between the excitation enhancement and emission enhancement factors. In both two cases, the values of EFs are linearly positive to the square of the EM field density.

Summary

In this work we demonstrated the fabrication of high-density nanodimer arrays with ultra-small gaps down to sub-10 nm by using a thin AAO membrane as a mask in angle-resolved shadow deposition. The dimer configuration generates strongly confined EM fields when excited by polarized light parallel to the dimer axis. The plasmonic di-

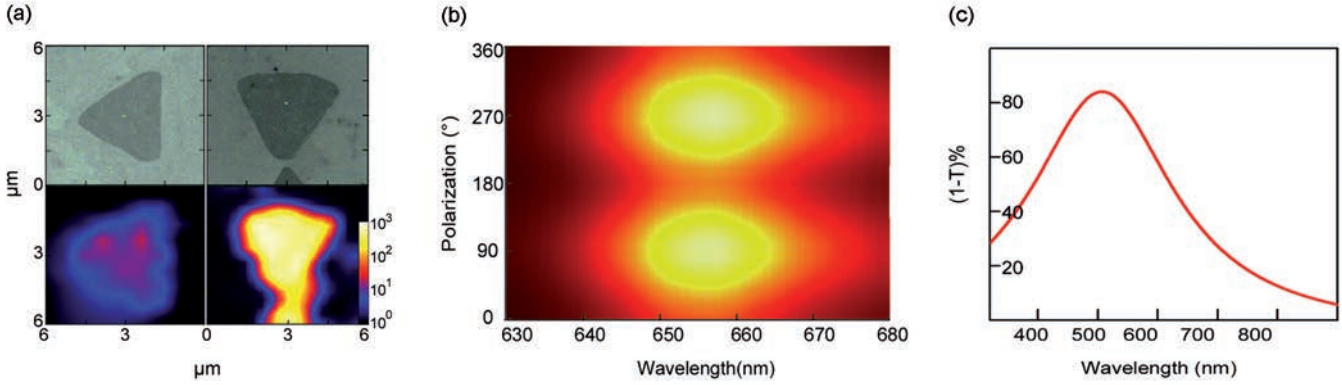

Figure 4: (a) Optical microscopy images of monolayer MoS_2 on substrates without (left) and with (right) plasmonic dimers and their corresponding PL intensity map spectrally integrated in the 630–680 nm range. (b) Polarization dependent PL mapping from the MoS_2/dimers. e) Extinction spectrum of plasmonic dimers fabricated on quartz substrate.

mers strongly enhance the photoluminescence of MoS_2 and the ensemble photoluminescence enhancement is up to ~160 times. Anisotropic polarization-dependent characteristics of photoluminescence from MoS_2 prove that the superior enhancement arises from the strongly confined electromagnetic fields in the vicinity of the dimer gaps. This work paves the path to develop effective and low-cost 2D materials-based optoelectronic devices.

[1] Q. Hao et al., Adv. Opt. Mater. 6 (2018) 1700984
[2] Q. HAO et al., Nanotechnology 28 (2017) 105301
[3] Q. HAO et al., ACS Appl. Mater. Inter. 9 (2017) 36199

Funding:

This work is partially supported by the German Research Foundation DFG (Grant FOR 1713, SCHM 1298/22-1 and Leibniz program) and Alexander von Humboldt Foundation.

Cooperation:

Nankai University, Tian Jin, China;
TU Chemnitz; Chemnitz, Germany

Research Area 4: Towards Products

High-strength FeCrMoVC cast alloys and their application as novel filler materials for hardfacing and repair welding of high-performance tool steels

J. Zeisig, J. Hufenbach, A. Fröhlich [1], N. Schädlich, D. Seifert, J. Freudenberger, O. Gottschall [2], S. Freeth [3], V. Kräusel [1], U. Kühn

Abstract

The increasing processing of high-strength alloys and composites in automotive industry and mechanical engineering requires robust high-performance tools. At IFW Dresden high-strength FeCrMoVC cast alloys are developed, which exhibit high macrohardness and high compressive strengths as well as a high wear resistance already in the as-cast state. Latest alloy designs lead to an improvement of the alloys' corrosion behavior as the mechanical and tribological properties are maintained. In contrast to conventional high-alloyed tool steels no time-consuming forming and heat treatment processes have to be executed since high-strength components are achieved by near-net-shape casting production under special casting conditions. Testing of cast tool prototypes for e.g. construction machineries show considerably prolonged service lives compared to currently used tool steels. Furthermore, the successful application of the developed FeCrMoVC cast alloys as novel filler materials for hardfacing and repair welding provides a cost-efficient and resource-conserving method for surface protection and refurbishment of high-performance tool steels.

New FeCrMoVC cast alloys for economical near-net-shape production of steel tools

High-performance tool steels are commonly applied for forming dies, cutting devices, mould inserts and other components, which undergo extremely high loadings and severe abrasive wear conditions. In general those high-strength steel tools are manufactured by an elaborate forming process after casting and expensive powder production, respectively. Furthermore, the carbide-rich martensitic microstructure is adjusted by multiple time-consuming heat treatments. Accordingly, there is a strong interest in developing steel tools, which can be fabricated by a near-net-shape casting process exhibiting relevant properties already in the as-cast state. Hence, at IFW Dresden research work is achieved by developing and testing of novel high-strength FeCrMoVC cast alloys for tool making by a special alloy design and casting technique [1–6].

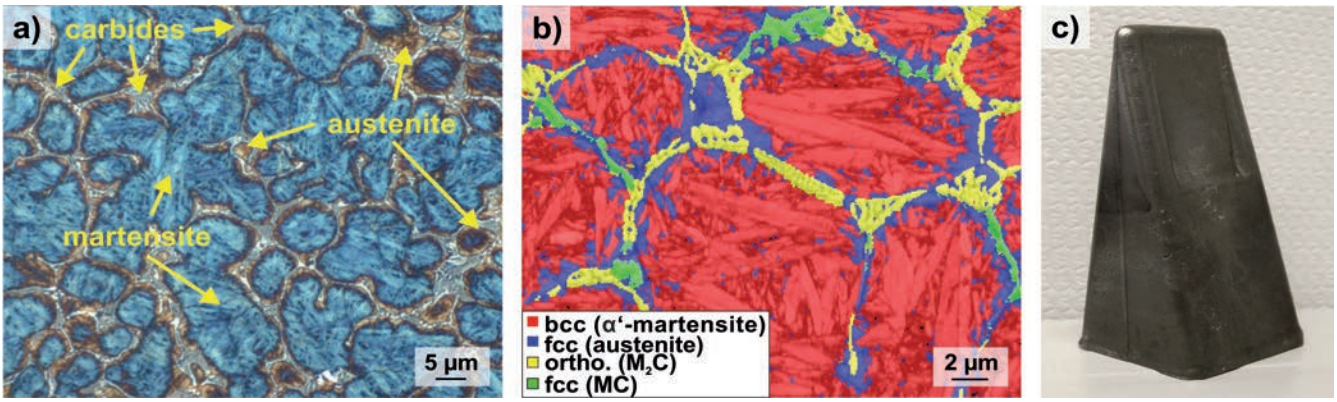

Figure 1: The developed Fe85Cr4Mo8V2C1 (wt%) alloy produced by a special casting technology at IFW Dresden exhibits an multiphase microstructure (a, b) leading to excellent mechanical and tribological properties of as-cast tool prototypes (c): **a)** optical micrograph of the as-cast microstructure after etching with Beraha I, **b)** EBSD map of the crystal structures for phase identification and **c)** thin-walled bucket tooth.

By using pure alloying elements and metal molds for realizing relatively high cooling rates, thin-walled components of the initially developed and patented Fe85Cr4Mo8V2C1 (wt%) alloy achieve hardnesses of more than 59 HRC and compressive strengths up to 3500 MPa combined with adequate ductility (fracture strain until 17 %) directly after casting without any subsequent heat treatment [2, 3]. The reason for the excellent properties is the as-cast microstructure consisting of martensite, retained austenite and a complex three-dimensional arranged network of hard MC- and M_2C-carbides (see Figures 1a, b) [2]. Thus, prototypes of Fe85Cr4Mo8V2C1 tools e. g. bucket teeth (Figure 1c) or knifes for medical filter production show significant higher service lives under industrial conditions than conventionally applied tool steels [7].

To further improve the properties of the initial cast alloy approaches on the alloy concept were carried out by modifying the FeCrMoVC alloy with tungsten and substituting molybdenum with boron, respectively. Thereby, the Fe85Cr4Mo1V1W8C1 and Fe92.65Cr4.2V2.1B0.05C1 alloy were developed attaining higher ultimate strengths under compressive load and less wear under abrasion [4, 5]. The newly developed chromium-rich Fe80Cr15Mo1V3C1 alloy enables an improvement of the corrosion resistance by forming a passive oxide layer on the surface and reducing the solution in corrosive media. Nevertheless, a high compressive strength and a high wear resistance can still be achieved so that the Fe80Cr15Mo1V3C1 alloy extend the field of application e. g. for cutting tools in the food industry [8].

FeCrMoVC cast alloys as novel filler materials for hardfacing and repair welding

In order to extend the tool lifetime, hardfacing and repair welding provides a cost-efficient and resource-conserving alternative compared to a continuous tool replacement. Especially for the repair and maintenance of forming and cutting tools with complex profiles as well as individual construction parts, laser cladding using filler wires with diameters down to 0.2 mm is a favorable technique. Thereby, worn areas and broken edges can be rebuilt close-contoured by an automatic or manual wire feeding. However, there is a low weldability of carbon-rich tool steels and constant increasing requirements of tool surfaces. Consequently, innovative filler materials especially in form of thin wires are continuously demanded.

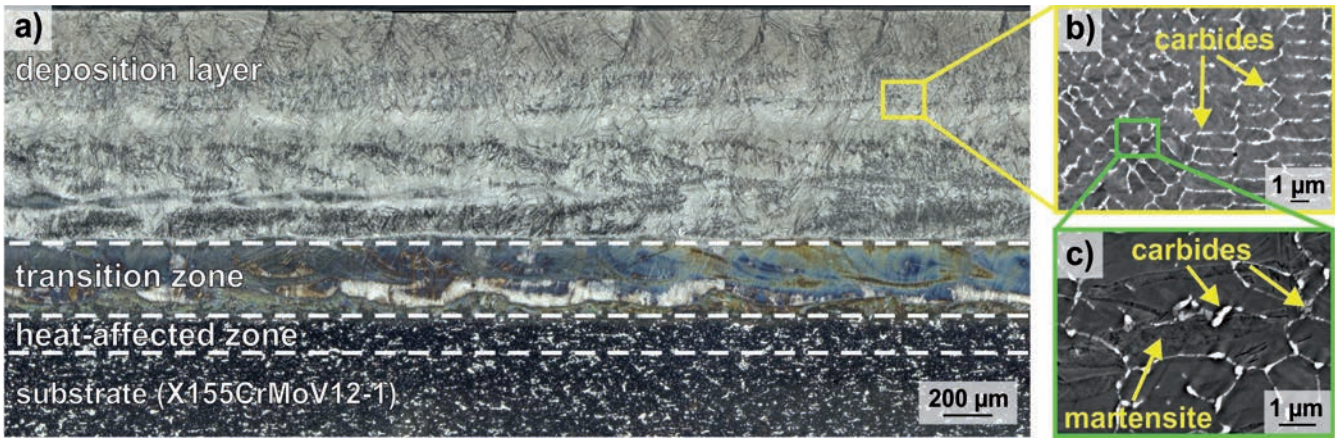

Figure 2: Results of microstructural analysis of Fe85Cr4Mo8V2C1 coatings on X155CrVMo12-1 cold-work steel substrates produced by laser cladding showing neither cracks nor pores: **a)** optical micrograph of the cross section after etching with Adler's etchant for visualization of characteristic coating sections and **b, c)** scanning electron micrographs of the rapidly solidified Fe85Cr4Mo8V2C1 microstructure.

Within the framework of ZIM projects the potential of the developed FeCrMoVC alloys as novel filler wire materials is investigated. For this purpose, first a technology to transfer the high-strength solidified cast materials into thin wires had to be developed. It is well-known that forming of carbon-rich and high-alloyed steels is difficult due to a reduced formability of the material. The high content of carbon and carbide forming elements like Cr or V leads to an enhanced work hardening whereby ductility is decreased. Moreover, the resulting carbides favor cracking during the forming process so that conventional production techniques, e. g. cold drawing, are not expedient. Therefore, a suited processing technology tailored to the chemical composition of the cast steels was developed allowing the fabrication of wires with diameters down to 0.3 mm out of Fe85Cr4Mo8V2C1 and Fe80Cr15Mo1V3C1. Furthermore, the laser welding process for different wire diameters was adjusted to transfer the excellent properties of the two FeCrMoVC alloys on different tool steel substrates to get crack-free, wear-resistant cladding layers with high hardness (≥ 60 HRC) (Figure 2).

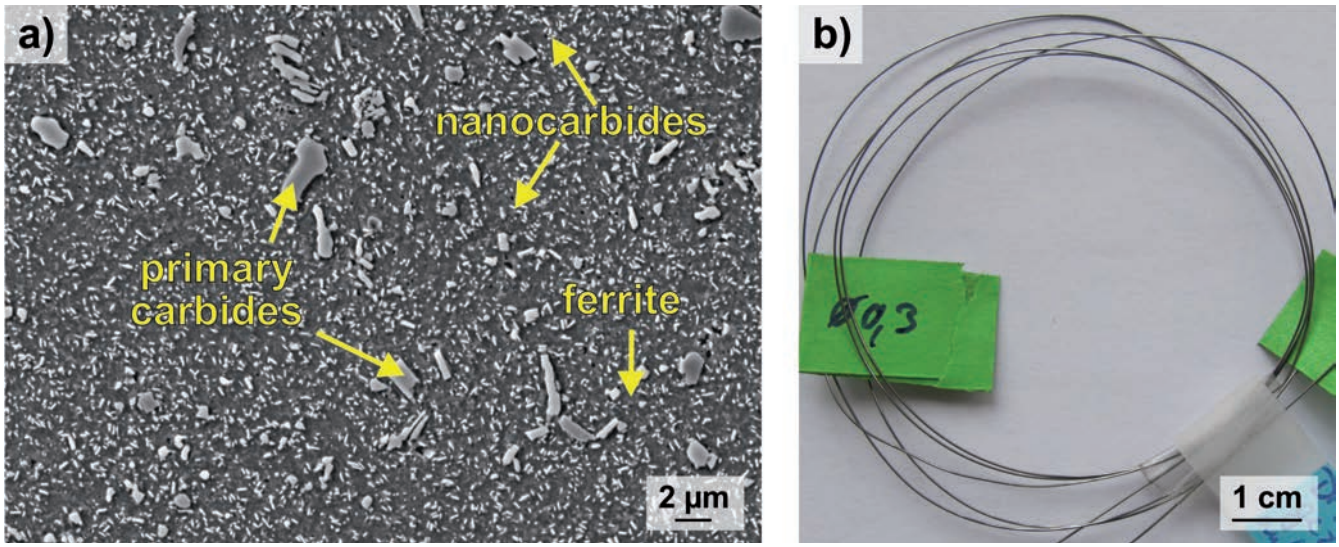

Figure 3: The Fe85Cr4Mo8V2C1 (wt%) alloy in form of a thin wire after several forming and heat treatment steps: **a)** scanning electron micrograph of the transformed microstructure and **b)** wire with a final diameter of 0.3 mm.

The production process of FeCrMoVC wires was developed on an industrial scale. After casting a cylindrical bar the resulting carbide network is broken up by subsequent forging. Due to a tailored soft annealing process the hard martensitic phase is transformed into soft ferrite and nanocarbides. Afterwards, wires with different thicknesses are produced with the help of an adjusted sequence of rotary swaging and annealing (Figure 3). The suitable laser parameters for the application of the FeCrMoVC wires were determined by parameter variation studies. By comprehensive welding tests with competing welding materials, a lower susceptibility to cracking and a higher hardness as well as an enhanced resistance under harsh abrasive wear conditions of the FeCrMoVC cladding layers could be confirmed [9]. Corrosion tests showed a reduced corrosion behavior of Fe80Cr15Mo1V3C1 coatings compared to Fe85Cr4Mo8V2C1 clads and a high potential of the Fe80Cr15Mo1V3C1 alloy as cladding material for corrosion-resistant tool steels like X90CrMoV18 cold-work steel.

This opens up the possibility to introduce the investigated FeCrMoVC alloys as novel filler materials for hardfacing and repair welding of high-performance steel tools [10].

[1] U. Kühn et al., Appl. Phys. Lett. 90 (2007) 261901/1.
[2] J. Hufenbach et al., Acta Mater. 60 (2012) 4468.
[3] U. Kühn et al., patent granted, DE102006024358B4.
[4] J. Hufenbach et al., J. Mater. Sci. 47 (2012) 267.
[5] J. Hufenbach et al., Mater. Sci. Eng. A 586 (2013) 267.
[6] J. Hufenbach et al., Mater. Sci. Eng. A 674 (2016) 366.
[7] U. Kühn et al., Konstruktion 7–8 (2011) IW5.
[8] J. Zeisig et al., patent application deposited.
[9] J. Zeisig et al., Wear 382 (2017) 107.
[10] J. Hufenbach et al., patent application deposited.

Funding

This work is funded by the Federal Ministry for Economic Affairs and Energy within the Framework of the ZIM projects EiSI-EnDra (project no. KF2466405CK3) and LaRS-EnLeg (project no. ZF4314102SU6).

Cooperations

[1] Institute for Machine Tools and Production Processes, TU Chemnitz
[2] LPT Laserpräzisionstechnik GmbH
[3] quada V+F Laserschweißdraht GmbH

Materials design for next generation batteries

S. Maletti, M. Madian, S. Oswald, L. Giebeler, D. Mikhailova

Abstract

As lithium-ion batteries have become one of the most widespread energy storage applications within the last decades, alternative energy storage applications gain more importance due to the non-abundancy of lithium. Several concepts exist suggesting either complete replacement of Li or significant reducing of Li amount in energy storage systems. Of course, these new concepts require the same extent of research, which was carried out in case of Li-ion batteries. This includes the exploration of new chemistries, searching for materials, which offer enhanced sustainability and better availability as well as the optimization of known concepts in order to maximize electrochemical performances. Here, we report on $Na_xCo_{0.5}Ti_{0.5}O_2$ as new cathode materials for Na-ion batteries, hybrid batteries with complex Nb oxides as cathodes and Mg anodes as examples of "beyond Li" concepts as well as target morphologies of TiO_2 with enhanced electrochemical properties for conventional Li-ion storage systems.

Beyond Li: development of new cathode materials for Na-ion batteries

Nowadays sodium-ion batteries are recognized as promising next generation batteries for stationary energy storage applications due to the low cost and abundance of sodium. The most important candidates for cathode application in Na-batteries are layered oxides. Generally, there are three related structural types of layered sodium materials, differing in sodium oxygen surrounding (octahedra or prisms) and the number of metal oxygen layers in the unit cell. A proper combination of several transition metals in the material allows optimization of the redox potential and a long cycle life of the electrode, which are determined through many parameters like stability of the crystal structure, cation diffusion path, robustness against side reactions with electrolyte components etc. In our work, we combined cobalt, providing a high redox potential, together with titanium, which enhances structural stability and may contribute to the electrochemical activity of the material at low cell potentials hence making the material suitable for both, cathodic and anodic application. We were the first to synthesize two new materials, O3-$Na_{0.95}Co_{0.5}Ti_{0.5}O_2$ (space group *R*-3*m*) and

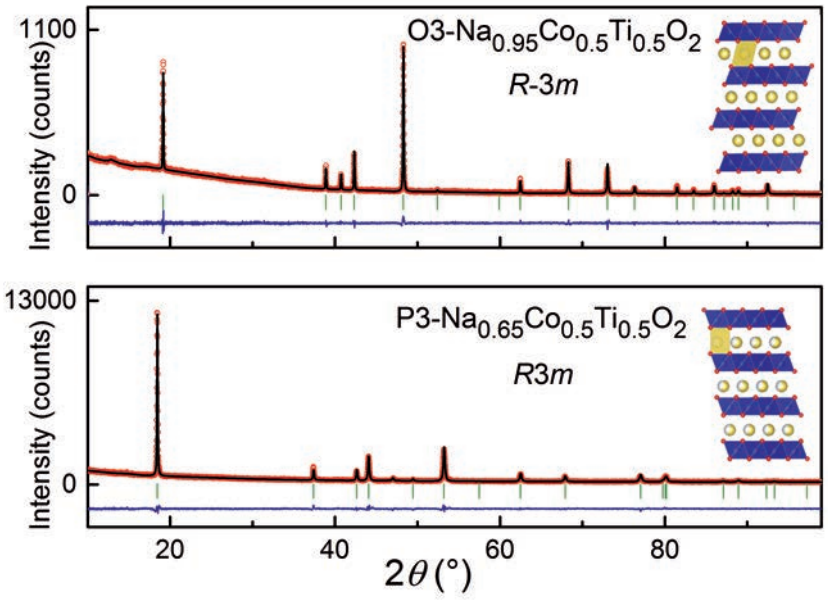

Figure 1: X-ray powder diffraction patterns of O3- and P3-$Na_xCo_{0.5}Ti_{0.5}O_2$ materials with the observed (red dots) and calculated (black solid line) curves together with their difference curves (blue solid line). Bragg positions are presented as green vertical lines, crystal structures are shown as insets.

P3-$Na_{0.65}Co_{0.5}Ti_{0.5}O_2$ (space group *R3m*), for application in sodium-ion batteries [1]. Their experimental and calculated X-ray powder diffraction patterns together with the crystal structures are presented in Figure 1.

According to XPS studies, Co^{2+} and Ti^{4+} are present in the O3 form, while the P3 form contains a mixture of Co^{3+}/Co^{2+} and Ti^{4+}. Both materials are stable in air. They exhibit high specific electrochemical capacities of 180–200 mAh/g between 0.2 and 4.2 V *vs.* sodium, showing, however, a large voltage difference between cell charging and discharging (potential hysteresis), see Figure 2.

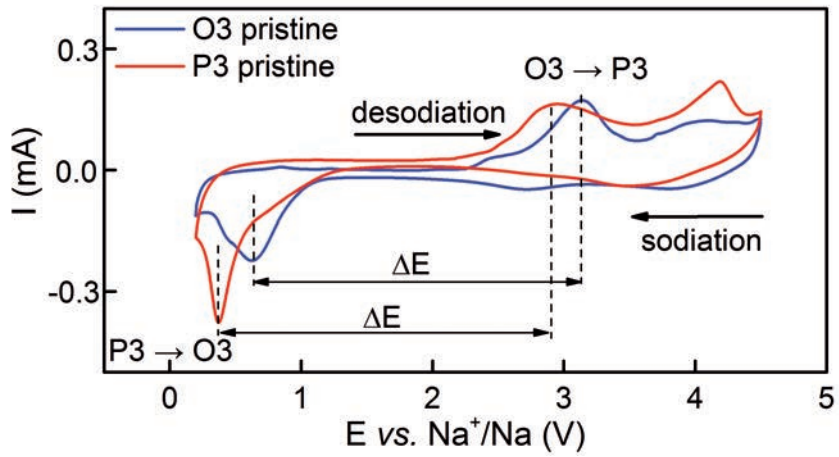

Figure 2: Cyclic voltammetry of $Na_xCo_{0.5}Ti_{0.5}O_2$. Redox processes corresponding to the phase transformations and the potential hysteresis are indicated. *Operando* synchrotron powder diffraction studies revealed only one phase transformation from the O3 form to P3 form during desodiation of the material between 3 V and 4 V *vs.* sodium (cell charge), while no structural changes besides conventional cell shrinkage was detected for the P3 form, thus indirectly confirming the stabilizing effect of Ti for the crystal structure. During cell discharge (sodiation of the material), the re-formation of the O3 form occurs only below 1 V *vs.* sodium (Figure 3). *Operando* synchrotron XAS studies confirmed the participation of Co in the redox process in both materials. Surprisingly, Ti reduction was inhibited down to 0.2 V in both phases, verifying their high structural stability.

Magnetization measurements of the O3 and P3 materials in different states of sodiation could shed light on the large cell polarization observed during the cycling process. Upon sodium removal from the O3 phase, high-spin Co^{2+} (d^7, S = 3/2) oxidizes to high-spin Co^{3+} (d^6, S = 2), while the transformation of O3 to P3 is accompanied by the transition of high-spin Co^{3+} to low-spin Co^{3+} (d^6, S = 0). This spin state transformation is reflected in the large volume change of CoO_6-octahedra in the structure, leading to the total volume shrinkage of the material. A small overpressure, always existing in the electrochemical cell, supports a volume decrease of the cathode during cell charging, but acts obstructive during cell discharging, when the volume of the material increases upon sodiation.

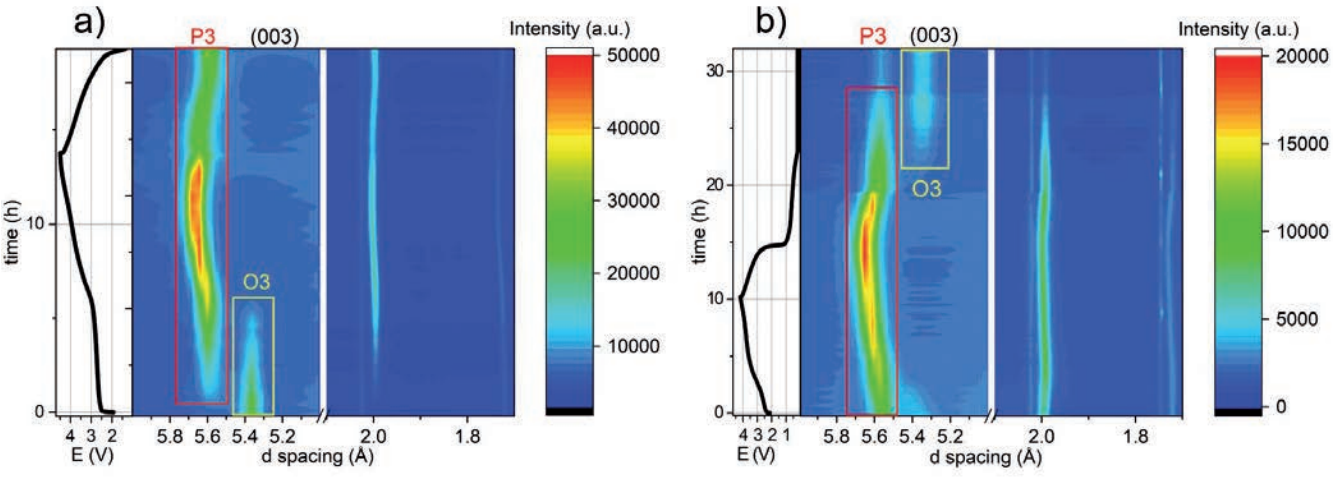

Figure 3: Part of *operando* synchrotron diffraction data from (a) O3- and (b) P3-$Na_xCo_{0.5}Ti_{0.5}O_2$ as cathodes in electrochemical cells with Na-anode during galvanostatic cycling at C/20, meaning 1 Na inserted/extracted for 20h (right), and corresponding voltage profile vs. time (left). Rectangles indicate the position of the (003) reflection for both phases.

Hybrid alkali and alkaline earth batteries for overcoming barriers in beyond-lithium energy storage

In addition to sodium, the electrochemical usage of magnesium is also attractive because of its increased safety and a higher theoretical gravimetric capacity. However, applicable magnesium-ion batteries are still far out of realization, mainly because of the lack of positive electrode materials, which are able to insert divalent cations. A very promising approach to overcome this issue is the concept of hybrid Mg, Li-batteries, which contain a dual salt electrolyte with both Mg and Li ions, a cathode available for Li ions, and a Mg anode (Figure 4). This concept allows the use of known lithium intercalation compounds, which are compatible with a dual salt Mg, Li-electrolyte, see Figure 4.

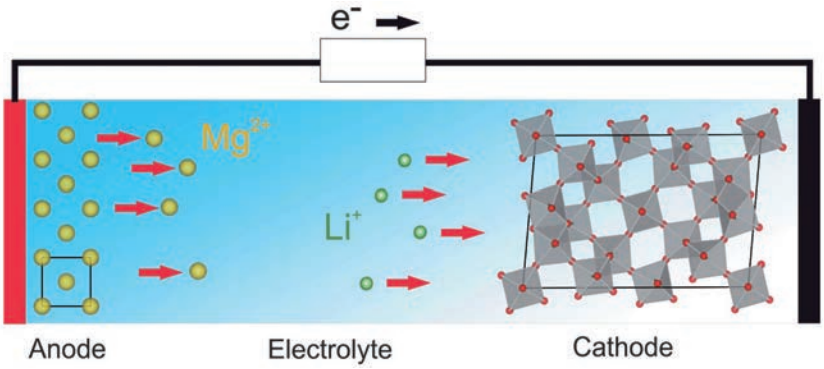

Figure 4: Schema of a hybrid Mg, Li-battery.

We studied $TiNb_2O_7$ and VNb_9O_{25} electrodes in Mg, Li-hybrid batteries and compared the achieved electrochemical performance with pure Li-ion batteries [2]. Although the Mg, Li-batteries exhibit lower initial capacities, they show a higher capacity retention and good coulombic efficiency (Figure 5). Crystal structures of both compounds consist of ReO_3-type blocks differently connected with each other (inset in Figure 5), providing enhanced diffusivity for inserted Li-ions.

Following the concept of hybrid Mg, Li-batteries, also Na, Li-batteries were proposed [3]. They overcome the major drawback faced in sodium-ion batteries, which is the larger size of the Na^+ cation in comparison to Li^+. Sodium host structures therefore need to offer more space and sustain a larger lattice expansion. By including Li^+ into the cell chemistry, well-known lithium hosts are made accessible as electrode materials.

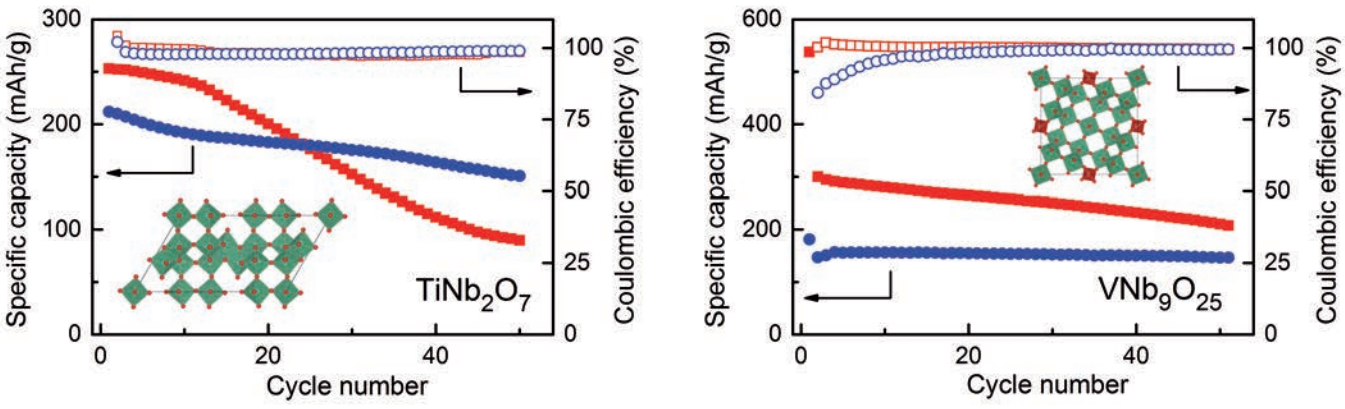

Figure 5: Discharge capacities with corresponding coulombic efficiencies for $TiNb_2O_7$ and VNb_9O_{25} in Li-ion batteries (red symbols) and in hybrid Mg, Li-batteries (blue symbols). The crystal structures are shown as insets.

We studied the electrochemical behavior of LiV_3O_8 electrodes in such hybrid Na,-Li-batteries with varying electrolyte compositions. The ratio of Na^+ and Li^+ in the electrolyte leads to an interesting interplay between both cations. While at high Li-contents, Li^+ is taken up selectively, both Na^+ and Li^+ are inserted at more Na-rich compositions. This leads to a formation of a) LiV_3O_8 + $Li_4V_3O_8$ or b) LiV_3O_8 + $Li_{0.7}Na_{0.7}V_3O_8$ structures upon cell discharge, see Figure 6.

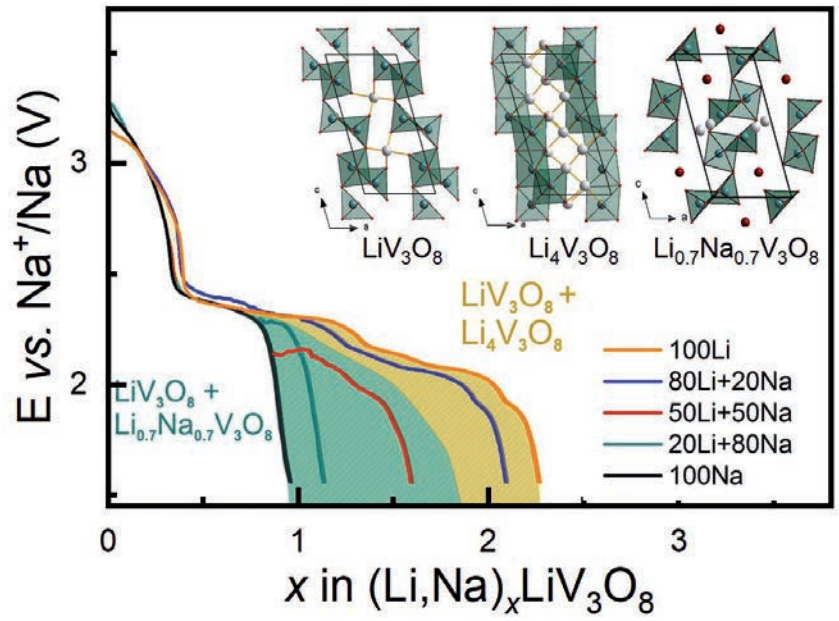

Figure 6: Potential-composition profiles of LiV_3O_8 electrodes in hybrid Na,Li-batteries with varying electrolyte compositions and corresponding crystal structures.

These structural transformations could be monitored by *operando* synchrotron diffraction, as shown exemplarily in Figure 7. To validate our conclusions, DFT calculations have been carried out, which confirm a preferred insertion of Na^+ into the $Li_{0.7}Na_{0.7}V_3O_8$ structure while LiV_3O_8 favors intercalation of additional Li^+.

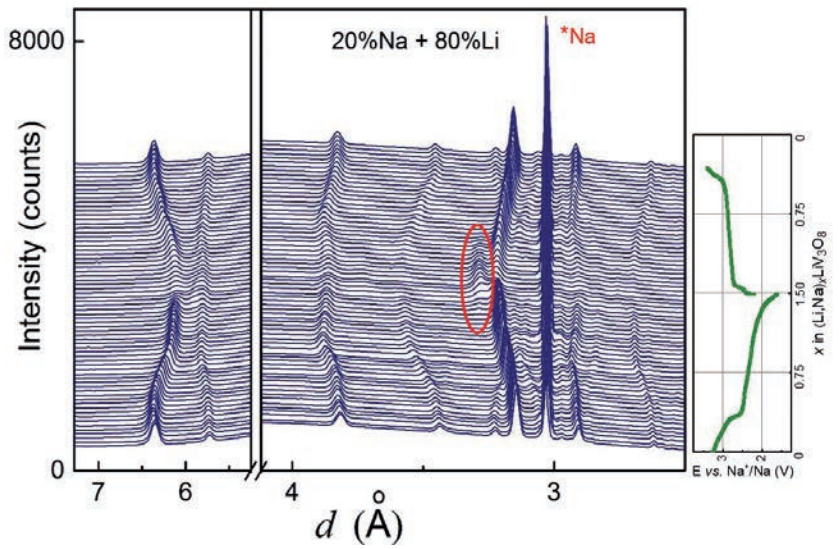

Figure 7: Operando synchrotron powder diffraction patterns and the corresponding voltage-composition profile of LiV_3O_8 in a hybrid Na,Li-battery. The red ellipse indicates new reflections and formation of the second phase.

Ternary CNTs@TiO_2/CoO Nanotube Composites as anodes for high-performance Li-Ion batteries

TiO_2 nanotubes synthesized by electrochemical anodization are discussed as very promising anodes for Li-ion batteries, due to their high structural stability, high surface area, safety, and low production cost. However, their poor electronic conductivity and low Li^+ diffusivity are the main drawbacks that prevent them from achieving

high electrochemical performance. In order to overcome these challenges, we propose the fabrication of composites containing anodically grown TiO_2/CoO nanotube arrays (Figure 8) with a surface modified by carbon nanotubes (CNTs). Such a composite should provide an enhanced Li conductivity due to the presence of defects in the TiO_2 structure with mixed Ti/Co occupancy of the cation site, and an enhanced electronic conductivity due to the presence of a highly conductive carbon nanotubes framework [4, 5]. A two-step preparation method of CNTs@TiO_2/CoO includes an initial anodic fabrication of well-ordered TiO_2/CoO nanotubes from a Ti-Co alloy of certain stoichiometry, followed by growing CNTs horizontally on the top of the oxide nanotubes using a simple spray pyrolysis technique.

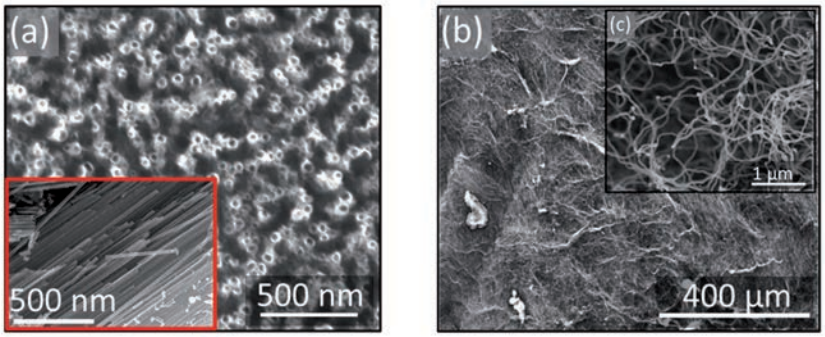

Figure 8: SEM images of (a) as-fabricated TiO_2/CoO nanotubes anodized at 60 V, and (b) TiO_2/CoO nanotubes coated by carbon nanotubes.

Electrochemical tests were performed on TiO_2, TiO_2/CoO and CNTs@TiO_2/CoO nanotubes (Figure 9). The presence of CoO in TiO_2 leads to the enhanced specific areal capacity without any stabilizing effects on the cycling behavior: the coulombic efficiency was noticeably less than 100 % (Figure 9a). The CNTs@TiO_2/CoO composites evidently showed higher specific capacities, excellent rate capability and a much more stable cycling behavior with coulombic efficiency close to 100% compared with TiO_2/CoO nanotubes without CNTs (Figure 9b).

Therefore, the unique 1D structure of such a hybrid CNTs@TiO_2/CoO composite with a highly conductive network of CNTs supports fast lithium insertion into the TiO_2/CoO framework resulting in significantly improved electrochemical performance compared to pure TiO_2 and TiO_2/CoO nanotubes, tested without CNTs under identical conditions.

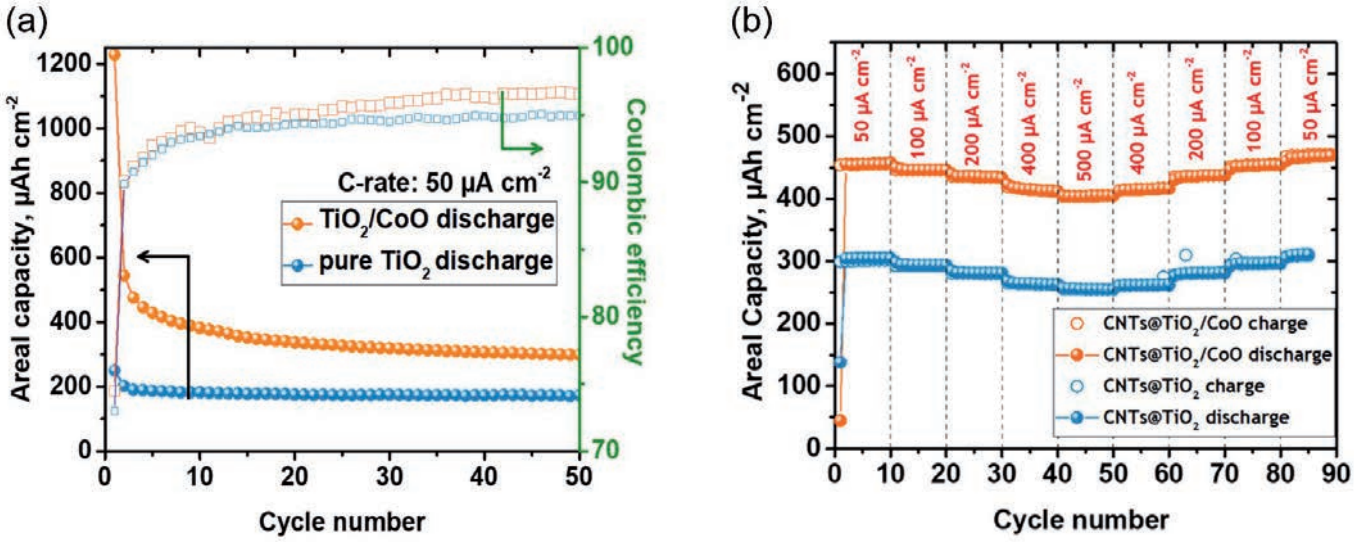

Figure 9: specific areal capacity and coulombic efficiency for (a) TiO_2 and TiO_2/CoO nanotubes, and (b) rate capability tests for a hybrid CNTs@TiO_2/CoO composite.

[1] S. Maletti et al., ACS Appl. Mater. Interfaces 2018, 10, 36108–36119.
[2] S. Maletti et al., MSE Congress Darmstadt 2018;
ISE Annual Meeting Bologna 2018.
[3] S. Maletti et al., J. Power Sources 2018, 373, 1–10.
[4] M. Madian et al., Materials 2017, 10, 678.
[5] M. Madian et al., Batteries 2018, 4, 7.

Funding:

European Union (ERDF-European Regional Development Fund) and the Free State of Saxony under grant numbers 100234960 (NaSBattSy), and 100225299 (TTKin), German Federal Ministry of Research and Education through the project ADNAMSES (grant no. 01DH14002).

Cooperation:

University of Augsburg, Technische Universität München,
Centre of Polymer and Carbon Materials (Zabrze, Poland),
National Research Centre (Giza, Egypt), TU Dresden, Fraunhofer IWS Dresden,
Fraunhofer IKTS Dresden, Karlsruhe Institute of Technology (KIT)

Powder-in-tube processing of magnetocaloric La (Fe, Co, Si)$_{13}$

M. Krautz, A. Funk, A. Waske [1], D. Seifert, J. Freudenberger, T. Gemming, K. Nielsch

Abstract

The powder-in-tube (PIT) technology was applied to La(Fe, Co, Si)$_{13}$ powder cladded by a thin seamless austenitic steel jacket. Wires appear to be promising in the search for alternative regenerator geometries, since they offer various possibilities of arrangements allowing to optimise heat transfer and pressure loss within the boundaries set by parallel plate and sphere beds.

Magnetic refrigeration

Magnetic refrigeration has headed forward towards application during the last years. Prototypes and teststands are being developed in order to evaluate different materials under equal conditions on one hand, but also on the development of shaping technologies for the production of thermally effective regenerator beds on the other hand [1]. These regenerator beds consist of a magnetocaloric material in a loose arrangement to allow a heat-exchanger fluid to flow through. Up to now, efforts were mainly focused on the production of packed particle beds and plane plates that can be stacked and separated in the regenerator bed by spacers to provide channels for the heat-exchanger fluid. Easy to fabricate, advantageous on the first sight, both configurations inhere processing difficulties that reduce their theoretical performance drastically once assembled and operated in a test device. The Japanese electronics company Fujikura has presented coiled Gd-wires with diameter from 0.25 to 0.5 mm as regenerator building blocks [2]. This approach is intriguing, since wires offer the possibility of a variety of arrangements (some of them are depicted in Figure 1d) either in cross-flow or parallel-flow configuration. Such wire-regenerators can exceed the coefficient of performance of conventional plate or sphere beds with similar heat transfer area [3, 4]. The necessity of substituting Gd as regenerator material is widely accepted, but shaping first-order substitute materials into thin wires is still a challenge. Although La(Fe, Si)$_{13}$ wires have been prepared successfully by melt-extraction, there is a high risk that after an annealing treatment, necessary to establish the magnetocaloric phase, the wires will break apart and mounting in a regenerator becomes impossible. Consequently, an alternative processing technology is required, that allows both cold working and also mechanically stabilisation of the wire. This is achieved by the powder-in-tube (PIT) process.

Powder-in-tube processing

Alloys based on the magnetocaloric La(Fe, Co, Si)$_{13}$-Phase are relatively tough and hard, and thus cannot be plastically deformed. The only way of shaping such materials implies the usage of outer shells within the cold working processes. In particular, in order to obtain a well-defined filamentary configuration, it is necessary to start with powders that are filled in metallic tubes. Consequently, the powder-in-tube (PIT) method is a very convenient way of processing the La(Fe, Co, Si)$_{13}$-Phase. This process was initially being developed for Nb3Sn wires [5] and has also been successfully applied to a branch of different superconducting wires. In particular, PIT wires based on Bi-cuprates [6] and MgB_2 [7] showing outstanding superconducting properties, have been developed at the IFW Dresden. This long-term experience in producing PIT wires is adapted to other materials, such as the magnetocaloric La(Fe, Co, Si)$_{13}$, straightforwardly. The PIT process is very attractive to applications, taking advantage of the well-established deformation techniques, which are widely

industrially available. In addition in the case of La(Fe, Co, Si)$_{13}$, low material costs represent another advantage over the benchmarking system of Gadolinium. The basic PIT process is schematically illustrated in Figure 1. Generally, the PIT wire is fabricated by packing stoichiometric amounts of powder particles into a tube, then sealed to form a billet. The billet is further on cold worked into wire composites. Intermediate, or final heat treatments are applied where appropriate. Upon this, the PIT technique is usually classified into two different processes: in situ and ex situ. In situ processing starts from elements or alloys, which are transformed to the desired phase during a final heat treatment, while ex-situ processing implies the usage of powder particles of the finally aimed phase.

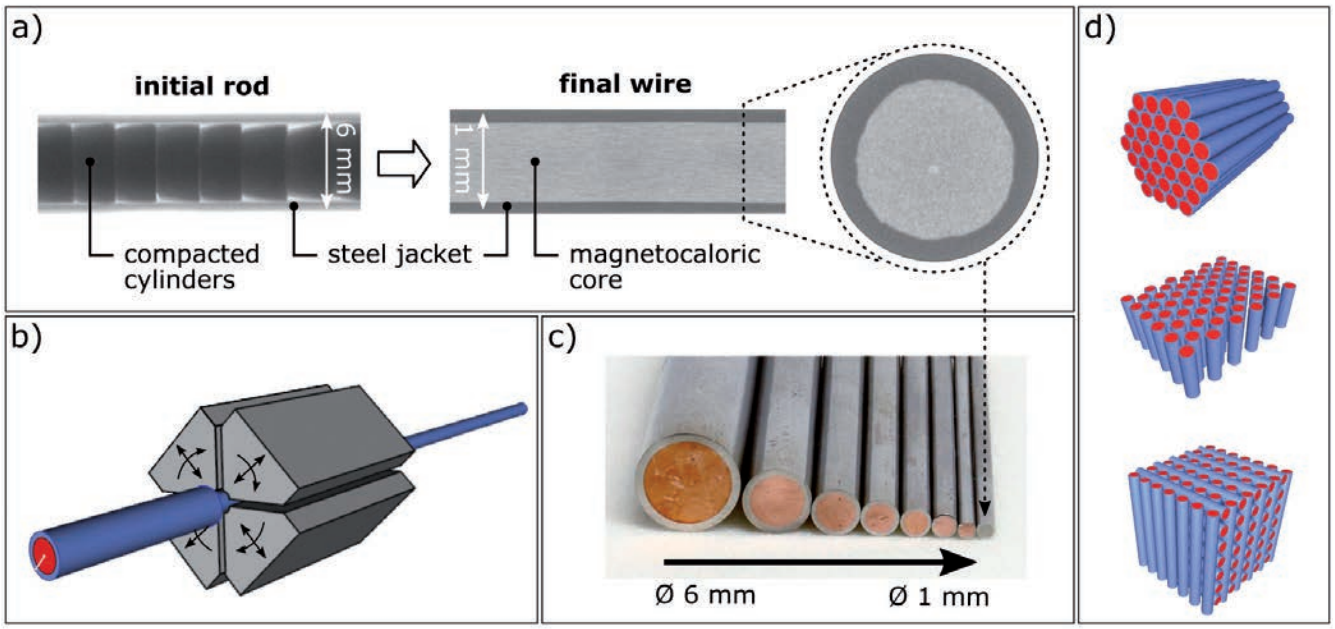

Figure 1: Radiograph of the steel tube filled with compacted pre-alloyed La(Fe, Co, Si)$_{13}$ cylinders before swaging. Clearly, the conical shape of the powder cylinders can be distinguished **(a, left)**. Tomographic slices of the swaged PIT wire with an outer diameter of 1 mm **(a, right)**. Schematic illustration of the PIT swaging process **(b)** and photograph of PIT wires after several swaging steps **(c)**. Copper cores are shown here to improve visibility. The right wire corresponds to the La(Fe, Co, Si)$_{13}$/steel combination discussed in this work. The sketches in **(d)** demonstrate possible designs of regenerators when wires are arranged differently.

The PIT technology has been progressing as an alternative deformation technique for producing wires from intrinsically brittle materials. However, there are some points that need addressing for future prospects. (i) Phase purity of the core and the minimization of an interdiffusion layer between the core and the jacket. Understanding and reducing non-functional phases is an urgent subject in order to enhance the overall performance. (ii) Densification of the core, as only a dense core yields improved functional properties, as, similar to impurities, voids and porosity reduce the connectivity between grains. (iii) Special attention is to be payed to the texture, which in the case of superconductors caused a significant enhancement of the functional properties. Therefore, more effort is required to understand how the texture is formed during the PIT deformation process of drawing, rolling and subsequent heat treatment and how it affects the functional properties. (iv) The fabrication of long length wires by the PIT process seems relatively easy. However, there are still numerous questions related to the processing window, which need to be addressed seriously. This also includes investigations of the basic deformation mechanisms in ultra-fine grained and brittle materials.

Getting La(Fe, Co, Si)$_{13}$ into good shape by powder-in-tube processing

Pre-alloyed La(Fe, Co, Si)$_{13}$ powder was compacted to cylinders with d = 5 mm p = 1 GPa in order to enhance the density of the core. Subsequently, the cylinders were packed into an AISI 316L austenitic steel tube with d_o = 6 mm and 0.5 mm wall thickness, i.e. d_i = 5 mm. The d_i^2/d_o^2 ratio = 0.69 defines the theoretical filling factor of the magnetocaloric core material. Figure 1a, left shows the X-ray absorption image of the filled steel tube and the conic shape of the grinded, compacted La(Fe, Co, Si)$_{13}$ powder billets. Cold work was applied by rotary swaging to a final wire diameter of 1 mm with a cross sectional reduction of approximately 20 % per step until a total logarithmic degree of deformation of φ = 3.58 was achieved. No necessity to apply an intermediate heat treatment was observed, thus, not performed. Figure 1a, right shows the tomographic slice of the as-deformed wire with 1 mm diameter and a surrounding steel jacket width of only approx. 100 µm. A heat treatment for only 10 min at 1050 °C is sufficient to form the magnetocaloric $NaZn_{13}$-type phase resulting in an entropy change close to the value of a pure reference sample. Additionally, a diffusion fringe between core and jacket with the width of about 5 µm appears, which increases with increasing annealing time.

Magnetocaloric properties of the powder-in-tube wire

Inducing microscopic defects by mechanical deformation affects the magnetic properties as observed in many material classes. In the as-deformed wire no clear magnetic transition is observed around room-temperature as expected since the core material is not magnetocaloric yet (Figure 2a, top). However, the deformed steel reference shows a low magnetisation which can be attributed to structural changes (martensite) in the austenitic phase during deformation. After a heat treatment of 10 min at 1050 °C these defects are reduced and the steel has a neglectable magnetisation again. Magnetic transitions near room-temperature are observed in all annealed samples (Figure 2a, bottom).

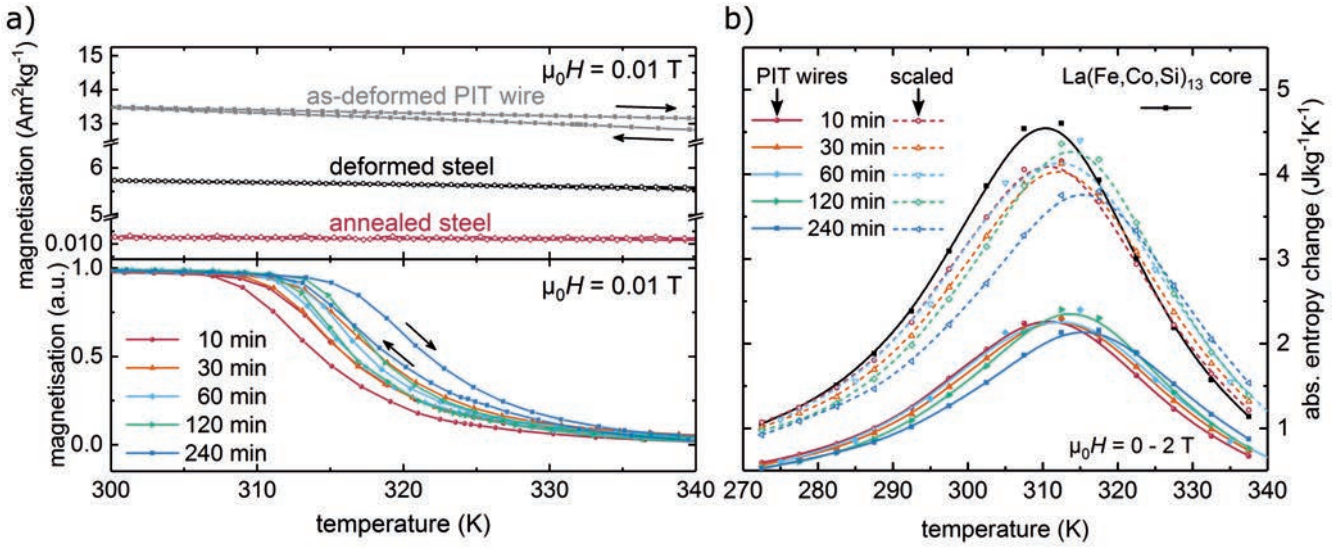

Figure 2: Temperature dependent magnetisation of as-deformed wire and steel reference **(a, top)** and of annealed PIT wires **(a, bottom)**. Entropy change of annealed PIT wires and reference core **(b)**, the curves from the PIT wires were scaled (dashed) to a hypothetic amount of 100 % magnetocaloric material in the wire for better comparison with the reference La(Fe, Co, Si)$_{13}$-core.

The transition in the shortest and longest annealed samples represent the boundaries in between which all intermediate annealed samples transform. Since the formation of the $NaZn_{13}$-type phase is driven by diffusion, a certain time should be provided for annealing in order to establish chemical equilibrium of the magnetocaloric phase, which is seen after annealing for 30 to 60 min. Figure 2b shows the comparison of entropy change of the core reference material and the annealed PIT wires in mass related units. The reference shows a maximum entropy change of about 4.5 J·kg^{-1}·K^{-1} which is in good agreement to a similar Co-doped alloy used in [8].

In comparison to the magnetocaloric core reference sample, the entropy change in the PIT wires is reduced by a factor of 0.5, which corresponds to the filling factor of approximately 58 vol. %. Scaling the specific entropy change, the values of the scaled entropy change (dashed lines) in the annealed samples are similar to that of the reference sample and lie within the error of the method. This clearly shows, that the magnetocaloric effect can be established in mechanically deformed $La(Fe, Co, Si)_{13}$ PIT wires by post-annealing and PIT processing of this material is achievable. For further information, please refer to our latest article [9].

The presented technology is not limited to $La(Fe, Co, Si)_{13}$/steel combination but can be extended to material pairs involving wire core materials with a first order transition, such as Fe_2P-type or Heusler alloys. Given the long period over which PIT wires have been developed to the present state, we believe that the challenges toward the realization of high-performance magnetocaloric wires will lead to an important breakthrough of these materials to practical applications.

[1] U. Legait et al., Int. J. Refrig. 37 (2014) 147–155.
[2] K. Ueno et al., Seventh II-IIr Int. Conf. Magn. Refrig. Room Temp. Thermag VII, Torino, Italy (2016) 43–46.
[3] P. V. Trevizoli et al., Appl. Energy. 187 (2017) 847–861.
[4] D. Vuarnoz et al., Appl. Therm. Eng. 37 (2012) 388–395.
[5] J. E. Kunzler, Rev. Mod. Phys. 33 (1961) 501–509.
[6] B. Wolf et al., Supercond. Sci. Technol. 9 (1996) Nr. 7, S. 589–597.
[7] W. Haessler et al., Supercond. Sci. Technol. 19 (2006) 512–520.
[8] J. D. Moore et al., J. Appl. Phys. 114 (2013) 043907 (9).
[9] A. Funk et al., Mater. Today Energy 9 (2018) 223–228.

Funding

This work has been financially supported by the German Research Foundation in the framework of SPP1599 “Ferroic Cooling” under grant WA3294/3-2 (A.W.) and by the Germany Federal Ministry for Economic Affairs and Energy under the project number 03ET1374B (M.K.).

Cooperation

[1] Bundesanstalt für Materialforschung und -prüfung, Berlin

Phase Transformations, Microstructure and Magnetic Properties of Novel MnAl-Based Permanent Magnets

T. G. Woodcock, T. Mix, F. Bittner, L. Feng, P. Zhao, F. Jürries, T. Schrefl[1], S. Bance[2], K. Nielsch

Abstract

The macroscopic magnetic properties of a material, which make it useful for applications, depend not only on the quantum effects which produce the magnetism but equally on a variety of interactions occurring within the material on the scale of nanometres to micrometres. Mastery of such materials therefore requires an approach comprising physics and materials science on multiple length scales. Here, alloying has been used to produce targeted changes in the chemical composition and crystal structure of MnAl-based materials via a novel phase transformation, thus improving the magnetic properties on the quantum level. In addition, progress in the highly challenging task of characterising the micro- and nanostructure of the materials has been achieved using state-of-the-art techniques. This work, in combination with advanced micromagnetic modelling based on the experimental results, allows in-depth understanding of various material defects and their influence on the magnetic properties.

Novel Phase Transformations in Mn-Al-Ga Alloys

MnAl is an intermetallic compound which has the potential to satisfy the requirements for a permanent magnet; however, the barrier to the application of this material is that the best magnetic properties reported to date fall far short of the estimated upper limits. Before industrial production of MnAl can be considered, a great deal of fundamental research in materials science and physics must be carried out in order to enable the material to fulfil its potential. One important aspect is that the ferromagnetic MnAl phase is thermodynamically metastable [1, 2]. Processing the material at high temperatures in order to improve the magnetic properties is therefore not possible due to the decomposition of the phase. The metastable ferromagnetic phase can produced in near-equiatomic Mn-Al alloys by undercooling the hexagonal, high temperature phase, ε [1]. The stability of MnAl can be improved somewhat by C-doping [2], but the phase remains metastable, moreover the Curie temperature is significantly degraded by the C addition [3]. In the Mn-Ga system, a thermody-

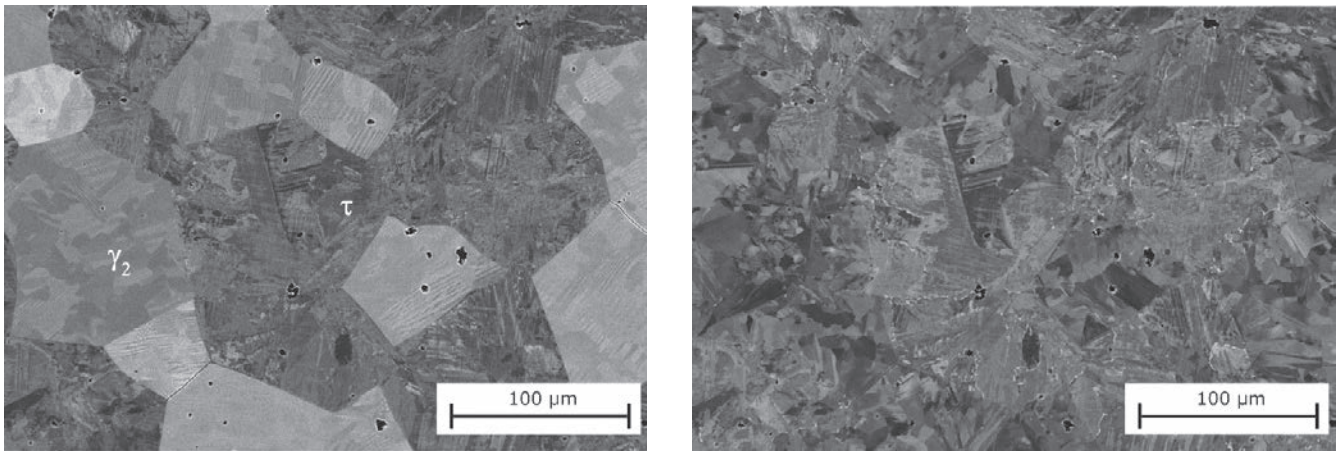

Figure 1: Backscattered electron images comparing the same areas of a Mn-Al-Ga sample before (top) and after (bottom) annealing at 500 °C. Before annealing (top) the γ2 phase (brighter areas) and the metastable $L1_0$ phase (darker areas) are both present. After annealing (bottom), the γ2 phase transformed into the thermodynamically stable $L1_0$ phase [5].

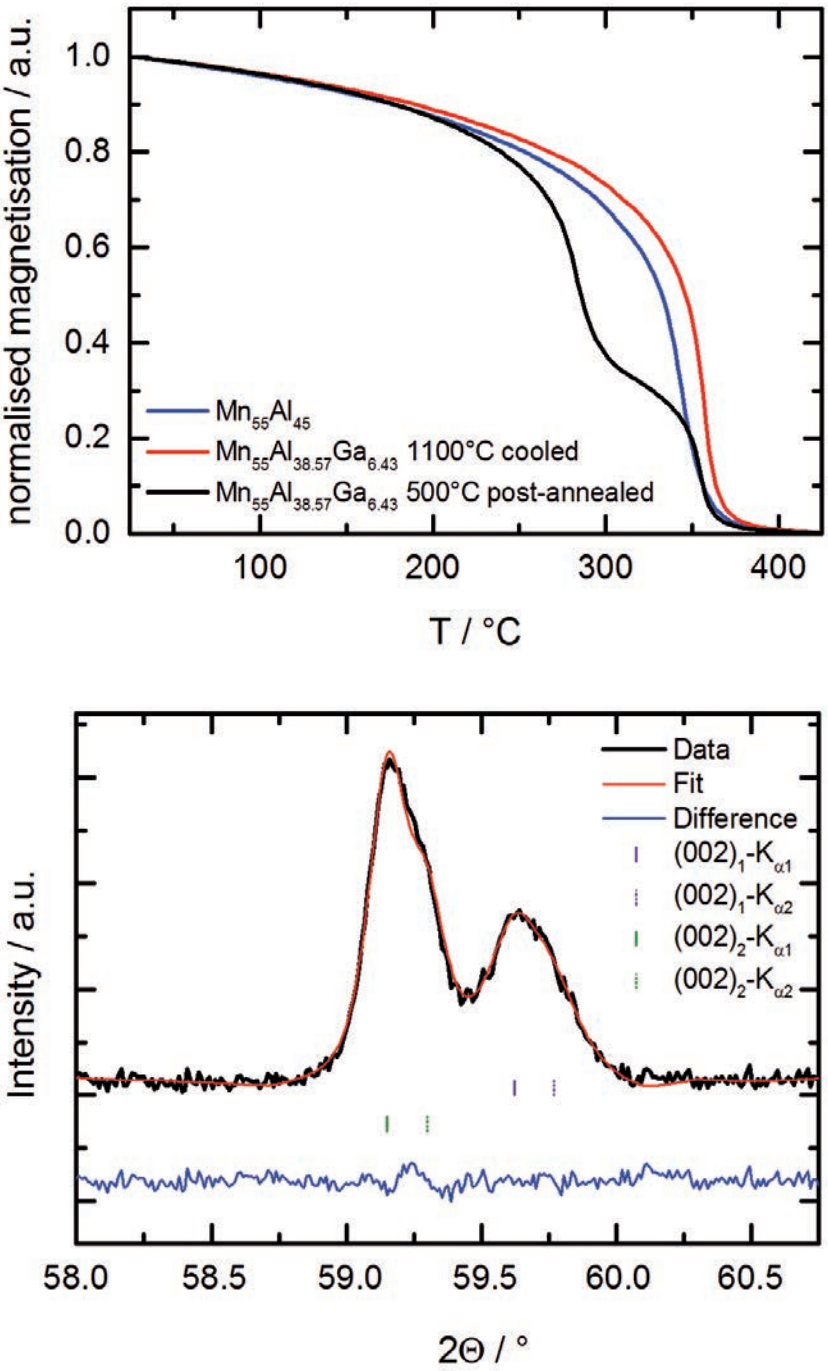

Figure 2: (top) magnetisation verses temperature curves for three samples, showing the Curie temperatures. The sample after annealing (black curve) contains two different magnetic phases with different Curie temperatures. (bottom) x-ray diffractogram of the annealed sample showing splitting of the (002) peak due to the different lattice parameters of the two magnetic phases [5].

namically stable, $L1_0$ phase with very good hard magnetic properties can be produced at near-equiatomic compositions [4], but the critical nature of global Ga supplies means that commercial application of bulk materials with approximately 50 at.% Ga is unviable. The challenge is to produce a thermodynamically stable ferromagnetic phase with a low Ga content.

Ternary Mn-Al-Ga alloys offer solutions to the above problems and we have shown that by substituting Al with Ga in $Mn_{55}Al_{45-x}Ga_x$ (at.%), a phase with the $L1_0$ crystal structure, which has excellent hard magnetic properties, can be produced at all ternary compositions between the metastable and stable binary end members [5]. In $Mn_{55}Al_{45-x}Ga_x$ with $5 < x \leq 9$, after appropriate heat treatments, both stable and metastable $L1_0$ phases can be made to coexist in the same ternary alloy (Figure 1). The two $L1_0$ phases differ in their lattice parameters and magnetic

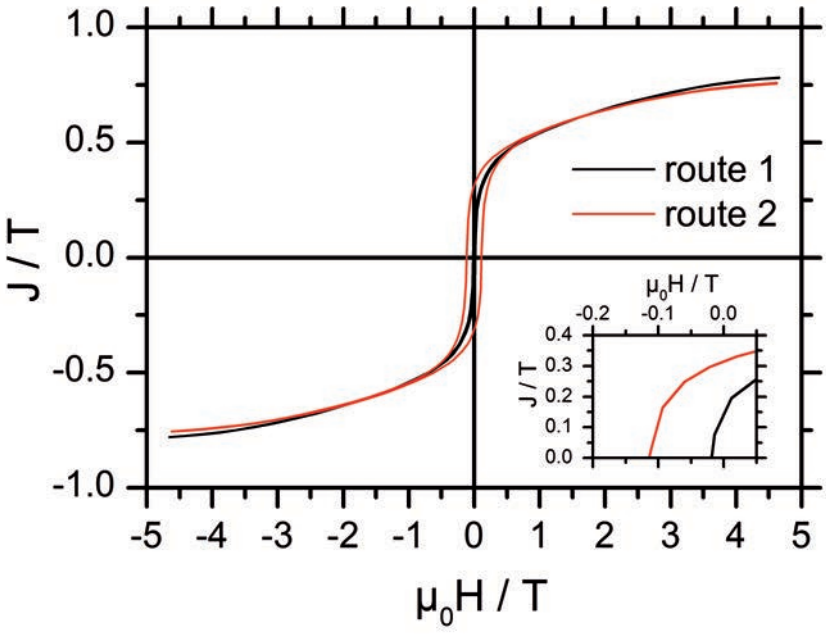

Figure 3: Magnetic hysteresis loops for MnAl samples transformed to the magnetic phase using routes 1 and 2. The difference in the magnetic properties of the two routes is visible and the inset emphasises the difference in the coercive field [7].

properties (Figure 2). The thermodynamically stable Mn-Al-Ga $L1_0$ phase, produced by adding just a few at.% Ga to MnAl, has the potential to revolutionize research on MnAl magnets, making it possible to process at elevated temperatures for longer times [5].

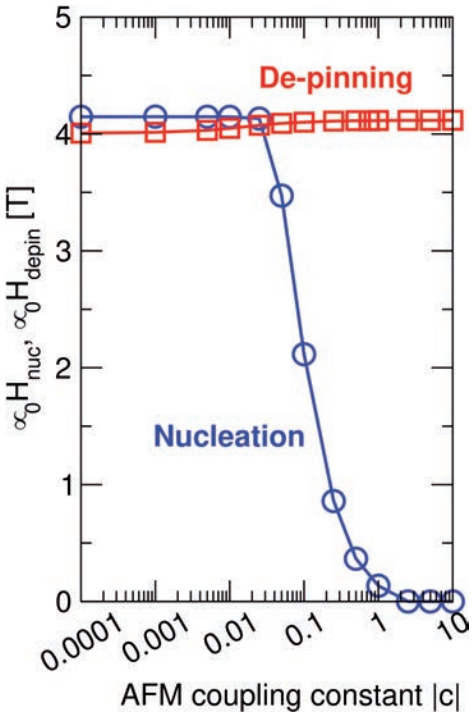

Figure 4: Calculated nucleation and depinning fields for a magnetic domain wall at an antiphase boundary (APB) in MnAl as a function of the antiferromagnetic (AFM) coupling constant. Strong AFM coupling is expected at APB in MnAl, indicating that nucleation of magnetic domain walls can proceed at very small applied field strength [8].

The Role of the Microstructure in Determining the Magnetic Properties

The microstructure of MnAl materials is characterised by a range of crystalline defects. Previous investigations using electron backscatter diffraction (EBSD) at IFW have shown that three different types of twin boundaries exist in MnAl materials [6]. Our recent investigations have revealed that the experimental procedure used to form the ferromagnetic phase in MnAl materials can also influence the magnetic properties (Figure 3) [7]. Investigations of the materials transformed via two different routes were carried out using both x-ray diffraction and EBSD. The results revealed that the density of dislocations was higher in materials produced via route 2, which alongside a refined grain size, led to the higher coercive field observed [7]. The stress field surrounding such dislocations was simulated and it was proposed that local changes in the interatomic distances of Mn atoms, due to the stress fields near dislocations cause local changes in the magnetic properties, thus having a pinning effect on magnetic domain walls [7].

Micromagnetic Modelling

In order to gain deeper understanding of the influence of material defects on the magnetic properties, micromagnetic simulations based on the experimental results were carried out as part of an international collaboration [8]. The structure of antiphase boundaries in MnAl is thought to lead to strong, local, antiferromagnetic coupling of the magnetic moments of the Mn atoms. These defects are highly detrimental for the macroscopic properties, as is shown by the plot of the calculated nucleation field verses the strength of the coupling constant (Figure 4). The results show that nucleation of magnetic domain walls can occur at very low fields at an-

tiphase boundaries and this reduces the hard magnetic performance of the material [8]. Similar investigations were carried out for twin boundaries, based on EBSD results from IFW, and the micromagnetic simulations showed radically different behaviour for these defects. Whereas the nucleation of domain walls at twin boundaries is predicted to be unfavourable, the depinning fields are low, indicating that twin boundaries are not effective pinning centres [8]. All of these results will be used to develop novel processing routes in order to enhance the fraction of features which are beneficial to the magnetic properties and to remove those which are deleterious.

[1] Kono H. J Phys Soc Japan 1958;13:1444.
[2] Koch AJJ, Hokkeling P, van der Steeg MG, de Vos KJ. J Appl Phys 1960; 31:75S.
[3] Pareti L, Bolzoni F, Leccabue F, Ermakov AE. J Appl Phys 1986; 59:3824.
[4] Mix T, Müller K-H, Schultz L, Woodcock TG. J Magn Magn Mater 2015; 391:89.
[5] Mix T, Bittner F, Müller K-H, Schultz L, Woodcock TG. Acta Mater 2017; 128:160.
[6] Bittner F, Schultz L, Woodcock TG. Acta Mater 2015; 101:48.
[7] Bittner F, Freudenberger J, Schultz L, Woodcock TG. J Alloys Compd 2017; 704:528.
[8] Bance S, Bittner F, Woodcock TG, Schultz L, Schrefl T. Acta Mater 2017; 131:48.

Acknowledgements

The authors would like to thank Dr. K.-H. Müller for many fruitful scientific discussions, and B. Gebel, M. Herrich, K. Pittruff, K. Berger, C. Damm, T. Sturm, A. Pöhl and Dr. K. Nenkov for excellent technical support.

Funding

DFG Project 380033763
DFG Project 326646134

Cooperation

[1] Danube University Krems, Austria
[2] Seagate Technology, Republic of Ireland
TU Dresden, Germany

Publications 2018

Monograph

1) Fomin, V.M., Physics of Quantum Rings (2018), S. XXVI, 585.

Journal articles

1) Agrapidis, C.E., van den Brink, J., Nishimoto, S., Ordered states in the Kitaev-Heisenberg model: From 1D chains to 2D honeycomb, Scientific Reports 8 (2018), S. 1815/1-18.
2) Agrapidis, C.E., van den Brink, J., Nishimoto, S., Numerical study of the Kitaev-Heisenberg chain, Physica B 536 (2018), S. 461-463.
3) Ajayakumar, M.R., Fu, Y., Ma, J., Hennersdorf, F., Komber, H., Weigand, J.J., Alfonsov, A., Popov, A.A., Berger, R., Liu, J., Muellen, K., Feng, X., Toward Full Zigzag-Edged Nanographenes: peri-Tetracene and Its Corresponding Circumanthracene, Journal of the American Chemical Society 20 140 (2018), S. 6240-6244.
4) Akash, K., Prabu, S.S.M., Gustmann, T., Jayachandran, S., Pauly, S., Palani, I.A., Enhancing the life cycle behaviour of Cu-Al-Ni shape memory alloy bimorph by Mn addition, Materials Letters 226 (2018), S. 55-58.
5) Alakshin, E.M., Kondratyeva, E.I., Nuzhina, D.S., Iakovleva, M.F., Kuzmin, V.V., Safiullin, K.R., Gubaidullin, A.T., Kikitsu, T., Kono, K., Klochkov, A.V., Tagirov, M.S., The self-assembly of DyF3 nanoparticles synthesized by chloride-based route, Journal of Nano-particle Research 12 20 (2018), S. 332/1-5.
6) Amorese, A., Caroca-Canales, N., Seiro, S., Krellner, C., Ghiringhelli, G., Brookes, N. B., Vyalikh, D. V., Geibel, C., Kummer, K., Crystal electric field in CeRh2Si2 studied with high-resolution resonant inelastic soft x-ray scattering, Physical Review B 24 97 (2018), S. 245130/1-9.
7) Avdoshenko, S., Fritz, F., Schlesier, C., Kostanyan, A., Dreiser, J., Luysberg, M., Popov, A., Meyer, C., Westerström, R., Partial magnetic ordering in one-dimensional arrays of endofullerene single-molecule magnet peapods, Nanoscale 10 (2018), S. 18153.
8) Aviles, F., May-Pat, A., Lopez-Manchado, M.A., Verdejo, R., Bachmatiuk, A., Ruemmeli, M.H., A comparative study on the mechanical, electrical and piezoresistive properties of polymer composites using carbon nanostructures of different topology, European Polymer Journal 99 (2018), S. 394-402.
9) Baek, S.-H., Bhoi, D., Nam, W., Lee, B., Efremov, D.V., Buechner, B., Kim, K.H., Tuning the interplay between nematicity and spin fluctuations in Na1-xLixFeAs superconductors, Nature Communications 9 (2018), S. 2139/1-8.
10) Baenitz, M., Schlender, P., Sichelschmidt, J., Onykiienko, Y.A., Zangeneh, Z., Ranjith, K.M., Sarkar, R., Hozoi, L., Walker, H.C., Orain, J.-C., Yasuoka, H., van den Brink, J., Klauss, H.H., Inosov, D.S., Doert, Th., NaYbS2: A planar spin-1/2 triangular-lattice magnet and putative spin liquid, Physical Review B 22 98 (2018), S. 220409/1-6.
11) Balach, J., Linnemann, J., Jaumann, T., Giebeler, L., Metal-based nanostructured materials for advanced lithium–sulfur batteries, Journal of Materials Chemistry A 46 6 (2018), S. 23127-23168.
12) Balach, J., Linnemann, J., Jaumann, T., Giebeler, L., Correction: Metal-based nanostructured materials for advanced lithium–sulfur batteries, Journal of Materials Chemistry A 46 6 (2018), S. 23903.
13) Bastien, G., Garbarino, G., Yadav, R., Martinez-Casado, F.J., Beltran Rodriguez, R., Stahl, Q., Kusch, M., Limandri, S.P., Ray, R., Lampen-Kelley, P., Mandrus, D.G., Nagler, S.E., Roslova, M., Isaeva, A., Doert, T., Hozoi, L., Wolter, A.U.B., Buechner, B., Geck, J., van den Brink, J., Pressure-induced dimerization and valence bond crystal formation in the Kitaev-Heisenberg magnet alpha-$RuCl_3$, Physical Review B 24 97 (2018), S. 241108/1-6.
14) Beguin, L., Jahn, J.-P., Wolters, J., Reindl, M., Huo, Y., Trotta, R., Rastelli, A., Ding, F., Schmidt, O.G., Treutlein, P., Warburton, R.J., On-demand semiconductor source of 780-nm single photons with controlled temporal wave packets, Physical Review B 20 97 (2018), S. 205304/1-8.
15) Bendt, G., Kaiser, K., Heckel, A., Rieger, F., Oing, D., Lorke, A., Perez Rodriguez, N., Schierning, G., Jooss, C., Schulz, S., Structural and thermoelectrical characterization of epitaxial Sb_2Te_3 high quality thin films grown by thermal evaporation, Semiconductor Science and Technology 10 33 (2018), S. 105002/1-9.
16) Biesner, T., Biswas, S., Li, W., Saito, Y., Pustogow, A., Altmeyer, M., Wolter, A.U.B., Buechner, B., Roslova, M., Doert, T., Winter, S.M., Valenti, R., Dressel, M., Detuning the honeycomb of alpha-$RuCl_3$: Pressure-dependent optical studies reveal broken symmetry, Physical Review B 22 97 (2018), S. 220401/1-5.
17) Brachmann, E., Seifert, M., Ernst, D., Menzel, S.B., Gemming, T., Pt-wire bonding optimization for electroplated Pt films on γ-Al_2O_3 for high temperature and harsh environment applications, Sensors and Actuators A: Physical 284 (2018), S. 129-134.
18) Brandenburg, A., Krylov, D.S., Beger, A., Wolter, A.U.B., Buechner, B., Popov, A.A., Carbide clusterfullerene DyYTiC@C-80 featuring three different metals in the endohedral cluster and its single-ion magnetism, Chemical Communications 76 54 (2018), S. 10683-10686.

19) Briffa, A.K.R., Zotos, X., High-temperature dynamics in quantum compass models, Physical Review B 6 97 (2018), S. 064406/1-5.
20) Buettner, A., Probst, A.-C., Emmerich, F., Damm, C., Rellinghaus, B., Doehring, T., Stollenwerk, M., Influence of sputtering pressure on microstructure and layer properties of iridium thin films, Thin Solid Films 662 (2018), S. 41-46.
21) Caglieris, F., Wuttke, C., Sykora, S., Süss, V., Shekhar, C., Felser, C., Büchner, B., Heß, C., Anomalous Nernst effect and field-induced Lifshitz transition in the Weyl semimetals TaP and TaAs, Physical Review B 20 98 (2018), S. 201107/1-6.
22) Cai, B., Huebner, R., Sasaki, K., Zhang, Y., Su, D., Ziegler, C., Vukmirovic, M.B., Rellinghaus, B., Adzic, R.R., Eychmueller, A., Core-Shell Structuring of Pure Metallic Aerogels towards Highly Efficient Platinum Utilization for the Oxygen Reduction Reaction (Kern-Schale-Strukturierung rein metallischer Aerogele für eine hocheffiziente Nutzung von Platin für die Sauerstoffreduktion), Angewandte Chemie - Internationale Edition 11 57 (2018), S. 2963-2966.
23) Canon Bermudez, G.S., Karnaushenko, D.D., Karnaushenko, D., Lebanov, A., Bischoff, L., Kaltenbrunner, M., Fassbender, J., Schmidt, O.G., Makarov, D., Magnetosensitive e-skins with directional perception for augmented reality, Science Advances 1 4 (2018), S. eaao2623/1-9.
24) Charnukha, A., Proepper, D., Zhigadlo, N.D., Naito, M., Schmidt, M., Wang, Zhe, Deisenhofer, J., Loidl, A., Keimer, B., Boris, A.V., Basov, D.N., Intrinsic Charge Dynamics in High-T_c AFeAs (O,F) Superconductors, Physical Review Letters 8 120 (2018), S. 087001/1-6.
25) Chavez, R., Angst, S., Hall, J., Maculewicz, F., Stoetzel, J. , Wiggers, H., Hung, L.T., Nong, N.V., Pryds, N., Span, G., Wolf, D.E., Schmechel, R., Schierning, G., Efficient p-n junction-based thermoelectric generator that can operate at extreme temperature conditions, Journal of Physics D 1 51 (2018), S. 014005/1-8.
26) Chen, B., He, J., Xi, Y., Zeng, X., Kaban, I., Zhao, J., Hao, H., Liquid-liquid hierarchical separation and metal recycling of waste printed circuit boards, Journal of Hazardous Materials 364 (2018), S. 388-395.
27) Chen, C.H., Krylov, D.S., Avdoshenko, S.M., Liu, F., Spree, L., Westerström, R., Bulbucan, C., Studniarek, M., Dreiser, J., Wolter, A.U.B., Büchner, B., Popov, A.A., Magnetic hysteresis in self-assembled monolayers of Dy-fullerene single molecule magnets on gold, Nanoscale 24 10 (2018), S. 11287-11292.
28) Chen, Y., Zopf, M., Keil, R., Ding, F., Schmidt, O.G., Highly-efficient extraction of entangled photons from quantum dots using a broadband optical antenna, Nature Communications 9 (2018), S. 2994/1-7.
29) Cheng, Y., Zhang, Z.-T., Sopu, D., Peng, C.-X., Wang, Y.-Y., Song, K.-K., Wang, L., Structural origin of dynamical relaxation in undercooled Cu50Zr50 metallic liquid, Journal of Non-Crystalline Solids 492 (2018), S. 33-40.
30) Chiasera, A., Meroni, C., Varas, S., Valligatla, S., Scotognella, F., Boucher, Y.G., Lukowiak, A., Zur, L., Righini, G.C., Ferrari, M., Photonic band edge assisted spontaneous emission enhancement from all Er^{3+} 1-D photonic band gap structure, Optical Materials 80 (2018), S. 106-109.
31) Choi, J.-H., Liu, S.Y., Zhang, W., Liu, Z.F., Ruemmeli, M.H., Charge Density Waves Driven by Peierls Instability at the Interface of Two-Dimensional Lateral Heterostructures, Small 50 14 (2018), S. 1803040/1-5.
32) Clercq, R. De, Dusselier, M., Poleunis, C., Debecker, D.P., Giebeler, L., Oswald, S., Makshina, E., Sels, B.F., Titania-Silica Catalysts for Lactide Production from Renewable Alkyl Lactates: Structure-Activity Relations, ACS Catalysis 9 8 (2018), S. 8130-8139.
33) Craco, L., Site-selective electronic structure of pure and doped $Ca_2O_3Fe_3S_2$, Physical Review B 4 98 (2018), S. 045130/1-7.
34) Craco, L., Carara, S.S., Microscopic description of orbital-selective spin ordering in $BaMn_2As_2$, Physical Review B 20 97 (2018), S. 205114/1-6.
35) Craco, L., Leoni, S., Microscopic description of localization-delocalization transitions in $BaFe_2S_3$, Physical Review B 19 98 (2018), S. 195107/1-7.
36) Cwik, J., Koshkidko, Y., de Oliveira, N.A., Mikhailova, A., Nenkov, K., Effect of composition changes on the structural, magnetic and thermodynamic properties in Tb1-xDyxNi2 intermetallic compounds, Journal of Alloys and Compounds 769 (2018), S. 588-596.
37) Cwik, J., Koshkidko, Y., Nenkov, K., Tereshina, E.A., Rogacki, K., Structural, magnetic and magnetocaloric properties of $HoNi_2$ and $ErNi_2$ compounds ordered at low temperatures, Journal of Alloys and Compounds 735 (2018), S. 1088-1095.
38) da Silva, M.R., Gargarella, P., Wolf, W., Gustmann, T., Kiminami, C. S., Pauly, S., Eckert, J., Bolfarini, C., Microstructural Characterization of a Laser Surface Remelted Cu-Based Shape Memory Alloy, Materials Research 3 21 (2018), S. e20171044/1-10.
39) Dai, G., Hu, X., Sievers, S., Fernandez Scarioni, A., Neu, V., Fluegge, J., Schumacher, H.W., Metrological large range magnetic force microscopy, Review of Scientific Instruments 9 89 (2018), S. 093703/1-9.
40) Darinskii, A.N., Weihnacht, M., Schmidt, H., FE analysis of surface acoustic wave transmission in composite piezoelectric wedge structures, Ultrasonics 84 (2018), S. 366-372.
41) Darinskii, A.N., Weihnacht, M., Schmidt, H., Surface acoustic wave electric field effect on acoustic streaming: Numerical analysis, Journal of Applied Physics 123 (2018), S. 014902/1-8.
42) Dash, S., Schleicher, B., Schwabe, S., Reichel, L., Heller, R., Faehler, S., Neu, V., Patra, A.K., Structural and magnetic properties of epitaxial Mn-Ge films grown on Ir/Cr buffered MgO(001), Journal of Physics D-Applied Physics 25 51 (2018), S. 255002/1-7.

43) Deng, L., Wang, S., Wang, P., Kuehn, U., Pauly, S., Selective laser melting of a Ti-based bulk metallic glass, Materials Letters 212 (2018), S. 346-349.

44) di Luca, M., Vittorio, O., Cirillo, G., Curcio, M., Czuban, M., Voli, F., Farfalla, A., Hampel, S., Nicoletta, F.P., Iemma, F., Electro-responsive graphene oxide hydrogels for skin bandages: The outcome of gelatin and trypsin immobilization, International Journal of Pharmaceutics 1-2 546 (2018), S. 50-60.

45) Diederichs, A.M., Thiel, F., Lienert, U., Pantleon, W., In-situ investigations of structural changes during cyclic loading of aluminium by high resolution reciprocal space mapping, International Journal of Fatigue 117 (2018), S. 206-216.

46) Diestel, A., Chekhonin, P., Niemann, R., Skrotzki, W., Nielsch, K., Faehler, S., Reducing Thermal Hysteresis in Epitaxial Ni-Mn-Ga-Co Films by Transformation Cycling, Physica Status Solidi B 2 255 (2018), S. 1700330/1-8.

47) Diestel, A., Niemann, R., Schleicher, B., Nielsch, K., Faehler, S., Reducing hysteresis losses by heating minor loops in magnetocaloric Ni-Mn-Ga-Co films, Energy Technology 8 6 (2018), S. 1463-1469.

48) Dmitrieva, E., Rosenkranz, M., Alesanco, Y., Vinuales, A., The reduction mechanism of p-cyanophenylviologen in PVA-borax gel polyelectrolyte-based bicolor electrochromic devices, Electrochimica Acta 292 (2018), S. 81-87.

49) Dmitrieva, E., Rosenkranz, M., Danilova, J.S., Smirnova, E.A., Karushev, M.P., Chepurnaya, I.A., Timonov, A.M., Radical formation in polymeric nickel complexes with N2O2 Schiff base ligands: An in situ ESR and UV-–vis-–NIR spectroelectrochemical study, Electrochimica Acta 283 (2018), S. 1742-1752.

50) Doentgen, J., Rudolph, J., Waske, A., Haegele, D., Modulation infrared thermometry of caloric effects at up to kHz frequencies, Review of Scientific Instruments 3 89 (2018), S. 033909/1-8.

51) Doerfler, S., Strubel, P., Jaumann, T., Troschke, E., Hippauf, F., Kensy, C., Schoekel, A., Althues, H., Giebeler, L., Oswald, S., Kaskel, S., On the mechanistic role of nitrogen-doped carbon cathodes in lithium-sulfur batteries with low electrolyte weight portion, Nano Energy 54 (2018), S. 116-128.

52) Drechsler, S.-L., Rosner, H., Grinenko, V., Aswartham, S., Morozov, I., Liu, M., Boltalin, A., Kihou, K., Lee, C. H., Kim, T., Evtushinsky, D., Tomczak, J.M., Johnston, S., Borisenko, S., Mass Enhancements and Band Shifts in Strongly Hole-Overdoped Fe-Based Pnictide Superconductors: KFe_2As_2 and $CsFe_2As_2$, Journal of Superconductivity and Novel Magnetism 3 31 (2018), S. 777-783.

53) Droste, M., Ullrich, C., Motylenko, M., Fleischer, M., Weidner, A., Freudenberger, J., Rafaja, D., Biermann, H., Fatigue behavior of an ultrafine-grained metastable CrMnNi steel tested under total strain control, International Journal of Fatigue 106 (2018), S. 143-152.

54) Du, M., Ye, S., Tang, J., Lv, S., Chen, J., Orava, J., Tao, G., Lan, P., Hao, J., Yang, Z., Qiu, J., Zhou, S., Scalable in-fiber manufacture of functional composite particles, ACS Nano 11 12 (2018), S. 11130-11138.

55) Du, N., Manjunath, N., Li, Y., Menzel, S., Linn, E., Waser, R., You, T.G., Burger, D., Skorupa, I., Walczyk, D., Walczyk, C., Schmidt, O.G., Schmidt, H., Field-Driven Hopping Transport of Oxygen Vacancies in Memristive Oxide Switches with Interface-Mediated Resistive Switching, Physical Review Applied 5 10 (2018), S. 054025/1-8.

56) Du, Y., Yin, Y., Wang, J., Wang, Z., Li, C., Baunack, S., Ma, L., Schmidt, O.G., Nanoporous Copper Pattern Fabricated by Electron Beam Irradiation on Cu3N Film for SERS Application, Physica Status Solidi B (2018), S. 1800378/1-5.

57) Dubraja, L.A., Juric, M., Popovic, J., Pajic, D., Krupskaya, Y., Kataev, V., Buechner, B., Zilic, D., Magneto-structural correlations in oxalate-bridged $Sr_{(II)}Cr_{(III)}$ coordination polymers: structure, magnetization, X-band, and high-field ESR studies, Dalton Transactions 11 47 (2018), S. 3992-4000.

58) Dufouleur, J., Xypakis, E., Buechner, B., Giraud, R., Bardarson, J.H., Suppression of scattering in quantum confined 2D helical Dirac systems, Physical Review B 1 97 (2018), S. 075401/1-10.

59) Duschek, K., Petr, A., Zehner, J., Nielsch, K., Leistner, K., All-electrochemical voltage-control of magnetization in metal oxide/metal nanoislands, Journal of Materials Chemistry C 31 online first (2018), S. 8411-8417.

60) Ebner, C., Escher, B., Gammer, C., Eckert, J., Pauly, S., Rentenberger, C., Structural and mechanical characterization of heterogeneities in a CuZr-based bulk metallic glass processed by high pressure torsion, Acta Materialia 160 (2018), S. 147-157.

61) Eckert, V., Leonhardt, A., Hampel, S., Buechner, B., Morphology of MWCNT in dependence on N-doping, synthesized using a sublimation-based CVD method at 750 °C, Diamand and Related Materials 86 (2018), S. 8-14.

62) Ehinger, D., Weise, J., Baumeister, J., Funk, A., Waske, A., Krueger, L., Martin, U., Microstructure and Deformation Response of TRIP-Steel Syntactic Foams to Quasi-Static and Dynamic Compressive Loads, Materials 5 11 (2018), S. 656.

63) Ehlen, N., Sanna, A., Senkovskiy, B.V., Petaccia, L., Fedorov, A.V., Profeta, G., Grueneis, A., Direct observation of a surface resonance state and surface band inversion control in black phosphorus, Physical Review B 4 97 (2018), S. 045143/1-10.

64) Eleazer, B.J., Smith, M.D., Popov, A.A., Peryshkov, D.V., Expansion of the (BB) Ru metallacycle with coinage metal cations: formation of B-M-Ru-B (M = Cu, Ag, Au) dimetalacyclodiboryls, Chemical Science 9 9 (2018), S. 2601-2608.

65) Engelhardt, S., Molin, C., Gebhardt, S., Faehler, S., Nielsch, K., Huehne, R., $BaZr_xTi_{1-x}O_3$ Epitaxial Thin Films for Electrocaloric Investigations, Energy Technology 8 6 (2018), S. 1526-1534.

66) Entel, P., Faehler, S., Hysteresis in Magnetocaloric, Electrocaloric, and Elastocaloric Refrigeration, Physica Status Solidi B 2 255 (2018), S. 1870109/1-1.
67) Entel, P., Gruner, M.E., Acet, M., Cakir, A., Arroyave, R., Duong, T., Sahoo, S., Faehler, S., Sokolvskiy, V.V., Properties and decomposition of Heusler alloys, Energy Technology 8 6 (2018), S. 1478-1490.
68) Entel, P., Gruner, M.E., Faehler, S., Acet, M., Cahir, A., Arroyave, R., Sahoo, S., Duong, T.C., Talapatra, A., Sandratskii, L., Mankowsky, S., Gottschall, T., Gutfleisch, O., Lazpita, P., Chernenko, V.A., Barandiaran, J.M., Sokolovskiy, V., Buchelnikov, V.D., Probing Structural and Magnetic Instabilities and Hysteresis in Heuslers by Density Functional Theory Calculations, Physica Status Solidi B 2 255 (2018), S. 1700296/1-14.
69) Espenhahn, T., Berger, D., Schultz, L., Nielsch, K., Huehne, R., Simulation of Force Generation Above Magnetic Tracks for Superconducting Levitation Systems, IEEE Transactions on Applied Superconductivity 4 28 (2018), S. 3600205/1-5.
70) Espenhahn, T., Berger, D., Schultz, L., Nielsch, K., Huehne, R., Levitation force measurement on a switchable track for superconducting levitation systems, Superconductor Science and Technology 12 31 (2018), S. 125007/1-8.
71) Facio, J., Efremov, D., Koepernik, K., You, J., Sodemann, I., van den Brink, J., Strongly Enhanced Berry Dipole at Topological Phase Transitions in BiTeI, Physical Review Letters 24 121 (2018), S. 246403/1-6.
72) Faehler, S., Caloric Effects in Ferroic Materials: New Concepts for Cooling, Energy Technology 8 6 (2018), S. 1394-1396.
73) Faehler, S., Pecharsky, V.K., Caloric effects in ferroic materials, MRS Bulletin 4 43 (2018), S. 264-268.
74) Fakhfouri, A., Devendran, C., Albrecht, T., Collins, D.J., Winkler, A., Schmidt, H., Neild, A., Surface acoustic wave diffraction driven mechanisms in microfluidic systems, Lab on a Chip 15 18 (2018), S. 2214-2224.
75) Faundez, J., Jorge, T.N., Craco, L., Spin-selective electronic reconstruction in quantum ferromagnets: A view from the spin-asymmetric Hubbard model, Physical Review B 11 97 (2018), S. 115149/1-6.
76) Fedorov, A., Yashina, L.V., Vilkov, O.Y., Laubschat, C., Vyalikh, D.V., Usachov, D.Y., Spin-polarized Fermi surface, hole-doping and band gap in graphene with boron impurities, Nanoscale 48 10 (2018), S. 22810-22817.
77) Fernandez-Barcia, M., Hoffmann, V., Oswald, S., Giebeler, L., Wolff, U., Uhlemann, M., Gebert, A., Electrodeposition of manganese layers from sustainable sulfate based electrolytes, Surface and Coatings Technology 334 (2018), S. 261-268.
78) Franca, S., van den Brink, J., Fulga, I., An anomalous higher-order topological insulator, Physical Review B 20 98 (2018), S. 201114/1-6.
79) Fu, Q., Azmi, R., Sarapulova, A., Mikhailova, D., Dsoke, S., Missiul, A., Trouillet, V., Knapp, M., Bramnik, N., Ehrenberg, H., Electrochemical and structural investigations of different polymorphs of TiO_2 in magnesium and hybrid lithium/magnesium batteries, Electrochimica Acta 277 (2018), S. 20-29.
80) Fuchs, S., Dey, T., Aslan-Cansever, G., Maljuk, A., Wurmehl, S., Buechner, B., Kataev, V., Unraveling the Nature of Magnetism of the $5d^4$ Double Perovskite Ba_2YIrO_6, Physical Review Letters 23 120 (2018), S. 237204/1-6.
81) Fuge, R., Liebscher, M., Schröfl, C., Damm, C., Eckert, V., Eibl, M., Leonhardt, A., Büchner, B., Mechtcherine, V., Influence of different hydrocarbons on the height of MWCNT carpets: Role of catalyst and hybridization state of the carbon precursor, Diamond and Related Materials 90 (2018), S. 18-25.
82) Fulga, I.C., Fallani, L. , Burrello, M., Geometrically protected triple-point crossings in an optical lattice, Physical Review B 12 97 (2018), S. 121402/1-5.
83) Funk, A., Freudenberger, J., Waske, A., Krautz, M., Getting magnetocaloric materials into good shape: Cold-working of La(Fe, Co, Si)13 by powder-in-tube-processing, Materials Today Energy 9 (2018), S. 223-228.
84) Funk, A., Zeilinger, M., Doetz, F., Soldatov, I., Schaefer, R., Waske, A., Hysteresis of MnFePSi Spherical Powder Ensembles Studied by Magneto-Optical Imaging, Physica Status Solidi B 2 255 (2018), S. 1700345/1-7.
85) Funk, A., Zeilinger, M., Miehe, A., Sopu, D., Eckert, J., Doetz, F., Waske, A., MnFePSi-based magnetocaloric packed bed regenerators: Structural details probed by X-ray tomography, Chemical Engineering Science 175 (2018), S. 84-90.
86) Gagkaeva, Z.V., Zhukova, E.S., Grinenko, V., Grebenko, A.K., Sidoruk, K.V., Voeikova, T.A., Dressel, M., Gorshunov, B.P., Terahertz-infrared spectroscopy of Shewanella oneidensis MR-1 extracellular matrix, Journal of Biological Physics 3 44 (2018), S. 401-417.
87) Gaididei, Y., Kravchuk, V.P., Mertens, F.G., Pylypovskyi, O.V., Saxena, A., Sheka, D.D., Volkov, O.M., Localization of magnon modes in a curved magnetic nanowire, Low Temperature Physics 7 44 (2018), S. 634-643.
88) Gajda, D., Morawski, A., Zaleski, A.J., Cetner, T., Haessler, W., Nenkov, K., Malecka, M., Rindfleisch, M.A., Tomsic, M., Significant enhancement of the critical current of MgB_2 wires through a reduction of the diameter using HIP method, Scripta Materialia 143 (2018), S. 77-80.
89) Gao, Z., Guo, S., Lu, X., Orava, J., Wagner, T., Zheng, L., Liu, Y., Sun, S., He, F., Yang, P., Ren, J., Yang, J., Controlling Selective Doping and Energy Transfer between Transition Metal and Rare Earth Ions in Nanostructured Glassy Solids, Advanced Optical Materials 13 6 (2018), S. 1701407/.

90) Garcia Fernandez, J., Vega Martinez, V., Thomas, A., de la Prida Pidal, V.M., Nielsch, K., Two-Step Magnetization Reversal FORC Fingerprint of Coupled Bi-Segmented Ni/Co Magnetic Nanowire Arrays, Nanomaterials 7 8 (2018), S. 548/1-15.

91) Garcia, C., Rosa, W.O., Garcia, J., Prida, V.M., Hernando, B., Lopez, J.A., Vargas, P., Ross, C.A., Magnetization Reversal in Radially Distributed Nanowire Arrays, The Journal of Physical Chemistry C 9 122 (2018), S. 5124-5130.

92) Gebert, A., Kochta, F., Voss, A., Oswald, S., Fernandez-Barcia, M., Kuehn, U., Hufenbach, J., Corrosion studies on Fe-30Mn-1C alloy in chloride-containing solutions with view to biomedical application, Materials and Corrosion 2 69 (2018), S. 167-177.

93) Geissler, D., Freudenberger, J., Wendrock, H., Zimmermann, M., Gebert, A., On sample size effects in fracture toughness determination of Bulk Metallic Glasses, Engineering Fracture Mechanics 202 (2018), S. 500-507.

94) Generalov, A., Falke, J., Nechaev, I.A., Otrokov, M.M., Guettler, M., Chikina, A., Kliemt, K., Seiro, S., Kummer, K., Danzenbaecher, S., Usachov, D., Kim, T.K., Dudin, P., Chulkov, E.V., Laubschat, C., Geibel, C., Krellner, C., Vyalikh, D.V., Strong spin-orbit coupling in the noncentrosymmetric Kondo lattice, Physical Review B 11 98 (2018), S. 115157/1-10.

95) Ghunaim, R., Damm, C., Wolf, D., Lubk, A., Buechner, B., Mertig, M, Silke Hampel, S., $Fe_{1-x}Ni_x$ Alloy Nanoparticles Encapsulated Inside Carbon Nanotubes: Controlled Synthesis, Structure and Magnetic Properties, Nanomaterials 8 8 (2018), S. 576/1-17.

96) Ghunaim, R., Eckert, V., Scholz, M., Gellesch, M., Wurmehl, S., Damm, C., Mertig, M., Hampel, S., Carbon nanotube-assisted synthesis of ferromagnetic Heusler nanoparticles of Fe3Ga (Nano-Galfenol), Journal of Materials Chemistry C 5 6 (2018), S. 1255-1263.

97) Ghunaim, R., Scholz, M., Damm, C., Rellinghaus, B., Klingeler, R., Buechner, B., Mertig, M., Hampel, S., Single-crystalline FeCo nanoparticle-filled carbon nanotubes: synthesis, structural characterization and magnetic properties, Beilstein Journal of Nanotechnology 9 (2018), S. 1024-1034.

98) Gooth, J., Schierning, G., Felser, C., Nielsch, K., Quantum materials for thermoelectricity, Mrs Bulletin 3 43 (2018), S. 187-192.

99) Grinenko, V., Sarkar, R., Materne, P., Kamusella, S., Yamamshita, A., Takano, Y., Sun, Y., Tamegai, T., Efremov, D.V., Drechsler, S.-L., Orain, J.-C., Goko, T., Scheuermann, R., Luetkens, H., Klauss, H.-H., Low-temperature breakdown of antiferromagnetic quantum critical behavior in FeSe, Physical Review B 20 97 (2018), S. 201102/1-5.

100) Grönke, M., Schmidt, P., Valldor, M., Oswald, S., Wolf, D., Lubk, A., Büchner, B., Hampel, S., Chemical vapor growth and delamination of -$RuCl_3$ nanosheets down to the monolayer limit, Nanoscale 40 10 (2018), S. 19014-19022.

101) Grove, T., Denkena, B., Maiss, O., Krodel, A., Schwab, H., Kuehn, U., Cutting mechanism and surface integrity in milling of Ti-5553 processed by selective laser melting, Journal of Mechanical Science and Technology 10 32 (2018), S. 4883-4892.

102) Gruner, M.E., Keune, W., Landers, J., Salamon, S., Krautz, M., Zhao, J.Y., Hu, M.Y., Toellner, T., Alp, E.E., Gutfleisch, O., Wende, H., Moment-Volume Coupling in La(Fe1-xSix)(13), Physica Status Solidi B 2 255 (2018), S. 1700465/1-12.

103) Gruner, M.E., Niemann, R., Entel, P., Pentcheva, R., Roessler, U.K., Nielsch, K., Faehler, S., Modulations in martensitic Heusler alloys originate from nanotwin ordering, Scientific Reports 8 (2018), S. 8489/1-12.

104) Guix, M., Weiz, S.M., Schmidt, O.G., Medina-Sanchez, M., Self-Propelled Micro/Nanoparticle Motors, Particle and Particle Systems Characterization 2 35 (2018), S. 1700382/1-31.

105) Gunes, T., Schaefer, R., Derebasi, N., Quantitative Analysis of Magnetic Field Distribution Around Circular Non-Magnetic Region in Grain-Oriented Fe-3%Si Steel , IEEE Transactions on Magnetics 2 54 (2018), S. 6500208/1-8.

106) Guo, F., Cui, B., Liu, Y., Meng, X., Cao, J., Zhang, Y., He, R., Liu, W., Wu, H., Pennycook, S.J., Cai, W., Sui, J., Thermoelectric SnTe with Band Convergence, Dense Dislocations, and Interstitials through Sn Self-Compensation and Mn Alloying, Small 37 14 (2018), S. 1802615/1-10.

107) Gustmann, T., Schwab, H., Kuehn, U., Pauly, S., Selective laser remelting of an additively manufactured Cu-Al-Ni-Mn shape-memory alloy, Materials and Design 153 (2018), S. 129-138.

108) Haas, S., Mosbacher, M., Senkov, O.N., Feuerbacher, M., Freudenberger, J., Gezgin, S., Voelkl, R., Glatzel, U., Entropy Determination of Single-Phase High Entropy Alloys with Different Crystal Structures over a Wide Temperature Range, Entropy 9 20 (2018), S. 654/1-12.

109) Habenicht, C., Schuster, R., Knupfer, M., Buechner, B., Investigation of indirect excitons in bulk 2H-MoS_2 using transmission electron energy-loss spectroscopy, Journal of Physics: Condensed Matter 20 30 (2018), S. 205502/1-8.

110) Habenicht, C., Sponza, L., Schuster, R., Knupfer, M., Buechner, B., Mapping of the energetically lowest exciton in bulk 1T-HfS_2, Physical Review B 15 98 (2018), S. 155204/1-9.

111) Haessler, W., Scheiter, J., Haedrich, P., Kauffmann-Weiss, S., Holzapfel, B., Oomen, M., Nielsch, K., Properties of ex-situ MgB_2 bulk samples prepared by uniaxial hot pressing and spark plasma sintering, Physica C 551 (2018), S. 48-54.

112) Han, X.L., Song, K.K., Zhang, L.M., Xing, H., Sarac, B., Spieckermann, F., Maity, T., Muehlbacher, M., Wang, L., Kaban, I., Eckert, J., Microstructures, Martensitic Transformation, and Mechanical Behavior of Rapidly Solidified Ti-Ni-Hf and Ti-Ni-Si Shape Memory Alloys, Journal of Materials Engineering and Performance 3 27 (2018), S. 1005-1015.

113) Hanft, D., Glosse, P., Denneler, S., Berthold, T., Oomen, M., Kauffmann-Weiss, S., Weis, F., Haessler, W., Holzapfel, B., Moos, R., The Aerosol Deposition Method: A Modified Aerosol Generation Unit to Improve Coating Quality, Materials 9 11 (2018), S. 1572/1-11.

114) Hantusch, M., Bessergenev, V., Mateus, M.C., Knupfer, M., Burkel, E., Electronic properties of photocatalytic improved Degussa P25 titanium dioxide powder, Catalysis Today 307 (2018), S. 111-118.

115) Hao, Q., Li, W., Xu, H., Wang, J., Yin, Y., Wang, H., Ma, L., Ma, F., Jiang, X., Schmidt, O.G., Chu, P.K., VO_2/TiN Plasmonic Thermochromic Smart Coatings for Room-Temperature Applications, Advanced Materials 10 30 (2018), S. 1705421/1-5.

116) Hao, Q., Pang, J., Zhang, Y., Wang, J., Ma, L., Schmidt, O.G., Boosting the Photoluminescence of Monolayer MoS2 on High-Density Nanodimer Arrays with Sub-10 nm Gap, Advanced Optical Materials 2 6 (2018), S. 1700984/1-6.

117) Hao, Q., Pang, J., Zhang, Y., Wang, J., Ma, L., Schmidt, O.G., Boosting the Photoluminescence of Monolayer MoS2 on High-Density Nanodimer Arrays with Sub-10 nm Gap, Advanced Optical Materials 2 6 (2018), S. 1700984/1-6.

118) Harnagea, L., Kumar, R., Singh, S., Wurmehl, S., Wolter, A.U.B., Buechner, B., Evolution of the magnetic order of Fe and Eu sublattices in $Eu_{1-x}Ca_xFe_2As_2$ (0 , Journal of Physics: Condensed Matter 41 30 (2018), S. 415601/1-8.

119) Harti, R.P., Strobl, M., Schäfer, R., Kardjilov, N., Tremsin, A.S., Gruenzweig, C., Dynamic volume magnetic domain wall imaging in grain oriented electrical steel at power frequencies with accumulative high-frame rate neutron dark-field imaging, Scientific Reports 8 (2018), S. 15754/1-7.

120) Hartwig, S., Schaefer, N., Schulze, M., Landsgesell, S., Abou-Ras, D., Blum, C.G.F., Wurmehl, S., Sokolowski, A., Buechner, B., Prokes, K., Inhomogeneities and superconductivity in poly-phase Fe-Se-Te systems, Physica B 531 (2018), S. 102-109.

121) He, R., Heyn, W., Thiel, F., Perez Rodriguez, N., Damm, C., Pohl, D., Rellinghaus, B., Reimann, C., Beier, M., Friedrich, J., Zhu, H., Ren, Z., Nielsch, K., Schierning, G., Thermoelectric properties of silicon and recycled silicon sawing waste, Journal of Materiomics (2018).

122) He, R., Schierning, G., Nielsch, K., Thermoelectric Devices: A Review of Devices, Architectures, and Contact Optimization, Advanced Materials Technologies, Advanced Materials Technologies 4 3 (2018), S. 1700256/1-17.

123) He, Y.K., Coey, J.M.D., Schaefer, R., Jiang, C.B., Determination of bulk domain structure and magnetization processes in bcc ferromagnetic alloys: Analysis of magnetostriction in $Fe_{83}Ga_{17}$, Physical Review Materials 1 2 (2018), S. 014412/1-11.

124) Heczko, O., Seiner, H., Stoklasova, P., Sedlak, P., Sermeus, J., Glorieux, C., Backen, A., Faehler, S., Landa, M., Temperature dependence of elastic properties in austenite and martensite of Ni-Mn-Ga epitaxial films, Acta Materialia 145 (2018), S. 298-305.

125) Heinze, L., Beltran-Rodriguez, R., Bastien, G., Wolter, A.U.B., Reehuis, M., Hoffmann, J.-U., Rule, K.C., Suellow, S., The magnetic properties of single-crystalline atacamite, $Cu_2Cl(OH)_3$, Physica B 536 (2018), S. 377-378.

126) Hentrich, R., Wolter, A.U.B., Zotos, X., Brenig, W., Nowak, D., Isaeva, A., Doert, T., Banerjee, A., Lampen-Kelley, P., Mandrus, D.G., Nagler, S.E., Sears, J., Kim, Y-J., Buechner, B., Hess, C., Unusual Phonon Heat Transport in alpha-$RuCl_3$: Strong Spin-Phonon Scattering and Field-Induced Spin Gap, Physical Review Letters 11 120 (2018), S. 117204/1-6.

127) Hettmann, D., Loeser, W., Blum, C.G.F., Wurmehl, S., Phase dynamics, structural, and magnetic properties of a Mn2.6Ga1-xSnx alloy series, Journal of Alloys and Compounds 748 (2018), S. 430-437.

128) Hossain, M., Telke, C., Abdkader, A., Sparing, M., Espenhahn, T., Hühne, R., Cherif, C., Beitelschmidet, M., Mathematical Modelling of Dynamic Yarn Path Considering the Balloon Control Ring and Yarn Elasticity in the Ring Spinning Process Based on the Superconducting Bearing Twisting Element, Fibres and Textiles in Eastern Europe 5 26 (2018), S. 32-40.

129) Hu, Y., Li, G., Chen, Z., The Importance of Contact Resistance in High-Mobility Organic Field-Effect Transistors Studied by Scanning Kelvin Probe Microscopy, IEEE Electron Device Letters 2 39 (2018), S. 276-279.

130) Hu, Y., Li, G., Peng, W., Chen, Z., Comparing the Gate Dependence of Contact Resistance and Channel Resistance in Organic Field-Effect Transistors for Understanding the Mobility Overestimation, IEEE Electron Device Letters 3 39 (2018), S. 421-423.

131) Huang, L., Wang, J., Chen, X., He, R., Shuai, J., Zhang, J., Zhang, Q., Ren, Z., The Effects of Excess Co on the Phase Composition and Thermoelectric Properties of Half-Heusler NbCoSb, Materials 5 11 (2018), S. 773.

132) Huang, S., Liu, L., Zheng, Y., Wang, Y., Kong, D., Zhang, Y., Shi, Y., Zhang, L., Schmidt, O.G., Yang, H.Y., Efficient Sodium Storage in Rolled-Up Amorphous Si Nanomembranes, Advanced Materials 20 30 (2018), S. 1706637/1-8.

133) Huang, S., Zhang, L., Liu, L., Li, J., Hu, H., Wang, J., Ding, F., Schmidt, O.G., Rationally engineered amorphous TiOx/Si/TiOx nanomembrane as an anode material for high energy lithium ion battery, Energy Storage Materials 12 (2018), S. 23-29.

134) Huebner , T., Martens, U., Walowski, J., Muenzenberg, M., Thomas, A., Reiss, G., Kuschel, T., Thermal conductivity of thin insulating films determined by tunnel magneto-Seebeck effect measurements and finite-element modeling, Journal of Physics D 22 51 (2018), S. 224006/1-5.

135) Hufenbach, J., Kochta, F., Wendrock, H., Voss, A., Giebeler, L., Oswald, S., Pilz, S., Kuehn, U., Lode, A., Gelinsky, M., Gebert, A., S and B microalloying of biodegradable Fe-30Mn-1C - Effects on microstructure, tensile properties, in vitro degradation and cytotoxicity, Materials and Design 142 (2018), S. 22-35.

136) Hugdal, H.G., Rex, S., Nogueira, F.S., Sudbo, A., Magnon-induced superconductivity in a topological insulator coupled to ferromagnetic and antiferromagnetic insulators, Physical Review B 19 97 (2018), S. 195438/1-9.

137) Huo, Z., Zhang, Y., Synthetic direct demodulation method and its applications in Insight-HXMT data analysis, Astronomy and Astrophysics 620 (2018), S. A151/1-10.

138) Iakovleva, M., Fuchs, S., Alfonsov, A., Grafe, H., Vogl, M., Aswartham, S., Wurmehl, S., Dey, T., Büchner, B., Vavilova, E., Kataev, V., Static and dynamic magnetism of the Ir-based double perovskites La_2BIrO_6 (B = Co, Zn) probed by magnetic resonance spectroscopies, Physical Review B 17 98 (2018), S. 174401/1-12.

139) Jayaraj, J., Thirathipviwat, P., Han, J., Gebert, A., Microstructure, mechanical and thermal oxidation behavior of AlNbTiZr high entropy alloy, Intermetallics 100 (2018), S. 9-19.

140) Jovari, P., Piarristeguy, A., Vaney, J.B., Kaban, I., Zitolo, A., Beuneu, B., Bednarcik, J., Delaizir, G., Monnier, J., Goncalves, A.P., Candolfi, C., Short range order of As40-xCuxTe60 glasses, Journal of Non-Crystalline Solids 481 (2018), S. 202-207.

141) Kaban, I., Agathopoulos, S., Valenza, F., Sommitsch, C., Schenk, J., Papaefthymiou, S., Karantzalis, A., EUROMAT 2017 Symposia on Processing, Journal of Materials Engineering and Performance 10 27 (2018), S. 4981-4982.

142) Kamashev, A.A., Leksin, P.V., Garif'yanov, N.N., Validov, A.A., Schumann, J., Kataev, V., Buechner, B., Garifullin, I.A., Superconducting spin-valve effect in a heterostructure containing the Heusler alloy as a ferromagnetic layer, Journal of Magnetism and Magnetic Materials 459 (2018), S. 7-11.

143) Kamashev, A.A., Validov, A.A., Schumann, J., Kataev, V., Buechner, B., Fominov, Y.V., Garifullin, I.A., Increasing the performance of a superconducting spin valve using a Heusler alloy , Beilstein Journal of Nanotechnology 9 (2018), S. 1764-1769.

144) Kamminga, M.E., Azhar, M., Zeisner, J., Maan, A.M.C., Buechner, B., Kataev, V., Baas, J., Blake, G.R., Mostovoy, M., Palstra, T.T.M., Spin-singlet formation in the spin-tetramer layered organic-inorganic hybrid $CH_3NH_3Cu_2Cl_5$, Physical Review Materials 6 2 (2018), S. 064405/1-7.

145) Kappenberger, R., Aswartham, S., Scaravaggi, F., Blum, C.G.F., Sturza, M.I., Wolter, A.U.B., Wurmehl, S., Buechner, B., Solid state single crystal growth of three-dimensional faceted LaFeAsO crystals, Journal of Crystal Growth 483 (2018), S. 9-15.

146) Kappenberger, R., Hammerath, F., Rousse, P., Afrassa, M.A., Haghighi, M.H., Kamusella, S., Prando, G., Lamura, G., Wolter, A.U.B., Moroni, M., Sanna, S., Carretta, P., Hess, C., Grafe, H.-J., Klauss, H.-H., Wurmehl, S., Buechner, B., Impact of concomitant Y and Mn substitution on superconductivity in $La_{1-y}Y_yFe_{1-x}Mn_xAsO_{0.89}F_{0.11}$, Physical Review B 5 97 (2018), S. 054522/1-11.

147) Karnaushenko, D., Karnaushenko, D., Grafe, H., Kataev, V., Büchner, B., Schmidt, O.G., Rolled-Up Self-Assembly of Compact Magnetic Inductors, Transformers, and Resonators, Advanced Electronic Materials 11 4 (2018), S. 1800298/1-7.

148) Kataeva, O., Metlushka, K., Ivshin, K., Kiiamov, A., Alfonsov, V., Khrizanforov, M., Budnikova, Y., Sinyashin, O., Krupskaya, Y., Kataev, V., Buechner, B., Knupfer, M., Electron Transfer and Unusual Chemical Transformations of F4-TCNQ in a Reaction with Mn-Phthalocyanine, European Journal of Inorganic Chemistry 28 (2018), S. 3344-3353.

149) Kauschke, V., Gebert, A., Calin, M., Eckert, J., Scheich, S., Heiss, C., Lips, K.S., Effects of new beta-type Ti-40Nb implant materials, brain-derived neurotrophic factor, acetylcholine and nicotine on human mesenchymal stem cells of osteoporotic and non osteoporotic donors, PLoS ONE 2 13 (2018), S. e0193468/1-18.

150) Khusnuriyalova, A.F., Petr, A., Gubaidullin, A.T., Sukhov, A.V., Morozov, V.I., Buechner, B., Kataev, V., Sinyashin, O.G., Yakhvarov, D.G., Electrochemical generation and observation by magnetic resonance of superparamagnetic cobalt nanoparticles, Electrochimica Acta 260 (2018), S. 324-329.

151) Kim, S.-Y., Lee, G.-Y., Park, G.-H., Kim, H.-A., Lee, A.-Y., Scudino, S., Prashanth, K.G., Kim, D.-H., Eckert, J., Lee, M.-H., High strength nanostructured Albased alloys through optimized processing of rapidly quenched amorphous precursors, Scientific Reports 8 (2018), S. 1090/1-12.

152) Kirbus, B., Brachmann, E., Hengst, C., Menzel, S., Additive manufacturing of 96 MHz surface acoustic wave devices by means of superfine inkjet printing, Smart Materials and Structures 7 27 (2018), S. 075042/1-9.

153) Klenovsky, P., Steindl, P., Aberl, J., Zallo, E., Trotta, R., Rastelli, A., Fromherz, T., Effect of second-order piezoelectricity on the excitonic structure of stress-tuned In(Ga)As/GaAs quantum dots, Physical Review B 24 97 (2018), S. 245314/1-6.

154) Koerner, J., Reiche, C.F., Buechner, B., Muehl, T., Theory and application of a novel co-resonant cantilever sensor, tm - Technisches Messen 6 85 (2018), S. 410-419.

155) Kovac, P., Husek, I., Kulich, M., Kovac, J., Melisek, T., Kopera, L., Perez, N., Haessler, W., Balog, M., Krizik, P., Berek, D., Lightweight MgB_2 wires with a high temperature aluminum sheath made of variable purity Al powder and Al_2O_3content, Superconductor Science and Technology 31 (2018), S. 085003/1-8.

156) Krahl, F., Giri, A., Tomko, J.A., Tynell, T., Hopkins, P.E., Karppinen, M., Thermal Conductivity Reduction at Inorganic-Organic Interfaces: From Regular Superlattices to Irregular Gradient Layer Sequences 11 5 (2018), S. 1701692/1-7.

157) Kravchuk, V.P., Sheka, D.D., Kakay, A., Volkov, O.M., Roessler, U.K., van den Brink, J., Makarov, D., Gaididei, Y., Multiplet of Skyrmion States on a Curvilinear Defect: Reconfigurable Skyrmion Lattices, Physical Review Letters 6 120 (2018), S. 067201/1-7.

158) Kravchuk, V.P., Sheka, D.D., Roessler, U.K., van den Brink, J., Gaididei, Y., Spin eigenmodes of magnetic skyrmions and the problem of the effective skyrmion mass, Physical Review B 6 97 (2018), S. 064403/1-10.

159) Krbal, M., Sopha, H., Pohl, D., Benes, L., Damm, C., Rellinghaus, B., Kupcik, J., Bezdicka, P., Subrt, J., Macak, J.M., Self-organized TiO_2 nanotubes grown on Ti substrates with different crystallographic preferential orientations: Local structure of TiO_2 nanotubes vS. photo-electrochemical response, Electrochimica Acta 264 (2018), S. 393-399.

160) Krehl, J., Guzzinati, G., Schultz, J., Potapov, P., Pohl, D., Martin, Jerome, Verbeeck, J., Fery, A., Buechner, B., Lubk, A., Spectral field mapping in plasmonic nanostructures with nanometer resolution, Nature Communications 9 (2018), S. 4207/1-6.

161) Krylov, D.S., Liu, F., Brandenburg, A., Spree, L., Bon, V., Kaskel, S., Wolter, A.U.B., Buechner, B., Avdoshenko, S.M., Popov, A.A., Magnetization relaxation in the single-ion magnet $DySc_2N@C_{-80}$: quantum tunneling, magnetic dilution, and unconventional temperature dependence, Physical Chemistry Chemical Physics 17 20 (2018), S. 11656--11672.

162) Kusch, M., Katukuri, V.M., Bogdanov, N.A., Buechner, B., Dey, T., Efremov, D.V., Hamann-Borrero, J.E., Kim, B.H., Krisch, M., Maljuk, A., Moretti Sala, M., Wurmehl, S., Aslan-Cansever, G., Sturza, M., Hozoi, L., van den Brink, J., Geck, J., Observation of heavy spin-orbit excitons propagating in a nonmagnetic background: The case of $(Ba,Sr)_2YIrO_6$, Physical Review B 6 97 (2018), S. 064421/1-6.

163) Kushnirenko, Y.S., Fedorov, A.V., Haubold, E., Thirupathaiah, S., Wolf, T., Aswartham, S., Morozov, I., Kim, T.K., Buechner, B., Borisenko, S.V., Three-dimensional superconducting gap in FeSe from angle-resolved photoemission spectroscopy, Physical Review B 18 97 (2018), S. 180501/1-6.

164) Kuvychko, I.V., Clikeman, T., Dubceac, C., Chen, Y.-S., Petrukhina, M.A., Strauss, S.H., Popov, A.A., Boltalina, O.V., Understanding Polyarene Trifluoromethylation with Hot CF3 Radicals using Corannulene, European Journal of Organic Chemistry 31 (2018), S. 4233-4245.

165) Kuzian, R.O., Klingeler, R., Lorenz, W.E.A., Wizent, N., Nishimoto, S., Nitzsche, U., Rosner, H., Milosavljevic, D., Hozoi, L., Yadav, R., Richter, J., Hauser, A., Geck, J., Hayn, R., Yushankhai, V., Siurakshina, L., Monney, C., Schmitt, T., Thar, J., Roth, G., Ito, T., Yamaguchi, H., Matsuda, M., Johnston, S., Malek, J., Drechsler, S.-L., Comment on 'Oxygen vacancy-induced magnetic moment in edge-sharing CuO_2 chains of Li_2CuO_2', New Journal of Physics 20 (2018), S. 058001/1-6.

166) Lai, K.T., Antonyshyn, I., Prots, Y., Valldor, M., Extended Chemical Flexibility of Cubic Anti-Perovskite Lithium Battery Cathode Materials, Inorganic Chemistry 21 57 (2018), S. 13296-13299.

167) Landers, J., Salamon, S., Keune, W., Gruner, M.E., Krautz, M., Zhao, J., Hu, M.Y., Toellner, T.S., Alp, E.E., Gutfleisch, O., Wende, H., Determining the vibrational entropy change in the giant magnetocaloric material LaFe11.6Si1.4 by nuclear resonant inelastic x-ray scattering, Physical Review B 2 98 (2018), S. 024417/1-14.

168) Leistenschneider, D., Zuerbes, K., Schneidermann, C., Graetz, S., Oswald, S., Wegner, K., Klemmed, B., Giebeler, L., Eychmueller, A., Borchardt, L., Mechanochemical Functionalization of Carbon Black at Room Temperature, C - Journal of Carbon Research 14 4 (2018), S. 1-9.

169) Leistner, K., Duschek, K., Zehner, J., Yang, M., Petr, A., Nielsch, K., Kavanagh, K.L., Role of Hydrogen Evolution during Epitaxial Electrodeposition of Fe on GaAs, Journal of The Electrochemical Society 4 165 (2018), S. H3076-H3079.

170) Leonov, A.O., Bogdanov, A.N., Crossover of skyrmion and helical modulations in noncentrosymmetricC ferromagnets, New Journal of Physics 20 (2018), S. 043017/1-7.

171) Leonov, A.O., Bogdanov, A.N., Inoue, K., Toggle-switch-like crossover between two types of isolated skyrmions within the conical phase of cubic helimagnets, Physical Review B 6 98 (2018), S. 060411/1-5.

172) Leonov, A.O., Inoue, K., Homogeneous and heterogeneous nucleation of skyrmions in thin layers of cubic helimagnets, Physical Review B 5 98 (2018), S. 054404/1-9.

173) Li, F.X., Hao, P.D., Yi, J.H., Sopu, D., Tan, J., Chong, X.Y., Eckert, J., Anisotropic elastic properties and phase stability of B2 and B19 CuZr structures under hydrostatic pressure, Intermetallics 98 (2018), S. 60-68.

174) Li, G., Garcia Fernandez, J., Lara Ramos, D., Barati, V., Perez Rodriguez, N., Soldatov, I., Reith, H., Schierning, G., Nielsch, K., Publisher Correction: Integrated microthermoelectric coolers with rapid response time and high device reliability, Nature Electronics 1 (2018), S. 605.

175) Li, G., Garcia Fernandez, J., Lara Ramos, D., Barati, V., Perez Rodriguez, N., Soldatov, I., Reith, H., Schierning, G., Nielsch, K., Integrated microthermoelectric coolers with rapid response time and high device reliability, Nature Electronics 1 (2018), S. 555–561.

176) Li, Y., Ding, F., Schmidt, O.G., Entangled-photons generation with quantum dots, Chinese Physics B 2 27 (2018), S. 020307/1-14.

177) Linseis, V., Hassan, Z.H., Reith, H., Garcia, J., Nielsch, K., Baumgart, H., Redel, E., Woias, P., Complete Thermoelectric Characterization of PEDOT:PSS Thin Films with a Novel ZT Test Chip Platform, Physica Status Solidi A 215 (2018), S. 1700930/1-5.

178) Linseis, V., Voelklein, F., Reith, H., Huehne, R., Schnatmann, L., Nielsch, K., Woias, P., Thickness and temperature dependent thermoelectric properties of Bi87Sb13 nanofilms measured with a novel measurement platform, Semiconductor Science and Technology 8 33 (2018), S. 085014/1-8.

179) Linseis, V., Voelklein, F., Reith, H., Nielsch, K., Woias, P., Advanced platform for the in-plane ZT measurement of thin films, Review of Scientific Instruments 1 89 (2018), S. 015110/1-9.

180) Linseis, V., Voelklein, F., Reith, H., Woias, P., Nielsch, K., Analytical Investigation of the Limits for the In-Plane Thermal Conductivity Measurement Using a Suspended Membrane Setup, Journal of Electronic Materials 6 47 (2018), S. 3203-3209.

181) Lipps, F, Arkenbout, A.H., Polyakov, A., Guenther, M., Salikhov, T., Vavilova, E., Klauss, H.-H., Buechner, B., Palstra, T.M., Kataev, V., Magnetic properties of the spin-1 chain compound $NiCl_3C_6H_5CH_2CH_2NH_3$, Low Temperature Physics 11 43 (2018), S. 1298-1304.

182) Liu, B., Yan, C., Si, W., Sun, X., Lu, X., Ansorge-Schumacher, M., Schmidt, O.G. , Ultralong-Discharge-Time Biobattery Based on Immobilized Enzymes in Bilayer Rolled-Up Enzymatic Nanomembranes, Small 13 14 (2018), S. 1704221/1-7.

183) Liu, X., Ma, T., Xu, Y., Sun, L., Zheng, L., Schmidt, O.G., Zhang, J., Rolled-up SnO2 nanomembranes: A new platform for efficient gas sensors, Sensors and Actuators B: Chemical 264 (2018), S. 92-99.

184) Liu, Z., Lou, R., Guo, P., Wang, Q., Sun, S., Li, C., Thirupathaiah, S., Fedorov, A., Shen, D., Liu, K, Lei, H., Wang, S., Experimental Observation of Dirac Nodal Links in Centrosymmetric Semimetal TiB_2, Physical Review X 3 8 (2018), S. 031044/1-7.

185) Liu, Z.-H., Yaresko, A.N., Li, Y., Evtushinsky, D.V., Dai, P.-C., Borisenko, S.V., Reduced electronic correlation effects in half substituted Ba(Fe1-xCox)(2)As-2, Applied Physics Letters 23 112 (2018), S. 232602/1-4.

186) Locus, R., Verboekend, D., d'Halluin, M., Dusselier, M., Liao, Y., Nuttens, N., Jaumann, T., Oswald, S., Mafra, L., Giebeler, L., Sels, B., Synthetic and Catalytic Potential of Amorphous Mesoporous Aluminosilicates Prepared by Postsynthetic Aluminations of Silica in Aqueous Media, ChemCatChem 6 10 (2018), S. 1385-1397.

187) Lode, A., Heiss, C., Knapp, G., Thomas, J., Nies, B., Gelinsky, M., Schumacher, M., Strontium-modified premixed calcium phosphate cements for the therapy of osteoporotic bone defects, Acta Biomaterialia 65 (2018), S. 475-485.

188) Loret, B., Gallais, Y., Cazayous, M., Zhong, R.D., Schneeloch, J., Gu, G.D., Fedorov, A., Kim, T.K., Borisenko, S.V., Sacuto, A., Raman and ARPES combined study on the connection between the existence of the pseudogap and the topology of the Fermi surface in Bi2Sr2CaCu2O8+delta, Physical Review B 17 97 (2018), S. 174521/1-6.

189) Loudon, J.C., Leonov, A.O., Bogdanov, A.N., Hatnean, M.C., Balakrishnan, G., Direct observation of attractive skyrmions and skyrmion clusters in the cubic helimagnet $Cu2OSeO_3$, Physical Review B 13 97 (2018), S. 134403/1-5.

190) Lu, T., Chen, W., Xu, W., Wang, P., Mao, M., Liu, Y., Fu, Z., The effects of Cr particles addition on the aging behavior and mechanical properties of SiC_p/7075Al composites, Materials Characterization 136 (2018), S. 264-271.

191) Lu, T., Scudino, S., Chen, W., Wang, P., Li, D., Mao, M., Kang, L., Liu, Y., , Fu, Z., The influence of nanocrystalline $CoNiFeAl_{0.4}Ti_{0.6}Cr_{0.5}$ high-entropy alloy particles addition on microstructure and mechanical properties of SiCp/7075Al composites, Materials Science and Engineering A 726 (2018), S. 126-136.

192) Lu, T., Scudino, S., Chen, W., Wang, P., Li, D., Mao, M., Kang, L., Liu, Y., Fu, Z., The influence of nanocrystalline CoNiFeAl0.4Ti0.6Cr0.5 high-entropy alloy particles addition on microstructure and mechanical properties of SiCp/7075Al composites, Materials Science and Engineering A-Structural Materials Properties Microstructure and Processing 726 (2018), S. 126-136.

193) Lu, T.W., Chen, W.P., Wang, P., Mao, M.D., Liu, Y.X., Fu, Z.Q., Enhanced mechanical properties and thermo-physical properties of 7075Al hybrid composites reinforced by the mixture of Cr particles and SiC_p, Journal of Alloys and Compounds 735 (2018), S. 1137-1144.

194) Lubenchenko, A.V., Batrakov, A.A., Ivanov, D.A., Lubenchenko, O.I., Lashkov, I.A., Pavolotsky, A.B., Schleicher, B., Albert, N., Nielsch, K., Air-Oxidation of Nb Nano-Films, Semiconductors 5 52 (2018), S. 678-682.

195) Madani, A., Naz, E.S.G., Harazim, S., Kleinert, M., Yin, Y., Ma, L., Schmidt, O.G., Multiplexing and tuning of a double set of resonant modes in optical microtube cavities monolithically integrated on a photonic chip, Optics Letters 19 43 (2018), S. 4703-4706.

196) Madian, M., Eychmueller, A., Giebeler, L., Current Advances in TiO_2-Based Nanostructure Electrodes for High Performance Lithium Ion Batteries, Batteries 1 4 (2018), S. 7/1-36.

197) Majumder, M., Manna, R.S., Simutis, G., Orain, J.C., Dey, T., Freund, F., Jesche, A., Khasanov, R., Biswas, P.K., Bykova, E., Dubrovinskaia, N., Dubrovinsky, L.S., Yadav, R., Hozoi, L., Nishimoto, S., Tsirlin, A.A., Gegenwart, P., Breakdown of Magnetic Order in the Pressurized Kitaev Iridate beta-Li_2IrO_3, Physical Review Letters 23 120 (2018), S. 237202/1-7.

198) Maletti, S., Giebeler, L., Oswald, S., Tsirlin, A.A., Senyshyn, A., Michaelis, A., Mikhailova, D., Irreversible Made Reversible: Increasing the Electrochemical Capacity by Understanding the Structural Transformations of $Na_xCo_{0.5}Ti_{0.5}O_2$, ACS Applied Materials and Interfaces 42 10 (2018), S. 36108-36119.

199) Maletti, S., Sarapulova, A., Tsirlin, A.A., Oswald, S., Fauth, F., Giebeler, L., Bramnik, N.N., Ehrenberg, H., Mikhailova, D., Electrochemical behavior of LiV_3O_8 positive electrode in hybrid Li,Na-ion batteries, Journal of Power Sources 373 (2018), S. 1-10.

200) Manna, K., Muechler, L., Kao, T.-H., Stinshoff, R., Zhang, Y., Gooth, J., Kumar, N., Kreiner, G., Koepernik, K., Car, R., Kübler, J., Fecher, G.H., Shekhar, C., Sun, Y., Felser, C., From Colossal to Zero: Controlling the Anomalous HallEffect in Magnetic Heusler Compounds via Berry Curvature Design, Physical Review X 4 8 (2018), S. 041045/1-10.

201) Materne, P., Bi, W., Alp, E.E., Zhao, J., Hu, M.Y., Jesche, A., Geibel, C., Kappenberger, R., Aswartham, S., Wurmehl, S., Büchner, B., Zhang, D., Goltz, T., Spehling, J., Klauss, H.-H., Suppression of the magnetic order in CeFeAsO: Nonequivalence of hydrostatic and in-plane chemical pressure, Physical Review B 1 98 (2018), S. 014517/1-11.

202) Materne, P., Bi, W., Zhao, J., Hu, M.Y., Kappenberger, R., Wurmehl, S., Aswartham, S., Büchner, B., Alp, E.E., Microscopic phase diagram of LaFeAsO single crystals under pressure, Physical Review B 17 98 (2018), S. 174510/1-6.

203) Mattern, N., Han, J.H., Nowak, R., Fabrichnaya, O., Kaban, I., Shuleshova, O., Sobczak, N., Experimental and thermodynamic assessment of the Gd-Ti-Zr phase diagram, Calphad 61 (2018), S. 237-245.

204) Mazalski, P., Kuswik, P., Sveklo, I., Soldatov, I., McCord, J., Schäfer, R., Wawro, A., Maziewski, A., Modification of magnetic properties of Pt/Co/Pt trilayers driven by nanosecond pulses of extreme ultraviolet irradiation, Journal of Magnetism and Magnetic Materials (2018).

205) Medina-Sanchez, M., Magdanz, V., Guix, M., Fomin, V.M., Schmidt, O.G., Swimming Microrobots: Soft, Reconfigurable, and Smart, Advanced Functional Materials 25 28 (2018), S. 1707228/1-27.

206) Medina-Sanchez, M., Xu, H., Schmidt, O.G., Micro- and nano-motors: the new generation of drug carriers, Therapeutic Delivery 4 9 (2018), S. 303-316.

207) Meinero, M., Caglieris, F., Lamura, G., Pallecchi, I, Jost, A., Zeitler, U., Ishida, S., Eisaki, H., Putti, M., Unusual thermoelectric properties of $BaFe_2As_2$ in high magnetic fields, Physical Review B 15 98 (2018), S. 155116/1-8.

208) Mendes, R.G., Wrobel, P.S., Bachmatiuk, A., Sun, J., Gemming, T., Liu, Z., Rümmeli, M., Carbon Nanostructures as a Multi-Functional Platform for Sensing Applications, Chemosensors 4 6 (2018), S. 60/1-28.

209) Mikhailova, D., Giebeler, L., Maletti, S., Oswald, S., Sarapulova, A., Indris, S., Hu, Z., Bednarcik, J., Valldor, M., Operando Studies of Antiperovskite Lithium Battery Cathode Material (Li_2Fe)SO, ACS Applied Energy Materials 11 1 (2018), S. 6593-6599.

210) Moo, J.G.S., Omar, A., Jaumann, T., Oswald, S., Balach, J., Maletti, S., Giebeler, L., One-Pot Synthesis of Graphene-Sulfur Composites for Li-S Batteries: Influence of Sulfur Precursors, C - Journal of Carbon Research 2 4 (2018), S. 1-17.

211) Morawski, A., Cetner, T., Gajda, D., Zaleski, A.J., Haessler, W., Nenkov, K., Rindfleisch, M.A., Tomsic, M., Przyslupski, P., MgB_2 wire diameter reduction by hot isostatic pressing - a route for enhanced critical current density, Superconductor Science and Technology 31 (2018), S. 075008/1-8.

212) Morrow, R., McGuire, M.A., Yan, J., Woodward, P.M., The Crystal Structure and Magnetic Behavior of Quinary Osmate and Ruthenate Double Perovskites LaABB′ O-6 (A = Ca, Sr; B = Co, Ni; B′ = Ru, Os), Inorganic Chemistry 6 57 (2018), S. 2989-3001.

213) Mulone, A., Nicolenco, A., Hoffmann, V., Klement, U., Tsyntsaru, N., Cesiulis, H., In-depth characterization of as-deposited and annealed Fe-W coatings electrodeposited from glycolate-citrate plating bath, Electrochimica Acta 261 (2018), S. 167-177.

214) Naidyuk, Y, Kvitnitskaya, O., Bashlakov, D., Aswartham, S., Morozov, I., Chernyavskii, I., Fuchs, G., Drechsler, S.-L., Huehne, R., Nielsch, K., Buechner, B., Efremov, D., Surface superconductivity in the Weyl semimetal $MoTe_2$ detected by point contact spectroscopy, 2D Materials 4 5 (2018), S. 045014/1-8.

215) Nakayama, K., Wang, Z., Trang, C.X., Souma, S., Rienks, E.D.L., Takahashi, T., Ando, Y., Sato, T., Observation of Dirac-like energy band and unusual spectral line shape in quasi-one-dimensional superconductor Tl2Mo6Se6, Physical Review B 14 98 (2018), S. 140502/1-5.

216) Narayanan, N., Senyshyn, A., Mikhailova, D., Faske, T., Lu, T., Liu, Z., Weise, B., Ehrenberg, H., Mole, R. A., Hutchison, W. D., Fuess, H., McIntyre, G. J., Liu, Y., Yu, D., Magnetic structure and spin correlations in magnetoelectric honeycomb $Mn_4Ta_2O_9$, Physical Review B 13 98 (2018), S. 134438/1-15.

217) Naumann, M., Knupfer, M., Complex momentum behavior of electronic excitations in beta-CuPc, The Journal of Chemical Physics 8 149 (2018), S. 084704/1-5.

218) Nayak, J., Kumar, N., Wu, S.-C., Shekkar, C., Fink, J., Rienks, E.D.L., Fecher, G.H., Sun, Y., Felser, C., Electronic properties of topological insulator candidate CaAgAs, Journal of Physics: Condensed Matter 4 30 (2018), S. 045501/1-5.

219) Naz, E.S.G., Fulga, I.C., Ma, L., Schmidt, O.G., van den Brink, J., Topological phase transition in a stretchable photonic crystal, Physical Review A 3 98 (2018), S. 033830/1-9.

220) Nekouie, V., Doak, S., Roya, A., Kuehn, U. , Silberschmidt, V.V., Experimental studies of shear bands in Zr-Cu metallic glass, Journal of Non-Crystalline Solids 484 (2018), S. 40-48.

221) Neu, V., Vock, S., Sturm, T., Schultz, L., Epitaxial hard magnetic $SmCo_5$ MFM tips – a new approach to advanced magnetic force microscopy imaging, Nanoscale 35 10 (2018), S. 16881-16886.

222) Niemann, A.C., Gooth, J., Felser, C., Nielsch, K., Universum im Kristall: Quantenanomalien in Weyl-Halbmetallen, Physik in unserer Zeit 49 4 (2018), S. 168-175.

223) Nogueira, F.S., Eremin, I., Katmis, F., Moodera, J.S., van den Brink, J., Kravchuk, V.P., Fluctuation-induced Neel and Bloch skyrmions at topological insulator surfaces, Physical Review B 6 98 (2018), S. 060401/1-6.

224) Nogueira, F.S., Nussinov, Z., van den Brink, J., Fractional Angular Momentum at Topological Insulator Interfaces, Physical Review B 22 121 (2018), S. 227001/1-6.

225) Ok, J.M., Baek, S.-H., Efremov, D., V, Kappenberger, R., Aswartham, S., Kim, J. S., van den Brink, J., Buechner, B., Nematicity and magnetism in LaFeAsO single crystals probed by ^{75}As nuclear magnetic resonance, Physical Review B 18 97 (2018), S. 180405/1-5.

226) Oka, T., Takeda, A., Sasaki, S., Ogawa, J., Fukui, S., Sato, T., Scheiter, J., Haessler, W., Katsuki, J., Miura, A., Yokoyama, K., Magnetic Flux Invasion and Field-Capturing in Pulsed-Field Magnetization for Layered MgB_2 Bulk Magnets, IEEE Transactions on Applied Superconductivity 4 28 (2018), S. 6800504/1-4.

227) Okulov, I., Boenisch, M., Okulov, A.V., Volegov, A.S., Attar, H., Ehtemam-Haghighi, S., Calin, M., Wang, Z., Hohenwarter, A., Kaban, I., Prashanth, K.G., Eckert, J., Phase formation, microstructure and deformation behavior of heavily alloyed TiNb- and TiV-based titanium alloys, Materials Science and Engineering A 733 (2018), S. 80-86.

228) Okulov, I.V., Okulov, A.V, Soldatov, I.V, Luthringer, B., Willumeit-Roemer, R., Wada, T., Kato, H., Weissmueller, J., Markmann, J., Open porous dealloying-based biomaterials as a novel biomaterial platform, Materials Science and Engineering C-Materials for Biological Applications 88 (2018), S. 95-103.

229) Omar, A., Boerrnert, F., Haft, M., Hampel, S., Loeser, W., Buechner, B., Wurmehl, S., Crystal growth of off-stoichiometric $Co_2Cr_{1-x}Al_{1+x}$ Heusler compounds: Avoiding the solid state miscibility gap, Journal of Crystal Growth 498 (2018), S. 103-108.

230) Oswald, S., Thoss, F., Zier, M., Hoffmann, M., Jaumann, T., Herklotz, M., Nikolowski, K., Scheiba, F., Kohl, M., Giebeler, L., Mikhailova, D., Ehrenberg, H., Binding Energy Referencing for XPS in Alkali Metal-Based Battery Materials Research (II): Application to Complex Composite Electrodes, Batteries 3 4 (2018), S. 36/1-19.

231) Otalora, J.A., Kakay, A., Lindner, J., Schultheiss, H., Thomas, A., Fassbender, J., Nielsch, K., Frequency linewidth and decay length of spin waves in curved magnetic membranes, Physical Review B 1 98 (2018), S. 014403/1-9.

232) Paerschke, E.M., Ray, R., Influence of the multiplet structure on the photoemission spectra of spin-orbit driven Mott insulators: Application to Sr_2IrO_4, Physical Review B 6 98 (2018), S. 064422/1-14.

233) Pagenkopf, F., Mueller, E., Knupfer, M., Electronic excitations of manganese phthalocyanine molecules, The Journal of Chemical Physics 4 148 (2018), S. 044701/1-5.

234) Pahlke, P., Sieger, M., Ottolinger, R., Lao, M., Eisterer, M., Meledin, A., Van Tendeloo, G., Haenisch, J., Holzapfel, B., Schultz, L., Nielsch, K., Huehne, R., Influence of artificial pinning centers on structural and superconducting properties of thick YBCO films on ABAD-YSZ templates, Superconductor Science and Technology 4 31 (2018), S. 044007/1-9.

235) Pandey, S., Scopigno, N., Gentile, P., Cuoco, M., Ortix, C., Topological quantum pump in serpentine-shaped semiconducting narrow channels, Physical Review B 24 97 (2018), S. 241103/1-5.

236) Panes-Ruiz, L.A., Shaygan, M., Fu, Y.X., Liu, Y., Khavrus, V., Oswald, S., Gemming, T., Baraban, L., Bezugly, V., Cuniberti, G., Toward Highly Sensitive and Energy Efficient Ammonia Gas Detection with Modified Single-Walled Carbon Nanotubes at Room Temperature, ACS Sensors 1 3 (2018), S. 79-86.

237) Pang, J., Bachmatiuk, A., Yin, Y., Trzebicka, B., Zhao, L., Fu, L., Mendes, R.G., Gemming, T., Liu, Z., Ruemmeli, M.H., Applications of Phosphorene and Black Phosphorus in Energy Conversion and Storage Devices, Advanced Energy Materials 8 8 (2018), S. 1702093/1-43.

238) Park, G.H., Nielsch, K., Thomas, A., 2D Transition Metal Dichalcogenide Thin Films Obtained by Chemical Gas Phase Deposition Techniques, Advanced Materials Interfaces online first (2018), S. 1800688/1-31.

239) Parsi Sreenivas, V.V., Winkler, A., Harazim, S., Schmidt, O.G., Ultraviolet transmittance of SU-8 photoresist and importance in multi-wavelength photolithography, Journal of Vacuum Science and Technology B 5 36 (2018), S. 051601/1-5.

240) Paschalidou, E.M., Fiore, G., Xue, Y., Scaglione, F., Celegato, F., Gebert, A., Oswald, S., Wolff, U., Rizzi, P., Battezzati, L., Comparing selective corrosion of Au-based amorphous, partially amorphous, and devitrified alloys, Journal of Alloys and Compounds 745 (2018), S. 212-216.

241) Pauly, S., Wang, P., Kuehn, U., Kosiba, K., Experimental determination of cooling rates in selectively laser-melted eutectic Al-33Cu, Additive Manufacturing 22 (2018), S. 753-757.

242) Pavlov, A.I., van den Brink, J., Efremov, D.V., Phonon-mediated Casimir interaction between finite-mass impurities, Physical Review B 16 98 (2018), S. 161410/1-5.

243) Pawlik, A.-S., Aswartham, S., Morozov, I., Knupfer, M., Buechner, B., Efremov, D.V., Koitzsch, A., Thickness dependent electronic structure of exfoliated mono- and few-layer 1T '-$MoTe_2$, Physical Review Materials 10 2 (2018), S. 104004/1-8.

244) Perucchi, A., Di Pietro, P., Lupi, S., Sopracase, R., Tebano, A., Giovannetti, G., Petocchi, F., Capone, M., Di Castro, D., Electrodynamic properties of an artificial heterostructured superconducting cuprate, Physical Review B 4 97 (2018), S. 045114/1-5.

245) Pfeiffer, M., Atkinson, P., Rastelli, A., Schmidt, O.G., Giessen, H., Lippitz, M., Lindfors, K., Coupling a single solid-state quantum emitter to an array of resonant plasmonic antennas, Scientific Reports 8 (2018), S. 3415/1-6.

246) Philippi, S., Schloerb, H., Mukherjee, D., Buechner, B., Muehl, T., Quasi-periodic magnetization reversal of ferromagnetic nanoparticles induced by torsional oscillations in static magnetic fields, Nanotechnology 40 29 (2018), S. 405503/2-11.
247) Pilz, S., Gebert, A., Voss, A., Oswald, S., Goettlicher, M., Hempel, U., Eckert, J., Rohnke, M., Janek, J., Calin, M., Metal release and cell biological compatibility of beta-type Ti-40Nb containing indium, Journal of Biomedical Materials Research B 5 106 (2018), S. 1686-1697.
248) Pilz, S., Geissler, D., Calin, M., Eckert, J., Zimmermann, M., Freudenberger, J., Gebert, A., Thermomechanical processing of In-containing ß-type Ti-Nb alloys, Journal of the Mechanical Behavior of Biomedical Materials 79 (2018), S. 283-291.
249) Pohl, D., Loeffler, S., Schneider, S., Tiemeijer, P., Lazar, S., Nielsch, K., Rellinghaus, B., The Role of Spatial Coherence for the Creation of Atom Size Electron Vortex Beams , Microscopy and Microanalysis S1 24 (2018), S. 920-921.
250) Popov, A.A., Redox-active metal–metal bonds between lanthanides in dimetallofullerenes, Current Opinion in Electrochemistry 8 (2018), S. 73-80.
251) Potapov, P., Longo, P., Lubk, A., A Novel Method for Automatic Determination of the Number of Meaningful Components in the PCA Analysis of Spectrum-Images, Microscopy and Microanalysis S1 24 (2018), S. 572-573.
252) Potapov, P., Meyer, M., Lubk, A., Pohl, D., Schultz, J., König, T.A.F., Fery, A., Surface Plasmon Modes in Long Chains of Au Nanoparticle, Microscopy and Microanalysis S1 24 (2018), S. 1748-1749.
253) Probst, A.-C., Stollenwerk, M., Emmerich, F., Buettner, A., Zeising, S., Stadtmueller, J., Riethmueller, F., Stehlikova, V., Wen, M., Proserpio, L., Damm, C., Rellinghaus, B., Doehring, T., Influence of sputtering pressure on the nanostructure and the X-ray reflectivity of iridium coatings, Surface and Coatings Technology 343 (2018), S. 101-107.
254) Pshenay-Severin, D.A., Ivanov, Y.V., Burkov, A.T., Novikov, S.V., Zaitsev, V.K., Reith, H., Electronic Structure and Thermoelectric Properties of Transition Metal Monosilicides, Journal of Electronic Materials 6 47 (2018), S. 3277-3281.
255) Puszkiel, J., Castro Riglo, M.V., Ramallo-López. J.M., Mizrahi, M., Gemming, T., Pistidda, C., Larochette, P.A., von Colbe, J.B., Klassen, T., Dornheim, M., Gennari, F., New Insight on the Hydrogen Absorption Evolution of the Mg-Fe-H System under Equilibrium Conditions, Metals 11 8 (2018), S. 967/1-13.
256) Pylypovskyi, O.V., Makarov, D., Kravchuk, V.P., Gaididei, Y., Saxena, A., Sheka, D.D., Engineered Chiral Skyrmion and Skyrmionium States by the Gradient of Curvature, Physical Review Applied 10 (2018), S. 064057/1-10.
257) Quereda, J., Ghiasi, T.S., You, J.-S., van den Brink, J., van Wees, B.J., van der Wal, C.H., Symmetry regimes for circular photocurrents in monolayer $MoSe_2$, Nature Communications 9 (2018), S. 3346/1-8.
258) Qureshi, N., Diaz, M. T. Fernandez, Chapon, L. C., Senyshyn, A., Schweika, W., Valldor, M., Magnetic structure of the swedenborgite $CaBa(Co_3Fe)O_{-7}$ derived by unpolarized neutron diffraction and spherical neutron polarimetry, Physical ReviewB 6 97 (2018), S. 064404/1-9.
259) Reck, A., Pilz, S., Thormann, U., Alt, V., Gebert, A., Calin, M., Heiss, C., Zimmermann, M., Effects of thermomechanical history and environment on the fatigue behavior of (ß)-Ti-Nb implant alloys, MATEC Web of Conference 165 (2018), S. 06001/1-8.
260) Reichlova, H., Schlitz, R., Beckert, S., Swekis, P., Markou, A., Chen, Y.-C., Kriegner, D., Fabretti, S., Park, G.H., Niemann, A., Sudheendra, S., Thomas, A., Nielsch, K., Felser, C., Goennenwein, S., Large anomalous Nernst effect in thin films of the Weyl semimetal Co2MnGa, Applied Physics Letters 21 113 (2018), S. 212405/1-5.
261) Reim, J.D., Rosen, E., Zaharko, O., Mostovoy, M., Robert, J., Valldor, M., Schweika, W., Neutron diffraction study and theoretical analysis of the antiferromagnetic order and the diffuse scattering in the layered kagome system $CaBaCo_2Fe_2O_7$, Physical Review B 14 97 (2018), S. 144402/1-11.
262) Reinhold, R., Mikhailova, D., Gemming, T., Missyul, A. B., Nowka, C., Kaskel, S., Giebeler, L., Silicon monophosphide as a possible lithium battery anode material, Journal of Materials Chemistry A 41 6 (2018), S. 19974-19978.
263) Reinhold, R., Stoeck, U., Grafe, H.-J., Mikhailova, D., Jaumann, T., Oswald, S., Kaskel, S., Giebeler, L., Surface and Electrochemical Studies on Silicon Diphosphide as Easyto-Handle Anode Material for Lithium-Based Batteries - the Phosphorus Path, ACS Applied Materials and Interfaces 8 10 (2018), S. 7096-7106.
264) Reja, S., Nishimoto, S., Phase diagram of the Hubbard-Holstein model on a four-leg tube system at quarter filling, Physical Review B 24 97 (2018), S. 245108/1-4.
265) Ren, W., Zhu, H., Zhu, Q., Saparamadu, U., He, R., Liu, Z., Mao, J., Wang, C., Nielsch, K., Wang, Z., Ren, Z., Ultrahigh Power Factor in Thermoelectric System $Nb_{0.95}M_{0.05}FeSb$ (M = Hf, Zr, and Ti), Advanced Science 7 5 (2018), S. 1800278/1-7.
266) Rhein, F., Helbig, T., Neu, V., Krispin, M., Gutfleisch, O., In-situ magnetic force microscopy analysis of magnetization and demagnetization behavior in Al^{3+} substituted Sr-hexaferrite, Acta Materialia 146 (2018), S. 85-96.
267) Richter, M., Hahn, S., Dmitrieva, E., Rominger, F., Popov, A., Bunz, U.H.F., Feng, X., Berger, R., Helical Ullazine-Quinoxaline-Based Polycyclic Aromatic Hydrocarbons, Chemistry - A European Journal 24 (2018), S. 1-9.
268) Rieder, M.-T., Sieberer, L.M., Fischer, M.H., Fulga, I.C., Localization Counteracts Decoherence in Noisy Floquet Topological Chains, Physical Review Letters 21 120 (2018), S. 216801/1-5.

269) Rizzo, F., Augieri, A., Kursumovic, A., Bianchetti, M., L. Opherden, L., Sieger, M., Huehne, R., Haenisch, J., Meledin, A., Van Tendeloo, G., MacManus-Driscollb, J.L., Celentanoa, G., Pushing the limits of applicability of REBCO coated conductor films through fine chemical tuning and nanoengineering of inclusions, Nanoscale 17 10 (2018), S. 8187-8195.

270) Rosova, A., Husek, I., Kulich, M., Melisek, T., Kovac, P., Dobrocka, E., Kopera, L., Scheiter, J., Haessler, W., Microstructure of undoped and C-doped MgB_2 wires prepared by an internal magnesium diffusion technique using different B powders, Journal of Alloys and Compounds 764 (2018), S. 437-445.

271) Roth, R., Guo, E.-J., Rafique, M., Doerr, K., Field-Polarity-Dependent Domain Growth in Epitaxial $BaTiO_3$ Films, Physica Status Solidi B-Basic Solid State Physics 7 255 (2018), S. 1700486/1-5.

272) Ruemmeli, M.H., Pan, Y., Zhao, L., Gao, J., Ta, H.Q., Martinez, I.G., Mendes, R.G., Gemming, T., Fu, L., Bachmatiuk, A., Liu, Z., In Situ Room Temperature Electron-Beam Driven Graphene Growth from Hydrocarbon Contamination in a Transmission Electron Microscope, Materials 6 11 (2018), S. 896/1-10.

273) Rümmeli, M., Ta, H.Q., Mendes, R., Gonzalez Martinez, I.G., Zhao, L., Gao, J., Fu, L., Gemming, T., Bachmatiuk, A., Liu, Z., New Frontiers in Electron-Beam Driven Chemistry in and around Graphene, Advanced Materials (2018), S. 1800715/1-22.

274) S. Agrestini, C.-Y. Kuo, K. Chen, Y. Utsumi, D. Mikhailova, A. Rogalev, F. Wilhelm, T. Förster, A. Matsumoto, T. Takayama, H. Takagi, M. W. Haverkort, Z. Hu, and L. H. Tjeng, Probing the $J_{eff} = 0$ ground state and the Van Vleck paramagnetism of the Ir^{5+} ions in layered $Sr_2Co_{0.5}Ir_{0.5}O_4$, Physical Review B 21 97 (2018), S. 214436/1-8.

275) Sablowski, J., Linnemann, J., Hempel, S., Hoffmann, V., Unz, S., Beckmann, M., Giebeler, L., Electrodeposited metal-organic framework films as self-assembled hierarchically superstructured supports for stable omniphobic surface coatings, Scientific Reports 8 (2018), S. 15400/1-11.

276) Salazar, C., Baumann, D., Haenke, T., Scheffler, M., Kuehne, T., Kaiser, M., Voigtlaender, R., Lindackers, D., Buechner, B., Hess, C., An ultra-high vacuum scanning tunneling microscope operating at sub-Kelvin temperatures and high magnetic fields for spin-resolved measurements, Review of Scientific Instruments 6 89 (2018), S. 065104/1-11.

277) Salem, M.S., Tejo, F., Zierold, R., Sergelius, P., Moreno, J.M.M., Goerlitz, D., Nielsch, K., Escrig, J., Composition and diameter modulation of magnetic nanowire arrays fabricated by a novel approach, Nanotechnology 6 29 (2018), S. 065602/1-8.

278) Salman, O.O., Funk, A., Waske, A., Eckert, J., Scudino, S., Additive Manufacturing of a 316L Steel Matrix Composite Reinforced with CeO_2 Particles: Process Optimization by Adjusting the Laser Scanning Speed, Technologies 25 6 (2018), S. 6010025/1-10.

279) San, L.K., Spisak, S.N., Dubceac, C., Deng, S.H.M., Kuvychko, I.V., Petrukhina, M.A., Wang, X.-B., Popov, A.A., Strauss, S.H., Boltalina, O.V., Experimental and DFT Studies of the Electron-Withdrawing Ability of Perfluoroalkyl (RF)Groups: Electron Affinities of PAH(RF)n Increase Significantly with Increasing RF Chain Length, Chemistry - A European Journal 24 (2018), S. 1441-1447.

280) Sánchez-Barriga, J., Ovsyannikov, R., Fink, J., Strong spin dependence of correlation effects in Ni due to Stoner excitations 26 121 (2018), S. 267201/1-6.

281) Sánchez-Barriga, J., Ovsyannikov, R., Fink, J., Strong Spin Dependence of Correlation Effects in Ni Due to Stoner Excitations, Physical Review Letters 121 (2018), S. 267201/1-6.

282) Sarac, B., Gammer, C., Deng, L., Park, E., Yokoyama, Y., Stoica, M., Eckert, J., Elastostatic reversibility in thermally formed bulk metallic glasses: nanobeam diffraction fluctuation electron microscopy, Nanoscale 3 10 (2018), S. 1081-1089.

283) Schaarschuch, R., Oertel, C.-G., Cao, G., Freudenberger, J., Brokmeier, H.-G., Skrotzki, W., Deformation mechanisms of nil temperature ductile polycrystalline B2 intermetallic compound YAg, Acta Materialia 151 (2018).

284) Schäfer, R., Soldatov, I., Arai, S., Power Frequency Domain Imaging on Goss-Textured Electrical Steel, Journal of Magnetism and Magnetic Materials online first (2018), S. 221-235.

285) Scharnweber, J., Chekhonin, P., Oertel, C.-G., Romberg, J., Freudenberger, J., Jaschinski, J., Skrotzki, W., Microstructure, Texture, and Mechanical Properties of Laminar Metal Composites Produced by Accumulative Roll Bonding, Advanced Engineering Materials online first (2018), S. 1800210/1-20.

286) Schierning, G., Bring on the heat, Nature Energy 3 (2018), S. 92-93.

287) Schlesier, C., Spree, L., Kostanyan, A., Westerstroem, R., Brandenburg, A., Wolter, A.U.B., Yang, S., Greber, T., Popov, A.A., Strong carbon cage influence on the single molecule magnetism in Dy-Sc nitride clusterfullerenes, Chemical Communications 70 54 (2018), S. 9730-9733.

288) Schliebe, C., Noll, J., Scharf, S., Gemming, T., Seifert, A., Spange, S., Lehmann, D., Zahn, D.R.T., Fiedler, B., Friedrich, J., Blaudeck, T., Lang, H., Nitrogen-containing porous carbon materials by twin polymerization, Colloid and Polymer Science 3 296 (2018), S. 413-426.

289) Schlitz, R., Amusan, A.A., Lammel, M., Schlicht, S., Tyne, T., Bachmann, J., Woltersdorf, G., Nielsch, K., Goennenwein, S.T.B., Thomas, A., Spin-hall-active platinum thin films grown via atomic layer deposition, Applied Physics Letters 24 112 (2018), S. 242403/1-4.

290) Schlitz, R., Kosub, T., Thomas, A., Fabretti, S., Nielsch, K., Makarov, D., Goennenwein, S.T.B., Evolution of the spin hall magnetoresistance in Cr_2O_3/Pt bilayers close to the Neel temperature, Applied Physics Letters 13 112 (2018).

291) Schnaubelt, L., Petzold, H., Dmitrieva, E., Rosenkranz, M., Lang, H., A solvent- and temperature-dependent intramolecular equilibrium of diamagnetic and paramagnetic states in Co complexes bearing triaryl amines, Dalton Transactions (2018), S. 1-10.

292) Schneider, S., Negi, D., Stolt, M.J., Jin, S., Spiegelberg, J., Pohl, D., Rellinghaus, B., Goennenwein, S., Nielsch, K., Rusz, J., Simple method for optimization of classical electron magnetic circular dichroism measurements: The role of structure factor and extinction distances, Physical Review Materials 11 2 (2018), S. 113801/1-9.

293) Schneider, S., Wolf, D., Stolt, M.J., Jin, S., Pohl, D., Rellinghaus, B., Schmidt, M., Büchner, B., Goennenwein, S., Nielsch, K., Lubk, A., Towards Induction Mapping of the 3D Spin Texture of Skyrmions, Microscopy and Microanalysis S1 24 (2018), S. 930-931.

294) Schneider, S., Wolf, D., Stolt, M.J., Jin, S., Pohl, D., Rellinghaus, B., Schmidt, M., Buechner, B., Goennenwein, S.T.B., Nielsch, K., Lubk, A., Induction Mapping of the 3D-Modulated Spin Texture of Skyrmions in Thin Helimagnets, Physical review letters 21 120 (2018), S. 217201/1-6.

295) Schoenecker, S., Li, X., Richter, M., Vitos, L., Lattice dynamics and metastability of fcc metals in the hcp structure and the crucial role of spin-orbit coupling in platinum, Physical Review B 22 97 (2018), S. 224305/1-10.

296) Scholz, M., Hayashi, Y., Khavrus, V., Chujo, D., Inoue, H., Hada, M., Leonhardt, A., Buechner, B., Hampel, S., Resistance-heating of carbon nanotube yarns in different atmospheres, Carbon 133 (2018), S. 232-238.

297) Schroeder, U., Richter, C., Park, M.H., Schenk, T., Pesic, M., Hoffmann, M., Fengler, F., Pohl, D., Rellinghaus, B., Zhou, C., Chung, C.-C., Jones, J., Mikolajick, T., Lanthanum-Doped Hafnium Oxide: A Robust Ferroelectric Material, Inorganic Chemistry 5 57 (2018), S. 2752-2765.

298) Schuermann, M., Shepheard, N., Frese, N., Geishendorf, K., Sudhoff, H., Goelzhaeuser, A., Rueckert, U., Kaltschmidt, C., Kaltschmidt, B., Thomas, A., Technical feasibility study for production of tailored multielectrode arrays and patterning of arranged neuronal networks, PLoS ONE 2 13 (2018), S. 1-20.

299) Schuster, R., Habenicht, C., Ahmad, M., Knupfer, M., Buechner, B., Direct observation of the lowest indirect exciton state in the bulk of hexagonal boron nitride, Physical Review B 4 97 (2018), S. 041201/1-5.

300) Schwabe, S., Schleicher, B., Niemann, R. , Huehne, R., Walter, P., Nielsch, K., Waske, A., Faehler, S., Probing the martensitic (micro) structure of magnetocaloric Heusler films by synchrotron diffraction, Energy Technology 8 6 (2018), S. 1453-1462.

301) Scudino, S., Bian, J.J., Shakur Shahabi, H., Sopu, D., Sort, J., Eckert, J., Liu, G., Ductile bulk metallic glass by controlling structural heterogeneities, Scientific Reports 8 (2018), S. 9174/1-7.

302) Scudino, S., Sopu, D., Strain Distribution Across an Individual Shear Band in Real and Simulated Metallic Glasses, Nano Letters 2 18 (2018), S. 1221-1227.

303) Seifert, F., Kern, F.L., Kezsmarki, I., Roessler, U., Wolf, D., Schneider, S., Pohl, D., Buechner, B., Lubk, A., Cryogenic TEM Studies of Bloch and Neel Skyrmion Textures in Lacunar Spinels and Cubic Helimagnets, Microscopy and Microanalysis S1 24 (2018), S. 946-947.

304) Seiro, S., Jiao, L., Kirchner, S., Hartmann, S., Friedemann, S., Krellner, C., Geibel, C., Si, Q., Steglich, F., Wirth, S., Evolution of the Kondo lattice and non-Fermi liquid excitations in a heavy-fermion metal, Nature Communicastions 9 (2018), S. 3324/1-7.

305) Sellschopp, K., Weise, B., Krautz, M., Cugini, F., Solzi, M., Helmich, L., Huetten, A., Waske, A., Interfacial Thermal Resistance in Magnetocaloric Epoxy-Bonded La-Fe-Co-Si Composites, Energy Technology 8 6 (2018), S. 1448-1452.

306) Senkovskiy, B., Usachov, D.Y., Fedorov, A.V., Haberer, D., Ehlen, N., Fischer, F.R., Grueneis, A., Finding the hidden valence band of N = 7 armchair graphene nanoribbons with angle-resolved photoemission spectroscopy, 2D Materials 3 5 (2018), S. 035007/1-8.

307) Senkovskiy, B.V., Usachov, D.Y., Fedorov, A.V., Marangoni, T., Haberer, D., Tresca, C., Profeta, G., Caciuc, V., Tsukamoto, S., Atodiresei, N., Ehlen, N., Chen, C., Avila, J., Asensio, M.C., Varykhalov, A.Y., Nefedov, A., Woell, C., Kim, T.K., Hoesch, M., Fischer, F.R., Grueneis, A., Boron-Doped Graphene Nanoribbons: Electronic Structure and Raman Fingerprint, ACS Nano 8 12 (2018), S. 7571-7582.

308) Shahid, R.N., Scudino, S., Microstructure and Mechanical Behavior of Al-Mg Composites Synthesized by Reactive Sintering, Metals 10 8 (2018), S. 762/1-14.

309) Shahid, R.N., Scudino, S., Strengthening of Al-Fe3Al composites by the generation of harmonic structures , Scientific Reports 8 (2018), S. 6484/1-12.

310) Shekhar, C., Kumar, N., Grinenko, V., Singh, S., Sarkar, R., Luetkens, H., Wu, S.-C., Zhang, Y., Komarek, A.C., Kampert, E., Skourski, Y., Wosnitza, J., Schnelle, W., McCollam, A., Zeitler, U., Kuebler, J., Yan, B., Klauss, H.-H., Parkin, S.S.P., Felser, C., Anomalous Hall effect in Weyl semimetal half-Heusler compounds RPtBi (R = Gd and Nd), PNAS Proceedings of the National Academy of Sciences of the Unidted States of America 37 115 (2018), S. 9140-9144.

311) Shi, W., Muechler, L., Manna, K., Zhang, Y., Koepernik, K., Car, R., van den Brink, J., Felser, C., Sun, Y., Prediction of a magnetic Weyl semimetal without spin-orbit coupling and strong anomalous Hall effect in the Heusler compensated ferrimagnet Ti_2MnAl, Physical Review B 6 97 (2018), S. 060406/1-6.

312) Shin, N., Zessin, J., Lee, M.H., Hambsch, M., Mannsfeld, S.C.B., Enhancement of n-Type Organic Field-Effect Transistor Performances through Surface Doping with Aminosilanes, Advanced Functional Materials 34 28 (2018), S. 1802265/1-7.

313) Shipulin, I., Richter, S., Thomas, A.A., Brandt, M., Aswartham, S., Huehne, R., Magnetotransport properties of $Ba(Fe_{1-x}Ni_x)_2As_2$ thin films grown by PLD method, Materials Research Express 12 5 (2018), S. 126001/1-5.

314) Sieberer, L.M., Rieder, M.-T., Fischer, M.H., Fulga, I., Statistical periodicity in driven quantum systems: General formalism and application to noisy Floquet topological chains, Physical Review B 21 98 (2018), S. 214301/1-12.

315) Sieger, M., Pahlke, P., Lao, M., Meledin, A., Eisterer, M., Van Tendeloo, G., Schultz, L., Nielsch, K., Huehne, R., Thick Secondary Phase Pinning-Enhanced YBCO Films on Technical Templates, IEEE Transactions on Applied Superconductivity 4 28 (2018), S. 8000505/1-5.

316) Siewierska, K.E., Teichert, N., Schaefer, R., Coey, J.M.D., Imaging Domains in a Zero-Moment Half Metal, IEEE Transactions on Magnetics online first (2018), S. S.1-4.

317) Siles, P.F., Devarajulu, M., Zhu, F., Schmidt, O.G., Direct Imaging of Space-Charge Accumulation and Work Function Characteristics of Functional Organic Interfaces, Small 12 14 (2018), S. 1703647/1-9.

318) Smili, B., Messaoud, A., Bouchelaghem, W., Abadlia, L., Fazel, N., Benmoussa, A., Kaban, I., Gasser, F., Gasser, J.G., Temperature dependence of the electrical resistivity and absolute thermoelectric power of amorphous metallic glass $Ni_{33.3}Zr_{66.7}$, Journal of Non-Crystalline Solids 481 (2018), S. 352-360.

319) Smirnova, E., Sotnikov, A., Zaitseva, N., Schmidt, H., Acoustic anomalies in $SrTiO_3$-$BiFeO_3$ solid solutions, Physics of the Solid State 1 60 (2018), S. 108-114.

320) Sniadecki, Z., Pierunek, N., Idzikowski, B., Wasilewski, B., Werwinski, M., Roessler, U.K., Ivanisenko, Y., Influence of structural disorder on the magnetic properties and electronic structure of YCO_2, Physical Review B 9 98 (2018), S. 094418/1-10.

321) Soldatov, I.V., Jiang, W., Velthuis, S.G.E., Hoffmann, A., Schaefer, R., Size analysis of sub-resolution objects by Kerr microscopy, Applied Physics Letters 26 112 (2018), S. 262404/1-5.

322) Song, K.K., Han, X.L., Pauly, S., Qin, Y.S., Kosiba, K., Peng, C.X., Gong, J.H., Chen, P.X., Wang, L., Sarac, B., Ketov, S., Muehlbacher, M., Spieckermann, F., Kaban, I., Eckert, J., Rapid and partial crystallization to design ductile CuZr-based bulk metallic glass composites, Materials and Design 139 (2018), S. 132-140.

323) Soni, A., Zhao, L., Ta, H.Q., Shi, Q., Pang, J., Wrobel, P.S., Gemming, T., Bachmatiuk, A., Rümmeli, M., Facile Graphitization of Silicon Nano-Particles with Ethanol Based Chemical Vapor Deposition, Nano-Structures and Nano-Objects 16 (2018), S. 38-44.

324) Stania, R., Seitsonen, A.P., Kunhardt, D., Buechner, B., Popov, A.A., Muntwiler, M., Greber, T., Electrostatic Interaction across a Single-Layer Carbon Shell, Journal of Physical Chemistry Letters 13 9 (2018), S. 3586-3590.

325) Stanković, I., Dašić, M., Otalora Arias, J., Garcia, C., A platform for nano magnetism - assembledferromagnetic and antiferromagnetic dipolar tubes, Nanoscale (2018), S. 1-15.

326) Stepanov, A., Fedorenko, S., Amirov, R., Nizameev, I., Kholin, K., Voloshina, A., Sapunova, A., Mendes, R., Ruemmeli, M., Gemming, T., Mustafina, A., Odintsov, B., Silica-coated iron-oxide nanoparticles doped with Gd(III) complexes as potential double contrast agents for magnetic resonance imaging at different field strengths, Journal of Chemical Sciences 9 130 (2018), S. UNSP 125/1-10.

327) Strizik, L., Yannopoulus, S.N., Benekou, V., Oswald, J., Pavlista, M., Prokop, V., Wagner, T., Orava, J., Photoluminescence in pulsed-laser deposited GeGaSbS:Er films, Optical Materials 85 (2018), S. 246-253.

328) Sugimoto, K., Nishimoto, S., Kaneko, T., Ohta, Y., Strong Coupling Nature of the Excitonic Insulator State in Ta_2NiSe_5, Physical Review Letters 24 120 (2018), S. 247602/1-5.

329) Suhak, Y., Schulz, M., Johnson, W.L., Sotnikov, A., Schmidt, H., Fritze, H., Electromechanical properties and charge transport of $Ca_3TaGa_3Si_2O_{14}$ (CTGS) single crystals at elevated temperatures, Solid State Ionics 317 (2018), S. 221-228.

330) Suhak, Y., Schulz, M., Sotnikov, A., Schmidt, H., Fritze, H., Electrical, Electromechanical and Piezoelectric Properties of $Ca_3TaGa_3Si_2O_{14}$ Resonators at Elevated Temperatures, Acta Physica Polonica A 4 133 (2018), S. 1069-1073.

331) Sun, H.C., Ning, Z.L., Wang, G., Liang, W.Z., Pauly, S., Huang, Y.J., Guo, S., Xue, X., Sun, J.F., In-situ tensile testing of ZrCu-based metallic glass composites, Scientific Reports 8 (2018), S. 4651/1-12.

332) Sykora, S., Becker, K.W., Many-body approach to Luttinger's theorem for the Kondo lattice, Physical Review B 24 98 (2018), S. 245139/1-9.

333) Ta, H.Q., Zhao, L., Yin, W., Pohl, D., Rellinghaus, B., Gemming, T., Trzebicka, B., Palisaitis, J., Jing, G., Persson, P.O.A., Liu, Z., Bachmatiuk, A., Ruemmeli, M.H., Single Cr atom catalytic growth of graphene, Nano Research 5 11 (2018), S. 2405-2411.

334) Taghvaeia, A.H., Shirazifarda, N.G., Ramasamy P., Bednarcik, J., Eckert, J., Thermal behavior, structural relaxation and magnetic study of a new Hf-microalloyed Co-based glassy alloy with high thermal stability, Journal of Alloys and Compounds 748 (2018), S. 553-560.

335) Tancredi, P., Moscoso Londono, O., Rivas Rojas, P.C., Wolff, U., Socolovsky, L.M., Knobel, M., Muraca, D., Strategies to tailor the architecture of dual Ag/Fe-oxide nano-heterocrystals - interfacial and morphology effects on the magnetic behavior, Journal of Physics D 29 51 (2018).

336) Tayari, V., Senkovskiy, B.V., Rybkovskiy, D., Ehlen, N., Fedorov, A., Chen, C.Y., Avila, J., Asensio, M, Perucchi, A., di Pietro, P., Yashina, L., Fakih, I., Hemsworth, N., Petrescu, M., Gervais, G., Grueneis, A., Szkopek, T., Quasi-two-dimensional thermoelectricity in SnSe, Physical Review B 4 97 (2018), S. 045424/1-9.

337) Taylor, A.E., Morrow, R., Lumsden, M.D., Calder, S., Upton, M.H., Kolesnikov, A.I., Stone, M.B., Fishman, R.S., Paramekanti, A., Woodward, P.M., Christianson, A. D., Origin of magnetic excitation gap in double perovskite Sr_2FeOsO_6, Physical Review B 98 (2018), S. 214422/1-6.

338) Thirupathaiah, S., Kushnirenko, Y., Haubold, E., Fedorov, A.V., Rienks, E.D.L., Kim, T.K., Yaresko, A.N., Blum, C.G.F., Aswartham, S., Buechner, B., Borisenko, S.V., Possible origin of linear magnetoresistance: Observation of Dirac surface states in layered $PtBi_2$, Physical Review B 3 97 (2018), S. 035133/1-6.

339) Thirupathaiah, S., Morozov, I., Kushnirenko, Y., Fedorov, A.V., Haubold, E., Kim, T.K., Shipunov, G., Maksutova, A., Kataeva, O., Aswartham, S., Buechner, B., Borisenko, S.V., Spectroscopic evidence of topological phase transition in the three-dimensional Dirac semimetal Cd-3(As1-xPx)(2), Physical Review B 8 98 (2018), S. 085145/1-5.

340) Tian, Y.Z., Xiong, T., Zheng, S.J., Bai, Y., Freudenberger, J., Pippan, R., Zhang, Z.F., Tsuji, N., Ultrafine-grained $CuAg_7Zr_{0.05}$ alloy with fully recrystallized microstructure, Materialia 3 (2018), S. 162-168.

341) Tian, Y.Z., Xiong, T., Zheng, S.J., Bai, Y., Freudenberger, J., Pippan, R., Zhang, Z.F., Tsuji, N., Ultrafine-grained $CuAg_7Zr_{0.05}$ alloy with fully recrystallized microstructure, Materialia online first (2018), S. 162-168.

342) Tirunilai, A.S., Sas, J., Weiss, K.-P., Chen, H., Szabo, D.V., Schlabach, S., Haas, S., Geissler, D., Freudenberger, J., Heilmaier, M., Kauffmann, A., Peculiarities of deformation of CoCrFeMnNi at cryogenic temperatures, Journal of Materials Research (2018), S. 1-14.

343) Tkachov, R., Stepien, L., Grafe, R., Guskova, O., Kiriy, A., Simon, F., Reith, H., Nielsch, K., Schierning, G., Kasinathan, D., Leyens, C., Polyethenetetrathiolate or polytetrathiooxalate? Improved synthesis, a comparative analysis of a prominent thermoelectric polymer and implications to the charge transport mechanism, Polymer Chemistry 36 9 (2018), S. 4543-4555.

344) Trabelsi, Z., Yahyaoui, M., Radhia, S.B., Boujdaria, K., Zallo, E., Schmidt, O.G., Atkinson, P., Chamarro, M., Testelin, C., Neutral, charged excitons and biexcitons in strain-free and asymmetric GaAs quantum dots fabricated by local droplet etching, Journal of Luminescence 197 (2018), S. 47-55.

345) Trepka, B., Erler, P., Selzer, S., Kollek, T., Boldt, K., Fonin, M., Nowak, U., Wolf, D., Lubk, A., Polarz, S., Nanomorphology Effects in Semiconductors with Native Ferromagnetism: Hierarchical Europium (II) Oxide Tubes Prepared via a Topotactic Nanostructure Transition, Advanced Materials 1 30 (2018), S. 1703612/1-7.

346) Ummethala, R., Fritzsche, M., Jaumann, T., Balach, J., Oswald, S., Nowak, R., Sobczak, N., Kaban, I., Ruemmeli, M.H., Giebeler, L., Lightweight, free-standing 3D interconnected carbon nanotube foam as a flexible sulfur host for high performance lithium-sulfur battery cathodes, Energy Storage Materials 10 (2018), S. 206-215.

347) Usachov, D.Y., Bokai, K.A., Marchenko, D.E., Fedorov, A.V., Shevelev, V.O., Vilkov, O.Y., Kataev, E.Y., Yashina, L.V., Ruehl, E., Laubschat, C., Vyalikh, D.V., Cobalt-assisted recrystallization and alignment of pure and doped graphene, Nanoscale 25 10 (2018), S. 12123-12132.

348) Usachov, D.Y., Fedorov, A.V., Vilkov, O.Y., Ogorodnikov, I.I., Kuznetsov, M.V., Grueneis, A., Laubschat, C., Vyalikh, D.V., Electron-phonon coupling in graphene placed between magnetic Li and Si layers on cobalt, Physical Review B 8 97 (2018), S. 085132/1-8.

349) Vale, J. G., Calder, S., Donnerer, C., Pincini, D., Shi, Y. G., Tsujimoto, Y., Yamaura, K., Sala, M. Moretti, van den Brink, J., Christianson, A. D., McMorrow, D. F., Evolution of the Magnetic Excitations in $NaOsO_3$ through its Metal-Insulator Transition, Physical Review Letters 22 120 (2018), S. 227203/1-6.

350) Vale, J.G., Calder, S., Donnerer, C., Pincini, D., Shi, Y.G., Tsujimoto, Y., Yamaura, K., Moretti Sala, M., van den Brink, J., Christianson, A.D., McMorrow, D.F., Crossover from itinerant to localized magnetic excitations through the metal-insulator transition in $NaOsO_3$, Physical Review B 18 97 (2018), S. 184429/1-17.

351) Valldor, M., Mikhailova, D., Giebeler, L., Lai, K.T., Spillecke, L., Grafe, H.-J., Buechner, B., Synthesis, Characterization, and Electrochemistry of Layered Chalcogenides LiCuCh (Ch = Se, Te), Inorganic Chemistry 12 57 (2018), S. 7201-7207.

352) Velkos, G., Krylov, D.S., Kirkpatrick, K., Liu, X., Spree, L., Wolter, A.U.B., Buechner, B., Dorn, H.C., Popov, A.A., Giant exchange coupling and field-induced slow relaxation of magnetization in Gd-2@C79N with a single-electron Gd-Gd bond, Chemical Communications 23 54 (2018), S. 2902-2905.

353) Vittorio, O., Le Grand, M., Makharza, S.A., Curcio, M., Tucci, P., Iemma, F., Nicoletta, F.P., Hampel, S., Cirillo, G., Doxorubicin synergism and resistance reversal in human neuroblastoma BE(2)C cell lines: An in vitro study with dextran-catechin nanohybrids, European Journal of Pharmaceutics and Biopharmaceutics 122 (2018), S. 176-185.

354) Vogl, M., Corredor, L.T., Dey, T., Morrow, R., Scaravaggi, F., Wolter, A.U.B., Aswartham, S., Wurmehl, S., Buechner, B., Interplay of 3d- and 5d-sublattice magnetism in the double perovskite substitution series $La_2Zn_{1-x}Co_xIrO_6$, Physical Review B 3 97 (2018), S. 035155/1-8.

355) Volkov, O.M., Sheka, D.D., Gaididei, Y., Kravchuk, V.P., Roessler, U.K., Fassbender, J., Makarov, D., Mesoscale Dzyaloshinskii-Moriya interaction: geometrical tailoring of the magnetochirality, Scientific Reports 8 (2018), S. 866/1-9.

356) Voronov, M., Hoffmann, V., Application of microsecond pulsed glow discharge to modern commercially available optical emission spectrometers for bulk elemental analysis, Journal of Analytical Atomic Spectrometry 4 33 (2018), S. 663-669.

357) Wang, C., Chen, C., Chang, C.-H., Tsai, H.-S., Pandey, P., Xu, C., Boettger, R., Chen, D., Zeng, Y.-J., Gao, X., Helm, M., Zhou, S., Defect-Induced Exchange Bias in a Single $SrRuO_3$ Layer, ACS Applied Materials and Interfaces 32 10 (2018), S. 27472-27476.

358) Wang, J., Hao, Q., Yin, Y., Ma, L., Schmidt, O.G., Surface-Enhanced Raman Scattering Enabled byMetal - Coated Dielectric Microspheres, Physica Status Solidi B (2018), S. 1800379/1-6.

359) Wang, J., Yin, Y., Hao, Q., Huang, S., Saei Ghareh Naz, E., Schmidt, O.G., Ma, L., External Strain Enabled Post-Modification of Nanomembrane-Based Optical Microtube Cavities, ACS Photonics 5 5 (2018), S. 2060-2067.

360) Wang, J., Yin, Y., Hao, Q., Yang, Y.-D., Valligatla, S., Saei Ghareh Naz, E., Li, Y., Saggau, C., Ma, L., Schmidt, O.G., Curved Nanomembrane-Based Concentric Ring Cavities for Supermode Hybridization, Nano Letters 11 18 (2018), S. 7261-7267.

361) Wang, J., Yin, Y., Hao, Q., Zhang, Y., Ma, L., Schmidt, O.G., Strong Coupling in a Photonic Molecule Formed by Trapping a Microsphere in a Microtube Cavity, Advanced Optical Materials 1 6 (2018), S. 1700842/1-8.

362) Wang, K., Pang, J., Li, L., Zhou, S., Li, Y., Zhang, T., Synthesis of hydrophobic carbon nanotubes/reduced graphene oxide composite films by flash light irradiation, Frontiers of Chemical Science and Engineering 3 12 (2018), S. 376-382.

363) Wang, L., Werner, J., Ottmann, A., Weis, R., Abdel-Hafiez, M., Sannigrahi, J., Majumdar, S., Koo, C., Klingeler, R., Magnetoelastic coupling and ferromagnetic-type in-gap spin excitations in multiferroic alpha-$Cu_2V_2O_7$, New Journal of Physics 20 (2018), S. 063045/1-11.

364) Wang, L.L., Popescu, M.N., Stavale, F., Ali, A, Gemming, T., Simmchen, J., Cu@ TiO_2 Janus microswimmers with a versatile motion mechanism, Soft Matter 34 14 (2018), S. 6969-6973.

365) Wang, P., Deng, L., Prashant, K.G., Pauly, S., Eckert, J., Scudino, S., Microstructure and mechanical properties of Al-Cu alloys fabricated by selective laser melting of powder mixtures, Journal of Alloys and Compounds 735 (2018), S. 2263-2266.

366) Wang, P., Gammer, C., Brenne, F., Gokuldoss Prahanth, K., Mendes, R.G., Ruemmeli, M.H., Gemming, T., Eckert, J., Scudino, S., Microstructure and mechanical properties of a heat-treatable Al-3.5Cu-1.5Mg-1Si alloy produced by selective laser melting, Materials Science and Engineering A 711 (2018), S. 562-570.

367) Wang, P., Gammer, C., Brenne, F., Niendorf, T., Eckert, J., Scudino, S., A heat treatable TiB_2/Al-3.5Cu-1.5Mg-1Si composite fabricated by selective laser melting: Microstructure, heat treatment and mechanical properties, Composites Part B 147 (2018), S. 162-168.

368) Wang, X., Shoaib, M., Wang, X., Zhang, X., He, M., Luo, Z., Zheng, W., Li, H., Yang, T., Zhu, X., Ma, L., Pan, A., High-Quality In-Plane Aligned CsPbX3 Perovskite Nanowire Lasers with Composition-Dependent Strong Exciton - Photon Coupling, ACS Nano 6 12 (2018), S. 6170-6178.

369) Wang, X.H., Inoue, A., Zhao, J.F., Kong, F.L., Zhu, S.L., Kaban, I., Stoica, M., Oswald, S., Fan, C., Shalaan, E., Al-Marzouki, F., Eckert, J., Yin, F.X., Li, Q., Liquid ejection temperature dependence of structure and glass transition behavior for rapidly solidified Zr-Al-M (M = Ni, Cu or Co) ternary glassy alloys, Journal of Alloys and Compounds 739 (2018), S. 1104-1114.

370) Wang, Z., Prashanth, K.G., Surreddi, K.B., Suryanarayana, C., Eckert, J., Scudino, S., Pressure-assisted sintering of Al–Gd–Ni–Co amorphous alloy powders, Materialia 2 (2018), S. 157-166.

371) Wang, Z., Zhu, M., Gou, S., Pang, Z., Wang, Y., Su, Y., Huang, Y., Weng, Q., Schmidt, O.G., Xu, J., Pairing of Luminescent Switch with Electrochromism for Quasi-Solid-State Dual-Function Smart Windows, ACS Applied Materials and Interfaces 37 10 (2018), S. 31697-31703.

372) Waske, A., Dutta, B., Teichert, N., Weise, B., Shayanfar, N., Becker, A., Huetten, A., Hickel, H., Coupling Phenomena in Magnetocaloric Materials, Energy Technology 8 6 (2018), S. 1429-1447.

373) Watson, M.D., Aswartham, S., Rhodes, L.C., Parrett, B., Iwasawa, H., Hoesch, M., Morozov, I., Buechner, B., Kim, T.K., Three-dimensional electronic structure of the nematic and antiferromagnetic phases of NaFeAs from detwinned angle-resolved photoemission spectroscopy, Physical Review B 3 97 (2018), S. 035134/1-11.

374) Weber, H., Orava, J., Kaban, I., Pries, J., Greer, A.L., Correlating ultrafast calorimetry, viscosity and structural measurements in liquid GeTe and Ge15Te85, Physical Review Materials 9 2 (2018), S. 093405/1-6.

375) Weheabby, S., Abdulmalic, M.A., Atzori, M., Sessoli, R., Aliabadi, A., Rüffer, T., Promotion of antiferromagnetic exchange interaction in multinuclear copper(ii) complexes via fused oxamato/oxamidato ligands, Dalton Transactions 45 47 (2018), S. 16164-16181.

376) Weise, B., Dutta, B., Teichert, N., Huetten, A., Hickel, T., Waske, A., Role of disorder when upscaling magnetocaloric Ni-Co-Mn-Al Heusler alloys from thin films to ribbons, Scientific Reports 8 (2018), S. 9147/1-10.

377) Weiss, M., Hoerner, A.L., Zallo, E., Atkinson, P., Rastelli, A., Schmidt, O.G., Winforth, A., Krenner, H.J., Multiharmonic Frequency-Chirped Transducers for Surface-Acoustic-Wave Optomechanics, Physical Review Applied 1 9 (2018), S. 014004/1-4.

378) Weiss, Z., Pickering, J.C., Hoffmann, V., Obituary Prof. Edward B. M. Steers (1931-2018), Spectrochimica Acta Part B: Atomic Spectroscopy 149 (2018), S. 241-242.

379) Weiss, Z., Pickering, J.C., Hoffmann, V., Sixty years of spectroscopic research: a tribute to Professor Edward B. M. Steers, Chemical Papers (2018).

380) Weiz, S.M., Medina-Sanchez, M., Schmidt, O.G., Microsystems for Single-Cell Analysis, Advanced Biosystems 2 (2018), S. 1700193/1-32.

381) Wellm, C., Zeisner, J., Alfonsov, A., Wolter, A.U.B., Roslova, M., Isaeva, A., Doert, T., Vojta, M., Buechner, B., Kataev, V., Signatures of low-energy fractionalized excitations in alpha-$RuCl_3$ from field-dependent microwave absorption, Physical Review B 18 98 (2018), S. 184408/1-6.

382) Weng, Q., Li, G., Feng, X., Nielsch, K., Golberg, D., Schmidt, O.G., Electronic and Optical Properties of 2D Materials Constructed from Light Atoms, Advanced Materials online first (2018), S. 1801600/1-24.

383) Wiegand, C., Zierold, R., Faust, R., Pohl, D., Thomas, A., Rellinghaus, B., Nielsch, K., Surface Modification of V-VI Semiconductors Using Exchange Reactions within ALD Half-Cycles, Advanced Materials Interfaces 5 5 (2018), S. 1701155/1-8.

384) Wiegand, C.W., Faust, R., Meinhardt, A., Blick, R.H., Zierold, R., Nielsch, K., Understanding the Growth Mechanisms of Multilayered Systems in Atomic Layer Deposition Process, Chemistry of Materials 6 30 (2018), S. 1971-1979.

385) Wolf, D., Huebner, R., Niermann, T., Sturm, S., Prete, P., Lovergine, N., Buechner, B., Lubk, A., Three-Dimensional Composition and Electric Potential Mapping of III-V Core-Multishell Nanowires by Correlative STEM and Holographic Tomography, Nano Letters 8 18 (2018), S. 4777-4784.

386) Wolf, D., Kübel, C., Electron Tomography for 3D Imaging of Nanoscale Materials, Practical Metallography - Praktische Metallographie 8 55 (2018), S. 527-538.

387) Wolff, A., Doert, T., Hunger, J., Kaiser, M., Pallmann, J., Reinhold, R., Yogendra, S., Giebeler, L., Sichelschmidt, J., Schnelle, W., Whiteside, R., Gunaratne, H.Q.N., Nockemann, P., Weigand, J.J., Brunner, E., Ruck, M., Low-Temperature Tailoring of Copper-Deficient Cu3-xP-Electric Properties, Phase Transitions, and Performance in Lithium-Ion Batteries, Chemistry of Materials 20 30 (2018), S. 7111-7123.

388) Wolff, U., Ambrozic, B., Zuzek Rozman, K., Leistner, K., Nielsch, K., Sturm, S., In-Situ Observation of the Reversible Electrochemical Deposition of Fe in a Transmission Electron Microscope, Microscopy and Microanalysis 1 24 (2018), S. 310-311.

389) Xi, L. X., Zhang, H., Wang, P., Li, H. C., Prashanth, K. G., Lin, K. J., Kaban, I., Gu, D. D., Comparative investigation of microstructure, mechanical properties and strengthening mechanisms of Al-12Si/TiB_2 fabricated by selective laser melting and hot pressing, Ceramics International 15 44 (2018), S. 17635-17642.

390) Xi, L., Kaban, I., Nowak, R., Bruzda, G., Sobczak, N., Eckert, J., Wetting, reactivity, and phase formation at interfaces between Ni–Al melts and TiB_2 ultrahigh-temperature ceramic, Journal of the American Ceramic Society 2 101 (2018), S. 911-918.

391) Xu, H., Medina-Sanchez, M., Magdanz, V., Schwarz, L., Hebenstreit, F., Schmidt, O.G., Sperm-Hybrid Micromotor for Targeted Drug Delivery, ACS Nano 1 12 (2018), S. 327-337.

392) Xu, X., Prüfer, T., Wolf, D., Engelmann, H.-J., Bischoff, L., Hübner, R., Heinig, K.-H., Möller, W., Facsko, S., von Borany, J., Hlawacek, G., Site-controlled formation of single Si nanocrystals in a buried SiO_2 matrix using ion beam mixing, Beilstein Journal of Nanotechnology 9 (2018), S. 2883-2892.

393) Yadav, R., Eldeeb, M.S., Ray, R., Aswartham, S., Sturza, M., Nishimoto, S., van den Brink, J., Hozoi, L., Engineering Kitaev exchange in stacked iridate layers: impact of inter-layer species on in-plane magnetism, Chemical Science (2018), S. 1-7.

394) Yadav, R., Pereiro, M., Bogdanov, A.N., Nishimoto, S., Bergmann, A., Eriksson, O., van den Brink, J., Hozoi, L., Heavy-mass magnetic modes in pyrochlore iridates due to dominant Dzyaloshinskii-Moriya interaction, Physical Review Materials 7 2 (2018), S. 074408/1-10.

395) Yadav, R., Rachel, S., Hozoi, L., van den Brink, J., Jackeli, G., Strain- and pressure-tuned magnetic interactions in honeycomb Kitaev materials, Physical Review B 12 98 (2018), S. 121107/1-6.

396) Yadav, R., Ray, R., Eldeeb, M., Nishimoto, S., Hozoi, L., van den Brink, J., Strong Effect of Hydrogen Order on Magnetic Kitaev Interactions in $H_3LiIr_2O_6$, Physical Review Letters 19 121 (2018), S. 197203/1-6.

397) Yakymovych, A., Weber, H., Kaban, I., Ipser, H., Dynamic viscosity of a liquid $Sn_{-3.0}Ag_{-0.5}Cu$ alloy with Ni nanoparticles, Journal of Molecular Liquids 268 (2018), S. 176-180.

398) Yamashita, A., Matsumoto, R., Tanaka, M., Hara, H., Iida, K., Holzapfel, B., Takeya, H., Takano, Y., Observation of zero resistance in as-electrodeposited FeSe, Solid State Communications 270 (2018), S. 72-75.

399) Yershov, K.V., Kravchuk, V.P., Sheka, D.D., Pylypovskyi, O.V., Makarov, D., Gaididei, Y., Geometry-induced motion of magnetic domain walls in curved nanostripes, Physical Review B 6 98 (2018), S. 060409/1-6.

400) Yin, Y., Wang, J., Lu, X., Hao, Q, Naz, E.S.G., Cheng, C., Ma, L., Schmidt, O.G., In Situ Generation of Plasmonic Nanoparticles for Manipulating Photon-Plasmon Coupling in Microtube Cavities, ACS Nano 4 12 (2018), S. 3726-3732.

401) You, J.S., Fang, S., Xu, S.Y., Kaxiras, E., Low, T., Berry curvature dipole current in the transition metal dichalcogenides family, Physical Review B 12 98 (2018), S. 121109/1-6.

402) Yuan, F., Grinenko, V., Iida, K., Richter, S., Pukenas, A., Skrotzki, W., Sakoda, M., Naito, M., Sala, A., Putti, M., Yamashita, A., Takano, Y., Shi, Z., Nielsch, K., Huehne, R., Universal scaling behavior of the upper critical field in strained $FeSe_{0.7}Te_{0.3}$ thin films, New Journals of Physics 20 (2018), S. 093012/1-9.

403) Yuan, X., Weyhausen-Brinkmann, F., Martin-Sanchez, J., Piredda, G., Krapek, V., Huo, Y., Huang, H, Schimpf, C., Schmidt, O.G., Edlinger, J., Bester, G., Trotta, R., Rastelli, A., Uniaxial stress flips the natural quantization axis of a quantum dot for integrated quantum photonics, Nature Communications 9 (2018), S. 3058/1-8.

404) Zalibera, M., Krylov, D.S., Karagiannis, D., Will, P.-A., Ziegs, F., Schiemenz, S., Lubitz, W., Reineke, S., Savitsky, A., Popov, A.A., Thermally Activated Delayed Fluorescence in a $Y_3N@C_{80}$ Endohedral Fullerene: Time-Resolved Luminescence and EPR Studies, Angewandte Chemie-International Edition 1 57 (2018), S. 277-281.

405) Zapf, M., Stuebinger, M., Jin, L., Kamp, M., Pfaff, F., Lubk, A., Buechner, B., Sing, M., Claessen, R., Domain matching epitaxy of $BaBiO_3$ on $SrTiO_3$ with structurally modified interface, Applied Physics Letters 14 112 (2018), S. 141601/1-5.

406) Zeeshan, M., Nautiyal, T., van den Brink, J., Kandpal, H.C., FeTaSb and FeMnTiSb as promising thermoelectric materials: An ab initio approach, Physical Review Materials 6 2 (2018), S. 065407/1-9.

407) Zhang, L., Tan, J., He, Z.Y., Jiang, Y.H., Effect of calcium pyrophosphate on microstructural evolution and in vitro biocompatibility of Ti-35Nb-7Zr composite by spark plasma sintering, Materials Science and Engineering C - Materials for Biological Applications 90 (2018), S. 8-15.

408) Zhang, L., Zhang, H., Ren, X., Eckert, J., Wang, Y.D., Zhu, Z., Gemming, T, Pauly, S., Amorphous martensite in beta-Ti alloys, Nature Communications 9 (2018), S. 506/1-8.

409) Zhang, L., Zhao, G., Tan, J., He, Z., Jiang, Y., Electrochemical Behavior in Simulated Physiological Solution of Ti-Nb-Zr-Calcium Pyrophosphate Composite with Enhanced Bioactivity by Spark Plasma Sintering, Journal of The Electrochemical Society 5 165 (2018), S. E221-E230.

410) Zhang, P., Wang, J., Sheng, W., Wang, F., Zhang, J., Zhu, F., Zhuang, X., Jordan, R., Schmidt, O.G., Feng, X., Thermoswitchable on-chip microsupercapacitors: one potential self-protection solution for electronic devices, Energy and Environmental Science 7 11 (2018), S. 1717-1722.

411) Zhang, S., Zhang, J., Zhang, Q., Barton, C., Neu, V., Zhao, Y., Hou, Z., Wen, Y., Gong, C., Kazakova, O., Wang, W., Peng, Y., Garanin, D.A., Chudnovsky, E.M., Zhang, X., Direct writing of room temperature and zero field skyrmion lattices by a scanning local magnetic field, Applied Physics Letters 13 112 (2018), S. 132405/1-5.

412) Zhang, X., Li, W., Feng, L., Chen, X., Hansen, A., Grimme, S., Fortier, S., Sergentu, D.-C., Duignan, T.J., Autschbach, J., Wang, S., Wang, Y., Velkos, G., Popov, A.A., Aghdassi, N., Duhm, S., Li, X., Li, J., Echegoyen, L., Schwarz, W.H.E., Chen, N., A Diuranium Carbide Cluster Stabilized Inside a C80 Fullerene Cage, Nature Communications 9 (2018), S. 2753.

413) Zhang, Y., Ishizuka, H., van den Brink, J., Felser, C., Yan, B.H., Nagaosa, N., Photogalvanic effect in Weyl semimetals from first principles, Physical Review B 24 97 (2018), S. 241118/1-6.

414) Zhang, Y., Sun, Y., Yan, B., Berry curvature dipole in Weyl semimetal materials: An ab initio study, Physical Review B 4 97 (2018), S. 041101/1-6.

415) Zhang, Z., Zhang, R.-W., Li, X., Koepernik, K., Yao, Y., Zhang, H., High-Throughput Screening and Automated Processing toward Novel Topological Insulators, The Journal of Physical Chemistry Letters 21 9 (2018), S. 6224-6231.

416) Zhang, Z.Q., Song, K.K., Sun, B.A., Wang, L., Cui, W.C., Qin, Y.S., Han, X.L., Xue, Q.S., Peng, C.X., Sarac, B., Spieckermann, F., Kaban, I., Eckert, J., Dual self-organised shear banding behaviours and enhanced ductility in phase separating Zr-based bulk metallic glasseS. , Philosophical magazine 19 98 (2018), S. 1744-1764.

417) Zhang, Z.T., Dmytriieva, D., Molatta, S., Wosnitza, J., Khim, S., Gass, S., Wolter, A.U.B., Wurmehl, S., Grafe, H.-J., Kuehne, H., Increasing stripe-type fluctuations in AFe_2As_2 (A = K, Rb, Cs) superconductors probed by ^{75}As NMR spectroscopy, Physical Review B 11 97 (2018), S. 115110/1-5.

418) Zhou, J., Zhu, H., Liu, T.-H., Song, Q., He, R., Mao, J., Liu, Z., Ren, W., Liao, B., Singh, D.J., Ren, Z., Chen, G., Large thermoelectric power factor from crystal symmetry-protected non-bonding orbital in half-Heuslers, Nature Communications 9 (2018), S. 1721/1-9.

419) Zhu, H., He, R., Mao, J., Zhu, Q., Li, C., Sun, J., Ren, W., Wang, Y., Liu, Z., Tang, Z., Sotnikov, A., Wang, Z., Broido, D., Singh, D.J., Chen, G., Nielsch, K., Ren, Z., Discovery of ZrCoBi based half Heuslers with high thermoelectric conversion efficiency, Nature Communications 9 (2018), S. 2497/1-9.

420) Zopf, M., Macha, T., Keil, R., Urunuela, E., Chen, Y., Alt, W., Ratschbacher, L., Ding, F., Meschede, D., Schmidt, O.G., Frequency feedback for two-photon interference from separate quantum dots, Physical Review B 16 98 (2018), S. 161302/1-6.

Contributions to conferences proceedings

1) Agrapidis, C., van den Brink, J., Nishimoto, S., Numerical Study of the Kitaev-Heisenberg chain as a spin model of the K-intercalated $RuCl_3$, Journal of Physics: Conference Series 969 (2018), S. 012112/1-5.
2) Biryukov, S., Sotnikov, A., Schmidt, H., SAW based tube rotation with wireless power transfer (2018).
3) Fomin, V.M., Fomin, V.M., Quantum Ring: A Unique Playground for the Quantum-Mechanical Paradigm Physics of Quantum Rings, Springer International Publishing, Series: NanoScience and Technology, ISBN: 978-3-319-95158-4, Chapter 1 (2018), S. 3-32.
4) Fomin, V.M., Fomin, V.M., Preface Physics of Quantum Rings, Springer International Publishing, Series: NanoScience and Technology, ISBN: 978-3-319-95158-4, Preface (2018), S. IX-XII.
5) Fomin, V.M., Gladilin, V.N., van Bree, J., Flatte, M.E., Devreese, J.T., Koenraad, P.M., Fomin, V.M., Self-organized Quantum Rings: Physical Characterization and Theoretical Modeling Physics of Quantum Rings, Springer International Publishing, Series: NanoScience and Technology, ISBN: 978-3-319-95158-4, Chapter 4 (2018), S. 91-120.
6) Fomin, V.M., Sidorenko, Anatolie, Topology-Driven Effects in Advanced Micro- and Nanoarchitectures Functional Nanostructures and Metamaterials for Superconducting Spintronics (2018), S. 195-220.
7) Freudenberger, J., Warlimont, H., Warlimont, H., Martienssen, W., Copper and Copper Alloys Springer Handbook of Materials Data, Springer Nature Switzerland AG, ISBN: 978-3-319-69741-3, Kap. B.12 (2018), S. 293-305.
8) Fuchs, G., Fischer, C., Holzapfel, B., Schuepp-Niewa, B., Warlimont, H., Warlimont, H., Martienssen, W., Superconductors Springer Handbook of Materials Data, Springer Nature Switzerland AG, ISBN: 978-3-319-69741-3, Kap. D.21 (2018), S. 701-752.
9) Fuchs, G., Schultz, L., de Haas, O., Holzapfel, B., Berger, D., Passively stable energy efficient MAGLEV system based on quantum levitation: The Supratrans (2018).
10) Koethe, A., Warlimont, H., Warlimont, H., Martienssen, W., Iron and Steels Springer Handbook of Materials Data, Springer Nature Switzerland AG, ISBN: 978-3-319-69741-3, Kap. B.09 (2018), S. 213-266.
11) Li, G., Garcia Fernandez, J., Sieger, T., Schnatmann, L., Lara Ramos, D., Barati, V., Perez Rodriguez, N., Reith, H., Schierning, G., Nielsch, K., Compact Telluride films prepared by electrochemical deposition and their applications for integrated micro-thermoelectric devices (2018).
12) Ma, L., Fomin, V.M., Schmidt, O.G., Fomin, V.M., Optical Berry Phase in Micro/Nano-rings Physics of Quantum Rings, Springer International Publishing, Series: NanoScience and Technology, ISBN: 978-3-319-95158-4, Chapter 2 (2018), S. 33-55.
13) Mueller, M., Harada, H., Warlimont, H., Warlimont, H., Martienssen, W., Magnetic Materials Springer Handbook of Materials Data, Springer Nature Switzerland AG, ISBN: 978-3-319-69741-3, Kap. D.22 (2018), S. 753-808.
14) Nazarova, E., Balchev, N., Buchkov, K., Nenkov, K., Kovacheva, D., Gajda, D., Fuchs, G., Miryala, M., Koblischka, M.R., Superconducting and Multiband Effects in FeSe with Ag AdditionSu (Chapter 8) High-Temperature Superconductors: Occurrence, Synthesis and Application (ISBN 978-1-53613-341-7), pp. 195-212, (Materials Science and Technologies); Nova Science Publishers (2018).
15) Schwotzer, D., Meyer-Plath, A., Rittinghausen, S., Creutzenberg, O., Leonhardt, A., Schaudien, D., Approaches on MWCNT diameters and its relation to tumor development; in: Naunyn-Schmiedeberg's Archives of Pharmacology, Naunyn-Schmiedeberg's Archives of Pharmacology Supplement 1 Abstracts of the 84th Annual Meeting of the German Society for Experimental and Clinical Pharmacology and Toxicology (DGPT) and the 20th Annual Meeting of the Association of the Clinical Pharmacology Germany (VKliPha) With contribution of the Arbeitsgemeinschaft für Angewandte Humanpharmakologie e. V. (AGAH), 391 (2018), S. 1-93.
16) Scudino, S., Edited by: Rahul Mitra, Cambridge: Woodhead Publishing, ISBN: 978-0-85709-346-2, 6 - Powder metallurgy of Al-based matrix composites reinforced with quasicrystalline particles: processing and mechanical properties, Intermetallic Matrix Composites Intermetallic Matrix Composites: Properties and Applications (2018), S. 147-163.
17) Weser, R., Sotnikov, A., Schmidt, H., Advanced characterization of surface acoustic wave fields at high temperature (2018).
18) Weser, R., Winkler, A., Menzel, S., Schmidt, H., Tuning of the acoustic boundary conditions for SAW-driven microfluidics (2018), S. 2 S.
19) Winkler, A., Richard, C., Oswald, F., Kamsma, D., Menzel, S., Gemming, T., Performance exploration of Acoustic Force Spectroscopy (AFS™) chips (2018), S. 2 S..

Invited talks

1) Agrapidis, C.E., Drechsler, S.-L., van den Brink, J., Nishimoto, S., Frustration induced topological order in the ferromagnetic frustrated J1-J2 chain, Department of Physics of Saarland University in Saarbruecken, Saarbruecken/Germany, 17.4.18 (2018).
2) Ahmad, M., Müller, E., Habenicht, C., Schuster, R., Knupfer, M., Büchner, B., Electron Energy Loss Spectroscopic Studies of WSe_2 Intercalated with Potassium, International Workshop on 2D Materials and Quantum Effect Devices, Pakistan Institute of Engineering and Applied Sciences (2018).
3) Boenisch, M., Calin, M., Stoica, M., Panigrahi, A., Zehetbauer, M., Waitz, T., Skrotzki, W., Eckert, J., Phase transformations in Ti-Nb alloys, Department of Materials Engineering, KU Leuven, Leuven/Belgium, 17.4.18 (2018).
4) Boenisch, M., Calin, M., Stoica, M., Panigrahi, A., Zehetbauer, M., Waitz, T., Skrotzki, W., Eckert, J., Phase transformations in Ti-Nb alloys, German Aerospace Center, Institute of Materials Research, Koeln/Germany, 15.2.18 (2018).
5) Borisenko, S., ARPES on topological and superconducting matter, Correlations in Electron Systems – from Quantum Criticality to Topology, ICTP, Trieste/Italy, 6.-17.8.18 (2018).
6) Borisenko, S., Systematic ARPES of iron-based superconductors as a test for theories, M2S-2018 Beijing/China, 19.-24.8.18 (2018).
7) Borisenko, S., ARPES from Dirac and Weyl materials, Erice Workshop 2018 "Majorana Fermions and Topological Materials Science", Erice/Italy, 21.-27.7.18 (2018).
8) Borisenko, S., Electronic structure of high-temperature superconductors, International Workshop on Recent Progress in Superconductivi Pyeongchang (Yo ngpyong)/South Korea, 8.-11.7.18 (2018).
9) Borisenko, S., Precise electronic structure of iron-based superconductors from ARPES, ICSM 2018, Antalya/Turkey, 29.4.-4.5.18 (2018).
10) Borisenko, S., ARPES on topological and superconducting matter, Correlated electron systems – novel developments, Center for Quantum Materials at the University of Minnesota, Minneapolis/USA, 16.-19.5.18 (2018).
11) Borisenko, S., Multi-Condensate Superconductivity and Superfluidity in Solids and Ultracold Gases, ICTP, Trieste/Italy, 14.-18.5.18 (2018).
12) Borisenko, S., ARPES on pnictides and cuprates, Multicomponent and Strongly Correlated Superconductivity, Nordita, Stockholm/Sweden, 7.-11.5.18 (2018).
13) Buechner, B., Anisotroper Magnetismus in -$RuCl_3$. Die Suche nach Kitaev-Spin-Fluessigkeiten und fraktionalen Spin-Anregungen, Kolloquium, Wuppertal/Germany, 8.1.18 (2018).
14) Buechner, B., Fractionalization and Transport of Spin Excitations in the Kitaev-System-$RuCl_3$, ToCoTronics 2018, Wuerzburg/Germany, 23.–27.7.18 (2018).
15) Calin, M., Gender and cultural diversity in scientific research, SELECTA Winter School, University of Cambridge, Cambridge/UK, 7.-12.1.18 (2018).
16) Calin, M., Abdi, S., Eckert, J., Gebert, A., Novel biocompatible Ni- and Cu-free Ti-based amorphous alloys: thermal stability, corrosion resistance and apatite-forming ability, 2018 Sustainable Industrial Processing Summit & Exhibition, 'Science of Intelligent and Sustainable Advanced Materials' Symposium, Rio de Janeiro/Brasil, 4.-7.11.18 (2018).
17) Calin, M., Abdi, S., Gostin, P.F., Eckert, J., Gebert, A., Biocompatible Ti-based metallic glasses: glass formation, thermal stability, corrosion resistance and apatite-forming ability, THERMEC 2018, Paris/France, 8.-13.7.18 (2018).
18) Calin, M., Bera, S., Abdi, S., Schmidt, R., Sarac, B., Eckert, J., Gebert, A., Designing bioactive Ni-free Ti-based glassy alloys for implant applications, The 12th International Conference on Bulk Metallic Glasses (BMG Xll), National University in Seoul, Seoul/ Republic of Korea, 27.-31.5.18 (2018).
19) Calin, M., Bera, S., Ramasamy, P., Sarac, B., Eckert, J., Thermoplastic formability of biocompatible Ti- and Zr-based bulk metallic glasses, 25th International Symposium on Metastablke Amorphous and Nanostructured Materials (ISMANAM), Rom/Italy, 2-6.7.18 (2018).
20) Calin, M., Bera, S., Ramasamy, P., Stoica, M, Eckert, J., Plasticity induced by minor addition of soft atoms in Ti-based bulk metallic glasses, The 7th International Conference on Advanced Materials and Structures - AMS 2018, Timisoara/Romania, 28.-30.3.18 (2018).
21) Calin, M., Boenisch, M., Pilz, S., Gebert, A., Zehetbauer, M., Eckert, J., Nanostructured SPD-processed beta-type Ti-Nb-based Materials for Implant Applications, NANO 2018, Hong Kong/China, 24.-29.6.18 (2018).
22) Ding, F., Recent progress on semiconductor entangled photon sources, Progress in Electromagnetics Research Symposium, Toyama/Japan, 1.-4.8.18 (2018).
23) Ding, F., A highly efficient entangled photon source, Chinese Institute of Electronics, Beijing/China, 28.4.18 (2018).
24) Ding, F., Near optimal entangled photon source in the solid state?, 9th International Conference on Metamaterials, Photonic Crystals and Plasmonics, Marseille/France, 24.6.-1.7.18 (2018).

25) Ding, F., Near-ideal entangled photon sources in the solid state?, cfaed Symposium "Advancing Electronics", Dresden/Germany, 19.3.18 (2018).
26) Ding, F., Semiconductor based quantum light source, Physikalisch-Technische Bundesanstalt, Braunschweig/Germany, 5.6.18 (2018).
27) Ding, F., Near-ideal entangled photon sources in the solid state?, Chinese Academy of Sciences, Beijing/China, 29.-30.1.18 (2018).
28) Faehler, S., Martensitic Microstructure: Modern Art or Science?, Institutskolloquium Max-Planck-Institut fuer Eisenforschung, Duesseldorf/Germany, 19.6.18 (2018).
29) Fink, J., Uses of Synchrotron Radiation for X-ray absorption spectroscopy, resonant elastic X-ray scattering, and inelastic resonant X-ray scattering, Winterschool on Synchrotron Techniques in Material Sience, Bose National Center for Basic Sciences, Kolkata/Indien, 25.-31.10.18 (2018).
30) Fink, J., Momentum and Doping Dependence of the Band Renormalization and Scattering Rates in Iron-based Superconductors Determined by ARPES, 12th International Conference on Materials and Mechanisms of Superconductivity and High-Temperature Superconductors, Bejing/China, 19.-24.8.18 (2018).
31) Fomin, V., Topology- and geomery-driven effects in nanoarchitectures, Seminar, Physikalisches Institut der J.-W.-Goethe-Universitaet, Frankfurt am Main/Germany, 24.10.18 (2018).
32) Fomin, V., Topology- and geomery-driven effects in nanoarchitectures, Seminar, CSEM (2018).
33) Fomin, V.M. , Topology- and geometry-driven effects in nanoarchitectures, International Workshop on Single Nanostructures, Nanomaterials, Aerogels and their Interactions: Combining Quantum Physics and Chemistry, Dresden/Germany, 27.-31.8.18 (2018).
34) Fomin, V.M., Topology- and geometry-driven effects in superconductor rolled-up nanoarchitectures, 5th International Conference and Exhibition for Nanotechnology NANOPIA 2018, Changwon/Republic of Korea, 7.-9.11.2018 (2018).
35) Fomin, V.M., Superconductivity in rolled-up nanoarchitectures: Novel phenomena, Seminar, Condensed Matter Physics Center, Universidad Autónoma de Madrid, Madrid/Spain, 7.6.18 (2018).
36) Fomin, V.M., Topology- and geometry-driven effects in nanoarchitectures, Seminar, Busan National University, Busan/Republik of Korea, 12.11.18 (2018).
37) Fomin, V.M., Geometry- and topology-driven effects in micro- and nanoarchitectures, 1st International Conference on Frontiers of Electronic Science and Technology (FEST), Chengdu/China, 12.-16.5.18 (2018).
38) Fomin, V.M., Topology- and geomery-driven effects in superconductor rolled-up nanoarchitectures, Seminar, Università degli Studi di Napoli Federico II, Naples/Italy, 17.10.18 (2018).
39) Fomin, V.M., Topology- and geometry-driven properties of advanced micro- and nanoarchitectures, Seminar, Instituto de Micro y Nanotecnología - CSIC, Madrid/Spain, 8.6.18 (2018).
40) Fomin, V.M., Novel topology-driven sensing: Quantum rings, 6th International Geo-hazards Research Symposium, Dresden/Germany, 4.-9.3.18 (2018).
41) Fomin, V.M., Topology- and geometry-driven effects in nanoarchitectures, 9th International Conference on Materials Science and Condensed Matter Physics, Chisinau/Republic of Moldova, 25.-28.9.18 (2018).
42) Fomin, V.M., Topology- and geometry-driven effects in advanced micro- and nanoarchitectures, The 20th International Conference on Superlattices, Nanostructures and Nanodevices (ICSNN 2018), Madrid/Spain, 23.-27.7.18 (2018).
43) Fomin, V.M., Topology-driven effects in advanced micro- and nanoarchitectures, 19th International Conference on Physics of Light-Matter Coupling in Nanostructures (PLMCN19), Chengdu/China, 14.-19.5.18 (2018).
44) Fomin, V.M., Topology- and geometry-driven properties of advanced micro- and nanoarchitectures, Seminar, Beijing Institute of Nanoenergy and Nanosystems, CAS, Beijing/China, 21.5.18 (2018).
45) Fomin, V.M., Topology- and geometry-driven effects in nanoarchitectures, Seminar Materials Science and Nanotechnology, Universita di Milano-Bicocca, Milan/Italy, 10.10.18 (2018).
46) Freudenberger, J., Thiel, F., Kauffmann, A., Seils, S., Heilmaier, M., Nielsch, K., Mechanical properties of solid solutions in the Au-Cu-Ni-Pd-Pt system, THERMEC'2018 (International Conference on processing and manufacturing of advanced materials processing, fabrication, properties, applications), Paris/France, 8.-13.7.18 (2018).
47) Fulga, I., Localization vS. decoherence in noisy Floquet topological chains, Workshop on Topological Phenomena in Quantum Materials, IFW Dresden, Dresden/Germany, 4.12.18 (2018).
48) Fulga, I., Localization vS. decoherence in noisy Floquet topological chains, Institute for Quantum Information, RWTH Aachen University, Aachen/Germany, 8.11.18 (2018).
49) Fulga, I., Localization vS. decoherence in noisy Floquet topological chains, 3rd WIS-MPI workshop, Jerusalem/Israel, 25.2.18 (2018).
50) Fulga, I., Scattering matrix invariants of Floquet topological phases, Niels Bohr Institute, University of Copenhagen, Copenhagen/Denmark, 15.1.18 (2018).

51) Geissler, D., Wendrock, H., Gostin, P.F., Freudenberger, J., Zimmermann, M., Gebert, A., Sample size effects on fracture toughness, cracking and stress corrosion cracking of Zr-base Bulk Metallic Glass, International Conference on Processing and Manufactering of Advanced Materials Processing, Fabrication, Properties, Applications (THERMEC 2018); Paris/France, 8.-13.7.18 (2018).
52) Gruner, M.E., Entel, P., Faehler, S., Interplay of magnetism and microstructure in functional Heusler alloys: A first-principles perspective, IOP Magnetism 2018, Manchester/UK, 10.4.18 (2018).
53) Haessler, W., MgB_2 superconducting permanent magnets prepared with nano-sized precursor powders, Materials Science and Engineering, Shibaura Institute of Technology Tokyo, Tokyo/Japan, 11.10.18 (2018).
54) Haessler, W., Some essential points in the in-situ preparation technique of MgB_2 bulks and wires, 6th International conference on Superconductivity and Magnetism 2018, Antalya/Turkey, 29.4.-4.5.18 (2018).
55) Haessler, W., MgB_2 - a technical superconductor in the shape of wires and bulks, Institute of High Pressure Physics, Polish Academy of Sciences, Warsaw/Poland, 7.3.18 (2018).
56) Hampel, S., Advanced fiber characteristics by improving with carbon nanotubes, Cotton, Bremen/Germany, 20.-23.3.18 (2018).
57) Hampel, S., Carbon nanohybrids for cancer therapy, HZDR, Dresden Rossendorf/Germany, 13.2.18 (2018).
58) Häßler, W., MgB_2 wires with high critical current density prepared by nano-sizedprecursor powders, Conference on Superconductivity and Particle Accelerators (2018).
59) Häßler, W., MgB_2 bulks and wires prepared with nano-sized precursor powders, Department of Applied Physics, Tokyo University of Agriculture and Technology, Tokyo/Japan, 10.10.18 (2018).
60) Hoffmann, V., Advances in Glow Discharge Optical Emission Spectrometry, Conference on Plasma Spectrochemistry, Amelia Island, Florida/USA, 8.-13.1.18 (2018).
61) Huehne, R., Coole Sache: Faszination Supraleitung, Schuelervortrag Gymnasium Wilkau-Hasslau, Wilkau-Hasslau/Germany, 20.6.18 (2018).
62) Hühne, R., Application of epitaxial $Pb(Mg_{1/3}Nb_{2/3})O_3$-$xPbTiO_3$(PMN-PT) thin films for strain engineering and electrocaloric studies, Center for Hybrid Nanostructures, Universität Hamburg, Hamburg/Germany, 11.12.2018 (2018).
63) Kaban, I., In situ XRD studies of structure and phase formation in undercooled liquids, Department of Mechanical Engineering, Tufts University, Medford, MA/USA, 19.3.18 (2018).
64) Kaban, I., Structure and properties of CuZrAl metallic glasses and composites, The 12th International Conference on Bulk Metallic Glasses B, Seoul National University, Seoul/Republic of Korea, 27.-31.5.18 (2018).
65) Kaban, I., Phase Formation and Microstructure Development by Non-Equilibrium Solidification, Seminar, Department of Engineering and Technology, University of Wisconsin Stout, Menomonie/WI, USA, 19.10.18 (2018).
66) Kaban, I., Non-equilibrium solidification of undercooled liquid metals, Schroers Research Group Seminar, Department of Mechanical Engineering & Materials Science, Yale University, New Haven/CT, USA, 12.10.18 (2018).
67) Karnaushenko, D., Shapeable microelectronics, 5th International Conference of Asian Union of Magnetics Societies (ICAUMS 2018), Jeju/South Korea, 3.-7.6.18 (2018).
68) Karnaushenko, D., Shapeable Microelectronics, Preistraegerkolloquium, Saechsische Akademie der Wissenschaften, Leipzig/Germany, 14.2.18 (2018).
69) Karnaushenko, D., Shape defined microelectronic functions, Symposium, Center for Bio-Convergences Spin System (BiC Spin), Daegu/South Korea, 1.6.18 (2018).
70) Karnaushenko, D., Shapeable microelectronics, Seminar at SPINTEC, CEA-UGA, Grenoble/France, 27.3.18 (2018).
71) Karnaushenko, D., Shapeable microelectronics, Special lecture for master students at Institut Neel, CNRS, Grenoble/France, 23.3.18 (2018).
72) Kataev, V., Sub-THz high-field ESR spectroscopy on spin-correlated and frustrated magnetic oxides, III. International Conference "Spin physics, spin chemistry and spin technology" (SPCT-2018), Novosibirsk/Russia, 10.-15.9.18 (2018).
73) Kataev, V., High-field magnetic resonance spectroscopies on spin-correlated quantum matter, Colloquium of the School of Physics, University of New South Wales, Sydney/Australia, 1.10.18 (2018).
74) Kataev, V., Insights into the novel magnetism of 5d spin-orbit Mott insulators from sub-THz high-field ESR spectroscopy, 3-d Joint Conference of the Asia-Pacific EPR/ESR Society and The International EPR (ESR) Society (IES) Symposium, Brisbane/Australia, 23.-27.9.18 (2018).
75) Kataev, V., Unusual magnetic continuum in the proximate spin liquid compound alpha-$RuCl_3$, International Conference on Superconductivity and Magnetism ICSM 2018, Antalya/Turkey, 29.4.-4.5.18 (2018).
76) Kosiba, K., Sopu, D., Zhang, L., Bednarcik, J., Pauly, S., Modulating Heterogeneity and Plasticity in Bulk Metallic Glasses: Role of Interfaces on Shear Banding, Korea Institute of Technology (KITECH), Seoul/Suedkorea, 25.5.18 (2018).
77) Krupskaya, Y., Molecular crystals as model systems for basic research on organic semiconductors, Institute seminar, Institute for Physics, University of Wuerzburg, Wuerzburg/Germany, 7.6.18 (2018).

78) Leistner, K., Voltage-programmable magnetism in metal oxide/metal thin films and nanoislands by electrolytic gating, Physics Colloquium of the Graz University of Technology and the Karl Franzens University of Graz, Granz/Austria, 13.11.18 (2018).
79) Leistner, K., Magnetoelectric and magneto-ionic control of magnetism in metal nanostructures, Quantum Theory of Materials, Peter Gruenberg Institut (PGI-1) und Institute for Advanced Simulation (IAS-1), Forschungszentrum Juelich/Germany, 12.12.18 (2018).
80) Leistner, K., Electrochemical Control of Epitaxial Growth and Magnetic Properties of Fe Nanostructures, AiMES (ECS and SMEQ Joint International Meeting) 2018, Cancun/Mexico, 2.10.18 (2018).
81) Leistner, K., Magneto-ionic manipulation of metal/oxide nanostructures in liquid electrolytes , International Workshop on Magneto-electric Actuation, Magneto-ionics and Related Phenomena in High-Surface Area Materials (IW-Mag 18), Barcelona/Spain, 28.5.18 (2018).
82) Leistner, K., Tailoring magnetism at the nanoscale by ionic approaches, Institut fuer Materialphysik, Westfaelische Wilhelms-Universitaet Muenster, Muenster/Germany, 7.6.18 (2018).
83) Leistner, K., Liquid solutions for energy-efficient voltage control of magnetism, RESOLV Seminar der Ruhr-Universität Bochum, Bochum/Germany, 12.11.18 (2018).
84) Li, G., Garcia Fernandez, J., Lara-Ramos, D., Barati, V., Perez-Rodriguez, N., Soldatov, I., Reith, H., Schierning, G., Nielsch, K., Fabrication of micro- thermoelectric coolers with high packing density and relevant device characterization, 667. WE-Heraeus-Seminar, Bad Honnef/Germany, 8.-11.4.18 (2018).
85) Li, G., Garcia Fernandez, J., Reith, H., Schierning, G., Nielsch, K., Micro-thermoelectric cooler devices: Design, fabrication and performance, 4th Novel Materials Symposium hosting the International Workshop on "Thermoelectric Nanomaterials", Berlin/Germany, 21.-22.6.18 (2018).
86) Linnemann, J., Determining and Distinguishing Electrochemical Capacitance and Capacity Values, e-MINDS (Cost Action MP1407), Training School Siofok/Hungary, 26.-30.3.18 (2018).
87) Ma, L., Optical geometric phase in Moebius ring and asymmetric microtube cavities, DPG Spring Meeting 2018, Berlin/Germany, 11.-16.3.18 (2018).
88) Ma, L.B., Optical coupling in on-chip integrable microtube cavities, Workshop on Low Dimensional Semiconductor Nanostructures and Integrated Devices, Changsha/China, 9.-11.5.18 (2018).
89) Ma, L.B., Photon-plasmon coupling in optoplasmonic microtube cavities, International Workshop on Single Nanostructures, Nanomaterials, Aerogels and their Interactions: Combining Quantum Physics and Chemistry, Dresden/Germany, 27.-31.8.18 (2018).
90) Medina Sanchez, M., Medical microbots: Challenges and opportunities, Japanese-German Frontiers of Science Symposium, Kyoto/Japan, 4.-7.9.18 (2018).
91) Medina-Sanchez, M., Microrobotics based on sperm cells: Control and imaging issues, Symposium "Bio-hybrid organic machines: an ambitious bridge between bioengineering and robotics" - 40th International Conference of the IEEE Engineering in Medicine and Biology Society EMBC2018, Honolulu/USA, 17.-21.7.18 (2018).
92) Medina-Sanchez, M., Sperm-hybrid micromotors towards in vivo fertilization and drug delivery, Workshop on Bio-inspired Magnetic Systems, Exeter/United Kingdom, 9.-11.7.18 (2018).
93) Medina-Sanchez, M., Hybrid sperm micromotors for targeted drug delivery, MCRC Workshop on Sperm Research for Cancer Treatment, Manchester/United Kingdom, 19.1.18 (2018).
94) Medina-Sanchez, M., Spermbots as a new strategy for artificial fertilization , 61st CeRA Seminar, University Clinique Muenster, Muenster/Germany, 7.3.18 (2018).
95) Medina-Sanchez, M., Cellular cargo delivery: Towards assisted fertilization by sperm-carrying micromotors, Gameeting, Dresden/Germany, 27.2.18 (2018).
96) Medina-Sanchez, M., Sperm micromotors and its potential to improve ART success and reproductive health, 20th European Testis Workshop, Obidos/Portugal, 25.5.18 (2018).
97) Melzer, M., Shapeable magnetic sensors, Seminar, Abteilung Zerstoerungsfreie Pruefung, Bundesanstalt fuer Materialforschung und -pruefung (BAM), Berlin/Germany, 12.3.18 (2018).
98) Melzer, M., Shapeable magnetic sensorics, IFW Dresden - NSYSU Taiwan Advanced Lecture Course, Dresden/Germany, 18.-23.7.18 (2018).
99) Melzer, M., Stretchable and imperceptible magnetoelectronics, 6th International Conference on Superconductivity and Magnetism, Antalya/Turkey, 29.4.-4.5.18 (2018).
100) Neu, V., Quantitative MFM - measuring stray field landscapes of magnetic and superconducting samples on the nanometer scale, International Conference on Tunneling through Nanoscience, Ravello/Italy, 17.- 20.10.18 (2018).
101) Neu, V., Thomas, A., Nielsch, K., Magnetic Force Microscopy - a quantitative method for measuring magnetization textures on the nanoscale, Seminar, Institut fuer Physik, Universitaet Greifswald, Greifswald/Germany, 4.12.18 (2018).

102) Neu, V., Vock, S., Reichel, L., Faehler, S., Schultz, L., Schaefer, R., Nielsch, K., Stripe domains in tetragonally distorted Fe-Co-C films with perpendicular anisotropy, International Conference on Advances in Magnetics, La Thuile/Italy, 4.-7.2.18 (2018).
103) Neu, V., Vock, S., Reichel, L., Mueller, A., Faehler, S., Schaefer, R., Suess, D., Schultz, L., Nielsch, K., Quantitative MFM - probing magnetization structures on the nanoscale, IEEE Confernerence on Advances in Magnetism (AIM'18), La Thuile/Italy, 4.-7.2.18 (2018).
104) Nielsch, K., Mikrostrukturierte Peltierkühler für Integrierte Bauelemente, Werkstoff-Kolloquium 2018: Effiziente Energiewandlung und –speicherung Institut für Werkstoff-Forschung des Deutschen Zentrums für Luft- und Raumfahrt, Köln/Germany, 4.12.18 (2018).
105) Nielsch, K., IntegratedMicro-Thermoelectric Coolers by Template Assisted Electrochemical Deposition, 256th ACS National Meeting and Exposition Boston/USA, 19.-23.8.18 (2018).
106) Nielsch, K., Why are Quantum Materials essential for Thermoelectric Energy Conversion? , Kolloquium, Institut für Physik, Universität Augsburg, Augsburg/Germany, 14.5.18 (2018).
107) Nielsch, K., Why are Quantum Materials essential for Thermoelectric Energy Conversion? , 37th International Conference on Thermoelectrics - ICT2018 Caen/Frankreich 1.-5.7.18 (2018).
108) Nielsch, K., Why are Quantum Materials essential for Thermoelectric Energy Conversion?, Science Talk /Kolloquium, Center for Nanointegration Duisburg-Essen (CENIDE), Essen/Germany, 15.1.18 (2018).
109) Nielsch, K., Why are Quantum Materials essential for Thermoelectric Energy Conversion?, Kolloquiums Vortrag am (Leibniz) - Paul Drude Institut Berlin, Berlin/Germany, 8.6.18 (2018).
110) Orava, J., Fast-crystallization-rate window in phase-change alloys, 2nd Sino-German Symposium on Electronic and Memory Materials, Xi'an/China, 5.-7.9.18 (2018).
111) Otalora, J.A., Lindner, J., Schultheiss, H., Kakay, A., Thomas, A., Nielsch, K., Towards a three dimensional curvilinear magnonic device, Deutsche Physikalische Gesellschaft (DPG), Berlin/Germany, 11.-16.3.18 (2018).
112) Otalora, J.A., Lindner, J., Schultheiss, H., Kakay, A., Thomas, A., Nielsch, K., Towards a three dimensional curvilinear magnonic device, Physics Faculty Seminars on Modern Trends in Physics Research, ADAM Mickiewcz University Poznan, Poznan/Poland, 11.7.18 (2018).
113) Park, G., Tynell, T.P, Thomas, A., Nielsch, K., State of the art TMDs materials, Korea Institute of Technology, Korea/South Korea, 1.8.18 (2018).
114) Park, G., Tynell, T.P., Thomas, A., Nielsch, K., ALD Protocols: Atomic layer deposition methods and way for fabrication of TMDs materials, Korea Institute of Technology, Korea/South Korea, 1.8.18 (2018).
115) Pauly, S., Gustmann, T., Deng, L., Kuehn, U., Selektives Laserschmelzen von metallischen Glaesern und Formgedaechtnislegierungen, Institut fuer Werkstofftechnik im Bereich des FB 15 Maschinenbau, Universitaet Kassel, Kassel/Germany, 4.6.18 (2018).
116) Perez Rodriguez, N., Chirkova, A., Wolf, C., Skokov, K.P., Woodcock, T.G., Gutfleisch, O., Baranov, N.V., Nielsch, K., Schierning, G., Seebeck effect at phase transitions- Order, disorder and entropy, CCMR 2018, Collaborative Conference on Materials Research, Incheon/South Korea, 25.-29.6.18 (2018).
117) Pöhl, A., Präparation galliumsensibler Materialien - FIB. Ultramikrotom und goldenes Händchen, IFW Dresden, Dresden/Germany, 10.4.18 (2018).
118) Pöhl, A., Präparation galliumsensibler Materialien - FIB. Ultramikrotom und goldenes Händchen, 14. Präparatorentreffen Berlin/Brandenburg, Institut für Optik und Atomare Physik der Technischen Universität Berlin, Berlin/Germany, 24.04.2018 (2018).
119) Popov, A., Spectroelectrochemistry of the Exohedrally and Endohedrally Functionalized Carbon Cages, 69th Annual Meeting of International Society of Electrochemistry (2018).
120) Popov, A., Endohedral metallofullerenes as robust single molecule magnets, International Winterschool on Electronic Properties of Novel Materials (IWEPNM 2018) (2018).
121) Popov, A., Fullerene-based single molecule magnets: bulk and surface magnetism, Center for Quantum Nanoscience at Ewha Womans University (2018).
122) Popov, A., Fullerene-based single molecule magnets: bulk and surface magnetism, 233th Eletrochemical Society Meeting (2018).
123) Popov, A., Giant Exchange Interactions between Lanthanide Ions inside Fullerene Cages: Towards SMMs with High Blocking Temperatures, International Conference on Coordination Chemistry (ICCC2018), Sendai/Japan, 30.7.-4.8.18 (2018).
124) Rellinghaus, B., Pohl, D., Towards quantitiative mapping of 3D spin textures in the transmission electron microscope, 3rd Sino-German Symposium on Advanced Electron Microscopy of Interface Structures and Properties of Materials, Peking/VR China, 24.-28.9.18 (2018).
125) Rellinghaus, B., Pohl, D., Schneider, S., Wolf, D., Lubk, A., Quantitiative Mapping of Spin Textures in the transmission electron microscope, International Workshop on "Future Perspectives on Novel Magnetic Materials", Santorini Island/Greece, 29.5.-3.6.18 (2018).

126) Schaefer, R., Micromagnetism, Magnetic Microstructure and their Magneto-Optical analysis, Semi-Plenary talk at the International Conference on Magnetic Materials and Applications (ICMAGMA-2018), NISER-Bhubaneswar, Jatni/India, 9.-13.12.18 (2018).
127) Schaefer, R., Magnetic Measurements, Lecture at the IEEE Magnetics Society Summer School 2018, Quito/Ecuador, 3.-8.6.18 (2018).
128) Schaefer, R., Imaging of Magnetic Domain Dynamics at Power Frequency, Semi-Plenary talk at the International Conference on Magnetic Materials and Applications (ICMAGMA-2018), ISER-Bhubaneswar, Jatni/India, 9.-13.12.18 (2018).
129) Schaefer, R., Soldatov, I., Imaging of Magnetic Domain Dynamics at Power Frequency, 2018 TMS Annual Meeting and Exhibition, Phoenix/USA, 11.-15.3.18 (2018).
130) Schaefer, R., Soldatov, I., Micromagnetism, Magnetic Microstructure and their Magneto-Optical analysis, Lecture at the Department of Physics, Universidad Tecnica Federico Santa Maria, Valparaiso/Chile, 25.9.18 (2018).
131) Schaefer, R., Soldatov, I., Micromagnetism, Magnetic Microstructure and their Magneto-Optical analysis, Plenary Lecture at the International Workshop on Magnetic Materials and Nanomaterials, Boumerdes/Algeria, 1.-4.10.18 (2018).
132) Schaefer, R., Soldatov, I., Micromagnetism, Magnetic Microstructure and their Magneto-Optical analysis, Seminar at the Department fuer Geo- und Umweltwissenschaften, Ludwig-Maximilians-Universitaet Muenchen, Muenchen/Germany, 18.5.18 (2018).
133) Schaefer, R., Soldatov, I., Micromagnetism, Magnetic Microstructure and their Magneto-Optical analysis, Lecture at the Department of Physics, Universidad Santiago de Chile, Santiago/Chile, 24.9.18 (2018).
134) Schierning, G., Nielsch, K., Integrated micro-thermoelectric coolers by template assisted electrochemical deposition, International Conference on Processing & Manufacturing of advanced materials: Processing, Fabrication, Properties, Applications (Thermec 2018), Paris/France, 8.-13.7.18 (2018).
135) Schmidt, O.G., Microtubular nanomembrane devices: From Nanophotonics to nanorobotics, 19th EuroSciCon Conference on Nanotechnology and Smart Materials, Amsterdam/The Netherlands, 4.-6.10.18 (2018).
136) Schmidt, O.G., Smart and soft motile microbots, Workshop on Soft Robotics at Small Scales Livorno/Italy, 24.4.18 (2018).
137) Schmidt, O.G., 3D microtubular architectures and devices, 2nd International Workshop on Advanced 3D Patterning, Dresden/Germany, 4.-5.10.18 (2018).
138) Schmidt, O.G. , Shrinking the unshrinkable: From visionary concepts to autonomous micromotors, XPOMET - Die Convention für Innovation und Hightech der Medizin, Leipzig/Germany, 21.-23.3.18 (2018).
139) Schmidt, O.G., Quantum dot quantum light sources, International Conference on Low-Dimensional Quantum Materials, Snowbird, Utah/USA, 10.-14.3.18 (2018).
140) Schmidt, O.G., Laudatio anlaesslich der Verleihung des Wilhelm-Ostwald-Nachwuchspreises 2017, Preistraegerkolloquium, Saechsische Akademie der Wissenschaften, Leipzig/Germany, 14.2.18 (2018).
141) Schmidt, O.G., Hybrid micro- and nanotubular devices for on and off-chip applications, International Conference on Functional Nanomaterials and Nanodevices 2018, Vienna/Austria, 3.-5.9.18 (2018).
142) Schmidt, O.G., Nanomembrane microtubular devices for on- and off-chip biomedical research and development, 6th European BioPharma Congress, Amsterdam/The Netherlands, 18.-19.9.18 (2018).
143) Schmidt, O.G., Cellular cyborg devices for on and off chip applications, Gameeting, Dresden/Germany, 27.2.18 (2018).
144) Schmidt, O.G., Swimming microrobots, MCRC Workshop on Sperm Research for Cancer Treatment, Manchester/United Kingdom, 19.1.18 (2018).
145) Schmidt, O.G., Hybrid micro- and nanodevices: Bridging research across disciplines, Workshop MS 60.4 ueber Neues in Physik, Chemie und Intelligenz Chemnitz/Germany, 23.4.18 (2018).
146) Schmidt, O.G., Microtubular nanomembranes: From 3D device architectures to cellular cyborg machinery, Colloquium, Leibniz Institute for New Materials, Saarbruecken/Germany, 8.5.18 (2018).
147) Schmidt, O.G., Self-assembled microtubular devices, Cfaed Summer Festival, Dresden/Germany, 29.8.18 (2018).
148) Schmidt, O.G., Self-assembled microtubular devices: From energy storage to cellular cyborg machinery, International Conference on Micro Nano Engineering 2018, Copenhagen/Denmark, 24.-27.9.18 (2018).
149) Schmidt, O.G., Science and fiction: From micromotors to spermbots, Edwards, Steptoe… and Dr Kershaw: An SRF symposium to mark the 40th anniversary of IVF, Manchester/United Kingdom, 25.7.18 (2018).
150) Schmidt, O.G., Nanophotonics with Nanomembranes, CEITEC Seminar, Brno University of Technology, Brno/Czech Republic, 30.10.18 (2018).
151) Schmidt, O.G., Nanophotonics with nanomembranes, Physics Department Colloquium, Indian Institute of Technology Delhi, New Delhi/India, 26.10.18 (2018).
152) Schmidt, O.G., Since and fiction: From micromotors to biomedical applications, 3rd Annual Conference of Indian Society of Nanomedicine, New Delhi/India, 25.-27.10.18 (2018).
153) Schmidt, O.G., Nanomembrane materials: From technologies to applications, Faculty Colloquium, TU Chemnitz, Chemnitz/Germany, 21.6.18 (2018).

154) Schmidt, O.G., Nanomembranes for on- and off-chip applications, International Workshop on Nanomembrane Origami Technology (2018).
155) Schmidt, O.G., Microtubular NEMS for on- and off-chip microfluidic applications, Bioselect Conference: Lab-on-a-Chip and Microfluidics Europe 2018, Rotterdam/The Netherlands, 5.-6.6.18 (2018).
156) Schmidt, O.G., Microtubular nanomembrane devices: From energy storage to reproduction technologies, 25th Nano Congress for Future Advancements, Dublin/Ireland, 16.-18.8.18 (2018).
157) Schneider, S., Wolf, D., Stolt, M.J., Jin, S., Pohl, D., Rellinghaus, B., Schmidt, M., Negi, D., Rusz, J., Buechner, B., Goennenwein, S.T.B., Nielsch, K., Lubk, A., Quantitative Mapping of the Skyrmion Spin Texture in FeGe, "Spins, waves and Interactions" seminar, Greifswald/Germany , 28.-30.8.18 (2018).
158) Soldatov, I., Magneto-optical Domain Imaging, Institut für Materialwissenschaft, Technische Universitaet Darmstadt, Darmstadt/Germany, 21.9.18 (2018).
159) Soldatov, I., Magneto-optical Domain Imaging, Fakultaet fuer Naturwissenschaften, Institut fuer Physik , Technische Universitaet Chemnitz, Chemnitz/Germany, 6.12.18 (2018).
160) Thomas, A., Memristive Tunnel Junctions, Werkstoffwissenschaftliches Kolloquium Universitaet Erlangen-Nuernberg, Nuernberg/Germany, 24.4.18 (2018).
161) Thomas, A., Atomic layer deposition at IFW, ALD Symposium des ALD Lab Saxony, Dresden/Germany, 10.12.2018 (2018).
162) Waske, A., Dzekan, D., Sellschopp, K., Stork, A., Nielsch, K., Faehler, S., Topology of Thermomagnetic Generators for the Conversion of low Temperature Waste Heat to Electricity, MRS Fall Meeting, Boston/USA, 25.-30.11.18 (2018).
163) Weser, R., Schmidt, H., Hochauflösende Analyse von SAW-Wellenfeldern bei hohen Temperaturen, 15. Polytec Vibrometer Anwenderkonferenz 2018, Waldbronn/Germany, 13.-14.11.18 (2018).
164) Winkler, A., Einführung in dieakustoelektronische Mikrofluidik, Vorlesung im Rahmen der Vorlesungsreihe „Biotechnologische Verfahren", Institut für Naturstofftechnik, Technische Universität Dresden, 21.06.2018 (2018).
165) Winkler, A., Einführung in die akustoelektronische Mikrofluidik, Vorlesung im Rahmen der Vorlesungsreihe „Mikrobiologie", Institut für Naturstofftechnik, Technische Universität Dresden, Dresden/Germany, 30.01.18 (2018).
166) Winkler, A., Acoustofluidics - acoustically-driven fluidics, Graduiertenkolleg Pulmosens, Research training group GRK 2203, Universitaet Ulm, Ulm/Germany, 17.5.18 (2018).
167) Winkler, A., SAW-based fluidatomization using mass-producible chip devices, Tropos Leipziger Meterologisches Kolloquium, Leibniz Institut für Troposphärenforschung e.V. Leipzig, 31.05.2018 (2018).
168) Winkler, A., Surface acoustic wave(SAW) Sensor and Actuator devices an issues in their realization, Kolloquium des SFB 1261 – Biomagnetic Sensing, Institut für Materialwissenschaft der Universität Kiel, 14.06.2018 (2018).
169) Winkler, A., Nanobeben auf Mikrochips, Tag der Naturwissenschaften am Städtischen Gymnasium Riesa, Riesa/Germany, 3.5.18 (2018).
170) Wolff, U., Ambrozic, B., Zuzek Rozman, K., Leistner, K., Nielsch, K., Sturm, S., In-Situ Observation of the Reversible Electrochemical Deposition of Fe in a Transmission Electron Microscope, Wigner Research Centre for Physics, Budapest/Hungary, 16.10.18 (2018).
171) Wolter-Giraud, A., Magnetic field and pressure induced magnetism of the Kitaev system alpha-$RuCl_3$, APS March Meeting 2018 Los Angeles/USA, 5.-9.3.18 (2018).

Patents 2018

Issues of patents (issue decision date)

DE 10 2018 200 483.8 (11707 DE)	Thermoelektrisches Material und Verfahren zur Herstellung eines thermoelektrischen Materials (08.12.2018) *Inventors:* Gabi Schierning, Felix Thiel, Jochen Friedrich, Christian Reimann, Maximilian Beier
EP 15 787 488.4 (11426 EP)	Kompakter Kondensator und Verfahren zu seiner Herstellung (27.08.2018) *Inventors:* Oliver G. Schmidt
DE 10 2016 118 953.7 (11621 DE)	Akustoelektrischer Oszillator (13.06.2018) *Inventors:* Günter Martin
KR 10-2013-7010515 (11009 KR)	Hochfeste, bei Raumtemperatur plastisch verformbare und mechanische Energie absorbierende Formkörper aus Eisenlegierungen (08.01.2018) *Inventors:* Uta Kühn, Jürgen Eckert, Uwe Siegel, Julia Kristin Hufenbach, Min Ha Lee
DE 10 2014 105 061.4 (11407 DE)	Wandler für akustische Oberflächenwellen mit einer natürlichen Vorzugsrichtung bei der Wellenabstrahlung (27.03.2018) *Inventors:* Günter Martin
CN 201480015934.0 (11309 CN)	Wellenleiter-Resonator-Bauelement und Verfahren zu seiner Herstellung (04.09.2018) *Inventors:* Stefan Böttner, Oliver G. Schmidt
14/773,064 (11309 US)	Wellenleiter-Resonator-Bauelement und Verfahren zu seiner Herstellung (04.05.2018) *Inventors:* Stefan Böttner, Oliver G. Schmidt
EP 13736529.2 (11213 EP)	Verfahren zur kontrollierten Bewegung von motilen Zellen in flüssigen oder gasförmigen Medien (25.07.2018) *Inventors:* Veronika Magdanz, Samuel Sanchez Ordonez, Oliver G. Schmidt
KR 10-2013-7016712 (11017 KR)	Verfahren zur Wärmebehandlung von hochfesten Eisenlegierungen (22.06.2018) *Inventors:* Julia Kristin Hufenbach, Stefanie Kohler, Uta Kühn, Jürgen Eckert
JP 2017-510913 (11418 JP)	Capacitor and Process for producing thereof (26.10.2018) *Inventors:* Daniel Grimm, Oliver G. Schmidt, Ivoyl Koutsaroff, Shoichiro Suzuki, Koichi Banno
JP 2017-510914 (11419 JP)	Roll-up Capacitor with Perovskite Dielectric and Process for producing thereof (26.10.2018) *Inventors:* Daniel Grimm, Oliver G. Schmidt, Shoichiro Suzuki, Akira Ando, Koichi Banno
EP15732568.9 (11414 EP)	Batterieträger (02.08.2017) *Inventors:* Markus Herklotz, Jonas Weiß, Lars Giebeler, Michael Knapp

Priority patent applications (priority date)

11707 DE	Thermoelektrisches Material und Verfahren zur Herstellung eines thermoelektrischen Materials (12.01.2018) *Inventors:* Gabi Schierning, Felix Thiel, Jochen Friedrich, Christian Reimann, Maximilian Beier
11818 DE	Probenadapter mit Steuerungselektronik (24.10.2018) *Inventors:* Lars Giebeler, Matthias Uhlemann
11827 DE	Verfahren zur Herstellung von einteiligen Bauelementen aus Formgedächtnismaterial sowie einteilige Bauelemente aus Formgedächtnismaterial und deren Verwendung (13.11.2018) *Inventors:* Simon Pauly, Konrad Kosiba, Uta Kühn
11808 DE	Akustofluidische Bauelemente und Verfahren zu ihrer Herstellung (22.05.2018) *Inventors:* Andreas Winkler, Christine Henze, Thomas Gemming

Graduation of young researchers

PhD Theses 2018

Nikolay Bogdanov	Anisotropic Interactions in Transition Metal Oxides, TU Dresden
Ariane Brandenburg	Synthese und Derivatisierung endohedraler Clusterfullerene, TU Dresden
Yan Chen	Semiconductor quantum dots entangled photon sources: From wavelength tunablity to high brightness
Alisa Chirkova	Magnetocaloric properties and microstructure of FeRh-based alloys, TU Dresden
Tobias Gustmann	Selektives Laserschmelzen von Kupfer-Basis-Formgedächtnislegierungen, TU Dresden
Rhea Kappenberger	Das System LaFeAsO in Poly- und Einkristallen, TU Dresden
Denis Krylov	Magnetic studies of endohedral fullerenes, TU Dresden
Alexander Lau	Symmetrie-enriched topological states of matter in insulators and semimetals, TU Dresden
Torsten Mix	Die L10-Struktur in Mn-Ga- und Mn-Al-Ga-Legierungen: magnetische Eigenschaften und Phasenumwandlungen, TU Dresden
Eric Müller	Electron energy-loss spectroscopy on transition-metal dichalcogenides and alpha-RuCl3, TU Dresden
Patrick Pahlke	Wachstum, Pinningeigenschaften und Granularität von dicken YBa2Cu3O7-δ-Schichten auf texturierten metallischen Substraten, TU Dresden
Ekaterina Pärschke	Interplay of Strong Correlation, Spin-Orbit Coupling and Electron-Photon Interactions in Quasi-2D Iridium Oxides, TU Dresden
Stefan Pilz	Thermomechanische Behandlung und mechanisches Verhalten von ß-Ti-Nb-Legierungen für den Einsatz als Osteosynthesematerial, TU Dresden
Stefan Richter	Neue Schichtarchitekturen Fe-basierter Supraleiter: Epitaktische Ba(Fe1-xNix)2As2 Dünnschichten und aufgerollte FeSe1–xTex Mikrostrukturen, TU Dresden
Jan Sander	Selektives Laserschmelzen hochfester Werkzeugstähle, TU Dresden
Christin Schlesier	Synthese und magnetische Eigenschaften von Dysprosium-Nitrid-Clusterfullerenen, TU Dresden
Frank Schmidt	Die Bedeutung der Segregations- und Oxidationsneigung Seltener Erden für die Einstellung hartmagnetischer intermetallischer Phasen in SmCo-basierten Nanopartikeln, TU Dresden
Romy Schmidt	Poröses Ti-45Nb als Träger Sr-modifizierter Hydroxylapatit-Schichten, TU Dresden
Holger Schwab	Selektives Laserschmelzen der Legierung 5553, TU Dresden
Hafiz Rub Nawaz Shahid	Strengthening of Al-based composites by microstrucral modification, TU Dresden
Max Sieger	Pinningmechanismen in YBa2Cu3O7-δ-Dickschichten mit nanoskaligen Fremdphasen, TU Dresden
Benjamin Stafford	Novel Pinning Landscapes in ISD-Buffered Coated Conductors, TU Dresden
Pei Wang	Al-3.5Cu-1.5Mg-1Si alloy and related materials produced by selective laser melting, TU Dresden
Yin Yin	Photon-plasmon coupling in optoplasmonic microtube cavities, TU Chemnitz
Josephine Zeisig	Neuartige FeCrMoVC-Legierungen für Hochleistungswerkstoffe – als Massiv- und Laserauftragschweißwerkstoffe, TU Dresden

Diploma and Master Theses 2018

Rorith Archaya	Quantum Transport Measurements in Dirac Semimetals, TU Dresden
Lukas Beyer	Herstellung magnetokalorischer Kompositdrähte mittels Powder-in-Tube-Verfahren, TU Dresden
Daniel Dzekan	Experimentelle Charakterisierung eines thermomagnetischen Generators, TU Dresden
Armita Farsiani	Soft robotic prosthetic arm, applying feedback from GMR sensors, TU Dresden
Matthias Gillig	Transportuntersuchungen an Weyl-Halbmetallen, TU Dresden
Lukas Graf	Transport properties of thin transition-metal dichalcogenide nanostructures, TU Dresden
Heiko Hädrich	Magnetkraftmikroskopie von magnetischen Nanopartikeln, Univ. Potsdam
Friedemann Wieland Heyn	Verarbeitung industrieller Silizium-Sägeabfälle zu nutzbaren Energiematerialien für die thermoelektrische Anwendung, TU Dresden
Spandana Jagadish	Simulation of temperature changes due to joule heating in nanostructures on different substrates around L-helium temperatures, TU Chemnitz
Felix Kern	Development and Implementation of Liquid He Cryo Electron Microscopy and First Experiments, TU Dresden
Alexander Kunzmann	Thermoelectric transport measurements at the metal-insulator transition of VO2 thin films, TU Dresden
Ada Lili Alvarado Leanos	Nanostructures for enhanced solid-state quantum light emitters, TU Dresden
Alaleh Mirhajivarzaneh	Giant magneto impedance sensors for tracking of microscopic self-propelled objects, TU Dresden
Yang Nan	Micro swimmer with integrated soft robotic arm, TU Chemnitz
Saghar Nazari	Giant magneto impedance element as a tool for mechanical characterization of Nano-objects, TU Dresden
Eric Pankenin	Novel sacrificial layers for rolled-up capacitors, TU Chemnitz
Johannes Schultz	Entwicklung der inelastischen Elektronenptychographie, TU Dresden
Mohammed Shehata	Quantum Transport Measurements in Weyl Semi Metals, TU Dresden
Lena Spillecke	NMR-Messungen an LiCuTe und LiCuSe, TU Dresden
Jingyi Sun	Making plasmonic dimer structure with electron beam lithography, TU Chemnitz
Pen Sun	Herstellung und Charakterisierung von dichalcogeniden Nanodrähten der Bi2Se3 Gruppe, TU Dresden
Yuanjun Tang	Lokale Analyse der Magnetisierungsprofile optisch geschriebener Domänen in FePt-Schichten, TU Dresden
Daniel Waas	Photoelektronenspektroskopie an organischen Ladungstransfergrenzflächen, TU Dresden
Martin Tränkner	Entwicklung und Konstruktion einer Hall-Effekt-Messstation; Hochschule Zittau/Görlitz
Sitao Wang	Fabrication microbatteries from 2D nanosheets based on Si/Ge, TU Dresden
Christoph Wellm	Microwave Absorption Studies on the Frustrated Kitaev Model Candidate Material α-RuCl3, TU Dresden
Johannes Winter	Herstellung und Charakterisierung von Titan-Tantal-basierten Hochtemperaturformgedächtnislegierungen, TU Dresden

Calls and Awards 2018

Calls on Professorships

Madhav Prasad Ghimire	Tribhuvan University in Kathmandu, Nepal, Associate Professorship
Ching-Hao Chang	National Cheng Kung University (NCKU), Taiwan, Assistant Professorship with Tenure Track
Seung-Ho Baek	Changwon National University, South Korea, Associate Professorship
Julia Körner	Leibniz Universität Hannover W2-Professur für mikro- und nanointegrierte Systeme
Simon Pauly	University of Applied Sciences Aschaffenburg

Important external awards

Simon Pauly	Masing-Gedächtnis-Preis 2018 der DMG
Oliver G. Schmidt	Gottfried-Wilhelm-Leibniz-Preis 2018 of the German Research Foundation (DFG)
Jeroen van den Brink	NOW-von Humboldt Award of the Netherlands Organization for Scientific Research

Internal IFW awards

Yan Chen	Tschirnhaus-Medal of the IFW for excellent PhD theses
Tobias Gustmann	Tschirnhaus-Medal of the IFW for excellent PhD theses
Alexander Lau	Tschirnhaus-Medal of the IFW for excellent PhD theses
Josephine Zeisig	Tschirnhaus-Medal of the IFW for excellent PhD theses

Scientific conferences and colloquia 2018

January 29–31	EPSQMat 2018: International Workshop on Electron and photon spectroscopies of quantum materials: status and perspectives, IFW Dresden
January 31	Honorary Colloquium on the occasion of the 80th birthday of Prof. Dr. Jörg Fink
February 1	Workshop of the DFG Priority Programme 1458 “High Temperature Superconductivity in Iron Pnictides“, IFW Dresden
March 11–16	Joint Conference of the Condensed Matter Divisions of the DPG and EPS – Session "Geometry and Topology-Controlled Nanoarchitectures", organized by Prof. Dr. V. Fomin, IFW Dresden – Symposium “Topology in Condensed Matter Physics (SYTO)”, Co-organizer Prof. Dr. Jeroen van den Brink, IFW Dresden – Symposium “Voltage Control of Functional Interfaces: Magneto-ionic Meet Memristive Systems (SYVC)”, Co-organizer Dr. Karin Leistner, IFW Dresden
March 28	Laureate Colloquium on the occasion of the Gottfried Wilhelm Leibniz Prize 2018 awarded to Prof. Dr. Oliver Schmidt
April 8–11	667. WE-Heraeus-Seminar on System-oriented approach to thermoelectrics: Materials – Interfaces – Devices in Bad Honnef, Germany
Aug. 28–3	Spin, waves & interactions 2018, Greifswald, Germany
Nov. 8–9	Workshop SPINTEC-IFW at SPINTEC Grenoble, France
Oct. 1–2	ECASIA19: 18th European Conference on Applications of Surface and Interface Analysis, Dresden
Dec. 4–5	UKRATOP Workshop "Topological Phenomena in Quantum Materials", IFW Dresden

IFW-Colloquia

Prof. Dr. Guenter Reiss, Bielefeld University,Thermal charge and spin currents in magnetic nanostructures, 16.05.2018

Prof. Dr. Bertram Batlogg, ETH Zürich, Transport and Trapping in Organic Molecular Crystals, 22.05.2018 (together with IAPP at TU Dresden)

Prof. Dr. Thomas Heine, TU Dresden, Where less is more: rational materials design with two-dimensional materials, 26.09.2018

Prof. Dr. Alessandro Troisi, Univ. of Liverpool, Designing organic semiconductors via model reduction, 20.11.2018

Prof. Dr. Harald Giessen, Univ. of Stuttgart, Watching plasmons spin on atomically flat single crystalline gold, 06.12.2018

Quantum Matter Colloquia

Prof. Xenophon Zotos, Univ. of Crete, Developments in the dynamics of low dimensional quantum magnets, 17.01.2018

Prof. Dr. Hitoshi Ohta, Kobe Univ., Japan, Recent developments of multi-extreme THz ESR – the high-sensitive membrane ESR and the high pressure ESR, 19.03.2018

Prof. Gwendal Feve, Univ. Pierre and Marie Curie, ENS, Paris, Quantum optics experiments with electrons, 21.03.2018

Prof. Eslam Ibrahim, Sohag University, Egypt, Recent Advances in Thermoelectric Materials: New Strategies for Achieving High Figure of Merit, 11.04.2018

Prof. Shahal Ilani, Weizmann Institute of Science, Rehovot, Israel, Quantum Design in Carbon Nanotubes, 25.04.2018

Prof. Beatriz Noheda,Univ. of Groningen, Functional domain walls in epitaxial oxides, 20.06.2018

Prof. Milan P. Allan, Leiden Univ., Netherlands, Universality of pseudogap and emergent order in lightly doped Mott insulators, 07.11.2018

Guests and Scholarships

Guest scientists (stay of 4 weeks and more)

Name	Home Institute	Home country
Dr. Allison, Morgan Charles	Univ. Sydney	Australia
Dr. Amigo, Maria Lourdes	Univ. de Cuyo	Italy
Dr. Amusan, Akinwumi Abimbola	Otto-von-Guericke Univ.Magdeburg	Nigeria
Dr. Baek, Seung Ho	National Univ. Korea	South Korea
Bahrami, Amin	Univ. of Mexico City	Islam. Rep. Iran
Dr. Barros, Leones Rita Daniela		Portugal
Dr. Bashlakov, Dmytro	National Academy of Sciences of Ukraine	Ukraine
Dr. Bastien, Gael	Univ. Grenoble Alpes	France
Benkocka, Monika	Univ. Usti nad Labem	Czech Rep.
Bhandari, Shalika Ram	Tribhuvan Univ. Nepal	Nepal
Dr. Chang, Ching-Hao	NCKU Taiwan	China
Dr. Craco, Luis	Univ. Federal de Mato Grosso	Brazil
Cutrano, Carla	Univ. of Inoannina	Italy
Dr. Darinskiy, Alexander	Institute for Crystallography Moscov	Russia
Prof. Dr. Dhagat-Jander, Pallavi	Oregon State Univ.	India
Dr. Dioguardi, Adam Paul	Los Alamos National Lab.	USA
Dr. Egunov, Aleksandr	Institute of Materials Science of Mulhouse	Russia
Dr. Ertugrul, Onur	Izmir Katip Celebi Univ. Türkei	Turkey
Fang, Shiang	Univ. of Harvard	China
Prof. Ganeev, Alexander	St. Petersburg State Univ.	Russia
Gonzalez Martinez, Ignacio G.	Center for Polymers and Carbon Materials Zabrze	Mexico
Dr. Gubal, Anna	St. Petersburg State Univ.	Russia
Dr. Guzzinati, Giulio	Univ. Antwerpen	Italy
Dr. He, Ran	Univ. of Houston	China
Ivshin, Kamil	Arbuzov Institute, Kazan	Russia
Izadi, Sepideh	Univ. of Isfahan	Iran, Islam. Rep.
Prof. Jander, Albrecht	Oregon State Univ.	USA
Jithin Vishnu, Jithin Vishnu	VIT Univ.	India
Prof. Kamieniarz, Grzegorz	Univ. Poznan	Polen
Dr. Kandpal, Hemchandra	Indian Institute of Technology Roorkee	India
Dr. Karmakar, Koushik	Indian Institute of Pune	India
Dr. Kataeva, Olga	Arbuzov Institute, Kazan	Russia
Dr. Kvitnytska, Oksana	Verkin Institute Kharkiv	Ukraine
Dr. Lee, Jae-Ki	Korea Electrotechn. Research Institute	South Korea
Prof. Dr. Lee, Kwan-Woo	Korea Univ.	South Korea
Dr. Lee, Minho	Korea Electrotechn. Research Institute	South Korea
Dr. Li, Yuan	Chinese Academy of Science, Beijing	China
Prof. Lishchynskyy, Igor	Vorkarpaten-Univ.	Ukraine
Dr. Malek, Jiri	Institute of Physics ASCR Prague	Czech Rep.
Prof. Manivasagam, Geetha	VIT Univ.	India

Name	Home Institute	Home country
Meinero, Martina	Univ. Genua	India
Dr. Morozov, Igor	Lomonosov Moscow State Univ.	Russia
Prof. Dr. Morr, Dirk	Univ. of Illinois at Chicago	USA
Muratovic, Senada	Ruder Boskovic Institute Zagreb	Croatia
Prof. Dr. Naidiuk, Iurii	Verkin Institute Kharkiv	Ukraine
Dr. Nussinov, Zohar	Washington Univ.	USA
Oki, Hayami	Univ. Niigata, Japan	China
Prof. Dr. Ovchinnikov, Yuri	Landau Institute	Russia
Prof. Dr. Pozek, Miroslav	Univ. Zagreb	Croatia
Dr. Reja, Sahinur	Univ. of Cambridge	India
Dr. Rusz, Jan	Uppsala Univ.	Sweden
Dr. Sadhukhan, Banasree	Univ. Kolkata Indian	India
Dr. Setti, Thirupathaiah	Indian Institute of Science	India
Shipulin, Ilya	Lebedev Physical Insititute, Moskau	Russia
Shipunov, Grigory	Lomonosov Moscow State Univ.	Russia
Silkin, Ilia	Lomonosov Moscow State Univ.	Russia
Singh, Harish Kumar	Theoretical Science Univ., India	India
Prof. Dr. Sobczak, Natalia	Foundry Research Institut	Poland
Dr. Sopu, Daniel	IC MAS Bochum	Romania
Sudarkova, Svetlana	Lomonosov Moscow State Univ.	Russia
Dr. Valligatla, Sreeramulu	CNR-IFN Trento	Italy
Dr. Vavilova, Evgeniia	Zavoisky Physical-Technical Institute Kazan	Russia
Dr. Volegov, Alexey	Ural Federal Univ.	Russia
Dr. Wang, Jiawei	Hong Kong Univ.	China
Dr. Wang, Jing	Univ. of Science a. Technology of China	China
Yang, Jingzhong		China
Dr. Yerin, Yuriy	Institute for Physics Nizhny Novgorod	Ukraine
Dr. You, Jhih-Shih	Harvard Univ.	Taiwan
Zhang, Yang	Tsinghua Univ.	China
Prof. Dr. Zotos, Xenophon	Univ. Crete	Greece

Scholarships

Name	Home Institute	Home country
Prof. Dr. Ling, Christopher	USA	Alexander von Humboldt Stiftung
Prof. Dr. Monaico, Eduard	Moldau, Rep.	Alexander von Humboldt Stiftung
Dr. Ghimire, Madhav Prasad	Nepal	Alexander von Humboldt Stiftung
Prof. Dr. Pozek, Miroslav	Croatia	Alexander von Humboldt Stiftung
Dr. Wenig, Qunhong	China	Alexander von Humboldt Stiftung
Dr. Morrow, Ryan Christopher	USA	Alexander von Humboldt Stiftung
Morari, Vadim	Moldau, Rep.	Alexander von Humboldt Stiftung
Dr. Wang, Xiaoxia	China	Alexander von Humboldt Stiftung
Herzog-Arbeitman, Abraham	USA	DAAD
Dr. Stepanov, Alexey	Russia	DAAD
Dr. Kamashev, Andrey	Russia	DAAD
Permana, Antonius Dimas Chandra	Indonesia	DAAD
Mershiev, Ivan	Russia	DAAD
Dedkova, Katerina	Czech Rep.	DAAD
Meinero, Martina	Italy	DAAD
Kuo, Mei-Tsan	Germany	DAAD
Ghunaim, Rasha	Palestinian territories	DAAD
Shahid, Rub Nawaz	Pakistan	DAAD
Dr. Makharza, Sami A M	Palestinian territories	DAAD
Dr. Bera, Supriya	India	DAAD
Prof. Dr. Ganesan, Vellaichamy	India	DAAD
Dr. Hong, Xiaochen	China	DAAD
Wu, Yuhao	China	DAAD
Dr. Yershov, Kostiantyn	Ukraine	BMBF UKRATOP
Dr. Romaka, Vitaliy	Ukraine	BMBF UKRATOP
Bezghuba, Volodymyr	Ukraine	BMBF UKRATOP
Salman, Omar Oday	Iraq	Graduate Academy TU Dresden
Thirathipviwat, Pramote	Thailand	Graduate Academy TU Dresden
Dr. Körner, Julia	Germany	DFG - Rückkehrstipendium
Dantas de Lima, Herik	Brazil	Univ. Federal do Rio Grande
de Almeida, Renan	Brazil	Univ. of Sao Paulo
Fernandes Andreoli, Angelo	Brazil	CAPES Foundation
Romero da Silva, Murillo	Brazil	CAPES Foundation
Batalha, Rodolfo Lisboa	Brazil	CAPES Foundation
Dr. Tynell, Tommi Paavo	Finland	Finish Cultural Foundation
Park, Eunmi	South Korea	Intern. Graduate School
Yousefli, Soroor	Islamic Republic of Iran	Iran
Dr. Smirnova, Ekaterina	Russia	Russia + DFG
Sabaghi, Davood	Islamic Republic of Iran	Iran
Lara Ramos, David Alberto	Mexico	National Council of Mexico
Shin, Daseul	South Korea	POSTECH
Gorbunov	Mikhail	Russia

Name	Home Institute	Home country
Wang, Dan	China	Soochow Univ.
Xu, Haifeng	China	China Scholarship Council
Chen, Hongyu	China	China Scholarship Council
Wang, Ju	China	China Scholarship Council
Feng, Le	China	China Scholarship Council
Deng, Liang	China	China Scholarship Council
Ding, Ling	China	China Scholarship Council
Liu, Lixiang	China	China Scholarship Council
Xue, Peng	China	China Scholarship Council
Lu, Qiongqiong	China	China Scholarship Council
Kang, Sun	China	China Scholarship Council
He, Tianbing	China	China Scholarship Council
Li, Tianming	China	China Scholarship Council
Lu, Tiwen	China	China Scholarship Council
Han, Xiaoliang	China	China Scholarship Council
Fan, Xingce	China	China Scholarship Council
Hao, Yajuan	China	China Scholarship Council
Li, Yang	China	China Scholarship Council
Liu, Zhenhui	China	China Scholarship Council
Li, Zichao	China	China Scholarship Council
Wang, Pei	China	China Scholarship Council

Guest stays of IFW memebers at other institutes 2018

Seung Ho Baek	Changwon National University Seoul, Korea, scientific cooperation, 22.07.2018 - 12.08.2018
Monica Fernandez Barcia	ETH Zürich, Switzerland, Training in ITN-SELECTA-Project, 17.02.2018 - 17.03.2018
Jeroen van den Brink	Univ. of Amsterdam, The Netherlands, NWO-Von Humboldt Research Award - Research stay, 03.09.2018 - 30.11.2018
Aliaksei Charnukha	University of California San Diego, USA, measurements, 06.05.2018-02.06.2018 & 18.11.2018-11.12.2018
Alexander Fedorov	St. Petersburg Univ. Russia, Spin ARPES Measurements, 08.02.2018-24.02.2018
Matthias Gillig	High Field Magnet Laboratory Nijmegen, The Netherlands, 01.05.2018-16.05.2018
Romain Giraud	CNRS Grenoble, France, Collaboration with Spintec Grenoble, 22.01.2017-08.02.2017, 09.04.2018-27.04.2018, 27.08.2018-12.09.2018
Junhee Han	Korea Institute of Industrial Technology KITECH, Seoul, South Korea, Research Cooperation, 01.06.2018 - 19.06.2018 & 13.11.2018 - 01.12.2018
Xiaochen Hong	High Field Magnet Laboratory Nijmegen, The Netherlands, 01.05.2018-16.05.2018
Ivan Kaban	Yale Univ., New Haven, USA, Research Cooperation, 29.09.2018 - 17.10.2018
Andrey Kamashev	Zavoisky Institute Kazan, Russia, Measurements and research cooperation, 12.03.2018-11.04.2018
Emmanouil Koutsouflakis	PSI Villigen, Switzerland and ESRF Grenoble, France, Measurements at Swiss Light Source and ESRF, 18.09.2018-09.10.2018
Rafael Gregorio Mendes	Soochow Univ. Suzhou, China, Measurements and Research Cooperation, 02.04.2018 - 27.04.2018
Lauritz Schnatmann	Ioffe Institue St. Petersburg, Russia, research stay in the framework of the DFG-RSF Project NI 616/22-1, 04.04.2018 - 30.05.18
Lukas Spree	PSI Villigen, Switzerland and ESRF Grenoble, France, Measurements at Swiss Light Source and ESRF, 18.09.2018-09.10.2018
Quang Huy Ta	Soochow Univ. Suzhou, China, Measurements and Research Cooperation, 08.12.2018 - 22.12.2018
Aoyu Tan	CNRS Grenoble, France, Collaboration with Spintec Grenoble, 28.08.2018-11.11.2018
Georgios Velkos	PSI Villigen, Switzerland, Measurements, 23.04.2018-08.05.2018
Xenophon Zotos	Heraklion Univ., Greece, Mercator fellowship & lectures, 28.02.2018-14.05.2018 & 29.07.2018-01.12.2018

Board of trustees

Dr. Babett Gläser, Saxonian Ministry of Science and Art - Head -
Dr. Peter Schroth, Federal Ministry of Education and Research
Prof. Dr. Gerhard Rödel, TU Dresden
Prof. Dr. Manfred Hennecke, Berlin

Scientific Advisory Board

Prof. Dr. Maria-Roser Valenti, Univ. Frankfurt, Germany -Head-
Prof. Dr. Robert H. Blick, Univ. Hamburg, Germany
Prof. Dr. Sang-Wook Cheong, Rutgers, USA
Prof. Dr. Andrey Chubukov, Univ. of Minnesota, USA
Prof. Dr. Ralph Claessen, Univ. Würzburg, Germany (up to 31.12.2018)
Prof. Dr. Matthias Göken, Univ. Erlangen-Nürnberg, Germany
Dr. Heinz Neubert, Siemens AG, Germany
Prof. Dr. Nini Pryds, TU Denmark Lyngby, Denmark
Dr. Jürgen Rapp, Robert Bosch GmbH, Germany
Prof. Dr. Roberta Sessoli, Univ. di Firenze, Italy
Prof. Dr. David Johnson, Univ. of Oregon (from 01.10.2018 on)